Microwave Imaging of Saturn's Deep Atmosphere and Rings

Thesis by

Arie William Grossman

In Partial Fulfillment of the Requirements
for the Degree of
Doctor of Philosophy

California Institute of Technology
Pasadena, California

1990
(Submitted May 30, 1990)

Dedicated to my parents
with love and affection.

Acknowledgements

It is a privilege to have been a graduate student in the division of Geological and Planetary Sciences at Caltech during a time of great discovery in our solar system. I am fortunate to have been able to work with talented and gifted people and am grateful to have this opportunity to thank them.

Above all, I am indebted to my advisor and mentor, Dewey Muhleman, whose guidance and advice have greatly contributed to my development as a scientist. This work began at his suggestion, and its completion would not have been possible without his assistance and encouragement. I am also grateful for his including me in his intellectual sphere and for sharing with me his curiosity and wisdom of the world we live in.

The observations presented here would not have been possible without the assistance of the people who make the VLA and the Owens Valley observatories operate at peak efficiency. I would especially like to thank Glenn Berge whose assistance and careful attention to detail have aided me enormously.

Many friends at Caltech have made the experience of graduate school enjoyable. I would especially like to thank Don Rudy, whose friendship and support have helped me greatly. I thank the rest of my friends by way of a story, which may help them to explain to their friends and loved ones why they persist with their graduate careers.

A man goes to a doctor and says, "Doctor, Doctor, I have a terrible problem. My brother thinks that he's a chicken."

The Doctor says, "Your brother isn't a chicken. Just tell him that."

"But I can't, " says the man, "we need the eggs."

With eternal gratitude, I wish to thank Sharon Vinick for her infinite patience and understanding during what must have been a very difficult and stressful time in her life. Her contribution to this work can be measured by her steadfast faith, support, and love during the difficult periods of this research. I treasure her curiosity and humor. Every day, I am reminded by her of the mystery and wonder of the universe.

Finally, I wish to thank my parents Vera and William Grossman, and my sister Dorit Grossman, for their confidence in me. This work would not have come to fruition without the love and support of my family. It is with great pleasure that I dedicate this work to my parents.

Abstract

This work presents an analysis of microwave images of Saturn's atmosphere and rings. Interferometer observations at wavelengths of 0.27, 2.01, 3.53, 6.17, and 20.13 centimeters and precise application of synthesis imaging techniques yielded brightness and polarization maps of unsurpassed resolution and sensitivity. Linear polarization is detected from the ring ansea, and brightness variations in the deep atmosphere and the rings are revealed for the first time.

The disk-integrated spectrum of Saturn is interpreted within the context of a radiative transfer model that requires the NH_3 mixing ratio to take on a value of 0.9 to 1.1 $\times 10^{-4}$ (0.5–0.6 times solar) directly below the ammonia ice cloud at a pressure of 1.4 bar. The NH_3 mixing ratio increases with depth to a value of 5.0 to 6.5 $\times 10^{-4}$ (2.9–3.7 times solar) at a pressure of 6 bar. The variation of NH_3 with depth can be entirely accounted for by the presence of 11–14 times solar abundance of H_2S, which reacts with NH_3 to produce a substantial NH_4SH cloud.

Latitudinal variations in brightness temperature indicate that the saturated vapor abundance of ammonia decreases by 50% from equator to pole within the cloud deck. At greater depths the latitudinal variations of ammonia are consistent with alternating zones of concentration and depletion caused by vertical motions. An apparent depletion in northern mid-latitudes is well-correlated with a decrease in infrared opacity and depressed cloud top levels, indicating deep-seated downwelling.

The size, composition, and shape of particles comprising the rings of Saturn are constrained by modeling the emission, scattering, and extinction of radiation by the rings. The observations can be fit by a incremental power-law particle size distribution with exponent in the range 2.6–3.0 for the combined A and B rings, assuming a classical many-particle-thick layer. The wavelength dependence of the optical depths places a strict lower limit of 1 cm on particle sizes in the classical rings. Observations of thermal emission from the rings further constrain the mass fraction of uniformly mixed silicate impurities to be less than 1%. Azimuthal variations in brightness and linear polarization rule out the possibility that the particles are smooth, convex objects, and favor a model in which the particles are irregularly shaped.

Contents

List of Figures

List of Tables

Chapter 1

Introduction

Saturn, the most distant planet known to ancient astronomers, has always been a source of wonder and mystery. The telescopic discovery of "rings" by Galileo in 1610, sparked interest in observations of the planet, but it was not until his death in 1642 that Saturn became a subject worthy of scientific study. The following centuries saw a remarkable increase in our knowledge of Saturn with the discovery by Cassini of a dark band separating the rings and faint markings on the disk. The true beauty and intricate structure of the rings and atmosphere was not appreciated until the Voyager spacecraft returned stunning close-up pictures.

Voyager observations showed the atmosphere to be a cloud-covered, turbulent regime, with strong axisymmetric zonal flows at velocities of up to 500 meters per second. The rings were revealed to be complex structures, heavily modified by dynamical interactions. The nature of the atmosphere below the visible cloud layer and the properties of the individual ring particles, however, were not well-constrained. Atmospheric observations, limited by the optically thick clouds, were restricted to the upper troposphere and stratosphere. Radio occultations of the rings were limited to probing the thinnest parts of the rings. These observations can be complemented by Earth-based microwave observations.

The Saturn system is no less beautiful in the microwave region of the electromagnetic spectrum. This work presents microwave images of unprecedented resolution and sensitivity at five wavelengths spanning the range 0.27-20.13 centimeters. Observations are also presented of the first detection of linearly polarized emission from the rings. At this wavelength, microwaves penetrate the cloud tops and probe the atmospheric to a level inaccessible to conventional remote sensing techniques. In addition, microwaves probe the rings at wavelengths comparable to the individual particle sizes, and can constrain the properties of these particles by sensing emission, scattering, and extinction of radiation from them.

This work is dedicated to the analysis and interpretations of these images. The

images are analyzed in the context of models that seek to explain specific aspects of the observations. The temptation is great, however, to focus on the details of model building and lose sight of the original problem. This work attempts to strike a balance between developing complex models that reproduce observed properties, and simple models that provide insight into the relevant physics.

1.1 Motivation

This study is primarily motivated by recent advances in radio interferometry and synthesis imaging techniques, which provide new tools for the study of planetary systems. Previous single-dish microwave observations of Saturn lacked resolution to properly distinguish the atmosphere from the rings. Early interferometric observations of Saturn were carried out on a small number of baselines, and suffered from poor sensitivity and resolution. As a result, observers were limited to fitting models to the visibility data rather than analyzing images. This type of analysis is inherently restricted to simple models and requires making some assumptions about the brightness distribution of Saturn. Aperture synthesis images of Saturn are free from many assumptions about the brightness distribution. The first aperture synthesis images of Saturn (Schloerb, 1979b) confirmed many of the initial results of microwave studies of Saturn and validated the technique of synthesis imaging.

The observations presented here were conducted at two of the world's premier microwave interferometers: the Very Large Array (VLA) and the Owens Valley millimeter wave interferometer. State-of-the-art, low-noise receivers and electronics were used to acquire high-quality data. Recent advances in synthesis imaging techniques were applied, where possible, to improve the quality of the data. The resulting images reveal a new and unexplored aspect of the Saturn system.

The microwave images of Saturn probe the atmosphere below the visible clouds in the range 1–10 bar. Previous determinations of atmospheric composition, temperature, and dynamics were limited to altitudes in the stratosphere and troposphere above this level. It is well known that the atmosphere is primarily composed of hydrogen and helium, with minor amounts of methane uniformly mixed throughout. Ammonia is observed in the troposphere, where it condenses to form an ice cloud, which most likely accounts for the visible cloud layer. The global abundance of ammonia at depth is not well known. Hydrogen

sulfide and water are also expected to be present based on a solar mix of elements, however neither have been directly detected. The composition below the cloud is not accessible to conventional remote sensing techniques, but the current microwave observations can place some constraints on the sub-cloud composition.

The primary source of atmospheric opacity at radio wavelengths is gaseous ammonia. Given a temperature profile of the atmosphere, microwave observations can be inverted to yield the abundance of ammonia with depth. The absolute determination of ammonia abundance is of interest for answering questions regarding the composition of the atmosphere, but ammonia also plays a vital role as a tracer of thermo-chemical and dynamical processes in the atmosphere. For example, ammonia readily reacts with hydrogen sulfide (H_2S) to form a particulate cloud of ammonium hydrosulfide (NH_4SH). Although this particulate cloud is not directly observable, the change in ammonia abundance by condensation in this cloud is, in theory, observable, and can be used to place constraints on the abundance of H_2S. Because ammonia is a condensate in the troposphere, observed variations in the horizontal distribution of ammonia are suggestive of vertical motions in the atmosphere.

The detection of a substantial radar echo from the rings coupled with their low brightness temperature has been interpreted to indicate that the ring particles are good scatterers and poor absorbers of microwaves. This is consistent with the properties of cold water ice and has some interesting consequences for radio observations. Because pure ice has a low emissivity at radio wavelengths, measurements of thermal emission at millimeter wavelengths can be used to constrain the size of the largest particles and the amount of silicate impurities mixed with the ice. At longer wavelengths the rings are efficient scatterers, and their brightness is primarily due to scattering of the thermal emission of Saturn. This presents a unique scattering experiment that contains some information about the scattering phase function and the shape of the individual ring particles. Finally, observations of the rings in the region where they occult the disk can be used to determine their optical depths and can place constraints on the size of the ring particles.

Microwave imaging is a powerful technique in our study of Saturn. It is hoped that the results presented here can be used in conjunction with other measurements and theories to increase our understanding of the Saturn system. While the results are presented specifically for the planet Saturn, the underlying analysis has wider applications to the study of the Jovian planets and rings systems as well as to the practical applications of synthesis

imaging in planetary astronomy.

1.2 Overview

This presentation proceeds in the natural order of scientific investigation from observation to analysis to modeling to interpretation, and hopefully ends with an enlightened understanding of the Saturn system. The chapters are organized as follows.

Chapter 2 begins with an introduction to the technique of interferometry and synthesis imaging. This is followed by a description of the observing instruments and the observing programs. The calibration and reduction of the data is also discussed. The chapter continues with a discussion of the practical details of imaging Saturn, and ends with a presentation of five images of radio brightness and three of linear polarization.

Chapter 3 presents some preliminary geometries and transformations necessary to analyze the images. The simple model consisting of uniformly bright regions is fit to the images. The images are transformed to geometries, which allows allowing a determination of atmospheric brightness variations as a function of latitude and ring brightness variations as a function of mean scattering angle in the ring plane.

Chapter 4 presents a thermo-chemical, radiative transfer model of the Saturn troposphere. The model is first applied in the forward or direct method. That is, the physical parameters of the atmosphere (pressure, temperature, composition, etc...) are specified and the resulting radiation field is compared with the observations. The inverse problem is more difficult, but a simple inversion is used to characterize the vertical distribution of ammonia. Implications of the results for the dynamics of the atmosphere is discussed.

Chapter 5 focuses on modeling and interpretation of the ring observations. The ring brightness is characterized by three terms: thermal emission, scattering, and extinction. Each component is used to constrain the size, composition, and shape of the ring particles.

The final chapter summarizes the major conclusions and results arising from this work. Open questions and directions for future research are discussed.

Chapter 2

Observations, Data Reduction and Imaging

Interferometric observations of Saturn were conducted during 1986–1988 when the inclination of the ring plane with respect to the Earth was near maximum. This geometry provided a clear unobstructed view of the Northern hemisphere of the planet as well as maximum spatial resolution on the ring ansea: an ideal situation for imaging the Saturn system.

The focus of this chapter is producing the highest quality images of Saturn from interferometer observations. Ironically, the interferometer telescope contains no equivalent to a focal plane; there is no eyepiece in which to view the target. The magnificent images of an interferometer are produced in a computer, and so, some discussion of the computational methods used to produce the final images of Saturn is warranted.

This chapter begins with a brief review of the principles of radio astronomy and interferometry with particular emphasis on those aspects applicable to planetary observations. This is followed by a description of the specific Saturn observing program and the subsequent calibration and data reduction techniques. The final section discusses the process of creating radio maps of Saturn, a technique referred to as imaging.

2.1 Theory of the Instrument

Because some readers may be unfamiliar with the operation of an interferometer, this section is devoted to a discussion of the theory of interferometry and aperture synthesis. Extensive reviews of the subject are given in Fomalont and Wright (1974), and in Thompson, Moran and Swenson (1986).

2.1.1 Visibility

Each antenna or element of an interferometer detects the incident radiation field as a function of time and position. The resulting signal from each pair of elements is multiplied in a correlator to produce the fundamental observable of an interferometer, the visibility function $\mathcal{V}(u,v,w)$. The visibility is expressed in units of *flux density* and is measured in watts per square meter per hertz ($\mathrm{W\,m^{-2}\,Hz^{-1}}$). The unit of flux density is the Jansky (Jy); $1\mathrm{Jy} = 10^{-26}\mathrm{W\,m^{-2}\,Hz^{-1}}$. The visibility is a function of the vector baseline separating the two elements, and has components (u,v,w) in a right-handed coordinate system where u and v are measured in a plane normal to the direction of interest, v to the north and u to the east. The component w is measured in the direction of the center of the field of view and this point defines a phase reference position for the observation.

The electrical phase of the two elements is continuously adjusted for the Earth's rotation so that a signal from the reference position, passing through the two elements, arrives at the correlator with the same phase. In this way the interferometer is electronically "pointed" to the region of interest.

The visibility function resulting from an observation provides little intuitive information. Instead one is usually interested in determining the distribution and direction on the sky of received energy. In mapping an extended radio source the desired quantity is the *radio brightness* or intensity, I, the units of which are $\mathrm{W\,m^{-2}\,Hz^{-1}\,sr^{-1}}$, that is, flux density per steradian. The natural unit of brightness on a radio map is usually expressed in terms of the solid angle of the resolving beam, hence, Jy/beam.

Often the radio brightness is expressed as a *brightness temperature* in units of Kelvin. This transformation can be derived by considering the thermal radiation from an ideal blackbody. According to the Planck law in the Rayleigh–Jeans approximation, the brightness is related to the physical temperature T of the radiating matter by the equation

$$I = \frac{2kT\nu^2}{c^2}, \tag{2.1}$$

in the domain where $h\nu \ll kT$. Here ν is the frequency, k is Boltzmann's constant, c is the velocity of light, and h is Planck's constant. For an observed brightness I originating from a solid angle Ω, one can rewrite equation 2.1 to define an equivalent brightness temperature T_B:

$$T_B = \frac{c^2 I}{2k\nu^2\Omega}. \tag{2.2}$$

Because intensity is directly proportional to brightness temperature in this limit, it is often convenient to replace intensity by brightness temperature.

The brightness refers to a particular direction on the sky. It is common to employ a Cartesian coordinate system on the sky centered on the phase reference position. The sky brightness, $I(x,y)$, can then be described as a function of eastward displacement x, and northern displacement y. This geometry naturally relates the observed visibility to the desired sky brightness.

2.1.2 Relationship between visibility and brightness

The general response of a two-element interferometer to the sky brightness is a sinusoidal fringe similar to Young's fringes, with a maximum response at the reference position. The measured visibility is the spatial coherence function of the incident electric field. The relationship between the measured visibility and the brightness distribution of an extended source is given by the van Cittert-Zernike Theorem (see Born and Wolf, 1980, p. 510 for a derivation). The visibility function and the apparent brightness are three-dimensional Fourier pairs. However, if we limit our observations to a small region of the sky, the w dependence of the visibility becomes negligible, and we are left with the simpler, two-dimensional Fourier relation between visibility and sky brightness:

$$\mathcal{V}(u,v) = \int_{\infty}^{\infty}\int_{\infty}^{\infty} I(x,y)e^{-2\pi i(ux+vy)}dxdy. \tag{2.3}$$

Because equation 2.3 is a Fourier transform, the direct inversion yields the sky brightness:

$$I(x,y) = \int_{\infty}^{\infty}\int_{\infty}^{\infty} \mathcal{V}(u,v)e^{2\pi i(ux+vy)}dudv. \tag{2.4}$$

It is clear from equation (2.4) that the sky brightness can be derived by measuring the visibility everywhere in the (u,v) plane. Aperture synthesis is essentially a technique whereby a large number of visibility samples are measured. This is accomplished by two methods. As the earth rotates, the projection on the sky of the baseline separating two elements traces out a path in the (u,v) plane. Earth rotation synthesis takes advantage of the rotation of the Earth to observe the visibility at many (u,v) positions. A less elegant solution is simply to move the elements from one spacing to another, and thereby sample at many (u,v) spacings. The observations reported here employ both methods of aperture synthesis.

In practice, $\mathcal{V}$ is not known everywhere, and the inverse transform given in equation 2.4 is not well-defined.

2.1.3 Inversion of visibility

The greatest deficiency in aperture synthesis is the undersampling of the visibility function in the (u, v) plane. In particular, the visibility is usually poorly sampled at the shortest spacings because of the finite diameter of the antennas, and at the longer spacing because of the limited length of the baselines. These limitations determine both the largest scale structures that can be observed, as well as the fine scale resolution in the final image. In addition, the (u, v) coverage may contain gaps and holes in unsampled regions.

The visibility sampling can be described by a sampling function, $S(u, v)$, that is zero where no data have been taken. The Fourier transform of the observed visibilities is then

$$I^D(x, y) = \int_{\infty}^{\infty} \int_{\infty}^{\infty} S(u, v)\mathcal{V}(u, v)e^{2\pi i(ux+vy)}dudv, \tag{2.5}$$

where $I^D(x, y)$ is called the "dirty" image (section 2.4.2 describes a deconvolution algorithm called CLEAN). Its relation to the true intensity distribution $I(u, v)$ is

$$I^D = I * B, \tag{2.6}$$

where the asterisk denotes convolution and

$$B(x, y) = \int_{\infty}^{\infty} \int_{\infty}^{\infty} S(u, v)e^{2\pi i(ux+vy)}dudv, \tag{2.7}$$

is the synthesized beam or point spread function corresponding to the sampling function $S(u, v)$. $B(x, y)$ is just the response of the interferometer to a point source of unit flux density.

Equation 2.6 says that the Fourier transform of the measured visibility I^D is the true intensity convolved with the synthesized beam B that usually contains large sidelobes, irregular structure, and poorly defined resolution. Section 2.4 discusses methods of recovering the true intensity by deconvolving the synthesized beam from the dirty map.

The synthesized beam is not to be confused with the primary beam or normalized reception pattern of the individual interferometer elements. This reception pattern describes the sensitivity of the antennas to the direction of arrival of radio radiation. The primary

beam falls rapidly to zero outside a region centered at the pointing center of the elements. The source, however, is usually small compared to the primary beam, and the effect requires at best a minor correction.

2.1.4 Polarimetry

The electromagnetic field is a vector phenomena, and the polarization properties carry interesting physical information. The vector electric field can be written

$$\mathbf{E} = \hat{\mathbf{e}}_{\mathbf{x}} E_x cos(\omega t) + \hat{\mathbf{e}}_{\mathbf{y}} E_y cos(\omega t - \delta), \tag{2.8}$$

where E_x and E_y are the electric field amplitudes in the x and y directions and δ is the phase difference between the two orthogonal modes.

The response of an interferometer to partially polarized radiation can be expressed by the four Stokes parameters (I, Q, U, V), which all have the same dimension, and are related to the amplitude components of the electric field, E_x and E_y. The Stokes parameters are defined as follows:

$$I = \left\langle E_x^2 + E_y^2 \right\rangle, \tag{2.9a}$$

$$Q = \left\langle E_y^2 - E_x^2 \right\rangle, \tag{2.9b}$$

$$U = \langle 2E_x E_y \cos\delta \rangle, \tag{2.9c}$$

$$V = \langle 2E_x E_y \sin\delta \rangle, \tag{2.9d}$$

where $\langle\rangle$ denotes a time average. Of the four Stokes parameters, I is a measure of the total power, Q and U represent the linearly polarized component (referenced to the plane defined by the x and y directions), and V represents the circularly polarized component.

The Stokes parameters can be converted to a direct measure of polarization by forming the following combinations:

$$p_l = \frac{\sqrt{Q^2 + U^2}}{I}, \tag{2.10a}$$

$$p_c = \frac{V}{I}, \tag{2.10b}$$

$$p_t = \frac{\sqrt{Q^2 + U^2 + V^2}}{I}, \tag{2.10c}$$

$$\psi = \frac{1}{2} \tan^{-1}\left(\frac{U}{Q}\right), \tag{2.10d}$$

where p_l, p_c, and p_t are the degrees of linear, circular, and total polarization, and ψ is the position angle of the plane of linear polarization.

For an unpolarized signal, $Q = U = V = 0$, while for a fully polarized signal, $I^2 = Q^2 + U^2 + V^2$. However, all four parameters are required to describe the general case of a partially polarized signal. In most cases we explicitly discuss the total intensity I, but because all the Stokes parameters have units of intensity, the term I can be replaced by a linear combination of the various Stokes parameters. Similarly, each of the Stokes parameters has an associated visibility function, that we denote $\mathcal{V}_I$, $\mathcal{V}_Q$, $\mathcal{V}_U$, and $\mathcal{V}_V$. Thus, one can map any Stokes parameter by using the appropriate Stokes visibility measurement.

2.2 Observations

Observations of Saturn at five wavelengths in the range 0.27-20.13 cm were conducted at the Very Large Array (VLA), constructed by the National Radio Astronomical Observatory and operated by Associated Universities Inc. under contract with the National Science Foundation, and at the Caltech Millimeter Wave Interferometer at the Owens Valley Radio Observatory (OVRO). This section describes the characteristics of the two instruments and provides a summary of the observing strategy.

2.2.1 The Very Large Array

The VLA synthesis telescope consists of twenty-seven 25 meter diameter antennas arranged in a Y shape on the Plains of San Augustin in New Mexico (Napier, Thompson, and Ekers, 1983). Each arm of the Y is about 21 km long in the North, Southwest, or Southeast direction. The antennas are moved among four standard, scaled configurations in which the most distant antenna is 21, 6.4, 1.95 or 0.59 km from the center of the array. The four standard configurations, termed the A, B, C, and D arrays, correspond to a maximum antenna separation of about 36, 11, 3, and 1 km. During array reconfiguration, the VLA operates in a hybrid mode in which the antennas on the North arm remain extended with respect to the other elements. The A/B configuration, for example, consists of 9 elements on the North arm in the 21 km, A, configuration, and the remaining elements in the shorter B configuration.

The antennas are equipped with cryogenically cooled receivers, and are connected to the correlator electronics by a low-loss waveguide. The cross-correlation products for each

of the 351 pairs of 4 independent IF signals are measured by a 50-MHz bandwidth digital correlator. This allows simultaneous reception in two orthogonal circular polarizations in two adjacent 50-MHz bands.

2.2.2 Centimeter observations at the VLA

Observations were conducted at the VLA during 1986-1988 and are summarized in Table 2.1. The observing date is shown in column 1. The observing wavelength, frequency, and effective bandwidth are shown in columns 2-4. Columns 5 and 6 show the position of Saturn, while columns 7, 8, and 9 show the array configuration, the maximum baseline in units of kilo-wavelengths ($\lambda \times 10^3$), and the effective received Stokes parameters. Columns 9 and 10 show the Geocentric distance to Saturn and the Saturnocentric latitude of the Earth.

Table 2.1: Summary of VLA observations of Saturn.

IAT Date	λ (cm)	ν (MHz)	Bw (MHz)	RA (h m)	DEC (d m)	Vla conf.	Max. Bl. ($\lambda \times 10^3$)	Stokes param.	Dist. (Au)	B^1
27 May 1986	20.13	1490	100	16 20	-19 24	A	180	IQUV	8.98	25.3
28 May 1986	20.13	1490	100	16 20	-19 23	A	180	IQUV	8.98	25.3
22 Jun 1986	6.17	4860	100	16 12	-19 07	A/B	360	IQUV	9.07	25.1
24 Jun 1986	6.17	4860	100	16 12	-19 06	A/B	360	IQUV	9.08	25.1
14 Jul 1986	2.01	14940	100	16 08	-18 59	B	550	IQUV	9.29	25.0
17 Jul 1986	20.13	1490	100	16 07	-18 58	B	55	IQUV	9.32	25.0
30 Sep 1986	2.01	1490	100	16 15	-19 35	B/C	370	IQUV	10.49	25.6
20 Jun 1988	3.53	8495	6.25	17 57	-22 18	C/D	65	I	9.03	26.5

[1]Saturnocentric latitude of the Earth.

The observations at 2.01, 6.17, and 20.13 cm were designed to achieve a suitable compromise between spatial resolution and sensitivity to low brightness features. In order to measure the visibility at many (u, v) spacings (see section 2.1.2) the interferometer tracked Saturn from horizon to horizon for periods as long as 8 hours. In addition, observations at 2.01 and 20.13 cm were made in two different array configurations with the expectation of combining both configurations to produce an improved map. A hybrid configuration was used in some cases to compensate for the low declination of Saturn and the resulting foreshortening of North-South baselines.

The observations at 2.01, 6.17, and 20.13 recorded the complex visibility on four

independent IFs: two in each orthogonal polarization in two adjacent bandwidths of 50 MHz. A large bandwidth results in smearing of the data in the radial direction. Therefore, this technique provides all four Stokes parameters with the effective sensitivity of a large, 100-MHz bandwidth but with the reduced smear corresponding to a bandwidth of 50 MHz.

The 1988 observations of Saturn at 3.53 cm were obtained simultaneously with an experiment designed to measure the radar echo from Saturn's rings. Thus the observational parameters were optimized for receiving the radar signal, and do not necessarily coincide with the best parameters for continuum observations. In particular, the observing bandwidth of 6.25 MHz decreased the sensitivity of the measurements, and only the left-circular polarization was received. As will be shown in section 2.4, this is equivalent to receiving only the I Stokes parameter, since the V stokes component is essentially zero. The array was in the compact configuration for the 3.53 cm observations, resulting in comparatively less resolution then the other observations. In addition, the experiment, which was scheduled to observe for 15 hours, yielded less than 3 hours of observational data. Nevertheless, the resulting observations provide one additional data point in the radio spectrum of Saturn.

2.2.3 The Owens Valley Radio Observatory millimeter interferometer

The OVRO millimeter interferometer, located near Big Pine, California, consists of three 10.4 meter diameter dishes aligned on a track that has the form of an inverted T (Masson *et al.*, 1985). The antennas are moveable among a set of fixed stations along the track out to a maximum distance of 100 meters on the East and West arms, and 140 meters on the North arm.

Each antenna is equipped with an SIS receiver (Woody, Miller, and Wengler, 1985), that is cryogenically cooled to maintain a system temperature of less than 200 K at a wavelength of 3 millimeters. The receiver is attached to a linearly polarized feed system, that maintains a fixed orientation with respect to the antenna. The single polarization IF signal from the receiver is detected in two sidebands of bandwidth 400 MHz in continuum mode, and the resulting signals from each antenna are correlated to provide three pairs of complex visibility measurements in each sideband. Although the receiver detects both sidebands, the receiver gain is optimized in one of the sidebands at the expense of the other. As a result, only one sideband contains a useful signal.

2.2.4 Millimeter observations at OVRO

Observations were conducted at OVRO over a period of 15 months during 1986-1988 and are summarized in Table 2.2. The observing date is shown in column 1. Columns 2 and 3 show the position of Saturn, while columns 4, 5, and 6 show the maximum projected baseline length in units of kilo-wavelengths ($\lambda \times 10^3$), the Geocentric distance to Saturn, and the Saturnocentric latitude of the Earth (also referred to as the ring angle, B).

Table 2.2: Summary of OVRO observations of Saturn.

IAT Date	RA (h m)	DEC (d m)	Max. Bl. ($\lambda \times 10^3$)	Dist. (Au)	B^1
27 Nov 1986	16 40	-20 39	16	10.99	26.3
20 Jan 1987	17 06	-21 22	21	10.73	26.6
21 Jan 1987	17 06	-21 22	21	10.72	26.6
1 Feb 1987	17 11	-21 27	24	10.58	26.6
4 Feb 1987	17 12	-21 28	24	10.54	26.6
30 May 1987	17 11	-21 20	29	9.03	26.5
7 Jun 1987	17 09	-21 18	17	9.01	26.5
19 Jan 1988	17 50	-22 18	54	10.87	26.7
20 Jan 1988	17 50	-22 18	54	10.87	26.7
21 Jan 1988	17 50	-22 18	40	10.86	26.6
22 Jan 1988	17 51	-22 18	40	10.85	26.6

[1]Saturnocentric latitude of the Earth.

Our primary intention was to minimize the variation in the ring angle (the Saturnocentric latitude of the Earth) so that observations at many (u, v) spacings could be combined to produce a single high-resolution map of the Saturn system. During the course of the observations, the Saturnocentric latitude of the Earth remained near constant at 26.5 ± 0.2 degrees. Observations tracked Saturn from horizon to horizon at a frequency of 110.210 GHz (0.27 cm) with an effective bandwidth of 400 MHz.

2.3 Calibration

The purpose of calibration is to remove, insofar as possible, the effect of instrumental factors in the measurement of the visibility. Such factors depend on the individual antennas or antenna pairs, and include determining the antenna position coordinates, deter-

mining the antenna pointing corrections, and adjusting the instrumental delays that assure that the signals from antenna pairs arrive at the correlator in phase. These calibrations take place before the actual observing begins.

The initial calibration determines the absolute gain of the individual antennas and baselines to a level of about 10% and, under normal operating conditions, the system is able to maintain this stability over a period of several hours. Further steps in the calibration procedure require the observations of one or more natural radio sources during the observing experiment that is described below and summarized in Table 2.3.

2.3.1 Gain calibration

After initial adjustment and calibration, the various system and instrumental gains are subject to slowly-varying changes as a result of variations in atmospheric refraction and absorption. This effect can be monitored by noting that the observed visibility $\tilde{\mathcal{V}}_{ij}(t)$ on a baseline between antennas i and j, is linearly related to the true visibility $\mathcal{V}_{ij}(t)$ by the equation

$$\tilde{\mathcal{V}}_{ij}(t) = \mathcal{G}_{ij}(t)\mathcal{V}_{ij}(t) + \epsilon_{ij}, \tag{2.11}$$

where $\mathcal{G}_{ij}$ is the baseline-based complex gain and ϵ_{ij} is stochastic complex noise.

One can use equation 2.11 to solve for the slowly-varying complex gain by observing a calibrator point source of known position and flux density S. This is usually a Quasi-Stellar Object (QSO). At the time t of the observation of the calibrator, the complex gain is

$$\mathcal{G}_{ij}(t) = \frac{\tilde{\mathcal{V}}_{ij}(t)}{S}. \tag{2.12}$$

The resulting gain solutions are then applied to the observations.

During the Saturn observations, the complex gains of the antennas were monitored by observing a secondary calibrator once every 15-30 minutes. Table 2.3 lists these calibrators, which were chosen for their ideal properties: compact structure, accurately known positions, proximity to Saturn, and large and constant flux density on the time-scale of the observations. Frequent observations of the secondary calibrators can remove slowly varying drifts in instrumental gain and atmospheric refractions. Calibration on shorter time-scales, by using the target source itself (self-calibration), is discussed in section 2.4.3.

The flux density of the secondary calibrators, which are highly variable on timescales of months, are bootstrapped by observations of primary flux calibrators that are known to be constant. Table 2.3 lists the primary calibrators, and the bootstrapped flux and standard error of the secondary sources.

2.3.2 Amplitude flux scale

Determining the absolute flux density of the secondary calibrators requires observing a source of known flux density. All observations at the VLA included at least one scan on the primary calibrator 3C286. The absolute flux scale of Baars *et al.* (1977) has established the flux of 3C286 relative to Cassiopeia A, and is a commonly-used flux scale at centimeter wavelengths. Careful attention was given to calibration at 6 and 20 centimeters where 3C286 is partially resolved. At 20 cm the solution was restricted to short baselines $< 18k\lambda$, while at 6 cm the solution was restricted to baselines $< 25k\lambda$. In addition, 3C286 was observed at nearly the same elevation angle as Saturn, in order to minimize systematic errors due to atmospheric attenuation and antenna gain fluctuations.

The absolute flux of 3C286 is believed to be accurate to a level of 3% over the range of observed wavelengths. This is the largest contribution to the systematic error in determining the absolute flux of the secondary calibrators and Saturn, and results in an absolute calibration uncertainty of less than 5% in the final VLA images of Saturn.

Millimeter wavelength observations are complicated by the lack of primary calibration standards. The millimeter absolute flux of secondary calibrator 1730-130 was measured relative to the planet Uranus. The absolute flux of Uranus has been determined accurately by Muhleman and Berge (1989) who measured its flux relative to Mars and derived a 2.6 millimeter brightness temperature of 122 ± 5 K for Uranus based on a radius of 25563 km. The absolute flux of Mars is based on a detailed thermal model discussed by Muhleman and Berge (1989) and by Rudy (1987). The observed amplitudes were adjusted for the partial resolution of Uranus on the longest baselines by modeling the brightness from a uniform disk of radius 25563 km.

The resulting 2.7 millimeter absolute flux of calibrator 1730-130 shows considerable variability over the course of the observations. During two of the observing sessions the flux of 1730-130 was also calibrated against the flux of Mars to determine the source and nature of the variation. Figure 2.1 shows that the absolute flux of 1730-130 as determined by

Table 2.3: Calibration summary.

IAT Date	λ	Secondary calibrators		Primary calibrator	
	(cm)	source	flux (Jy)	source	flux (Jy)
27 Nov 1986	0.27	1730-130	5.38 ± 0.08	Uranus	10.30
20 Jan 1987	0.27	1730-130	5.47 ± 0.05	Uranus	10.44
21 Jan 1987	0.27	1730-130	5.47 ± 0.05	Uranus	10.45
1 Feb 1987	0.27	1730-130	5.28 ± 0.10	Uranus	10.58
4 Feb 1987	0.27	1730-130	5.28 ± 0.10	Uranus	10.62
30 May 1987	0.27	1730-130	3.92 ± 0.13	Uranus	12.53
7 Jun 1987	0.27	1730-130	3.92 ± 0.13	Uranus	12.57
19 Jan 1988	0.27	1730-130	2.67 ± 0.09	Uranus	10.32
20 Jan 1988	0.27	1730-130	2.67 ± 0.09	Uranus	10.33
21 Jan 1988	0.27	1730-130	2.67 ± 0.09	Uranus	10.34
22 Jan 1988	0.27	1730-130	2.67 ± 0.09	Uranus	10.35
14 Jul 1986	2.01	1519-273	2.37 ± 0.14	3C286	3.45
		1657-261	4.98 ± 0.29	3C286	3.45
30 Sep 1986	2.01	1519-273	1.81 ± 0.04	3C286	3.45
		1657-261	3.31 ± 0.50	3C286	3.45
20 Jun 1988	3.53	1730-130	5.63 ± 0.03	3C286	5.16
22 Jun 1986	6.17	1519-273	1.75 ± 0.02	3C286	7.44
		1657-261	1.77 ± 0.02	3C286	7.44
24 Jun 1986	6.17	1519-273	1.75 ± 0.02	3C286	7.44
		1657-261	1.77 ± 0.02	3C286	7.44
27 May 1986	20.13	1519-273	1.34 ± 0.05	3C286	14.39
		1657-261	0.70 ± 0.01	3C286	14.39
28 May 1986	20.13	1519-273	1.34 ± 0.05	3C286	14.39
		1657-261	0.70 ± 0.01	3C286	14.39
17 Jul 1986	20.13	1519-273	1.30 ± 0.03	3C286	14.39
		1657-261	1.01 ± 0.03	3C286	14.39

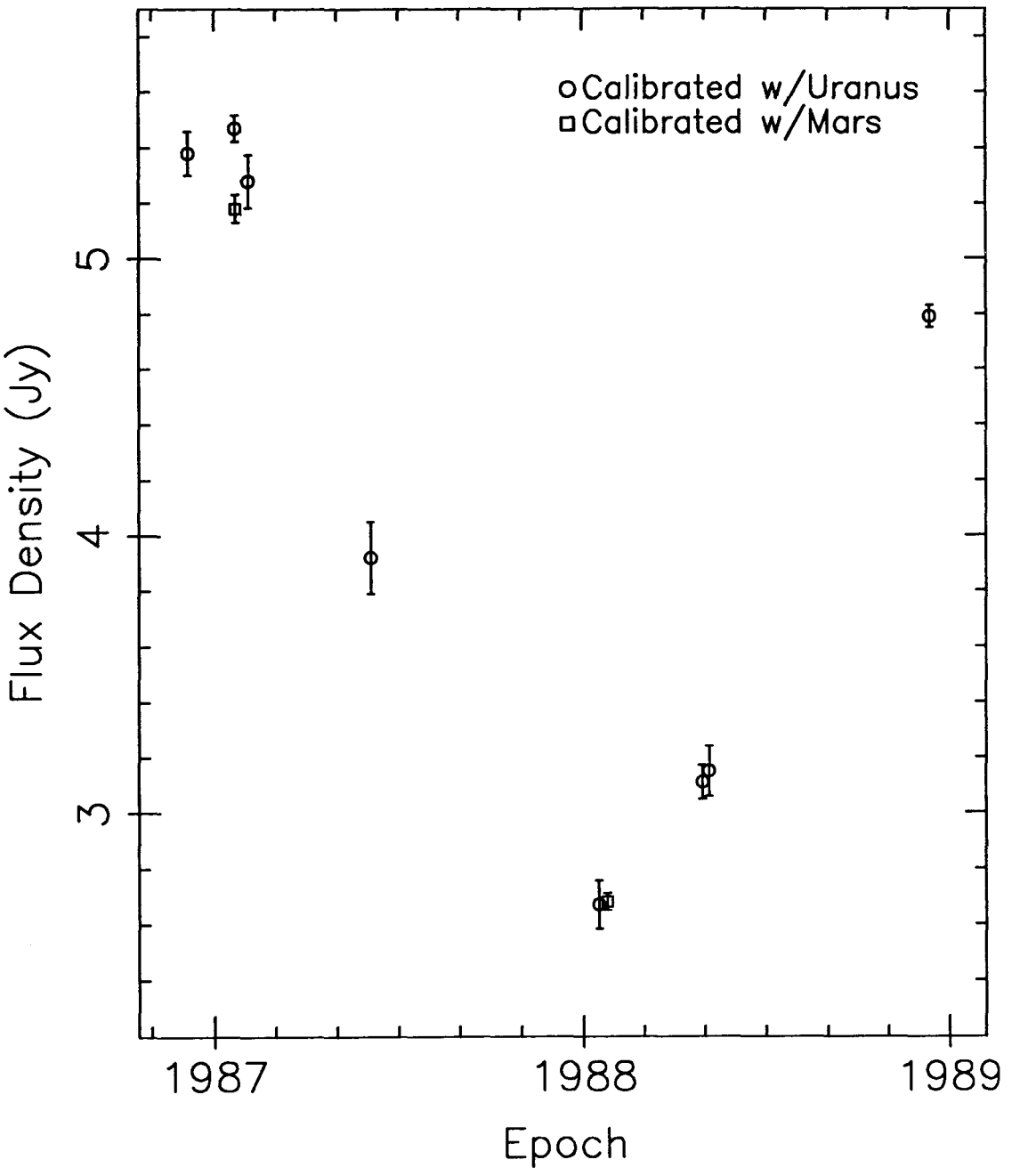

Figure 2.1: Flux density of 1730-130 at $\lambda = 0.27$ cm based on absolute calibration with Uranus ($T_B = 122$ K, radius = 25563 km) and Mars ($T_B = 210$ K, radius = 3378 km).

observing Uranus and Mars is consistent with a smooth variation over a period of two years, and that the standard error in the flux of 1730-130 is less than the variations. Recent observations by Muhleman and Berge have also been included in fig. 2.1. The final absolute uncertainty in the millimeter flux of Saturn is conservatively estimated at less than 6%.

2.3.3 Polarization calibration

The polarization state of an electric field can be measured by observing with two orthogonal polarizations. At the VLA we measure the right-circular polarization (R) and left-circular polarization (L) and produce the four cross correlation products: RR^*, LL^*, RL^*, and LR^*, where * denotes complex conjugate. The previous discussion concerned the calibration of the parallel-hand correlations, RR^* and LL^*. This section discusses the calibration of the opposite-hand correlations.

If the dual-polarization feeds were precisely orthogonal, then the previous calibrations of the parallel-hand correlations would suffice to calibrate the cross-polarization terms, except for any phase difference between them. In practice, the antenna feeds are not exactly orthogonal, and this results in some leakage, i.e., the left-circular channel detects some right-circular flux, and the right-circular channel detects some left-circular flux.

The leakage term can be easily calculated by observing an unpolarized source. For an alt-azimuth mounted antenna, such as the VLA, the source polarization and antenna polarization differentially rotate during a track. This allows simultaneous determination of the antenna leakage term and the source polarization by observing a polarized calibrator. Fortunately the same calibrators used for determining amplitude and phase are also ideal for calibrating the leakage term. Calibrator 1657-261 was observed for over a range of more that 100 degrees in parallactic angle, and this coverage was used to solve for the leakage term to an accuracy of better than 1% at all wavelengths.

The final step in polarization calibration requires determining the relative phase difference between the two polarizations. This is equivalent to determining the position angle of linear polarization. Calibration is achieved by observing a source of known polarization. The primary calibrator, 3C286, is a highly linearly polarized source with a polarization angle of 33 degrees. Observations of 3C286 were used to solve for the phase difference between the two polarizations, and the corrections were applied. This calibration also corrects for any differential Faraday rotation introduced by the ionosphere.

2.4 Synthesis Imaging

The previous section described the calibration of visibility data, the fundamental observable of an interferometer. The visibility, however, provides little direct information of astronomical interest for a complex object such as Saturn. Early interferometric observations of Saturn (Berge and Read, 1968; Briggs, 1973; Berge and Muhleman, 1973; Briggs 1974; Cuzzi and Dent, 1975; Janssen and Olsen, 1978; Schloerb *et al.*, 1979b) were carried out on a small number of baselines. The observed visibilities usually did not have sufficient coverage of the (u, v) plane to warrant mapping. Instead, the observers were limited to fitting models to the visibility data. For a small number of visibilities, model fitting is efficient and useful, but for a large number of data points, more direct methods of estimating the sky brightness are usually more productive.

Initially, models have been used to solve for the brightness and position of a uniform ellipse. More sophisticated models tested for emission and absorption by the rings, limb-darkening in the atmosphere, and the presence of radiation belts. Such models, however, require making some assumptions about the brightness distribution of Saturn. The technique of aperture synthesis mapping produces a map of Saturn's radio emission that is free from any assumptions about the source brightness distribution. As the number of baselines increased, and the techniques for mapping and deconvolution developed, aperture synthesis maps confirmed many of the initial results of visibility modeling. These maps unambiguously detected emission from Saturn's rings (Schloerb *et al.*, 1979a), and detected absorption by the rings and brightness asymmetry on the disk of Saturn (de Pater and Dickel, 1982).

The observations presented here are a far cry from the early days of radio interferometry. The VLA observations typically record visibilities on 351 baselines, producing over 1,000,000 measurements during the course of an observing run. Maps produced from these data sets contain far more detail and structure than obtainable from visibility modeling. Therefore we focus here on determining the distribution of sky brightness, a process collectively referred to as imaging. In some respects, the process of imaging can be considered a method of visibility fitting. Schwartz (1978) has argued that the CLEAN algorithm, used here, is equivalent to fitting the visibility to a sum of sines and cosines.

In order to increase resolution and sensitivity, we combine the observations at identical wavelengths to produce one visibility data set at each of five wavelengths (see

Tables 2.1 and 2.2). This section describes the sequence of steps by which the observed visibilities of Saturn are used to produce a map of Saturn's brightness and polarization. The terms *map*, *image* and, *brightness distribution* are used interchangeably to denote the result of this process. We begin with a discussion of the relationship between the observed visibility and the brightness. The CLEAN deconvolution algorithm is described, and the practical details of its implementation on the Saturn data are presented. We describe how the results of the CLEAN deconvolution can be used to improve the sensitivity of the data – a technique referred to as self-calibration. We conclude by presenting images of brightness at five wavelengths and linear polarization at three wavelengths and analyzing the errors associated with these maps.

The following discussion of synthesis imaging is by no means complete, but is meant to describe the specific steps that lead to the high-resolution images of Saturn. Specific details of mapping techniques can be found in *Synthesis Imaging in Radio Astronomy* (Perley *et al.*, 1989). The Astronomical Image Process System (AIPS), developed by the National Radio Astronomy Observatory (NRAO), and described in *The Aips Cookbook*, serves as the basis for the software implementation of the processing algorithms.

2.4.1 Fourier transform imaging

The most straightforward method of estimating the brightness distribution of the sky from the measured visibility data is by forming the Fourier transform. This initial dirty map is related to the measured visibility by the equation:

$$I^D(x,y) = \int_{\infty}^{\infty}\int_{\infty}^{\infty} S(u,v)W(u,v)\mathcal{V}(u,v)e^{2\pi i(ux+vy)}dudv, \tag{2.13}$$

where $S(u,v)$ is the sampling function that is equal to one where the visibility is measured and zero elsewhere, and $W(u,v)$ is a general weighting function.

By employing the convolution theorem, I^D is related to the true sky brightness I by the relation,

$$I^D = I * B, \tag{2.14}$$

where the asterisk denotes convolution and

$$B(x,y) = \int_{\infty}^{\infty}\int_{\infty}^{\infty} S(u,v)W(u,v)e^{2\pi i(ux+vy)}dudv. \tag{2.15}$$

Equation 2.14 shows that the dirty map is the true intensity convolved with the "dirty" beam that is just the Fourier transform of the sampling function times the weighting function. The sampling function is fixed by the distribution of baselines and observing geometry. The weighting function, however, can be chosen to enhance certain aspects of the data. For example, choosing $W(u,v)$ to be inversely proportional to the variance in the visibility will optimize the signal-to-noise in the final image, while choosing $W(u,v)$ to be inversely proportional to the local density of data results in a smooth beam with small sidelobes.

In estimating the brightness of Saturn, we choose a "natural" weighting scheme that assigns to each visibility sample a weight proportional to the duration of the sample. Such a weighting scheme maximizes the signal-to-noise ratio in the final image. The Fourier transform of the weighting function and the sampling function results in a beam with a large central peak and many positive and negative sidelobes and ripples. The sidelobes come in all shapes and sizes and can be related to gaps and features in the visibility sampling. Figure 2.2 shows a contour map of the 2 cm beam with sidelobes extending out to several Saturn radii. Section 2.4.2 describes the CLEAN deconvolution process that is used to remove the effects of convolution with the dirty beam for the strong signal, intensity maps. The polarization maps are much weaker and cannot be CLEANed. Therefore, the "dirty" polarized maps provide the only estimate of polarized brightness. In this case, the beam sidelobes are reduced by multiplying the visibilities by a Gaussian weighting function at the expense of increasing the width of the main lobe of the synthesized beam.

In practice Eq. 2.13 is evaluated by using a discrete Fourier transform

$$I^D(x,y) = \sum_{n=1}^{N} S(u_n,v_n)W(u_n,v_n)\mathcal{V}(u_n,v_n)e^{2\pi i(u_n x + v_n y)}, \tag{2.16}$$

for the $n = 1$ to N observed visibilities. The evaluation of $I^D(x,y)$ on a $m \times m$ grid of points by Eq. 2.16 requires roughly $m^2 N \approx m^4$ computations. Direct use of Eq. 2.16 becomes computationally prohibitive for many points. Instead we make use of the fast Fourier transform (FFT) algorithm, by first gridding the observed visibilities on a regular grid of size $m \times m$. Evaluation of Eq. 2.16 then requires only $\sim m^2 \log_2 m$ operations.

The approximation to I given by I_D is just a starting point for the deconvolution of the beam from I. The sidelobes from bright features obscure many faint features that may be present. However, the true sky brightness, I, is contaminated by some noise, and in case of low signal-to-noise, such as in the polarization images, the sidelobes are less than

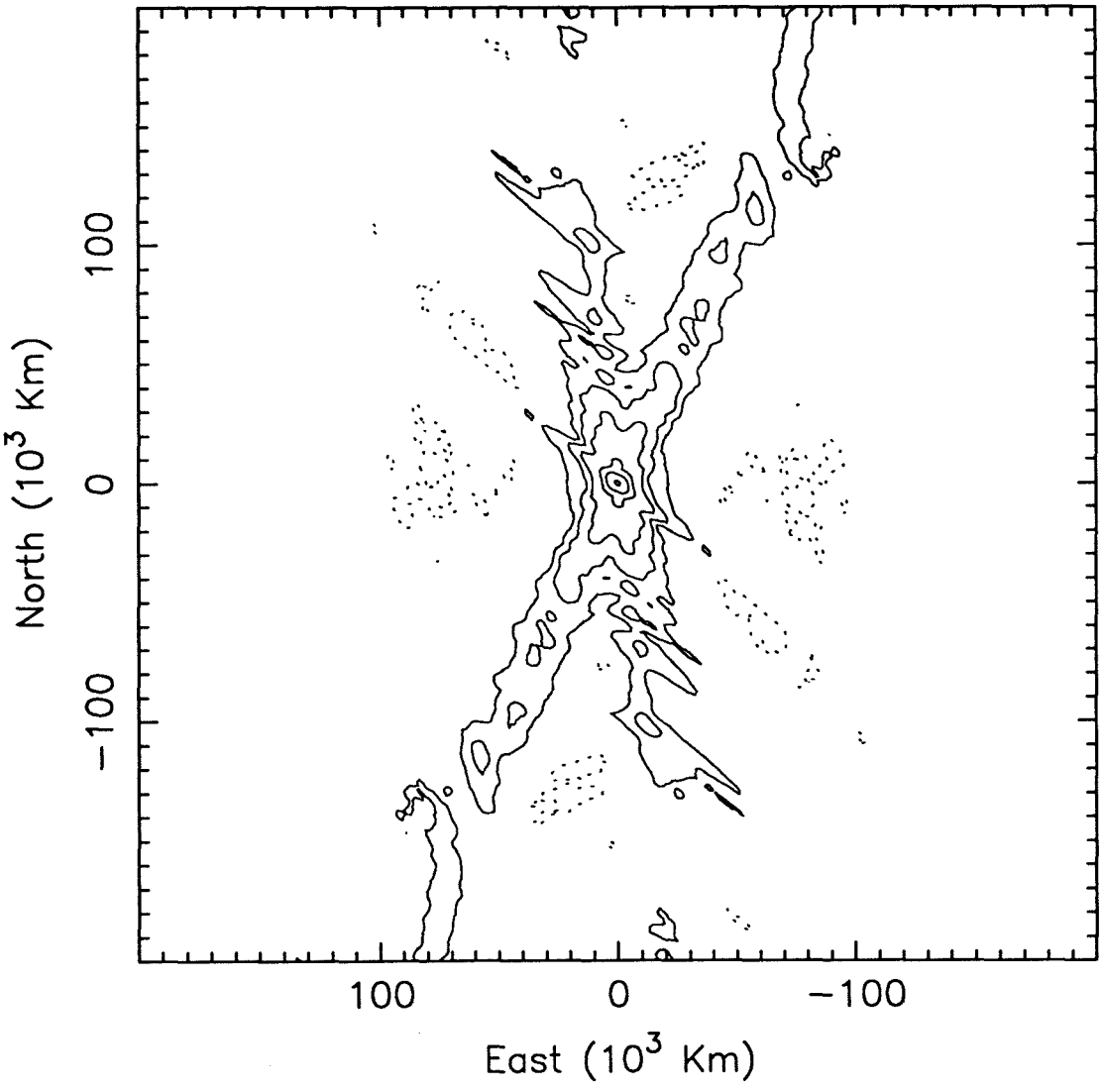

Figure 2.2: Dirty beam at a wavelength of 2 cm. Solid contours at 90%, 50%, 30%, 10%, 5%, 2% and dotted contours at -2%.

the noise level in the map and deconvolution does not improve the image.

2.4.2 Clean deconvolution

As described in section 2.4.1, an interferometer provides samples of the complex visibility function of the sky at various points in the (u, v) plane. The visibility function is related to the source intensity by a Fourier transform relation (Eq. 2.13), and the transformed visibilities (the dirty map) are just the true sky brightness convolved with the beam (Eq. 2.14).

Let us now consider solutions to the convolution equation (Eq. 2.14) that reconstruct the true sky brightness I. If I is a solution to the convolution equation (Eq. 2.14), and Z is a distribution such that $B * Z = 0$ then $I + Z$ is also a solution to the convolution equation. Clearly Z is a distribution with spatial frequencies that were not adequately sampled by the interferometer. The problem of image construction can thus be described as finding the proper invisible distribution Z to merge with the sampled brightness I. We can gain some help in deciding which of the infinite invisible distributions Z to chose, by introducing some *a priori* knowledge as a constraint. For example, we require that the Stokes parameter I be positive within a known region and zero elsewhere. Such constraints are contained in the CLEAN deconvolution algorithm.

The CLEAN algorithm, introduced by Hogbom (1974) and later modified by Clark (1980), is a simple iterative subtraction scheme that represents the source by a set of discrete point sources. The final CLEAN image is the set of these points, known as clean-components, convolved with a smooth, Gaussian beam: the CLEAN beam.

The algorithm begins by selecting the brightest peak, in absolute value, in the dirty image I^D. This selection is confined to a region in the sky known to contain the source. The dirty beam B, multiplied by a gain factor ≤ 1, is subtracted from the dirty image at the position of the peak. The brightest peak in the residual map is selected next, and the procedure continues subtracting a fraction of the beam at that peak point until the remaining peak is below some specified level. This successive iteration replaces the image with a set of delta-functions referred to as clean-components. At this point the removed clean-components are convolved with a Gaussian, which approximates the central lobe of the beam, and then added to the residuals. This procedure corrects itself by selecting both positive and negative components.

The Cotton-Schwab (Schwab, 1984) modification of the CLEAN process eliminates aliasing noise and gridding errors by subtracting the clean-components from the ungridded visibility data directly. The clean-components are found as before, in the dirty map of the residual visibilities. This algorithm, as implemented in the AIPS task MX, is used exclusively for CLEANing the Saturn maps.

The CLEAN deconvolution process has the advantage of being conceptually easy to understand. Schwartz (1979) has shown that CLEAN is equivalent to a least squares fitting of the visibilities to a set of sines and cosines. Furthermore, he has shown the conditions for convergence are generally met by interferometric data. CLEANing of extended objects, such as Saturn, present unique problems. To facilitate the process, the iteration begins with an initial clean-component model of an elliptical disk, chosen to best represent the disk of Saturn. CLEAN then only needs to find the small perturbations from this disk model, due to brightness variations in the atmosphere and rings of Saturn. In order to assure convergence, the iteration on Saturn is allowed to proceed until the clean-components are reduced in magnitude to the root-mean-square (RMS) level of the noise in the residual map and an equal number of positive and negative clean-components are selected. At this point the iteration has replaced all the detectable flux in the map with a set of clean-components. Further cleaning contributes no additional flux, and only rearranges the noise pattern in the residual map.

The success of the CLEAN algorithm in removing the spurious sidelobes of Saturn that obscure the low brightness of the rings is remarkable. Figure 2.3 shows the 2 cm dirty map. The influence of the beam is clearly evident. Flux from Saturn is pushed to the edge of the field and obscures the faint ring flux. Indeed, the rings of Saturn appear to be regions of negative brightness. In contrast, fig.2.4 shows the same image after CLEANing 20,000 components with a gain of 0.1. The beam sidelobes are effectively removed. The image now clearly indicates flux from the rings and the slight depression of contours in the South due to occultation of the disk by the rings.

All the CLEANed I Stokes parameter maps show improvement in comparison with the dirty maps. Nevertheless, additional improvement is possible by attempting to reduce the random noise introduced by the Earth's atmosphere.

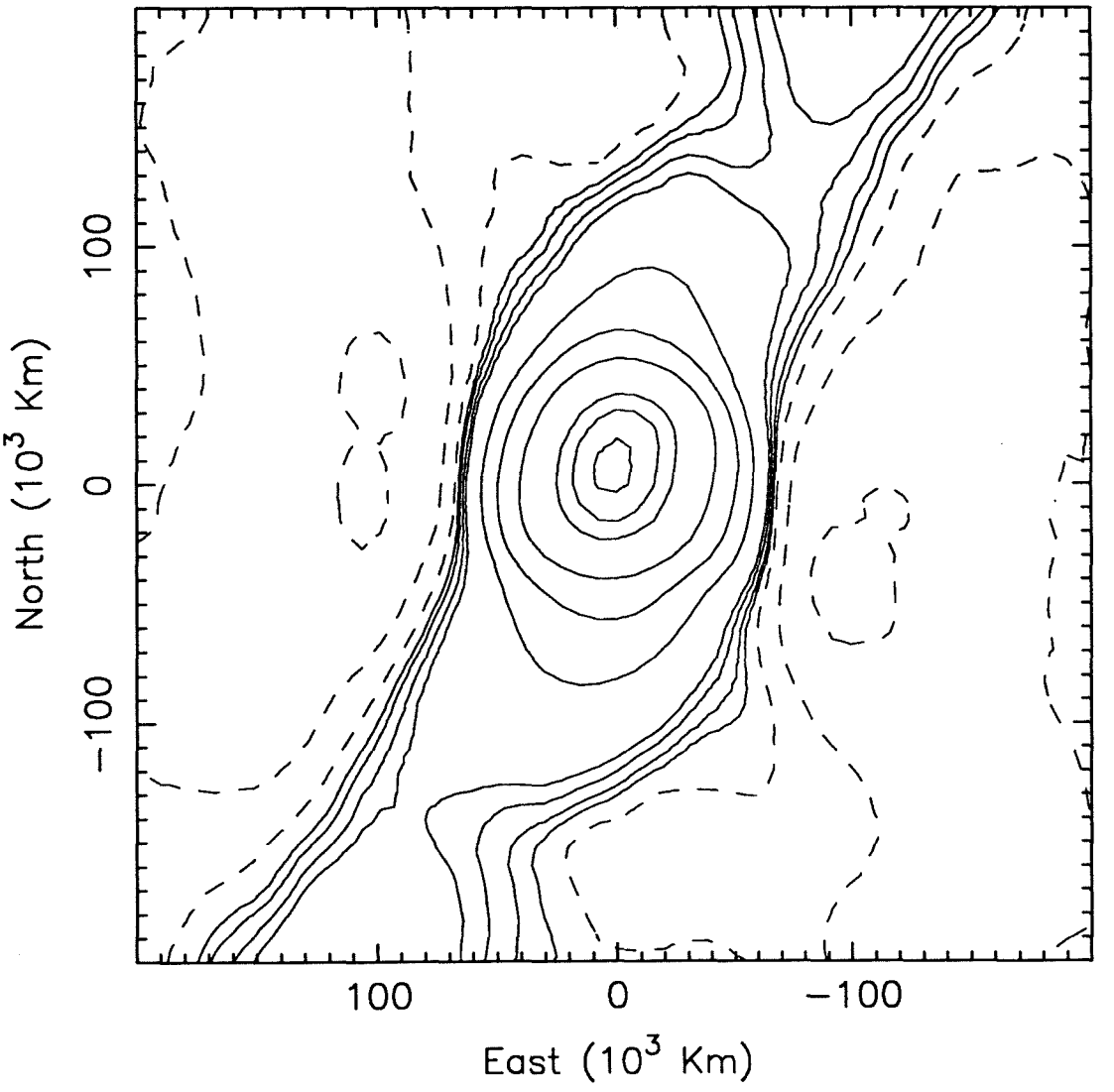

Figure 2.3: Dirty map of Saturn intensity at a wavelength of 2 cm. Solid contours at 99%, 95%, 70%, 50%, 30%, 10%, 7%, 4%, 2% and dashed contours at -2%, -10%, -20%. Beam sidelobes are responsible for leaking Saturn flux to the edge of the field and obscuring the faint ring flux.

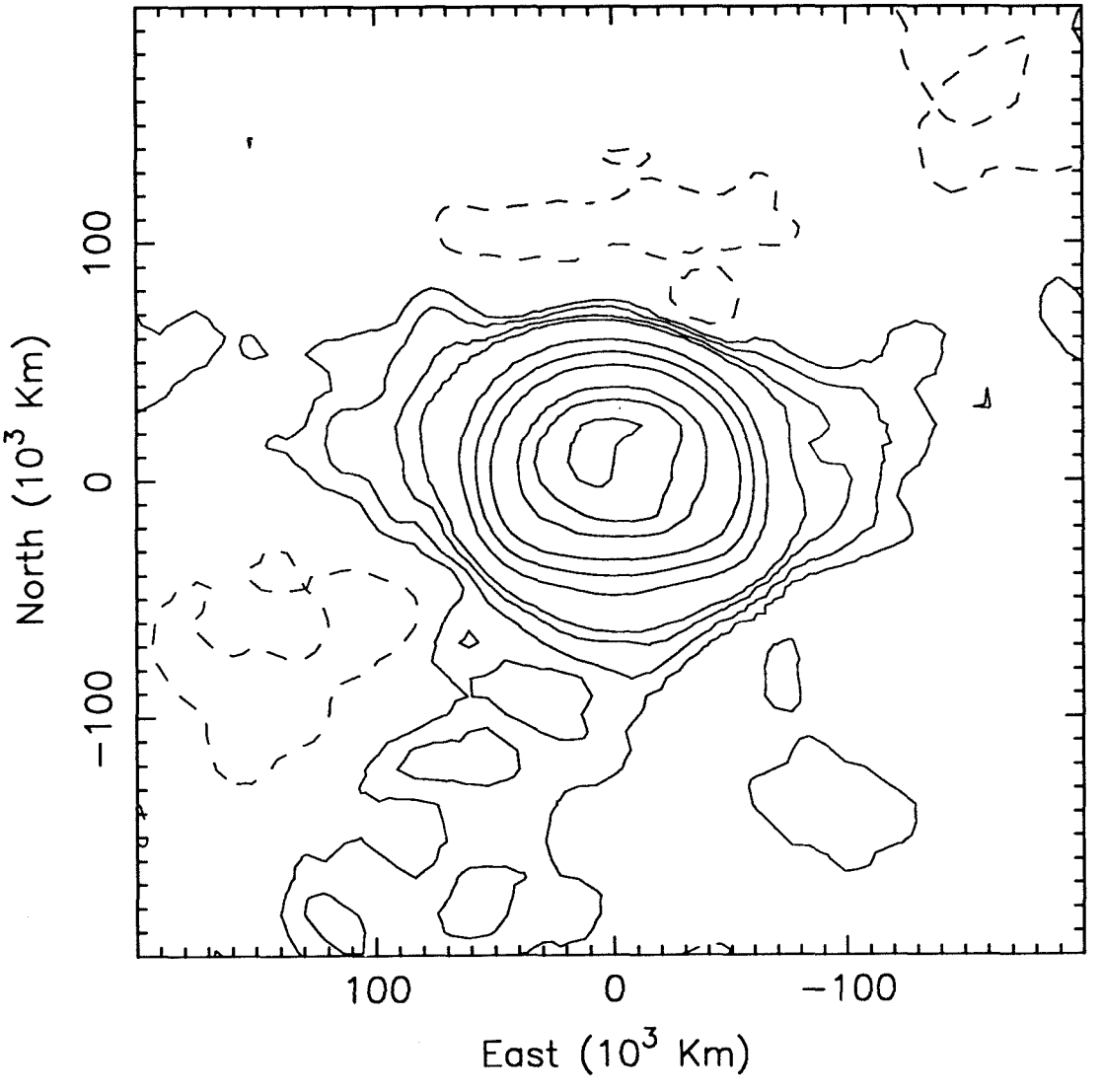

Figure 2.4: Clean map of Saturn intensity at a wavelength of 2 cm. Solid contours at 99%, 95%, 70%, 50%, 30%, 10%, 7%, 4%, 2% and dashed contours at -2%, -10%, -20%. The ring is now visible on either side of Saturn.

2.4.3 Self-Calibration

The major source of error in aperture synthesis is produced by changes in the propagation properties of the troposphere and ionosphere (Bohlander, McMillan and Gallagher, 1985). The radiation wavefront is distorted by refraction from dry air and water vapor on length scales comparable to the baseline and on time scales of a few minutes. The net effect is to introduce a random fluctuation in the visibility phase. The visibility amplitude generally remains unaffected.

Errors in visibility amplitude and phase that are slowly varying can be removed by the standard methods of calibration (section 2.3.1). Phase errors that occur on shorter time scales contribute significantly to the extended low-level noise component in the maps. These errors can be reduced, to a limited extent, by applying *a priori* information to constrain the visibilities and maps. This technique is generally referred to as self-calibration or hybrid mapping.

The technique of self-calibrations relies on the concept of phase closure. Jennison (1958) noted that if three antennas are combined to form three pairs of interferometers, the phase error at any given antenna vanishes in the sum of the phases around the loop of three antennas. To demonstrate this, note that the observed phase $\tilde{\Theta}_{ij}$ on a baseline connecting antennas i and j, is linearly related to the true phase Θ_{ij}, by the relation

$$\tilde{\Theta}_{ij} = \Theta_{ij} + \phi_i - \phi_j, \tag{2.17}$$

where ϕ_i and ϕ_j are the phase errors associated with antennas i and j. The closure phase is just the sum of the observed phases around the loop and is given by

$$\tilde{\Phi}_{ijk} = \tilde{\Theta}_{ij} + \tilde{\Theta}_{jk} + \tilde{\Theta}_{ki} = \Theta_{ij} + \Theta_{jk} + \Theta_{ki} = \Phi_{ijk}. \tag{2.18}$$

Thus the observed closure phase is identical to the true closure phase. In other words, the sum of the phases around a loop is independent of the phase errors of the individual antennas, and contains information about the structure of the observed object.

In practice, the closure phase is never explicitly calculated. Instead, one can see from the definition of closure phase, that any change to the phase of a single antenna leaves the closure phase unchanged. Therefore, the closure phase constraints can be used to allow the antenna phases to be free parameters in an overdetermined estimation of sky brightness

(Cornwell, 1989, gives a concise description of the problem. For a thorough treatment see Pearson and Readhead, 1984).

As shown in section 2.3.1, the observed visibility $\tilde{\mathcal{V}}_{ij}(t)$ on a baseline between antennas i and j, is linearly related to the true visibility $\mathcal{V}_{ij}(t)$ by the equation

$$\tilde{\mathcal{V}}_{ij}(t) = g_i(t)g_j^*(t)\mathcal{V}_{ij}(t) + \epsilon_{ij}, \tag{2.19}$$

where $g_i(t)$ and $g_j(t)$ represent the complex gain of the individual array elements and ϵ_{ij} represents the random noise. This model makes use of the generally valid assumption that the complex gain associated with the visibility on a baseline can be factored into an expression involving just the gains of the individual elements. The basis of self-calibration is to allow the element gains to be free parameters. In this context, the N antenna gains are solutions in an overdetermined problem utilizing the $\frac{1}{2}N(N-1)$ complex visibility measurements.

In practice, the self-calibration process is initialized by forming a model of the sky brightness $\hat{I}$, either from *a priori* information or from an intial CLEANed map. The model brightness is transformed to produce a set of model visibilities $\hat{\mathcal{V}}$. New solutions to the complex antenna gains as a function of time are found by minimizing the sum of the squares of the difference between the model visibilities, $\hat{\mathcal{V}}$, corrected by the complex gain, and the observed visibilities:

$$\sum_{ij} \left[\tilde{\mathcal{V}}_{ij}(t) - g_i(t)g_j^*(t)\hat{\mathcal{V}}_{ij}(t)\right]^2. \tag{2.20}$$

The observed visibilities are corrected by the gain solutions, and a new CLEANed map is produced from the results. This map then serves as the model for the next iteration of gain solutions. The process usually converges after a few iterations when the gain corrections become negligible.

The primary requirement for self-calibration to be successful is that the number of elements in an array be large. In other words, for an array consisting of N elements, the number of constraints, $\frac{1}{2}N(N-1)$, must be larger then the number of unknowns, N. This condition is easily satisfied for the VLA observations, but not for the three-element OVRO data set. As a result, self-calibration did not improve the 0.27 cm maps. An additional condition for self-calibration to be successful is that the source flux on any given baseline be

greater than the noise on that baseline for the gain solution time interval. This condition was met on all VLA data except the 20 cm data, which suffered from poor signal-to-noise.

Self-calibration was thus successfully applied to three VLA visibility data sets at wavelengths of 2.01, 3.53, and 6.17 cm as measured by the improvement in the signal-to-noise-ratio (SNR). Because phase errors are the dominant effect of atmospheric corruption, only the phase component of the antenna gains was adjusted in the solution of Eq. 2.20. The amplitude gains were untouched, thus ensuring a consistent amplitude flux scale. The improvement of self-calibration is noticeable in the comparison of fig. 2.5 with fig. 2.4, which shows the 2 cm clean map after four iterations of self-calibration. The random noise appears to have been reduced after self-calibration. However, there is still some measurable noise in the map that limits the ultimate sensitivity of this technique.

2.4.4 Sensitivity

Brightness sensitivity in aperture synthesis maps is limited by several effects, even after removing sidelobes with the CLEAN deconvolution technique and correcting for atmospheric errors with self-calibration. This section discusses the sources of noise that contribute to the images and concludes with an estimate of the limiting sensitivity of the Saturn maps.

One unavoidable source of noise is random, statistical, Gaussian noise that is added to the measured signal and is due to the 3 K microwave background, the galactic background, thermal noise generated by the atmosphere, thermal noise picked up from the ground, noise due to attenuation in the feed and waveguide, noise injected with the calibration signal, and noise in the receiver itself. In general, the sensitivity is limited by other non-random effects such as confusion, radio-frequency interference, calibration errors, imperfect CLEANing, distortion caused by non-negligible frequency and time averaging, and atmospheric phase instabilities not removed by self-calibration. Some of these sources of noise introduce artifacts into the image, but in most cases they appear as additive, random noise, and increase the general level of noise in the maps. Thus the root-mean-square (RMS) deviation in a region of the map away from Saturn is a good estimate of the noise in the map.

The RMS deviation in the Saturn maps is summarized in column 8 of Table 2.4. This value is a good estimate of the relative error in the pixels of the map. The largest

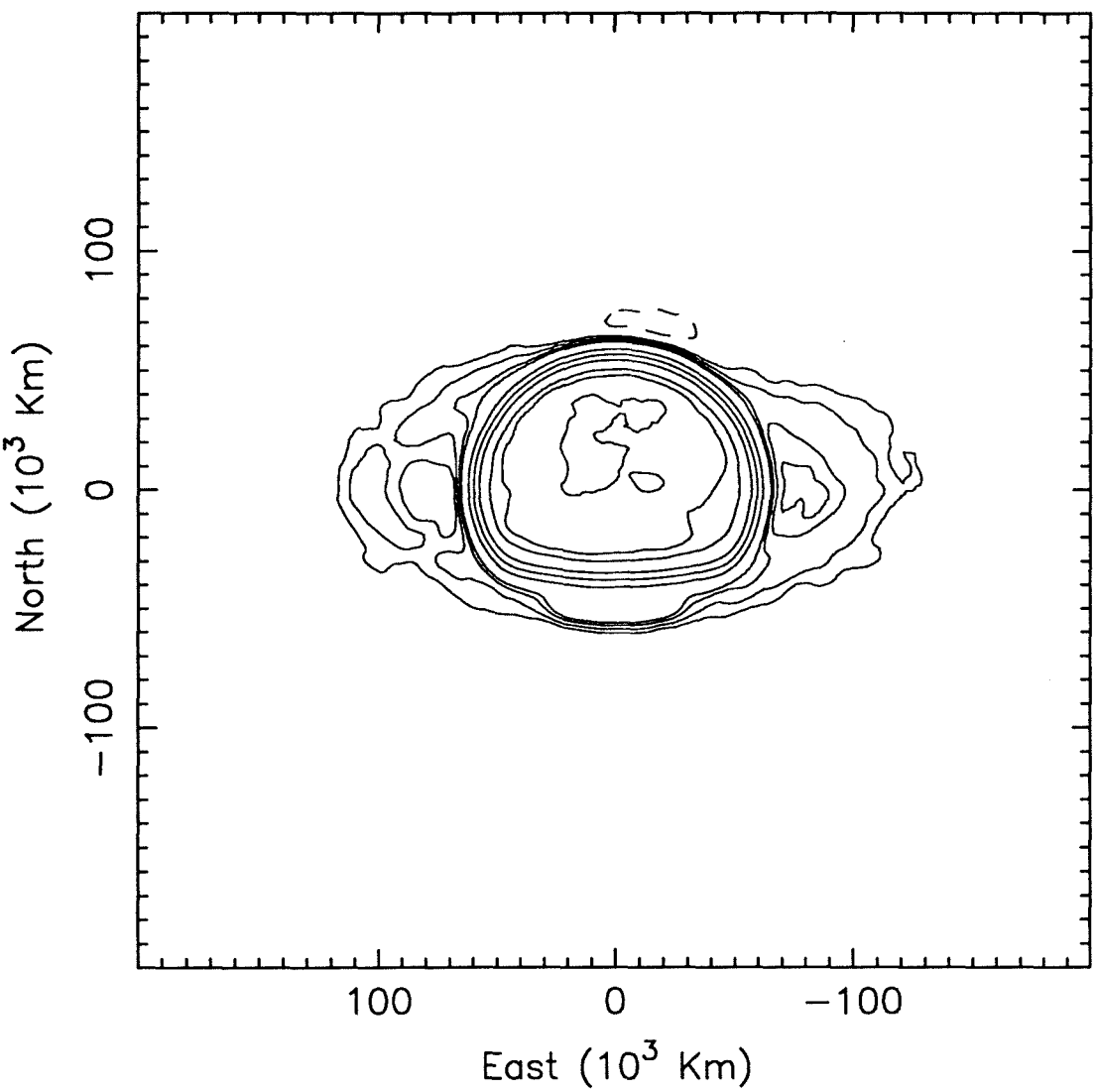

Figure 2.5: Clean map of Saturn intensity at a wavelength of 2 cm after self-calibration. Solid contours at 99%, 95%, 70%, 50%, 30%, 10%, 7%, 4%, 2% and dashed contours at -2%, -10%, -20%. The image shows much improvement after application of self-calibration.

errors are associated with maps that were not self-calibrated and once again confirms the validity of the self-calibration technique. This also suggests that a large source of noise is due to random phase fluctuations associated with individual antennas. The lowest RMS deviations are associated with the polarization maps (P_l') that were not even CLEANed or self-calibrated! This can be understood if we consider the contribution of self-noise, that is, random phase errors associated with calibration or baseline errors that distribute the source flux over all regions of the map. The intrinsically weaker polarization maps thus contribute less self-noise than the much stronger I Stokes maps. The extra sensitivity of the polarization maps has been achieved largely by sacrificing resolution by tapering the visibilities. This results in a larger beam.

The effect of self-noise has been included in column 9 of Table 2.4, which shows the ratio of the brightest point in the map to the RMS noise. This dynamic range is an estimate of quality in the map and is best for those maps that were both self-calibrated and CLEANed. The Saturn maps are summarized in the next section.

2.4.5 Saturn maps

This section presents the principle microwave images of Saturn that serve as the foundation for subsequent analysis and modeling. Altogether eight maps at five different wavelengths are produced. The map's characteristics are summarized in Table 2.4 and are presented in figs. 2.7 through 2.14.

The first column of Table 2.4 shows the reference figure number. The second and third columns show the wavelength and the type of map. The fourth and fifth columns indicate whether self-calibration was applied to the map and whether sidelobes were removed by the CLEAN technique. The sixth and seventh columns indicate the approximate resolution of the map by giving the average full-width at half-maximum (FWHM) of the beam in kilometers and in units of Saturn radii, R_S. The eighth column provides an estimate of the standard error in the maps as measured by the RMS deviations in a region of the map away from Saturn. The final column shows the dynamic range of the map by taking the ratio of the brightest point to the standard error.

An attempt was made to self-calibrate all wavelengths, however, due to poor sensitivity at 0.27 and 20.13 cm, only maps at 2.01, 3.53, and 6.17 were successfully self-calibrated. In these cases, only the phases were allowed to be free parameters; amplitudes

Table 2.4: Saturn map summary.

Figure	λ (cm)	Map type	Self-calibration?	CLEAN?	Beam FWHM (km $\times 10^3$)	R_S	RMS deviations (Kelvin)	Dynamic range
2.7	0.27	I	no	yes	29.0	0.48	3.2	48
2.8	2.01	I	yes	yes	9.1	0.15	0.8	200
2.9	2.01	P_l'	yes	no	14.7	0.24	0.1	9
2.10	3.53	I	yes	yes	26.2	0.43	0.5	379
2.11	6.17	I	yes	yes	7.9	0.13	1.0	201
2.12	6.17	P_l'	yes	no	13.1	0.22	0.1	13
2.13	20.13	I	no	yes	13.0	0.22	3.7	68
2.14	20.13	P_l'	no	no	32.3	0.54	0.1	8

were fixed. Initially all available Stokes visibilities were mapped. Four Stokes parameters were available at 2.01, 6.17, and 20.13 cm, however, only the I Stokes parameter, or intensity, was available at 0.27 and 3.53 cm. As expected, no signal was evident in any of the V Stokes maps. The I Stokes maps were CLEANed in order to remove the contamination by beam sidelobes as described in section 2.4.2. The signals in the Q and U Stokes maps, however, were sufficiently weak that the sidelobes were negligible. These maps were not cleaned.

The Q and U Stokes maps are difficult to interpret by themselves. Thus, meaningful maps of linear polarization, P_l, and position angle of polarization, ψ, were produced by combining the Q and U maps as follows:

$$P_l = \sqrt{Q^2 + U^2}, \tag{2.21a}$$

$$\psi = \frac{1}{2}\tan^{-1}\left(\frac{U}{Q}\right), \tag{2.21b}$$

Thus defined, the polarization amplitude in the presence of random noise is not a Gaussian probability distribution, but is closer to a Rice distribution (Wardle and Kronberg, 1974). This can lead to systematic errors in estimating the polarization, P_l, for weak signals. The best estimate of the polarization amplitude, P_l', is thus found by applying the following correction

$$P_l' = \sqrt{P_l^2 - \sigma^2}, \tag{2.22}$$

where σ^2 is the variance of the random Gaussian noise (Wardle and Kronberg, 1974). The polarization angle is an unbiased estimator of the true position angle, and thus requires no

correction.

Figure 2.6 shows the approximate viewing geometry of the maps. The North pole is tilted toward the observer and the rings are near maximum opening angle. The maps of total intensity at five wavelengths show the same general features at varying degrees of resolution and sensitivity. The disk of Saturn is seen as a bright hemisphere, partially occulted by the rings in a region referred to as the cusp. The rings are observed as faint features extending on either side of the disk. In maps of linear polarization, the rings appear to be linearly polarized in the north-south direction at all three wavelengths of 2.01, 6.17, and 20.13 cm. Some residual polarization is also observed on the disk of Saturn, however, this is not significant because it is below the estimated calibration error of 1%. These maps will be analyzed in greater detail in the following chapters.

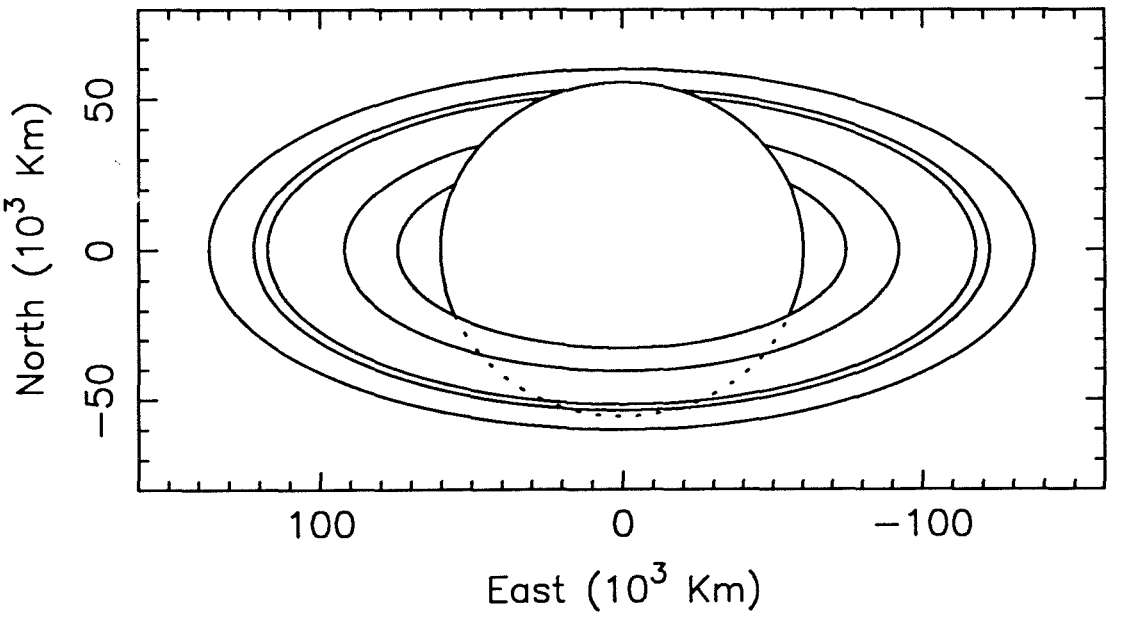

Figure 2.6: Viewing geometry for Saturn maps. Boundaries are taken from Table 3.1, and show the classical rings in order of decreasing radius: A, Cassini Division, B and C.

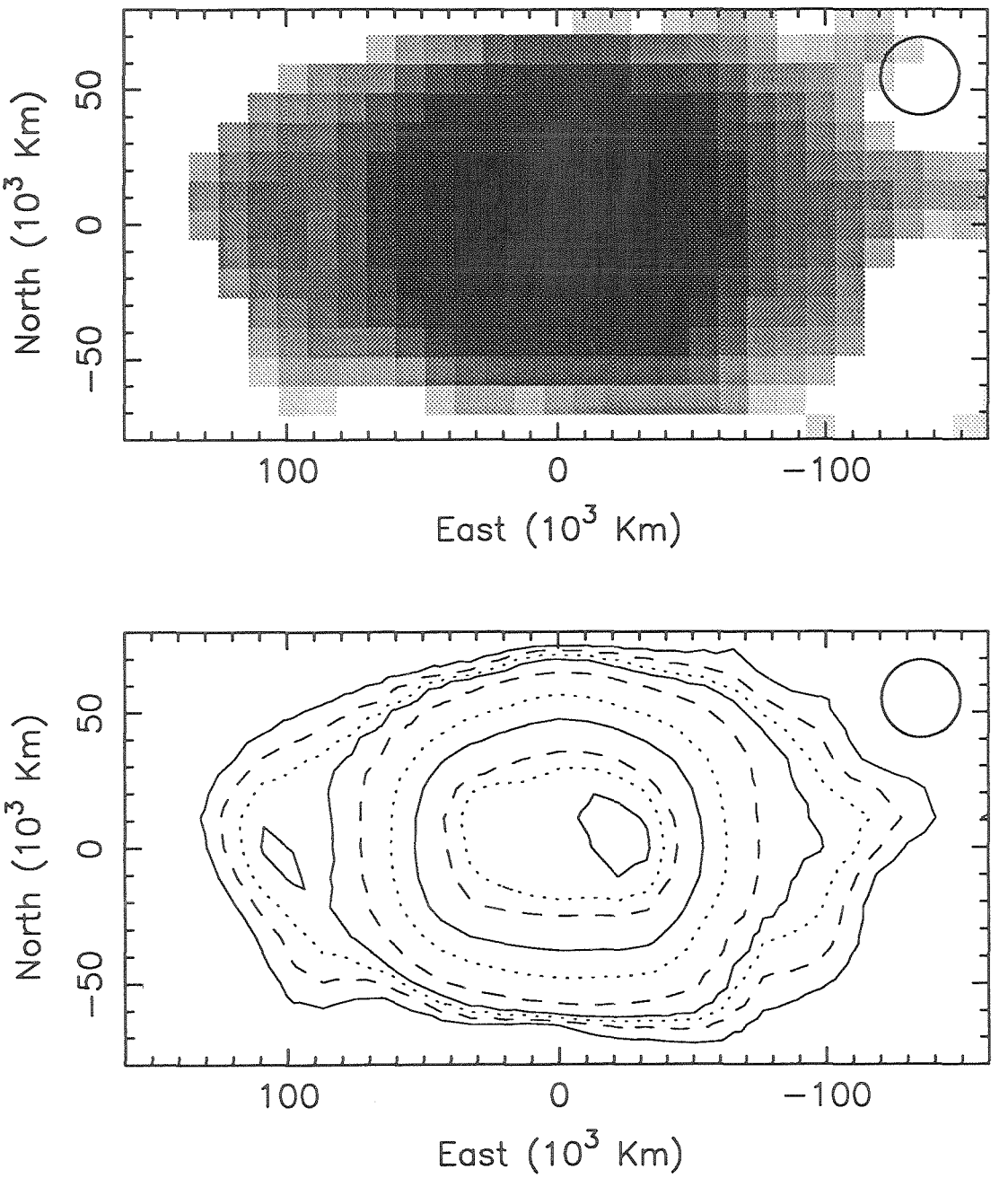

Figure 2.7: Saturn intensity map at a wavelength of 0.27 cm. Top shows a grey-scale representation. Bottom shows a contour map with contours at 6, 10, 14, 18, 30, 60, 90, 120, 130 and 140 K. Ellipse indicates beam FWHM.

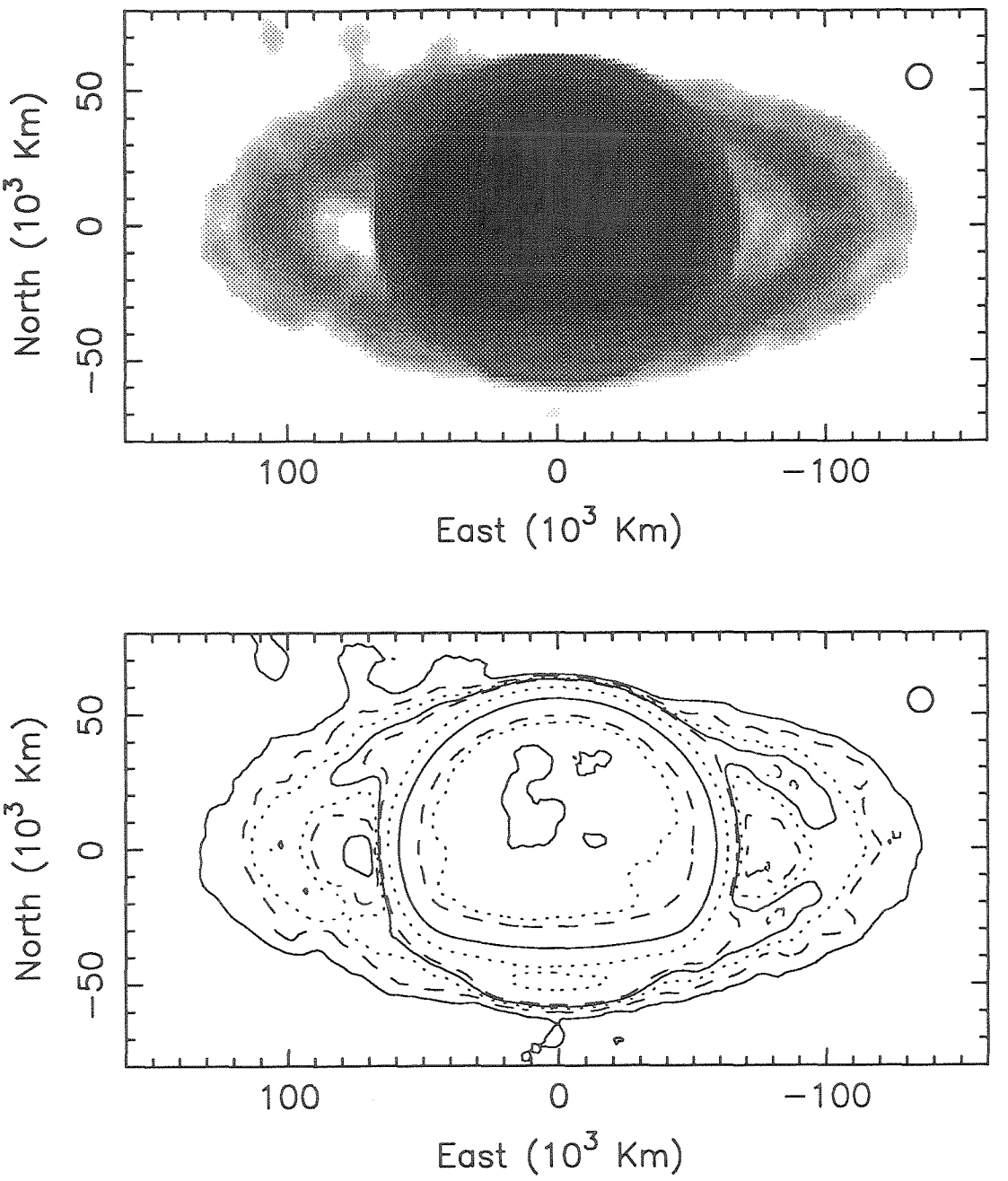

Figure 2.8: Saturn intensity map at a wavelength of 2.01 cm. Top shows a grey-scale representation. Bottom shows a contour map with contours at 1, 3, 5, 7, 9, 30, 80, 130, 135 and 140 K. Ellipse indicates beam FWHM.

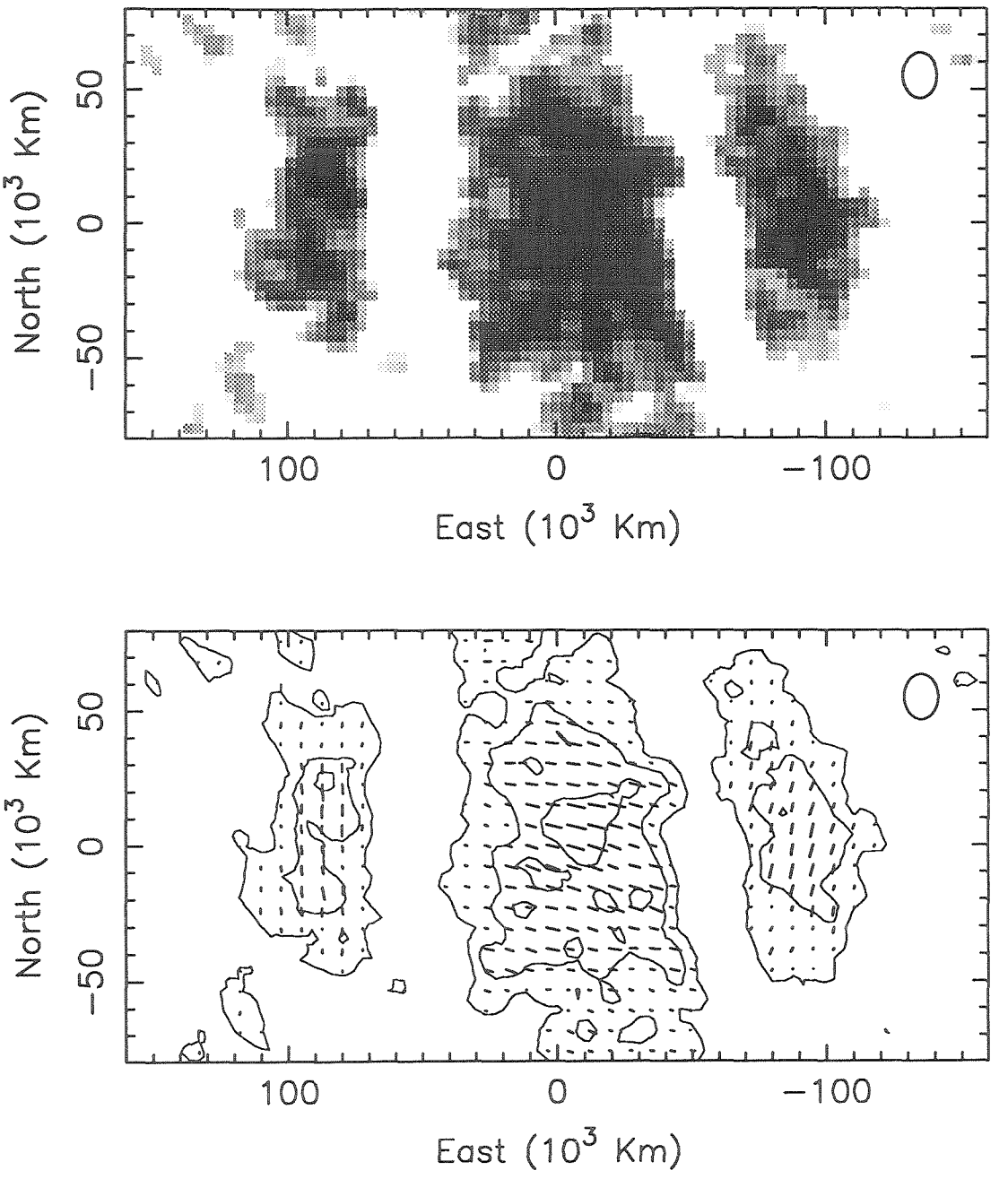

Figure 2.9: Saturn linearly polarized intensity map at a wavelength of 2.01 cm. Top shows a grey-scale representation of linearly polarized brightness. Bottom shows a contour map with contours at 0.3, 0.5 and 0.7 K. Vectors indicate magnitude and direction of linear polarization. Ellipse indicates beam FWHM.

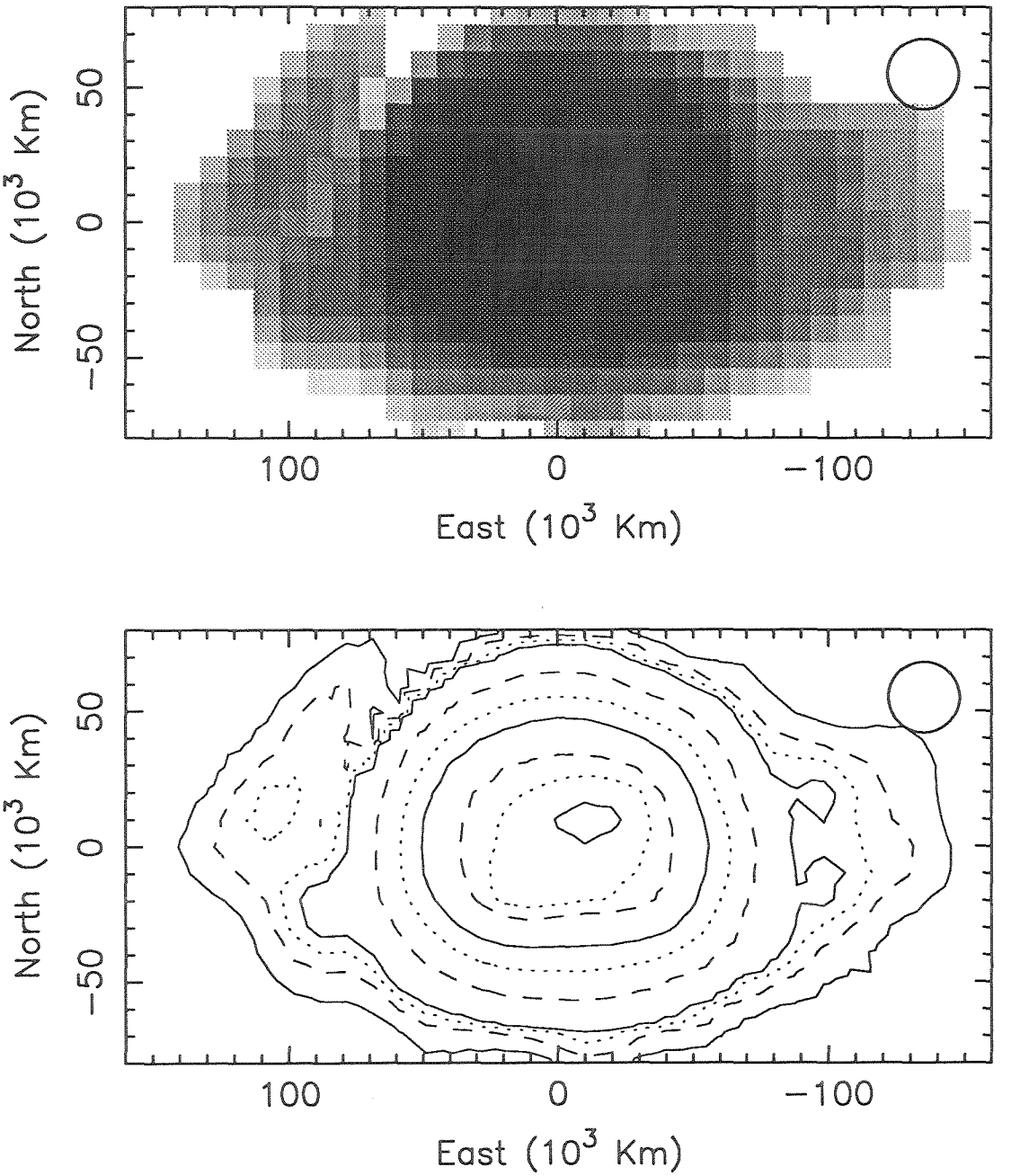

Figure 2.10: Saturn intensity map at a wavelength of 3.53 cm. Top shows a grey-scale representation. Bottom shows a contour map with contours at 1, 3, 5, 7, 30, 70, 110, 150, 160 and 167 K. Ellipse indicates beam FWHM.

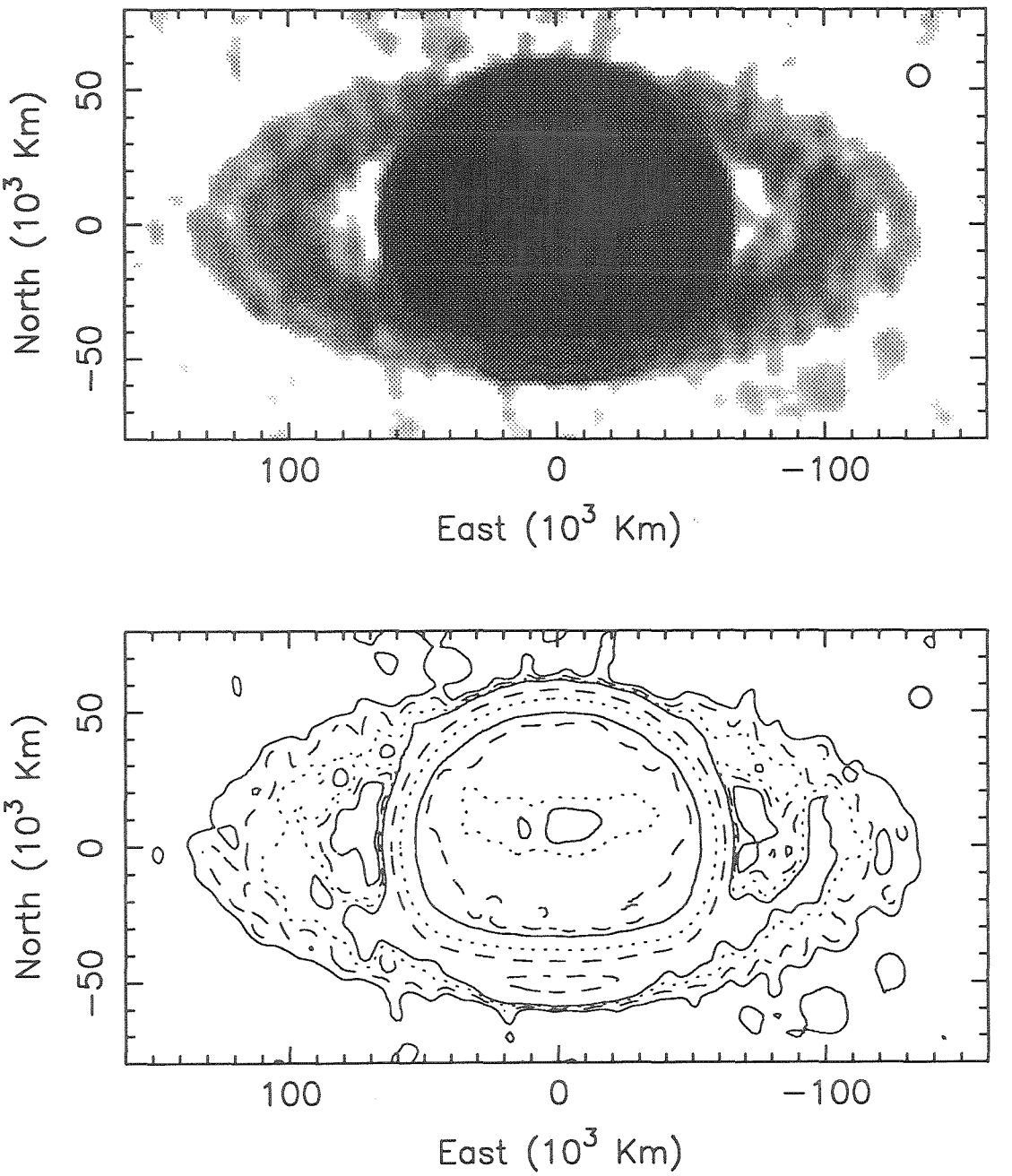

Figure 2.11: Saturn intensity map at a wavelength of 6.17 cm. Top shows a grey-scale representation. Bottom shows a contour map with contours at 2, 4, 6, 8, 40, 100, 160, 170, 180 and 185 K. Ellipse indicates beam FWHM.

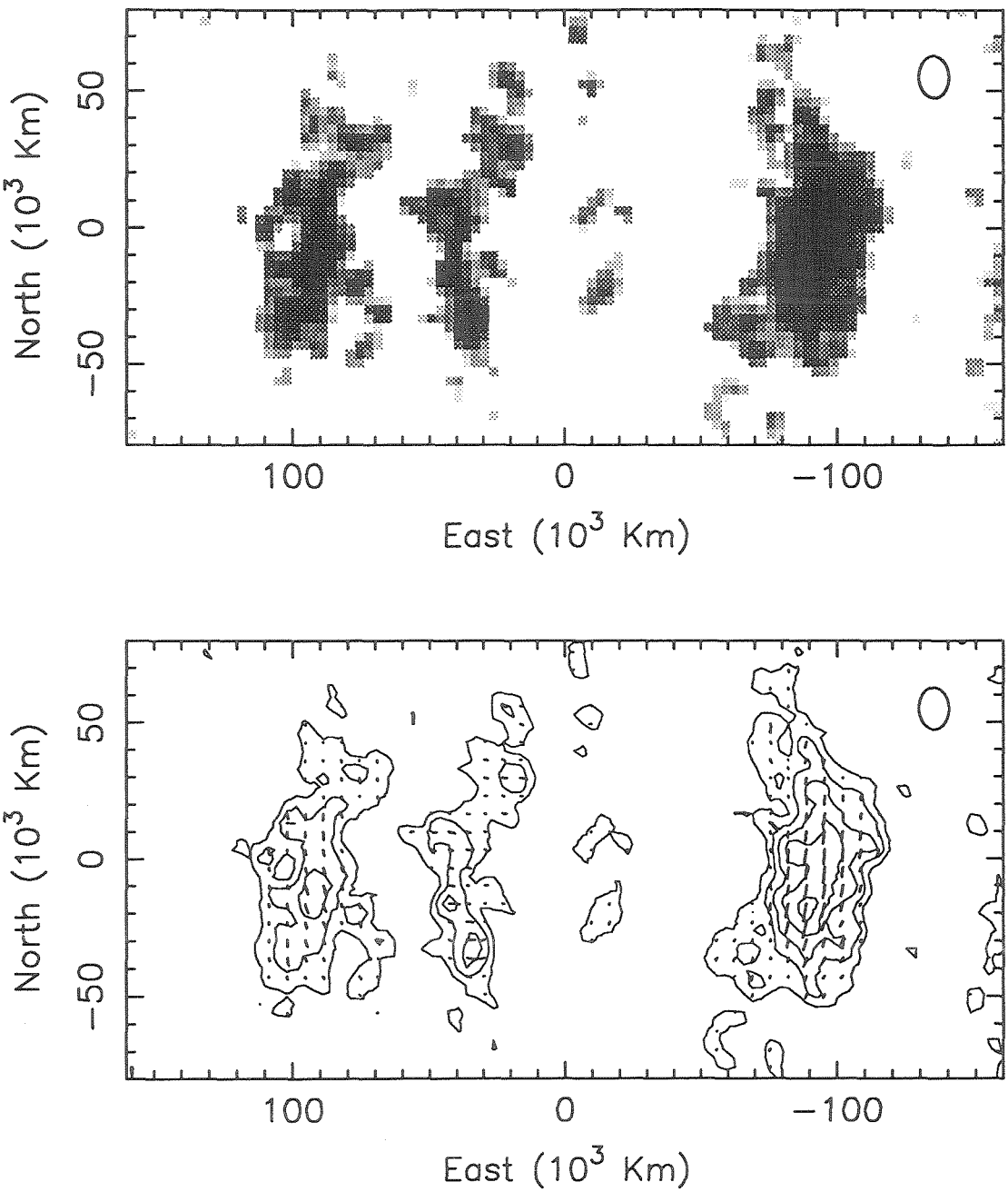

Figure 2.12: Saturn linearly polarized intensity map at a wavelength of 6.17 cm. Top shows a grey-scale representation of linearly polarized brightness. Bottom shows a contour map with contours at 0.5, 0.7, 0.9, 1.1 and 1.3 K. Vectors indicate magnitude and direction of linear polarization. Ellipse indicates beam FWHM.

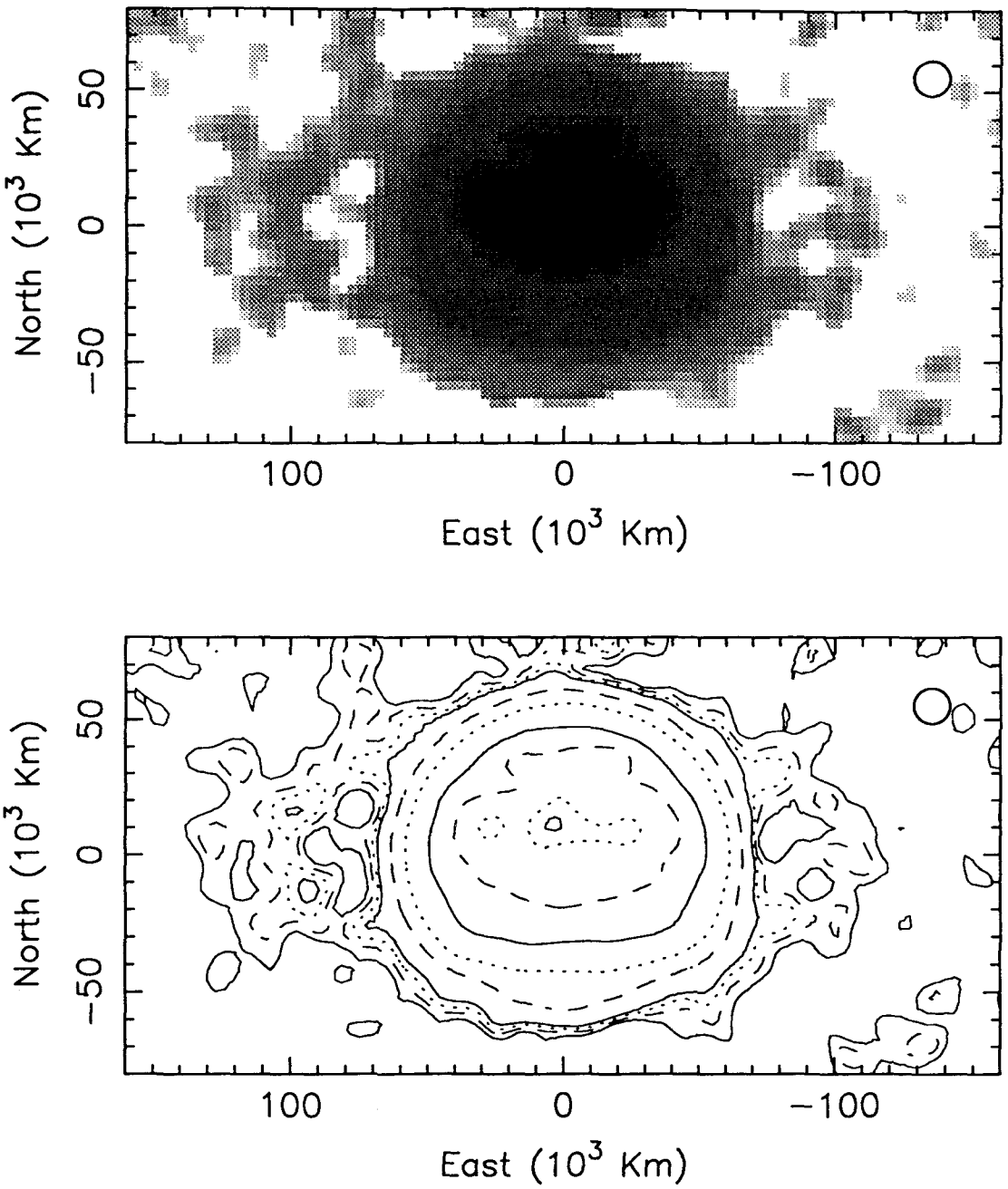

Figure 2.13: Saturn intensity map at a wavelength of 20.13 cm. Top shows a grey-scale representation. Bottom shows a contour map with contours at 4, 7, 10, 13, 40, 100, 200, 230, 245 and 255 K. Ellipse indicates beam FWHM.

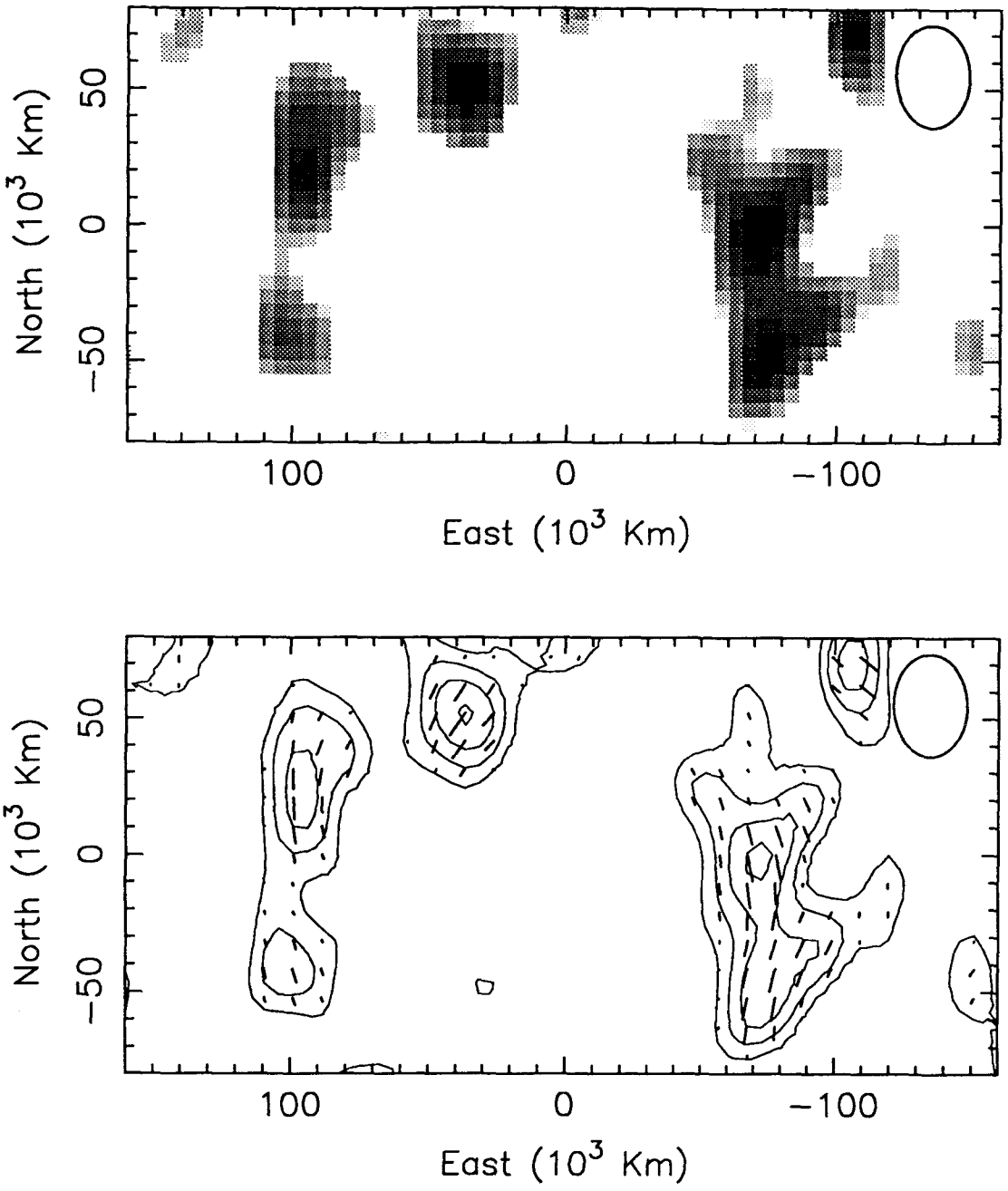

Figure 2.14: Saturn linearly polarized intensity map at a wavelength of 20.13 cm. Top shows a grey-scale representation of polarized brightness. Bottom shows a contour map with contours at 0.7, 0.9, 1.1 and 1.3 K. Vectors indicate magnitude and direction of linear polarization. Ellipse indicates beam FWHM.

Chapter 3

Image Analysis

The eight Saturn images presented in the previous chapter contain a wealth of information for study and analysis. In this chapter we present an initial analysis of the images themselves using simple physical models of the Saturn system. In later chapters the images are analyzed in the context of a complete atmosphere and ring radiative transfer model.

We begin this chapter by finding the precise position of Saturn in the VLBI reference frame and establishing a consistent geometry for subsequent analysis. A subtle but often overlooked correction for the background flux level is discussed and applied to determining absolute brightness temperatures. For comparison with previous observations, a whole disk and ring model of uniform brightness is fit to the maps. This model-fit provides a starting point as well as a constraint for discussing more detailed models which include the effects of the brightness variability observed in the maps.

The images of Saturn in Chapter 2 show intricate structure and brightness variations in the atmosphere of Saturn and on the rings. It is precisely these variations that we wish to dissect and analyze in terms of useful physical parameters. The atmospheric brightness variations are shown to be functions of three parameters: limb darkening, gravitational acceleration, and latitude. Although the limb darkening and gravitational dependence of the intrinsic brightness is interesting, it is the variation with latitude that is most revealing about the dynamical and thermo-chemical nature of Saturn's deep atmosphere. Similarly, the ring brightness variations are reduced to useful geometries and presented in terms of azimuthal variations. We begin by discussing some preliminaries.

3.1 Image Transformation

The aperture synthesis images of Saturn are presented in a natural coordinate system as they would appear to an observer with radio eyes. For the purpose of quantitative analysis, however, the images need to be transformed onto a more useful coordinate system. Here we present a consistent geometry for transforming the images to an atmosphere reference frame and a ring reference frame.

3.1.1 Position determination

The discovery of Quasi-Stellar Objects (QSO) has established a precise astronomical coordinate system for the VLBI reference frame. Radio tracking of planetary space probes has linked the planetary coordinate system to the VLBI frame to an accuracy of better $\pm 0.''03$ for the inner planets (Newhall, Preston and Esposito, 1984). However, here we establish a self-consistent analysis by determining the position of Saturn with respect to the VLBI frame.

The JPL Development Ephemeridies–200 (Standish, 1982) was used to observe Saturn with respect to the well-known calibration QSOs (see section 2.3). Although position offsets could be measured in the maps themselves, we attempt to fit the visibility data directly for position. This is in part because the position determination is required prior to precise imaging (CLEANing and self-calibration).

The visibility of Saturn is modeled as a uniform elliptical disk by the equation:

$$\mathcal{V}(\beta) = \frac{J_1(2\pi\beta)}{\pi\beta} F_0(\lambda) e^{2\pi i(u\Delta\alpha\cos\delta + v\Delta\delta)}, \tag{3.1}$$

where u and v are East and North components of the projected baseline expressed in wavelengths, $\Delta\alpha$ is the ephemeris error in right ascension, $\Delta\delta$ is the ephemeris error in declination, $F_0(\lambda)$ is the flux density at wavelength λ, and β is baseline length normalized to Saturn's radius. The observed visibilities were fit to Eq. 3.1 allowing the position offsets, the disk radii, and the flux density to be free parameters.

The results of the least-squares-fit for the disk radii and flux density are not physically meaningful because the simple elliptical model does not correspond to the brightness distribution of Saturn, which includes extended emission from the rings and extinction from the rings (see figs. 2.7 – 2.14). However, the fitting of an elliptical disk model for position requires only the assumption of symmetry in the brightness of Saturn. The millimeter

data set was not used in the fitting since it is much less sensitive than the centimeter VLA data. The offset of the true position of Saturn with respect to the JPL–DE200 ephemeris as determined by fitting at all four wavelengths is given by:

$$\begin{aligned} \Delta\alpha \cos\delta &= -0''.25 \pm 0''.05 \\ \Delta\delta &= +0''.01 \pm 0''.08 \end{aligned}$$

This result is similar to that found by Muhleman *et al.* (1985), who observed Titan with the VLA and estimated the position offset of Saturn to be

$$\begin{aligned} \Delta\alpha \cos\delta &= -0''.20 \pm 0''.03 \\ \Delta\delta &= +0''.03 \pm 0''.03 \end{aligned}$$

In fact, Muhleman *et al.* found the ephemeris reference frame for the outer planets to be in error by roughly -0.2 arc sec for Jupiter, Saturn, and Uranus.

3.1.2 Geometry

Once the center of Saturn is found, a uniform coordinate system is easily established. The equatorial radius, $R_e = 60268$ km, and the polar radius, $R_p = 54364$ km, are taken from the 1 bar pressure level as determined by the Voyager radio occultation experiment (Lindal, 1985). This roughly corresponds to the level at which the optical depth is about 1 on the limb. The figure of Saturn along the line-of-sight is modeled by an ellipse and the apparent polar radius, which differs from the true polar radius due to the tilt angle of the pole along the line of sight, B, is computed by:

$$R_p' = \sqrt{R_e^2 \sin^2 B + R_p^2 \cos^2 B}. \tag{3.2}$$

The rings are assumed to lie in the equator plane and the ring boundaries are taken from the four classical rings: A, Cassini Division, B, and C. Where higher resolution and sensitivity are warranted, we also consider the D and F rings and sub-rings as determined by significant variations in radio optical depth (Marouf, 1986). Selected geometrical parameters and boundaries are summarized in Table 3.1.

Figures 3.1 and 3.2 show the observing geometry in a coordinate system centered on Saturn. The unit vector $\hat{z}$ is directed along the line of sight from Saturn to Earth while

Table 3.1: Selected Geometrical Parameters.

Region	sub-Ring	Radial distance	
		R_s	(km)
Polar radius		0.902	54364
Equatorial radius		1.000	60268
———		1.110	66970
D Ring			
———		1.235	74490
C Ring	inner C		
C Ring	———	1.380	83275
C Ring	outer C		
———		1.526	92060
B Ring	inner B		
B Ring	———	1.737	104800
B Ring	outer B		
———		1.948	117535
Cassini Division			
———		2.023	122060
A Ring	inner A		
A Ring	———	2.145	129425
A Ring	outer A		
———		2.267	136790
F Ring		2.330	140550

the xy plane coincides with the projected sky plane, x to the west and y to the north. At each observed point on the map, $P(x,y)$, we wish to calculate several quantities of interest. Using the boundaries in Table 3.1 and Eq. 3.2, the point $P(x,y)$ can be mapped to a region on the disk or rings.

For a point $P(x,y)$ on the disk of Saturn we are interested in computing the planetocentric latitude, ϕ, the planetographic latitude, ϕ', and the longitude with respect to the sub-Earth meridian, λ, as shown in fig. 3.1. This is accomplished by first rotating the (x,y,z) coordinate system around the x axis by an angle $-B$ to new coordinates (x',y',z'). The new primed coordinates are determined by

$$x' = x, \tag{3.3a}$$

$$y' = y\cos B - z\sin B, \tag{3.3b}$$

$$z' = y\sin B + z\cos B, \tag{3.3c}$$

and the constraint

$$\frac{x'^2}{R_s^2} + \frac{y'^2}{R_p^2} + \frac{z'^2}{R_s^2} = 1, \tag{3.4}$$

where R_s and R_p are the equatorial and polar radii respectively. In the primed coordinate system the quantities of interest are given by:

$$\lambda = \tan^{-1}\left(\frac{x'}{z'}\right), \tag{3.5a}$$

$$\phi = \tan^{-1}\left(\frac{y'}{\sqrt{x'^2+z'^2}}\right), \tag{3.5b}$$

$$\phi' = \phi + \tan^{-1}\left(\frac{e\sin 2\phi}{1-e\sin^2\phi}\right), \tag{3.5c}$$

where the oblateness is $e = (R_s - R_p)/R_s = 0.09796$. Equation 3.5c is derived from Clairaut's approximation for the level surfaces of a rotating spheroid (see Zharkov and Trubitsyn, 1978, p. 258). In terms of these parameters, the cosine of the emission angle, μ, which is just the angle between the line-of-sight and the local vertical, is given by

$$\mu \equiv \cos\theta = \cos\phi'\cos B\cos\lambda + \sin\phi'\sin B. \tag{3.6}$$

Similarly, for a point $P(x,y)$ on the rings, we are interested in computing the radius in the equator plane, ρ, and the azimuth with respect to the sub-Earth meridian, θ,

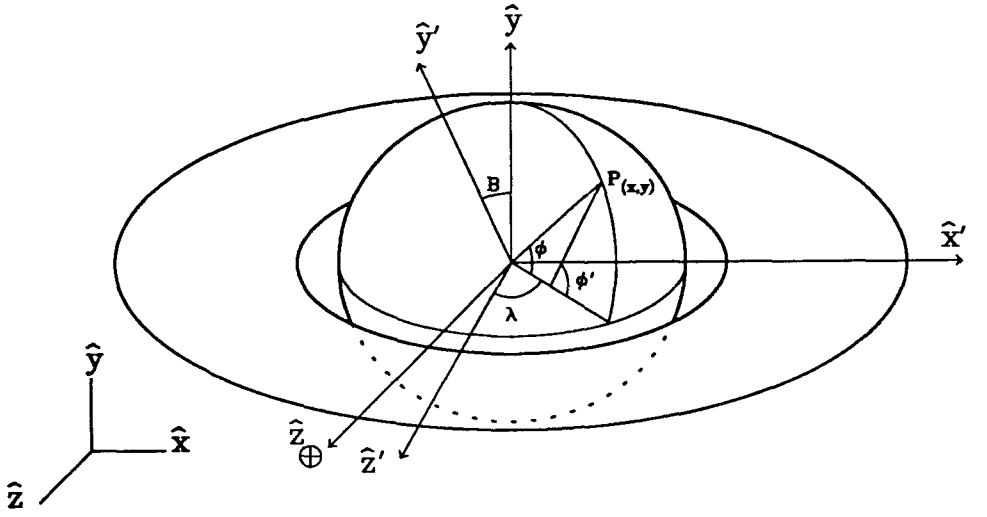

Figure 3.1: Transformation to atmosphere coordinate system.

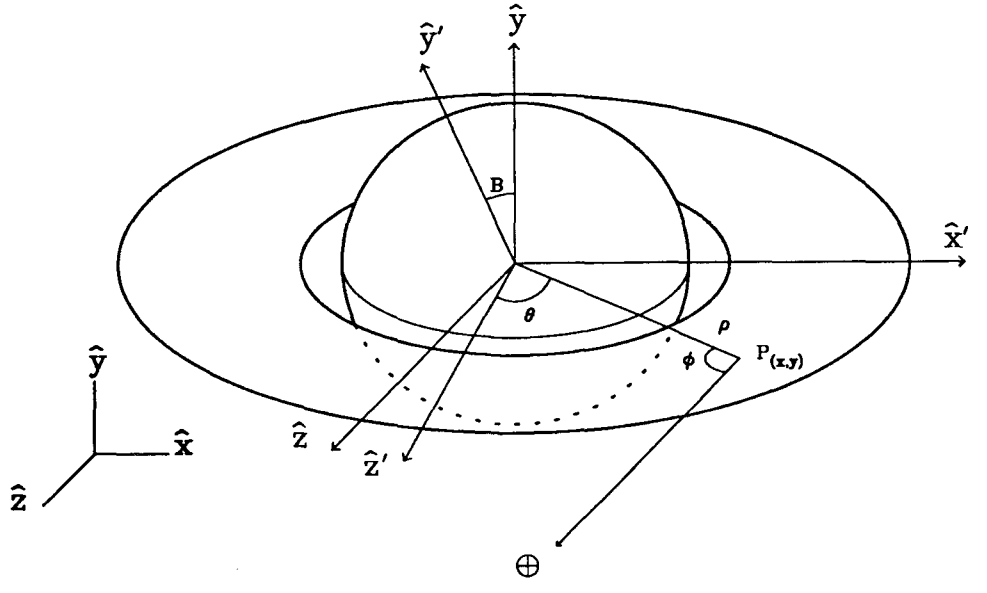

Figure 3.2: Transformation to ring coordinate system.

as shown in fig. 3.2. These quantities are simply:

$$\rho = \sqrt{x'^2 + z'^2}, \tag{3.7a}$$

$$\theta = \tan^{-1}\left(\frac{x'}{z'}\right), \tag{3.7b}$$

Also of interest is the average phase angle, ϕ, the angle between Saturn, P, and the Earth. This is the supplement of the average scattering angle, α, given by

$$\cos\phi \equiv \cos(\pi - \alpha) = -\cos\theta\cos B. \tag{3.8}$$

3.1.3 Microwave Background Correction

The high sensitivity of these observations requires that the finite brightness of the background be considered. This is a subtle, but often overlooked correction to the planetary temperature (Schloerb, Muhleman, and Berge, 1976; Ulich, 1981; Briggs and Sackett, 1989). If this is neglected the true temperature may be underestimated by as much as several tens of Kelvin at centimeter wavelengths, where the contribution of the galactic background is significant.

Saturn's brightness is measured against a smooth, non-zero background with brightness contribution from the primordial 2.7 K cosmic microwave background (CMB) radiation. All observations reported here were sufficiently far removed from the galactic equator that we need not consider the contribution of the galactic thermal and non-thermal radiation. What then is the effect of the CMB? The Fourier transform of a uniform signal is a delta-function at the zero coordinate. Similarly, the response of an interferometer to the 2.7 K uniform background is negligible everywhere except at a baseline of length zero, where it is exactly 2.7 K. This is an example of an invisible distribution (see section 2.4.2). The net result is that the interferometer effectively subtracts a uniform 2.7 K from the sky, not just from the background, but also from the position of Saturn. Thus, 2.7 K must be added to the brightness of Saturn's atmosphere to correct for this effect.

The same conclusion can be reached from another perspective. Consider the response of an interferometer to a planet with brightness temperature equal to the background. In this case, the net sky brightness both on and off the planet would be uniform, and the planet would be undetectable. A similar effect is observed at decimeter observations of the moon, which appears as a cool screen in contrast to the CMB (Krotikov and Pelyushenko, 1987).

The correction is somewhat more complicated for the rings, which are partially transparent to radio waves. For a ring of arbitrary optical depth τ, the transmitted component of the CMB is simply $T_{CMB}e^{-\tau}$, where $T_{CMB} = 2.7\ K$. In the case of conservative scattering, the remaining $T_{CMB}(1 - e^{-\tau})$ is scattered into 4π steradians. However, the reciprocity property of the scattering function exactly replaces the radiation scattered out of the beam by radiation incident from 4π, which is scattered *into* the beam (see Chandrasekhar, 1960, p. 94). Thus, to first order, no correction to the ring brightness temperature is required. This effect can be understood by considering two extreme examples. If the rings are almost completely transparent ($\tau \ll 1$), then the background is detected at the position of the rings, and the interferometer correctly subtracts this amount. On the other hand, if the rings are optically thick ($\tau \gg 1$), then the rings effectively scatter the CMB from 4π steradians into the line-of-sight, and the interferometer correctly subtracts it.

Therefore, in subsequent reduction to brightness temperatures, an additional 2.7 K is added to the atmosphere brightness temperature. No correction is made to the rings.

3.2 Integrated Brightness

In this section, integrated brightness for selected regions of Saturn are determined by fitting a model of uniform brightness. This serves as a means for comparison with previous single-dish and interferometer observations, as well as a constraint on more detailed models that include brightness deviations from the uniform model.

3.2.1 Least squares modeling

Integrated brightness for specific regions is not directly obtainable from the images presented in section 2.4. The finite size of the convolving beam (point-spread function) distorts the boundary that would otherwise separate distinct regions. For example, convolution of the beam with the disk spreads flux beyond the edge of the disk onto the rings and cusp (the ring-occulted region of the disk), and increases their apparent brightness. We attempt to solve for the integrated brightness by developing a linear model that takes into account the affect of the finite beam, and simultaneously solves for the integrated brightness of the disk, rings and cusp of Saturn.

Distinct regions on Saturn are modeled as areas of uniform brightness T_i. These areas are convolved with a beam identical to that of the map, and summed to produce a

model brightness distribution. A reduced χ^2 is generated:

$$\chi^2 = \sum_{x,y} \left[\frac{T(x,y) - \sum_i B * T_i(x,y)}{\sigma(x,y)} \right]^2, \tag{3.9}$$

where the sum is over all pixels, (x,y). $T(x,y)$ is the image, $\sigma(x,y)$ is the associated relative error, B is the beam, and $*$ denotes convolution. The χ^2 is minimized while varying all the parameters to give the best-fit solution T_i and their associated formal errors. The success of the least-squares-fit is most sensitive to the initial noise in the images, as well the beam resolution in the images, which limits the ability to discriminate between small features. In general, the number of independent pixels in a region must be greater than the number of free parameters in the fit to give an uncorrelated, reliable result. For this reason, the Cassini Division is not fully separable in images with poor resolution.

The results of the least-squares-fit, for the images of total brightness (I Stokes parameter), are shown in Table 3.2 along with formal errors of the fit. Saturn is modeled as three regions of uniform brightness: disk, ring, and cusp (the ring-occulted region of the disk). Where possible, the ring and cusp are further separated into distinct regions that include various combinations of the classical rings as well as the four individual rings. Results are omitted in cases in which there was insufficient sensitivity and resolution to obtain uncorrelated fits. The standard errors of the fit in each case are much greater than the uncertainty in any single pixel. This is in part because the uniform brightness model is a poor representation of the data, which clearly varies in brightness within any one region. Therefore, the large formal errors in the least-squares-fit do not represent fundamental uncertainties in the data, but rather, the inadequacies of the model. A more detailed analysis of high-resolution variations in the images is postponed until sections 3.3 and 3.4.

3.2.2 Integrated atmosphere brightness

The first row of Table 3.2 shows the disk-integrated brightness temperature of Saturn's Northern hemisphere at five wavelengths after correction for the microwave background. This spectrum of five data points is plotted in fig. 3.3 along with other disk-resolved interferometer observations and single-dish observations that have been corrected to remove the effect of Saturn's rings by the method of Klein *et al.* (1978). Other data points were taken from Ulich (1981), Courtin *et al.* (1977), Werner *et al.* (1978), de Pater and Dickel (1982),Ulich *et al.* (1984), Dowling *et al.* (1987), and Briggs and Sackett (1989).

Table 3.2: Results of fitting uniform brightness models to I Stokes parameter.

Region	Brightness Temperature T_B[1] (K) at λ_{cm}				
	0.27 cm	2.01 cm	3.53 cm	6.17 cm	20.13 cm
Disk	137.3 ± 4.5	140.1 ± 0.5	161.4 ± 3.7	176.4 ± 0.6	230.9 ± 2.6
Rings:					
A+Cd+B+C	16.7 ± 3.6	4.8 ± 0.9	3.5 ± 2.9	5.1 ± 1.2	6.1 ± 2.4
A+B+C	18.3 ± 3.9	5.3 ± 1.1	3.7 ± 3.4	5.5 ± 1.5	6.8 ± 2.7
A+B	19.4 ± 4.2	5.6 ± 0.8	4.9 ± 3.2	5.9 ± 0.7	7.1 ± 2.4
A	10.2 ± 13.9	3.8 ± 1.0	4.1 ± 13.5	4.2 ± 1.0	5.3 ± 5.0
Cd	—	0.1 ± 3.6	—	0.3 ± 3.5	0.0 ± 28.3
B	26.9 ± 14.1	7.6 ± 0.8	7.7 ± 8.0	7.8 ± 0.8	9.6 ± 4.1
C	10.9 ± 16.7	2.9 ± 1.2	0.0 ± 15.5	2.8 ± 1.2	3.4 ± 6.6
Cusp:					
A+Cd+B+C	85.2 ± 10.5	52.2 ± 2.5	95.4 ± 11.7	78.0 ± 3.5	118.7 ± 7.2
A+B+C	84.9 ± 10.6	49.5 ± 2.9	95.5 ± 11.8	75.6 ± 3.9	117.6 ± 7.5
A+B	49.3 ± 16.8	14.5 ± 3.0	39.3 ± 20.3	28.6 ± 2.4	58.6 ± 9.4
A	—	20.2 ± 16.6	—	52.2 ± 16.0	81.5 ± 30.1
Cd	—	92.4 ± 20.0	—	118.9 ± 22.7	—
B	—	14.7 ± 2.6	—	20.5 ± 2.5	52.8 ± 15.6
C	—	99.6 ± 2.4	—	153.9 ± 2.5	193.0 ± 15.6

[1]Standard errors are given. Absolute errors are 6% at 0.27 cm and 5% otherwise.

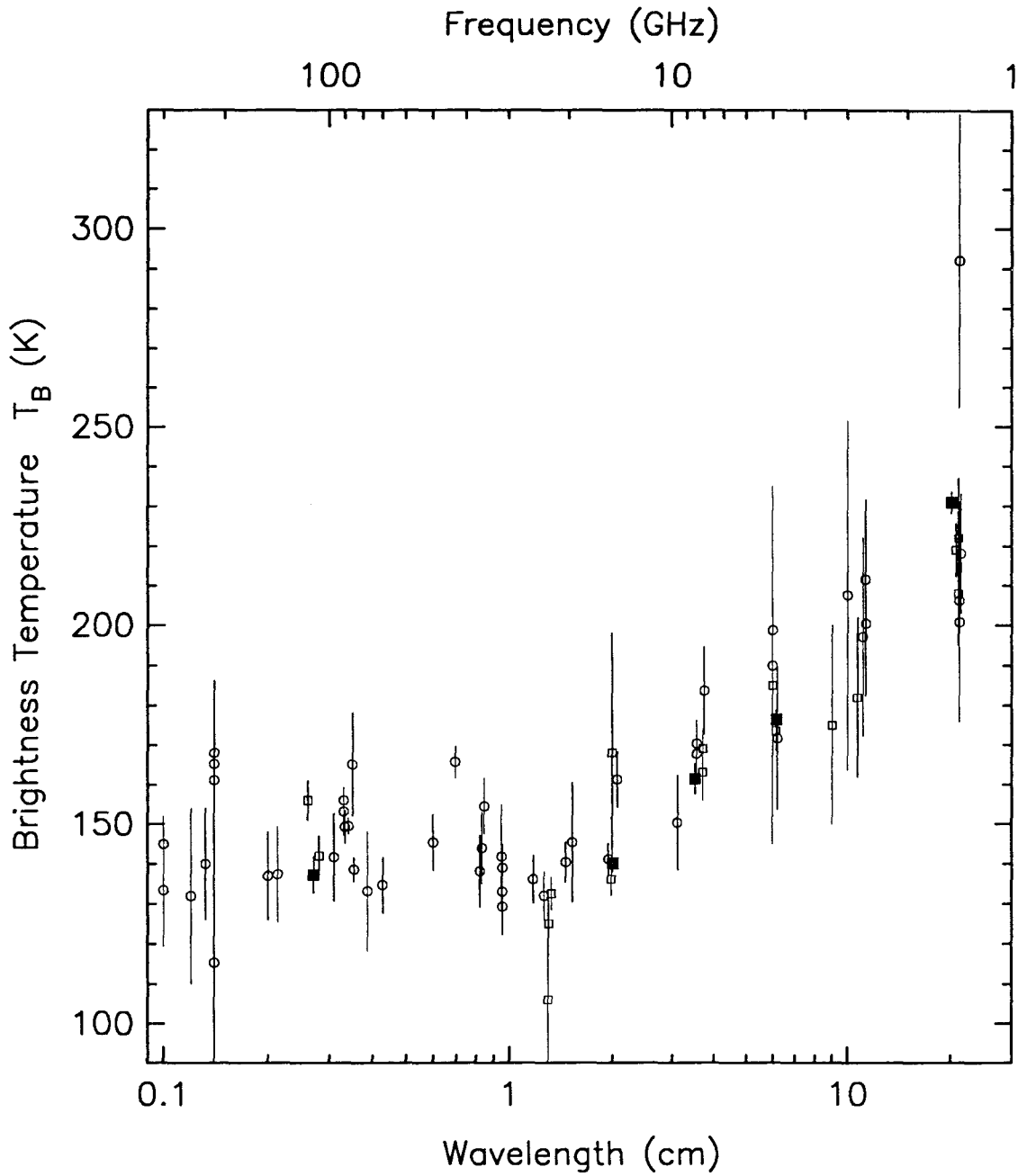

Figure 3.3: Disk-integrated brightness temperature spectrum from this work and others. Squares represent disk-resolved interferometer observations while circles represent single-dish observations that have been corrected to remove the influence of the rings. Solid squares are the new data presented in this work.

The disk brightness temperatures reported here show good agreement with the overall spectra of previous observations. Reported differences that exceed the standard error can be largely attributed to systematic errors in calibration, or perhaps to real changes on long time-scales. In particular, the difference between the current 0.27 cm brightness of 137 K and that of Dowling *et al.* (1987) of 156 K, which was obtained on the same OVRO interferometer, suggests a real variation in the millimeter-wavelength brightness temperature on a time-scale of a few years. Alternately, the discrepancy may be attributed to real hemispherical asymmetry, since the current observations pertain only to the Northern hemisphere of Saturn.

The microwave spectrum of Saturn shows the general properties common to all the microwave spectra of the giant planets (de Pater and Massie, 1985). These characteristics include a minimum near 1.3 cm and an increase in temperature at longer wavelengths. It has been suggested that the increase in brightness with wavelength is due to synchrotron radiation (Luthey, 1973), as is the case for Jupiter. However, Berge and Read (1968) showed that the long wavelength radiation is primarily confined to the disk of Saturn. Since then it has become clear that the microwave spectrum of Saturn can be explained in terms of thermal emission by an atmosphere whose temperature increases with depth and opacity decreases with wavelength (Gulkis *et al.*, 1969). Furthermore, Wrixon and Welch (1970) concluded that the spectrum is consistent with the NH_3 inversion band, centered at 1.25 cm, as the primary source of opacity. Thus we can explain why the microwave brightness of the giant planets, Jupiter, Saturn, Uranus, and Neptune is roughly 150 K near 1.25 cm. This corresponds to the temperature at which NH_3 vapor saturates at pressures found in the troposphere of the giant planets. The exact shape of the whole-disk spectrum as well as the variations in brightness across the disk are related to the vertical profile of temperature and opacity. Chapter 4 develops a complete radiative transfer model for comparison with the observations.

3.2.3 Integrated ring brightness

Table 3.2 also shows the results of the least-squares fit of a uniform brightness model to the ring and cusp (ring-occulted portion of the disk) regions. Under some circumstances, the improved resolution and sensitivity allow separation of ring and cusp brightness into individual components. During observations at wavelengths of 0.27 and 3.52 cm the

rings were near a maximum opening angle, and the A ring and Cassini Division obscured little of the disk. In these cases, no cusp observations were obtainable. The uniform-brightness model was also applied to test for an East-West asymmetry in the rings, and for evidence of emission from the F and D rings. The results were not statistically different from zero for the East-West asymmetry and the brightness of the F and D rings.

Figure 3.4 shows brightness temperature of the combined A and B rings over the wavelength rage 0.02–20.0 cm taken from this work and others (Esposito *et al.*, 1984; Dowling *et al.*, 1987). The results of Table 3.2 are generally consistent with the previous observations and exhibit the general characteristics of the ring spectrum. The ring brightness drops very rapidly in the range 100 μm to 1 mm, attaining a minimum near 3 cm, and then slowly rising at longer wavelengths. The brightness temperature of the classical rings is far less than their thermometric temperature of 80–90 K (Froidevaux, 1981). This information, combined with high radar reflectivity of the rings (Goldstein and Morris, 1973), has lead to the conclusion that the ring particles are composed of low-loss dielectrics, of a size comparable to the centimeter wavelengths, which are effective scatterers but poor emitters and absorbers of microwaves (Schloerb *et al.*, 1980; Cuzzi *et al.*, 1978, 1980). Such a model is also consistent with the absorption properties of cold particles composed primarily of water ice (Pollack *et al.*, 1973). Therefore, the microwave flux of the rings is the result of both intrinsic ring emission and diffuse scattering of planetary emission by the rings.

At short wavelengths the ring flux is dominated by the thermal emission component, while at longer wavelengths the scatted component becomes the dominant source of flux. The transition wavelength between these two regimes, at least for the combined A and B ring, occurs near the region of minimum brightness at 3 cm. Several authors have attempted to model the contribution to the ring flux from these two components (Cuzzi and Van Blerkom, 1974; Cuzzi *et al.*, 1980; Muhleman and Berge, 1982; Janssen and Olsen, 1978) with limited success.

The scattered component is somewhat more complicated to assess because models suggest that it has a strong azimuthal variability and a slight wavelength dependence (Cuzzi *et al.*, 1980; Muhleman and Berge, 1982). No published model, however, includes a full treatment including polarization. Previous observations suffered from poor sensitivity and resolution, and as a result, observational tests of the azimuthal brightness variations were inconclusive (Schloerb *et al.*, 1979a, p248; Dowling *et al.*, 1987, p514). Section 3.4

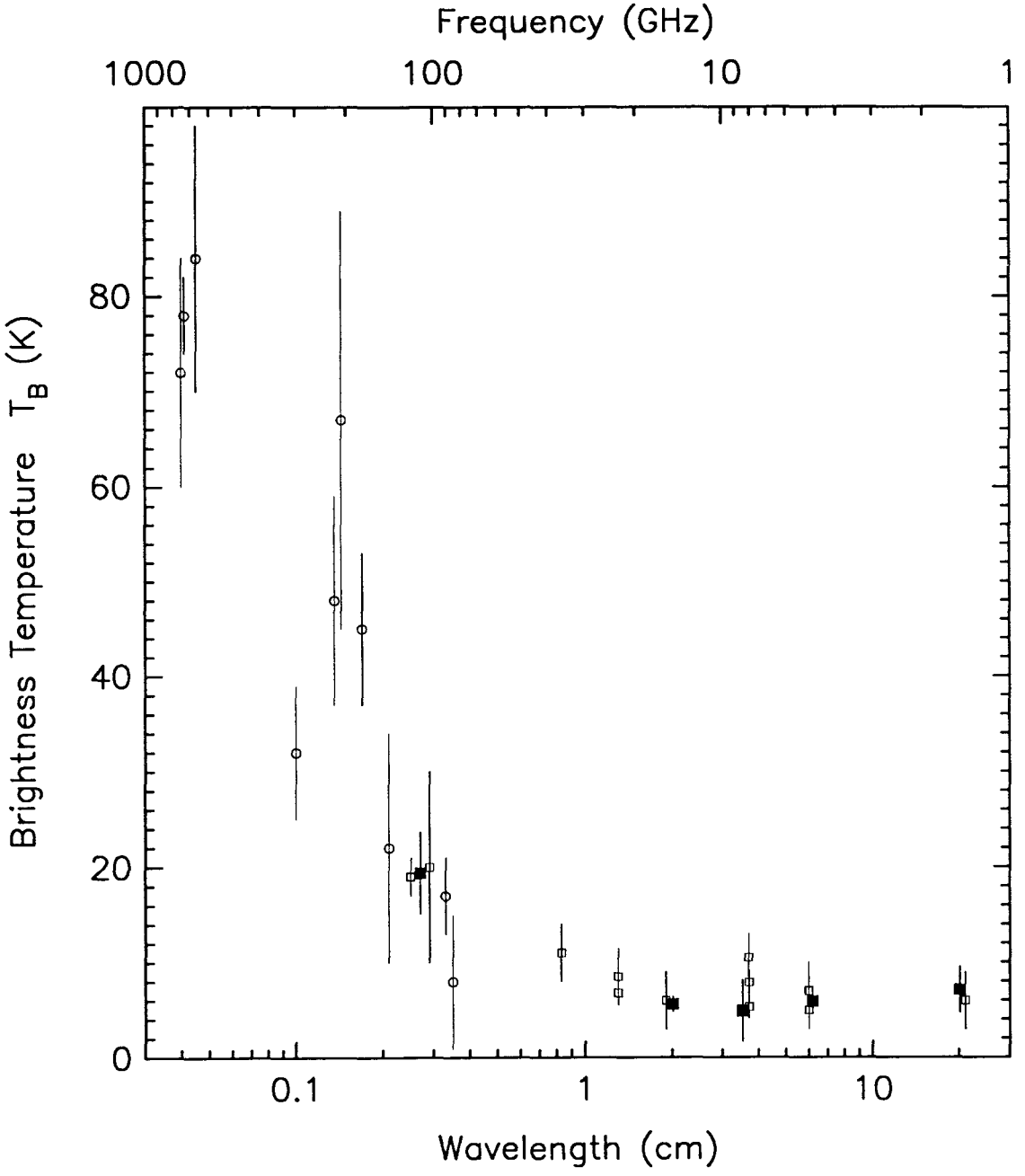

Figure 3.4: Integrated brightness temperature spectrum for combined A and B rings from this work and others. Squares represent disk-resolved interferometer observations while circles represent single-dish observations that have been corrected to remove the influence of the rings. Solid squares are the new data of this work.

presents the first published results of azimuthal ring brightness variations (preliminary results published in Grossman *et al.*, 1989). In addition, chapter 5 presents an analysis of these results in terms of a complete radiative transfer model, including wavelength dependence, polarization, and azimuthal variation. For now, we restrict ourselves to a qualitative discussion of the integrated ring brightness values.

At all wavelengths, the B ring appears brighter than the other resolved rings. This is consistent with the notion that the emitted and scattered flux is proportional to optical depth. The thin C ring, however, appears nearly as bright as the A ring. This is simply the result of Saturn subtending a much larger angle as seen from the C ring than as seen from the A ring, despite the low optical depth of the C ring. In order to understand these effects, we need to consider the optical depth of the rings.

3.2.4 Ring optical depth

Aside from brightness temperature, perhaps the most diagnostic measure of the rings is their optical depth, τ (the term optical depth and radio depth are used interchangeably). This quantity relates the intensity of radiation transmitted through a ring I_t to the incident radiation I_0:

$$I_t = I_0 e^{-\tau}. \tag{3.10}$$

For a ring composed of many discrete particles, the optical depth at wavelength λ is a measure of the second moment of the size distribution through the dependence

$$\tau(\lambda) = \int_{r\sim\lambda/\pi}^{\infty} \pi r^2 Q_e(r,\lambda) n(r) dr, \tag{3.11}$$

where r is the particle radius, $Q_e(r,\lambda)$ is the extinction efficiency, and $n(r)dr$ is the number of particles per unit area with radii between r and $r+dr$. The lower limit of the integration results because for particles much smaller than the wavelength, Q_e rapidly decreases in the Rayleigh scattering limit ($Q_e \sim (\frac{r}{\lambda})^4$). Observations at a variety of wavelengths thus allows a rough determination of the particle number density between the corresponding limits.

For particles much larger than the wavelength, Q_e asymptotically approaches 2. This is a consequence of Babinet's principle, which states that in the geometrical optics limit, a particle intercepts an amount of energy equal to its geometrical cross-section, while also diffracting an equal amount of the incident energy into a narrow cone of angular radius $\theta_d \simeq$

$\lambda/2r$ (van de Hulst, 1957). As a result, the total amount of energy removed from the incident field is exactly *twice* the particle cross-section. In the case of Earth-based or spacecraft observations of Saturn's rings however, the diffracted energy is rarely distinguishable from the incident radiation, and the applicable extinction efficiency in equation 3.11 approaches ~ 1 (Cuzzi and Pollack, 1978; Cuzzi, 1985). This occurs for a variety of reasons. For spacecraft occultations at visible wavelengths, the diffracted light is spread out over such a narrow beam that it is essentially collected by the detector along with the incident light. For Earth-based occultations at visible wavelengths, the ring particles adjacent to the line-of-sight diffract light into the observer's field of view. In the present case of occultation observations of the disk of Saturn, the large angular size of the disk replaces light diffracted out of the line-of-sight with light that would not have otherwise reached the detector. In all these cases, when the diffracted component is not effectively removed from the incident beam, the appropriate efficiency is $Q_e \sim 1$. A different situation applies to the optical depth as measured by the Voyager radio occultation experiment. The diffracted energy is distinguished from the incident signal by its Doppler shift, and is explicitly excluded from calculations of optical depth (Tyler *et al.*, 1983).

Measurements of ring optical depth have been obtained at a variety of wavelengths from the Voyager spacecraft including ultraviolet (Esposito *et al.*, 1983), visible (Smith *et al.*, 1981), infrared (Hanel *et al.*, 1982), and radio (Tyler *et al.*, 1981), and are summarized in Table 3.3. The 3.5 cm radio occultation optical depths indicate the range of observed optical depth and are generally twice as large as equation 3.11 would indicate. For comparison with other optical depths, the radio occultation values should be halved.

Table 3.3: Selected ring optical depths from Voyager.

Ring region	$\lambda = 2640$Å[1]	$\lambda \sim 5000$Å[2]	$\lambda \sim 30\mu$m[3]	$\lambda = 3.5$ cm[4]
A	0.54 ± 0.17	0.40 ± 0.08	0.40 ± 0.05	$0.65 - 0.80$
Cd	0.12 ± 0.16	0.08 ± 0.02	0.07 ± 0.04	$0.15 - 0.65$
B	1.61 ± 0.31	> 1	0.80 ± 0.20	> 1
C	0.11 ± 0.10	0.10 ± 0.02	0.10 ± 0.03	$0.02 - 0.28$

[1]From Voyager PPS, Esposito *et al.*, 1983.
[2]From Voyager ISS, Smith *et al.*, 1981.
[3]From Voyager IRIS, Hanel *et al.*, 1982. Values only apply to outer B and C ring.
[4]From Voyager RSS, Tyler *et al.*, 1981.

The general consensus of these observations is that the ring particles are well-

represented by a power-law size distribution of the form

$$n(r) \propto r^{-q}, \tag{3.12}$$

with power law index in the range $2.8 < q < 3.4$ (Marouf *et al.*, 1983; Zebker *et al.*, 1985). Furthermore, the power law has a sharp lower cutoff at $r \sim 1$ cm and gradual upper cutoff in the neighborhood of $r \sim 5$ m. Many attempts have been made to measure this value from Earth at radio wavelengths. Here we present independent estimates of the ring optical depths at five wavelengths, and compare our results with previous models as well as with Voyager radio occultations.

The rings are modeled as a uniform slab of diffuse scatters of optical depth τ. The brightness of the cusp region is then due to thermal emission from the rings, scattering of Saturn emission by the rings, and direct transmission of Saturn flux, attenuated by $e^{-\tau/\sin|B|}$. The first two components are combined into T_{ring}, and the net brightness temperature of the cusp can be written:

$$T_{\rm cusp} = T_{\rm ring} + T_{\rm disk} e^{-\tau/\sin|B|}, \tag{3.13}$$

where once again, B is the Saturnocentric latitude of the Earth. Strictly speaking, $T_{\rm disk}$ refers to the disk brightness directly behind the cusp and $T_{\rm ring}$ refers to the ring emission directly at the cusp, however, for now, these values will be estimated using the whole-disk brightness and the integrated ring brightness. Solving Eq. 3.13 for τ yields the results shown in Table 3.4 for those regions where the cusp brightness was measured.

Table 3.4: Normal ring optical depth in extinction.

Ring region	τ[0.27cm]	τ[2.01cm]	τ[3.53cm]	τ[6.17cm]	τ[20.13cm]
A+Cd+B+C	0.31 ± 0.07	0.46 ± 0.02	0.25 ± 0.06	0.37 ± 0.02	0.31 ± 0.03
A+B+C	0.32 ± 0.07	0.49 ± 0.03	0.25 ± 0.06	0.39 ± 0.03	0.31 ± 0.03
A+B	0.68 ± 0.25	1.16 ± 0.15	0.68 ± 0.27	0.86 ± 0.05	0.64 ± 0.08
A	—	0.91 ± 0.43	—	0.55 ± 0.14	0.47 ± 0.22
Cd	—	0.17 ± 0.09	—	0.16 ± 0.08	—
B	—	1.27 ± 0.16	—	1.11 ± 0.09	0.71 ± 0.12
C	—	0.15 ± 0.01	—	0.06 ± 0.01	0.08 ± 0.04

The optical depths derived using this simple model are likely to underestimate the true ring optical depth. This is because the uniform brightness model used to derive $T_{\rm ring}$

may not be representative of the ring brightness in front of the planet where brightness may be enhanced due to increased forward scattering (Dowling *et al.*, 1987). This effect is highly wavelength dependent (Cuzzi *et al.*, 1980), and is greatest at the shortest wavelength, where the forward scattering may be highly pronounced. This may explain why the 0.27 cm optical depths are anomalously low. We correct for this effect in chapter 5, by explicitly including the angular dependence of the scattered emission. Nevertheless, the optical depths in Table 3.4 admit some comparisons.

The optical depths appear to decrease with increasing wavelength. This implies that the ring, as a whole, is more transparent at longer wavelengths and places some constraints on the size distribution of centimeter-sized particles. As was first suggested by Voyager radio occultation (Tyler *et al.*, 1983), the Cassini Division, which has low brightness, has a significant optical depth. This observation and the similarity of the opacity at 2.01 and 6.17 cm indicated a deficiency of centimeter sized particles.

It is interesting to compare the microwave optical depths with those obtained at ultraviolet, visible, and infrared wavelengths (Table 3.3). Their similarity argues for a sharp cutoff in the size distribution near a value of 1 cm.

Optical depths of the rings are also significant in determining the apparent brightness of the rings. This allows us to check the extinction optical depth derived above with upper limits to optical depths derived from a scattering model of the ring's brightness. At an arbitrary point on the ring surface, corresponding to a distance ρ from the center of the planet, the angular size of the disk of Saturn is given by

$$\Omega = 2\pi \left(1 - \sqrt{1 - \frac{R^2}{\rho^2}} \right), \tag{3.14}$$

where R is the radius of the planet. We model the rings as an opaque slab, thus the radiation arriving from the disk of Saturn is restricted to half the value suggested by Eq. 3.14. We calculate the brightness of the rings by assuming that the integrated brightness averaged over the ring can be replaced by a model that scatters uniformly into 2π steradians. We neglect multiple scattering, and absorption, by setting the single-scattering albedo $\varpi_0 = 1$. The net brightness of the rings due to scattering is then given by:

$$T_{\rm ring} = \frac{\Omega}{4\pi} T_{\rm disk} (1 - e^{\tau / \sin\theta}), \tag{3.15}$$

where the term in parenthesis represents the fraction of radiation intercepted by the rings, and the $\sin\theta$ term represents the mean incidence angle on the rings.

We can then place an upper bound on the optical depth by solving Eq. 3.15 for τ, and using the values in Table 3.2 as an upper limit for $T_{\rm ring}$. These results are contained in Table 3.5, and generally are consistent with the optical depths due to extinction. The model is clearly inadequate at 0.27 cm where the assumption that all the ring flux is scattered breaks down. However, at other wavelengths, the model gives reasonable upper bounds to the optical depths of the rings.

Table 3.5: Upper bound to normal ring optical depth.

Ring region	τ[0.27cm]	τ[2.01cm]	τ[3.53cm]	τ[6.17cm]	τ[20.13cm]
A+Cd+B+C	∞	0.54	0.31	0.44	0.39
A+B+C	∞	0.61	0.33	0.48	0.44
A+B	∞	0.75	0.51	0.58	0.52
A	∞	0.50	0.45	0.42	0.40
Cd	—	0.01	—	0.02	0.00
B	∞	1.01	0.83	0.75	0.69
C	1.35	0.26	0.00	0.20	0.18

3.2.5 Integrated ring polarization

The least-squares formalism of section 3.2.1 is also applied to the maps of linear polarization at 2.01, 6.17, and 20.12 cm wavelength. The resulting integrated linear polarization is shown in the first section of Table 3.6 for the usual ring areas. Least-squares fitting of the 20 cm map was unable to obtain uncorrelated fits to the individual rings.

The polarized brightness is expressed in units of Kelvin, however it is more useful to divide this by the total ring brightness to get a percentage polarization (Eq. 2.10), which is shown in the second section of Table 3.6. The third section shows the results of the least-squares fit to the maps of polarization angle (Eq. 2.10), where the angle is measured counter-clockwise from North.

Certain trends are evident in Table 3.6. The magnitude of linear polarization, expressed as a percent of total ring brightness, increases with wavelength. With the exception of the Cassini Division, which shows little to no polarization, the percent polarization is inversely related to the ring optical depth. That is, the amount of polarization at a given

Table 3.6: Saturn integrated linear polarization.

Ring region	2.01 cm	6.17 cm	20.13 cm
P_l' ; linear polarization (K)			
A+Cd+B+C	0.41 ± 0.06	0.63 ± 0.08	1.4 ± 0.7
A+B+C	0.45 ± 0.07	0.70 ± 0.08	1.5 ± 0.8
A+B	0.43 ± 0.07	0.67 ± 0.09	1.7 ± 0.8
A	0.57 ± 0.22	0.77 ± 0.24	—
Cd	0.00 ± 0.84	0.00 ± 0.90	—
B	0.48 ± 0.16	0.82 ± 0.18	—
C	0.46 ± 0.21	0.62 ± 0.24	—
$100P_l'/I$; percent linear polarization			
A+Cd+B+C	9 ± 2	12 ± 3	23 ± 11
A+B+C	8 ± 2	13 ± 4	22 ± 14
A+B	8 ± 2	11 ± 2	24 ± 14
A	15 ± 7	18 ± 7	—
Cd	0 ± 7	0 ± 7	—
B	6 ± 2	11 ± 3	—
C	16 ± 10	22 ± 10	—
ψ ; angle of linear polarization[1]			
A+Cd+B+C	$-4° \pm 12$	$+3° \pm 14$	$+5° \pm 51$
A+B+C	$-5° \pm 14$	$+4° \pm 16$	$+6° \pm 55$
A+B	$-2° \pm 14$	$+2° \pm 16$	$+5° \pm 62$
A	$+9° \pm 46$	$-8° \pm 49$	—
Cd	$-9° \pm 177$	$+18° \pm 180$	—
B	$-3° \pm 33$	$+3° \pm 35$	—
C	$-32° \pm 45$	$+13° \pm 49$	—

[1]Measured counter-clockwise from North.

wavelength increases from the B to the A to the C ring. Finally, the angle of polarization is predominantly in the plane of scattering (Saturn-ring-Earth plane). All these factors suggest that the polarization is a direct result of a scattering process.

Lyot was the first to observe polarization effects in planetary observations (1929). Since then many observations of polarized emission at visible wavelength have been studied (Coffeen and Hansen, 1974; Dollfus, 1961), including polarization of Saturn's rings (Dollfus, 1979a). Polarization of Saturn's rings at visible wavelengths has been attributed to several effects including scattering of incident sunlight at the surface of blocks. At radio wavelengths, polarization from solid surfaces of the planetary limbs has also been studied extensively (Clark and Kuz'min, 1965) and is largely the result of the difference in the Fresnel reflection coefficient for vertical and horizontal directions. However, this model is not a satisfactory explanation of the polarization of the rings because it requires the surfaces to have a preferred orientation. In chapter 5 we explore the polarization properties of the rings in the context of a radiative transfer model that includes scattering.

3.3 Atmosphere Brightness Variations

Microwave images of Saturn (see figs. 2.7–2.13) show spatial variability in the absolute brightness of the atmosphere. Some of these variations are caused by geometrical effects, others are real, latitudinal variations. In this section, zonal mean brightness variations are examined before and after correction for viewing geometry.

3.3.1 Longitudinal averaging

The Saturn images were obtained after integrating for as much as eight hours. Some of the maps are even made from data obtained several days or weeks apart. Therefore, the maps are smeared in longitude and any variability in longitudinal brightness is irrecoverable. Instead, we make use of the longitudinal smearing by averaging in longitude as an attempt to increase the sensitivity of our results. Thus, longitudinal homogeneity is assumed. We begin by taking averages in latitude and emission angles.

As a first step, we consider only those data points on the disk of Saturn greater than a beam-width from the edge of the disk or cusp. This subset of data is largely free from dilution by the beam. Each data point at coordinates (x, y) is transformed to planetographic latitude, ϕ', and emission angle, θ, according equations 3.5c and 3.6. The points are binned

in latitude and emission angle, with each bin corresponding to roughly one-third of a beam-width. This overstates the resolution somewhat. The binned results are shown in figs. 3.5 and 3.6 for each of the five wavelengths. Error bars indicate the root-mean-square (RMS) scatter of the data in each bin.

Figure 3.5 shows considerable brightness variability with latitude, especially at the longer wavelengths. Most noticeable is a peak in brightness occurring at 30–40°at 6 and 20 cm wavelengths. The plot also shows the noticeable effect of limb-darkening in decreasing the brightness towards higher latitudes. In some instances it is not clear what effects are true latitudinal variations and what are simply due to changes in emission angle. Furthermore, the RMS deviations within a latitude bin are greater than the standard error on any single pixel. This suggests that the deviations within each bin are real, not just random scatter.

Figure 3.6 shows the average effect of limb-darkening. At large emission angles, the brightness can be reduced by as much as 20% or more. This suggests that the latitudinal brightness curves are corrupted by the limb-darkening and that the limb-darkening curves are biased by the latitudinal variations. For example, points at high latitudes are observed at large emission angles, and so are generally negatively biased with respect to points at lower latitudes. Similarly, points viewed near normal incidence in fig. 3.6 predominantly sample sub-Earth latitudes. The RMS deviations in each bin indicated a real variation with latitude at each emission angle. This suggests a method of simultaneously recovering both latitudinal variations and emission angle effects independent of each other.

3.3.2 Improved brightness variations

The brightness of a point at position (x, y) in the atmosphere of Saturn is a function of several parameters. In this section we develop a linear decomposition model that removes the effect of viewing angle and reduces the latitudinal brightness variations to a normal viewing angle. The brightness variations are easy to compare once they are reduced to a common geometry.

The dependence of brightness on emission angle (also known as limb-darkening) has been studied extensively for the atmospheres of the giant planets (Valdes *et al.*, 1982), and is the result of an increased path length through the atmosphere when viewing at a slant angle. For atmospheres that decrease in temperature with increasing altitude, the net

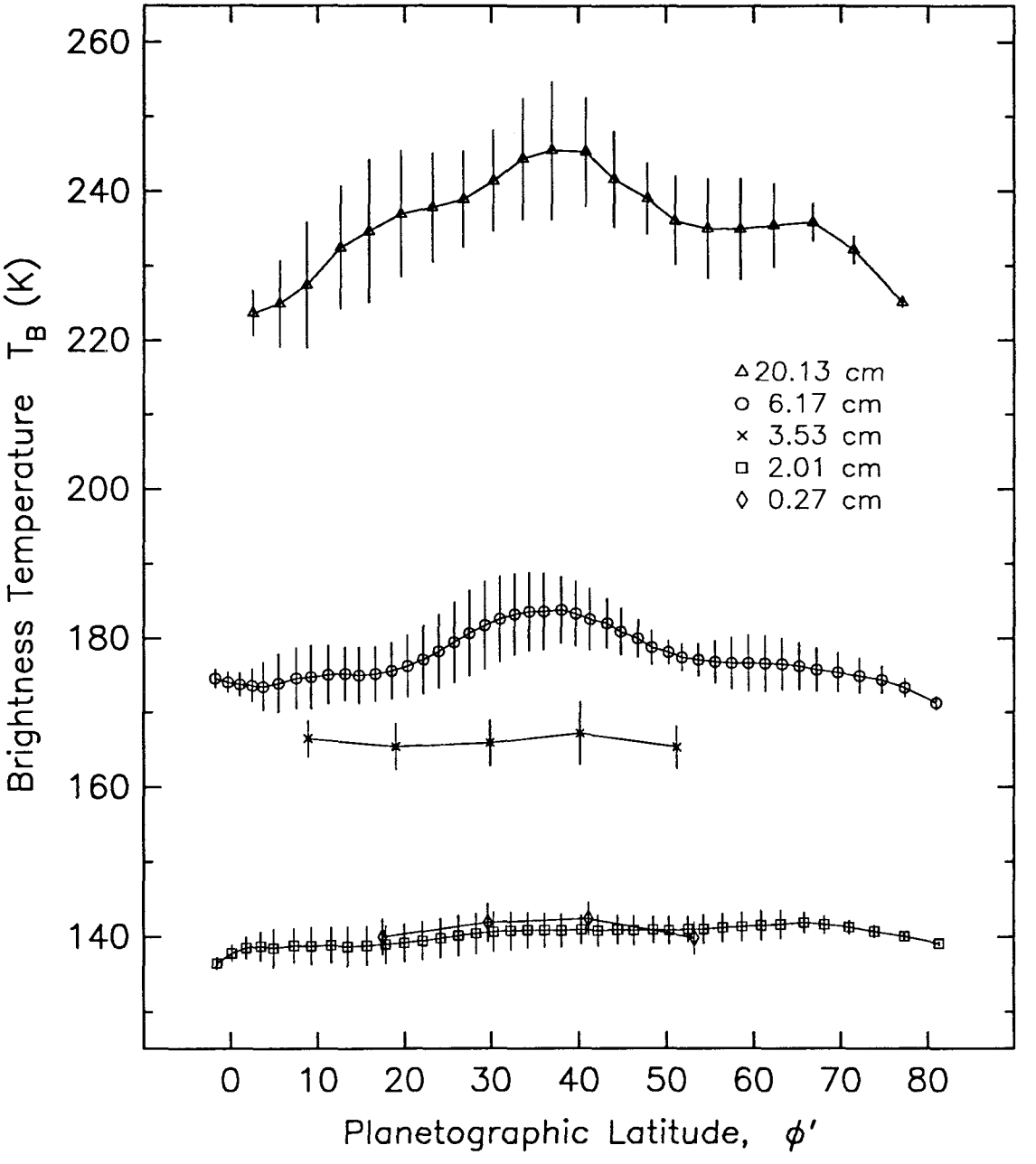

Figure 3.5: Zonally averaged latitudinal brightness temperature from data points greater than a beam-width from the edge of the disk. Error bars indicate the standard deviation in each bin. The statistical error of the mean is typically much smaller. Resolution is typically three to four data points in latitude.

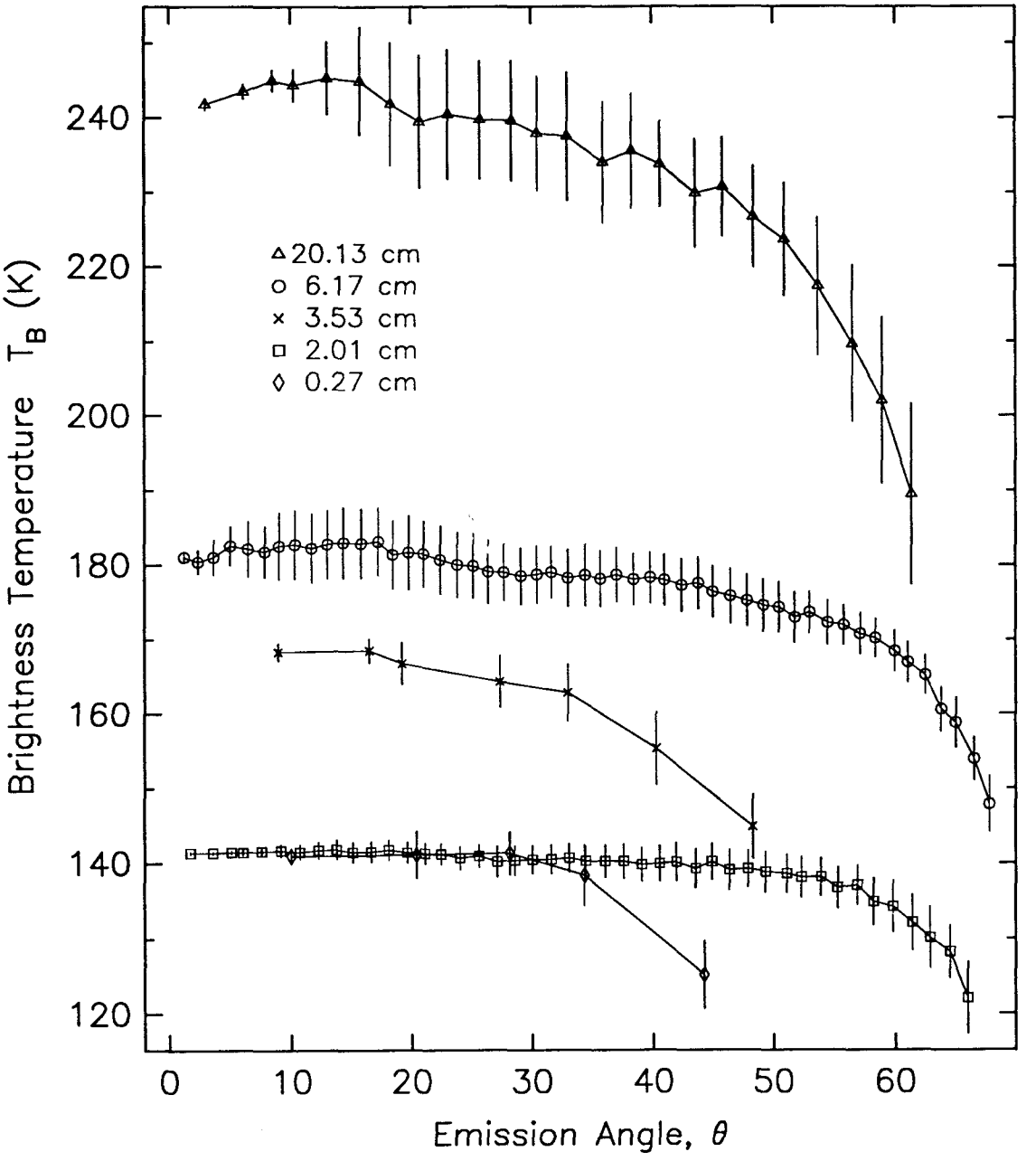

Figure 3.6: Average binned limb darkening from data points greater than a beam-width from the edge of the disk. Data at 0.27 and 3.53 cm show effects of convolution with the edge of the disk. Error bars indicate the standard deviations in each bin. The statistical error of the mean is typically much smaller.

effect is a darkening at large emission angles, hence limb-darkening.

We model the brightness variations as a function of two parameters: the cosine of the emission angle, μ, and the planetocentric latitude, ϕ'. The net brightness is then the sum of these components:

$$T_B(x,y) = T_B(\phi') + \Delta T_B(\mu), \tag{3.16}$$

where $\Delta T_B(\mu = 1) = 0$. To allow for the most general case, the limb-darkening is modeled by a four-term Legendre polynomial:

$$\Delta T_B(\mu) = a_1 + a_2\mu + a_3(3\mu^2 - 1)/2 + a_4(5\mu^3 - 3\mu)/2. \tag{3.17}$$

The brightness at each point is simultaneously fit for limb darkening and variation with latitude. The results, along with the formal errors are shown in fig. 3.7. In comparison with fig. 3.5, the latitudinal brightness variations are much improved. The effect of limb-darkening is removed and the estimated error on each point is decreased.

The latitudinal brightness, after removal of the effect of viewing geometry, shows considerable variability on many length scales. The bright band visible in the 6 cm map (fig. 2.11) is clearly observed at both 6 and 20 cm along with other bands, especially deep in the atmosphere. An equator-to-pole warming, which increases with depth, is evident. This is due, in part, to the change in gravitational acceleration from equator-to-pole, and is further developed in the full radiative transfer model discussed in chapter 4.

3.4 Ring Brightness Variations

The microwave images in figs. 2.7–2.13 suggest the presence of radial and azimuthal brightness variations in the rings. Clearly, variations in radius are expected from the variation of optical depth at radio wavelengths (Tyler *et al.*, 1983). Previous observations have lacked the sensitivity and resolution to distinguish azimuthal variations, however, brightness variations with azimuth are expected on the basis of theoretical modeling alone (Cuzzi *et al.*, 1980). In this section, we present the variations in ring brightness as a function of radius, scattering angle, and frequency for the total brightness, I stokes parameter, as well as for linear polarization. These results are compared to theoretical radiative transfer models in chapter 5.

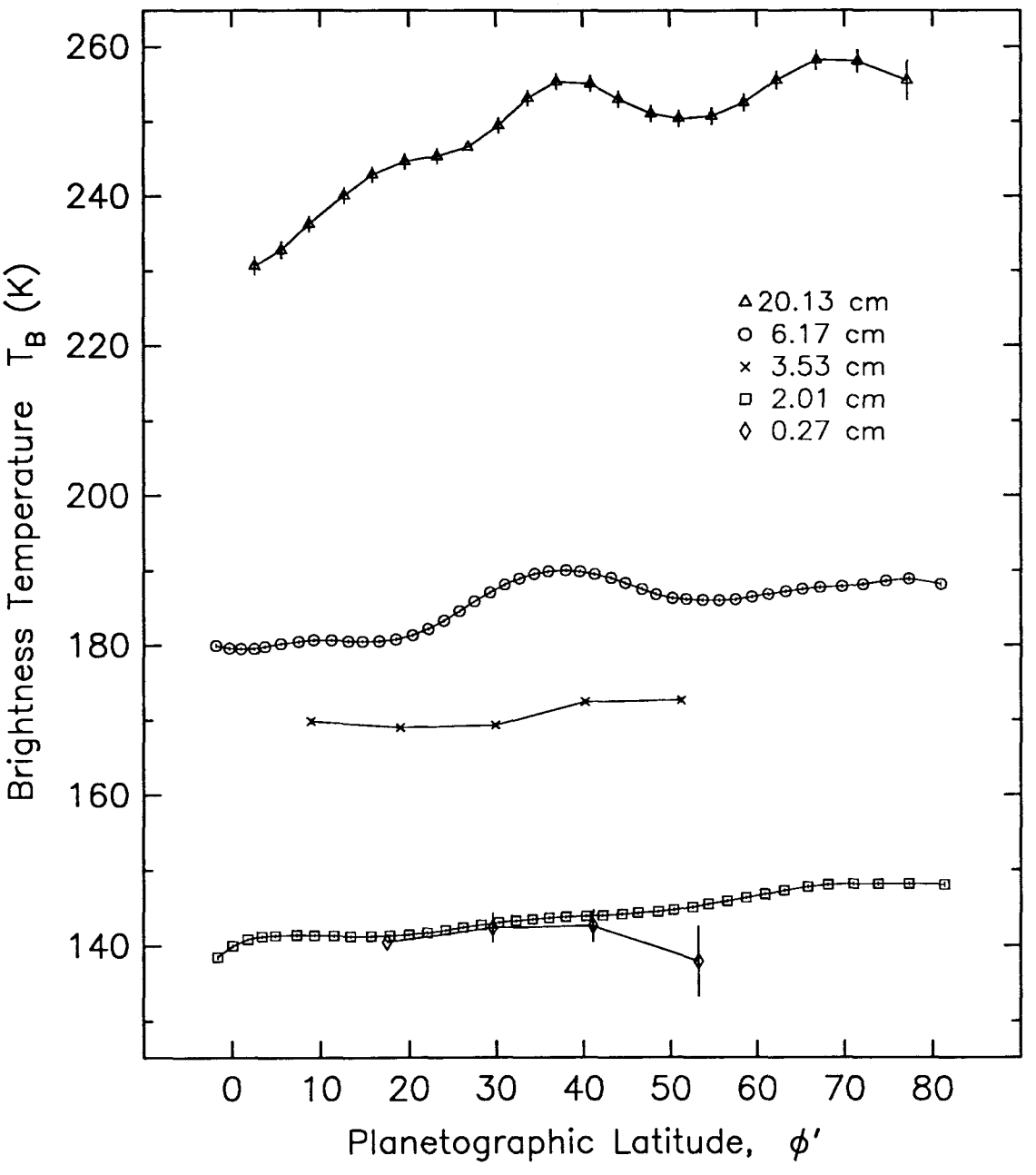

Figure 3.7: Latitudinal brightness temperatures corrected for viewing geometry. A linear least-squares method removed the effect of limb-darkening. The increase in brightness from equator-to-pole reflects the relative decrease in height between levels of constant pressure. Error bars indicate the standard error of the fit. Resolution is typically three to four data points in latitude.

Table 2.4 summarizes the pertinent characteristics of the maps used in this study. The limiting factor in the analysis of ring brightness is the resolution of the synthesized beam in each of the maps. At wavelengths of 2.01, 6.17, and 20.13 cm, the beam is sufficient to resolve the classical A, B, and C rings at the ansea, but not the Cassini Division. Therefore, results presented for the Cassini Division are highly correlated with the A and B rings. At wavelengths of 0.27 and 3.53 cm the beam-width is comparable to the width of the widest ring, the B ring, at the ansea. For completeness, we present results for all five wavelengths, keeping in mind the limits imposed by the beam resolution. Furthermore, we restrict the analysis to those data points greater than a full beam-width from the edge of the disk and cusp, thereby eliminating any influence from these brighter regions.

3.4.1 Variations with radius

Ring brightness from the five maps of total brightness are binned in radius according to the ring boundaries presented in Table 3.1. The average values and standard errors of each bin are shown in fig. 3.8.

The results are qualitatively consistent with the fit of a uniform brightness model (Table 3.2), except where limited by the beam resolution. The B ring appears brighter than the other rings, and the inner B ring appears the brightest of all. The result for the Cassini Division is highly correlated with the brightness of the A and B rings, and as a result, is intermediate between the A and B ring brightness. Beam widths of about 10,000 km are obtained at 2.01, 6.17, and 20.13 cm, and with the exception of the Cassini Division, the results for the individual rings are reliable.

Linearly polarized ring brightness is also binned in radius and shown in fig. 3.9. Here the beam-widths are 15000, 13000, and 32000 km at 2.01, 6.17, and 20.13 cm respectively. Therefore the results for the individual ring regions are not completely independent. Nevertheless, some similarities are present. The inner B ring appears brightest in linear polarization as it does in total brightness. In general, the results of the binning process are consistent with the results of the least-squares fit to regions of uniform brightness (Table 3.6). The error bars in the figures represent the scatter of the data within each bin and are larger than the estimated error for any single pixel. Some of this scatter is due to real variations in azimuth.

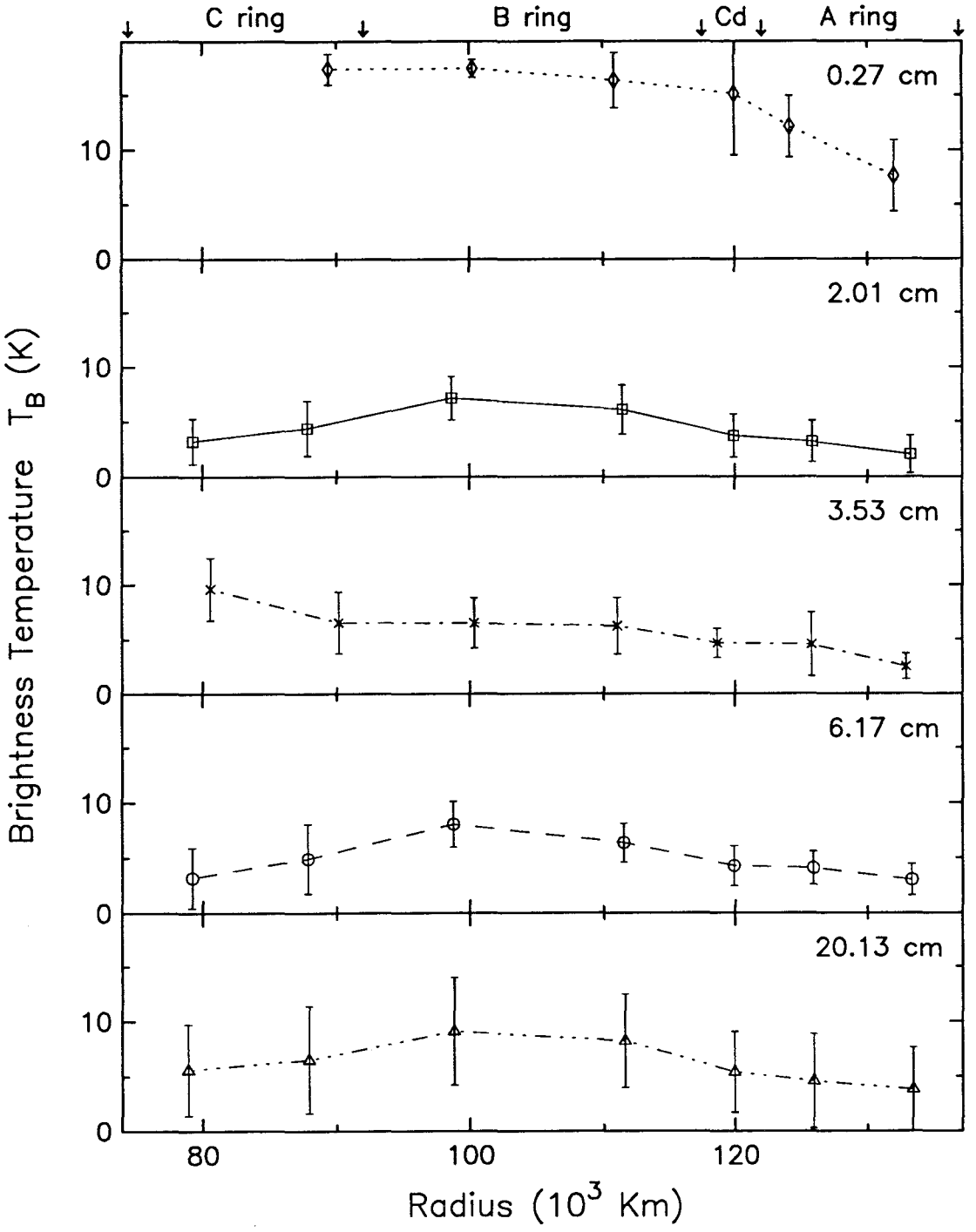

Figure 3.8: Ring brightness as a function of radius. Error bars indicate the standard error based on scatter of the data.

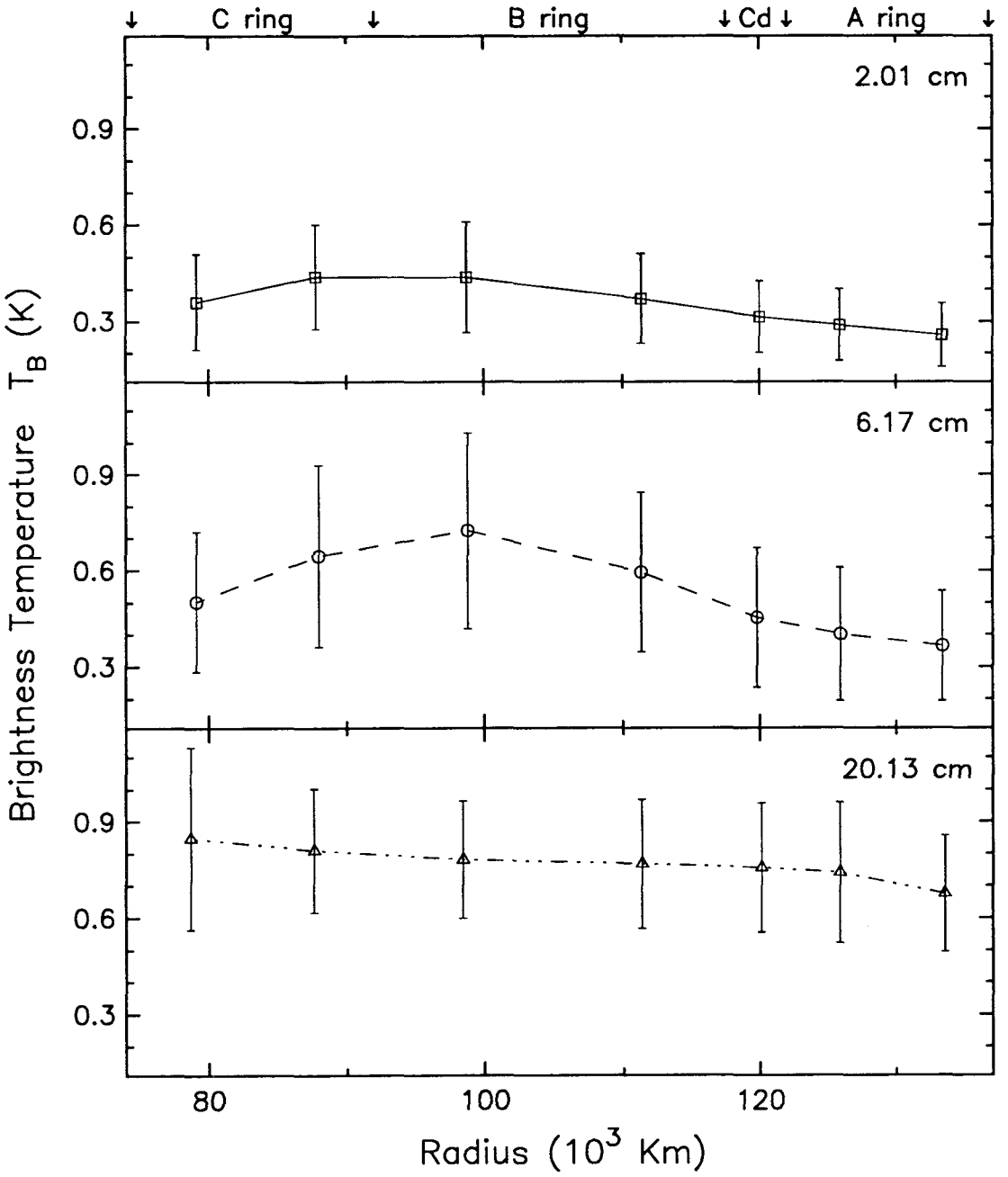

Figure 3.9: Linearly polarized ring brightness as a function of radius. Error bars indicate the standard error based on scatter of the data.

3.4.2 Variations with azimuth

Because much of the flux from the rings is due to scattering, some variation of brightness with azimuth is expected for non-isotropic scattering particles. In this case, the relevant measure is the scattering angle, α, which takes into account the changing inclination angle of the rings and is related to the azimuth according to Eq. 3.8. For forward scattering $\alpha = 0$, while for backscatter $\alpha = 180$.

Ring brightness from the five maps of total brightness are binned in scattering angle and shown in fig. 3.10. The error bars indicate the standard error based on the scatter of the data, however, the data points are not entirely independent from neighboring points. At wavelengths of 2.01, 6.17, and 20.12 cm the resolution is sufficient to obtain independent curves for the three classical rings. For completeness, binned results for 0.27 and 3.53 cm are also presented for the rings.

The angular variation in brightness of the rings exhibits some features common to the scattering phase function of single particles. In particular, the curves appear to be peaked in the forward and backward direction, and show a minimum at intermediate scattering angles. With the exception of the C ring, the azimuthal variations exhibit a symmetry about $\alpha = 90°$. The C ring shows a pronounced peak in the forward direction compared to the other rings. There is no evidence in any ring for the azimuthal asymmetry observed at optical wavelengths in the A ring (Franklin *et al.*, 1987). In chapter 5 we explore radiative transfer models that satisfy the angular variations of the data.

The angular dependence of the linearly polarized component is also of interest. Figure 3.11 shows the angular variations of the linearly polarized maps. Although the error bars are quite large, the linearly polarized brightness exhibits a symmetry about $\alpha = 0$. The brightness appears greatest at intermediate scattering angles, and is a minimum at large and small scattering angles. This result will be explored in greater detail in chapter 5.

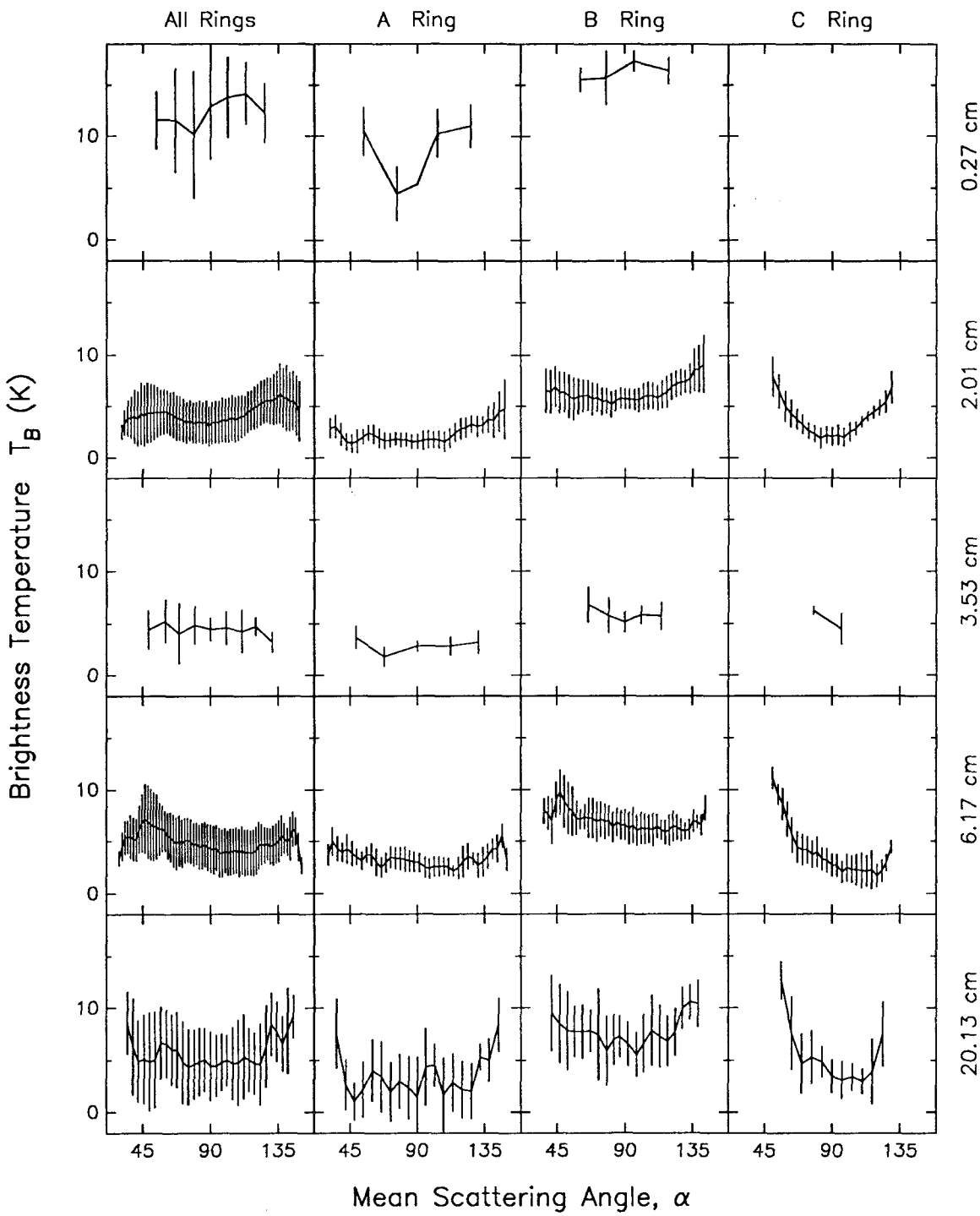

Figure 3.10: Ring brightness as a function of scattering angle. Error bars indicate the standard error based on scatter of the data.

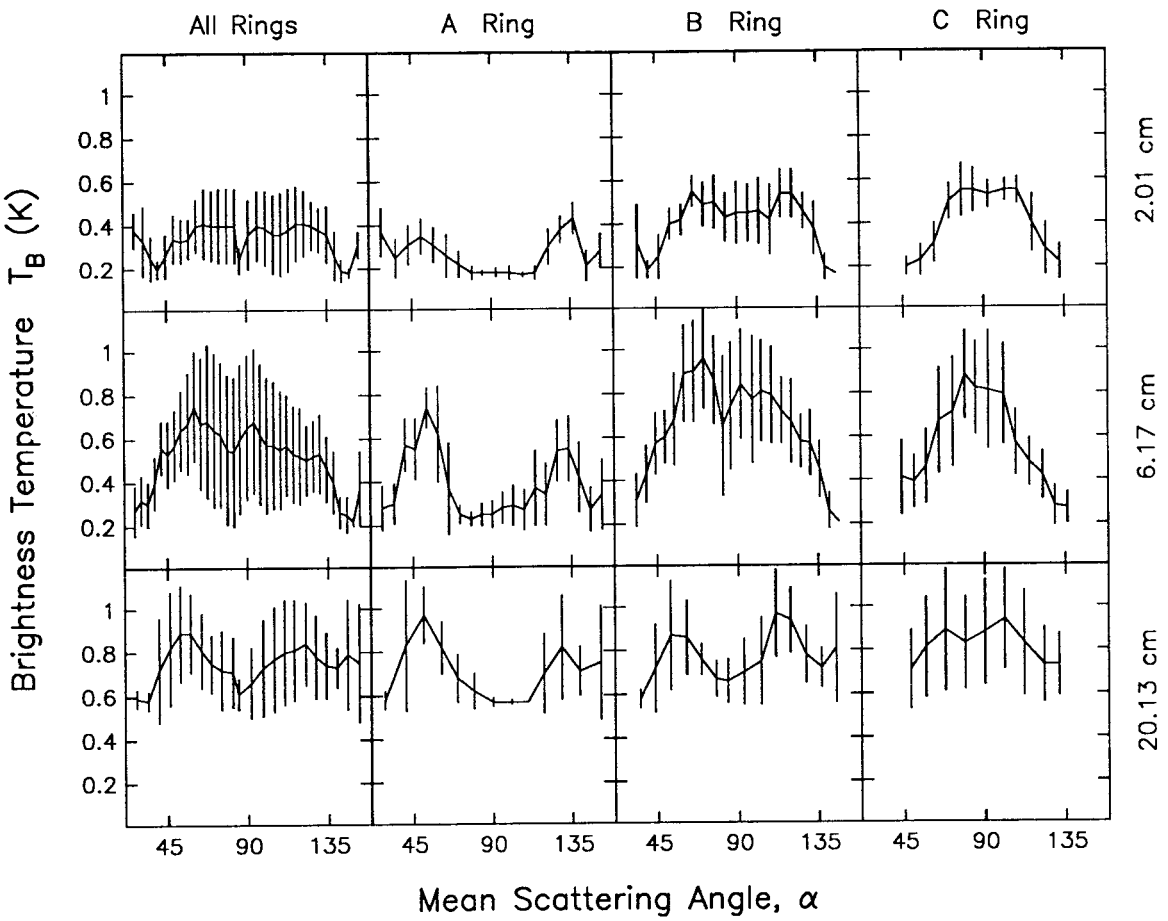

Figure 3.11: Linearly polarized ring brightness as a function of scattering angle. The linear polarization is usually perpendicular to the mean scattering plane. Error bars indicate the standard error based on scatter of the data.

Chapter 4

Atmospheric Modeling and Analysis

In previous chapters we have described the observations and data reduction methods that yield exquisite and beautiful microwave images of Saturn to our eyes. In this chapter we develop a theoretical framework that gives the observations some substance and form in our minds.

The atmosphere of Saturn in the region above the visible cloud tops has been extensively studied from Earth-based observatories as well as from spacecraft. Yet fundamental uncertainties about the composition and dynamics of the deep atmosphere still remain. The inventory of heavy elements remains incomplete (Lunine, 1989). Although it appears that the atmosphere is enriched in the volatiles CH_4, NH_3, and PH_3, large uncertainties remain on the exact mixing ratios and on the vertical and horizonal distribution and variability of these species. The volatiles H_2O and H_2S, which are expected to be among the basic constituents of the atmospheres of the giant planets, have not been detected.

We begin by constructing an elaborate physical model of the atmosphere of Saturn, sufficient to characterize the microwave radiation field. The model itself is a synthesis of previous attempts to characterize and understand the physics and chemistry of the deep atmosphere of Saturn (de Pater and Massie, 1985; Briggs and Sackett ,1989) and the Jovian planets in general (Weidenschilling and Lewis, 1973; Atreya, 1986). The model is then used to constrain both the global properties of the atmosphere as well as the fine-scale, highly-resolved structure.

Two methods are used to compare the models and observations. First, the parameters describing the atmosphere (i.e., pressure, temperature, distribution of absorbers) are prescribed and the radiation field is calculated. This is the direct problem of remote sounding, and the focus here is primarily on applications of this method. Alternately, we consider some simple applications of the inverse problem. That is, given the radiation field, find the distribution of temperature and absorber. However, this is a much more difficult problem,

because the solution is somewhat ill-defined. The effects of temperature and absorption are not always linear and separable. So the real difficulty is not of finding a solution, but of deciding which of any number of solutions is most appropriate for the current problem.

4.1 The Radiative Transfer Model

In this section, the details of the atmospheric radiative transfer model are presented. Much of the modeling is based on general radiative transfer theory (Houghton *et al.*, 1984) and similar models developed for the Giant Planets (Wrixon and Welch, 1970; de Pater and Massie, 1984; Hofstadter and Muhleman, 1988; Briggs and Sackett, 1989). Throughout, the atmosphere is assumed to be in local thermodynamic equilibrium, and the transport of radiation involves only absorption and emission; scattering can be neglected.

4.1.1 Equation of transfer

At any frequency in the microwave where an atmospheric constituent absorbs radiation it will also emit radiation according to Kirchhoff's Law. Thus, the intensity of radiation at the top of the atmosphere will be a function of the distribution of the absorbers and the vertical profile of temperature.

Consider an infinitely deep, horizontally stratified atmosphere, in which the vertical coordinate, z, increased upwards. Furthermore, consider a thin layer of the atmosphere at height z and of thickness dz at constant temperature $T(z)$ and characterized by an absorption coefficient $\alpha_\nu(z)$, where the subscript ν explicitly includes the wavelength dependence of the absorption. In the Rayleigh-Jeans limit, the layer emits radiation in direction μ proportional to $T(z)\alpha_\nu(z)dz/\mu$, where μ is the cosine of the angle between the vertical and the emission angle and scattering has been neglected. The intensity of this radiation observed at the top of the atmosphere is reduced by absorption in the intervening layers by a factor $e^{-\tau/\mu}$, where

$$\tau(z) = \int_z^\infty \alpha_\nu(z')dz'. \tag{4.1}$$

Thus, the observed differential brightness temperature at the top of the atmosphere due to a layer of thickness dz at height z is given by

$$dT_B(z,\mu) = T(z)\alpha_\nu(z)e^{-\int_z^\infty \alpha_\nu(z')dz'/\mu}dz/\mu. \tag{4.2}$$

The total brightness temperature along any ray in direction μ is found by integrating over all layers

$$T_B(\mu,\nu) = \int_0^\infty T(z)\alpha_\nu(z)e^{-\int_z^\infty \alpha_\nu(z')dz'/\mu}dz/\mu = \int_0^\infty T(z)K(z,\mu)dz/\mu. \qquad (4.3)$$

In other words, the total brightness temperature is the weighted average of the temperature of the atmosphere, weighted by the weighting function $K(z,\mu)$.

4.1.2 Layered atmosphere model

The atmosphere is modeled as a finite number of plane-parallel, homogeneous layers. Each layer is uniquely specified in terms of pressure, temperature, and composition. This is sufficient to determine the absorption at each level and thus determine the weighting function. The radiative transfer integral (Eq. 4.3) is then easily evaluated by replacing the integral with a sum over more than 1000 layers of the model atmosphere:

$$T_B(\mu,\nu) = \sum_{z_0=200\text{bar}}^{0.1\text{bar}} T(z)K(z,\nu)\Delta z + T(z_0)e^{-\tau(z_0)}, \qquad (4.4)$$

where the last term is a correction factor to account for any contribution to the brightness from below the lower cutoff at 200 bar. The limits of the sum and the number of layers are empirically chosen to encompass the range probed by microwaves. The uncertainty in evaluating the radiative transfer integral in a finite number of pressure steps is empirically estimated to be less than 0.01%.

Because the temperature and absorption naturally depend on pressure, the vertical coordinate is modeled in terms of pressure (measured in bar). Transforming from altitude coordinates to pressure coordinates is accomplished by applying the ideal gas law to the equation of hydrostatic equilibrium

$$dz = -\left(\frac{RT}{\overline{m}gP}\right)dP, \qquad (4.5)$$

where R is the universal gas constant, $\overline{m}$ is the mean molecular weight of the atmosphere, and g is the acceleration of gravity in the vertical. The mean molecular weight, $\overline{m}$, varies with height in the atmosphere as the composition changes. The effective acceleration of gravity changes considerably with latitude due to the oblateness of Saturn and the variability of winds.

The net acceleration is represented as a vector g in the meridional plane with radial and latitudinal components given by:

$$\mathbf{g} = \mathbf{u}_r g_r + \mathbf{u}_\phi g_\phi, \tag{4.6}$$

where $\mathbf{u}_r$ and $\mathbf{u}_\phi$ are unit vectors in the radial and latitudinal directions respectively. The vector components are approximated to second-order by

$$\begin{aligned} g_r(r,\phi) &= -\frac{GM}{r^2}\left\{1 - 3J_2\left(\frac{R_S}{r}\right)^2 P_2(\phi) - 5J_4\left(\frac{R_S}{r}\right)^4 P_4(\phi)\right\} \\ &\quad + \frac{2}{3}\omega^2 r\left[1 - P_2(\phi)\right] \qquad (4.7a) \\ g_\phi(r,\phi) &= -\frac{GM}{r^2}\left\{J_2\left(\frac{R_S}{r}\right)^2 \frac{dP_2(\phi)}{d\phi} + J_4\left(\frac{R_S}{r}\right)^4 \frac{dP_4(\phi)}{d\phi}\right\} \\ &\quad - \frac{1}{3}\omega^2 r \frac{dP_2(\phi)}{d\phi}, \qquad (4.7b) \end{aligned}$$

where r is the radius to the center of mass, ϕ is the planetocentric latitude, G is the universal gravitational constant, M is the mass of Saturn, and ω is the angular velocity (Lindal *et al.*, 1985). The zonal harmonic coefficients are $J_2 = 1.6331 \times 10^{-2}$ and $J_4 = -9.14 \times 10^{-8}$ normalized to an equatorial radius of $R_S = 60268$ km (Hubbard and Marley, 1989).

The presence of winds is included in the model by modifying the angular velocity as follows:

$$\omega = \omega_{III} + \frac{V}{r\cos\phi}, \tag{4.8}$$

where V is the eastward zonal wind velocity and $\omega_{III} = 1.6378 \times 10^{-4}\,\mathrm{rad\,sec^{-1}}$ is the system III rotation rate of the interior (Kaiser *et al.*, 1984). However, the net effect of the winds comparable to those measured at the cloud tops ($\sim 500\,\mathrm{m\,sec^{-1}}$) is negligible, and initially $V = 0$ in the model.

The results of equation 4.7 are also used to calculate the planetographic latitude, which is given by

$$\phi' = \phi + \tan^{-1}\left(\frac{g_\phi}{g_r}\right). \tag{4.9}$$

The radius of the 1-bar surface of constant pressure is approximated by the second-order Darwin-de Sitter spheroid equation:

$$r(\phi) = R_S\left[1 - e\sin^2\phi - (\frac{3}{8}e^2 + k)\sin^2 2\phi\right], \tag{4.10}$$

where $e = \frac{3}{2}J_2 + \frac{1}{2}q$, $q = \omega^2 R_S^3/GM$ and k is the second-order correction given by Zharkov and Trubitsyn (1978).

Each layer of the atmosphere is assigned a constant pressure, and a corresponding constant temperature and absorption coefficient are calculated based on the composition of the atmosphere and physical relations discussed in the following sections.

4.1.3 Composition

The model atmosphere consists of hydrogen(H_2), helium (He), methane (CH_4), ammonia (NH_3), water (H_2O), and hydrogen sulfide (H_2S). These six constituents are sufficient to characterize the physical state of the atmosphere and the microwave radiation field. Hydrogen, helium, methane, and ammonia have been detected at Saturn (Conrath *et al.*, 1984), and comprise the bulk of the observed atmosphere. Ammonia is the principle microwave absorber, and produces the observed clouds in the visible, which obscure the deep atmosphere. Although water and hydrogen sulfide have never been directly observed on Saturn, their presence is expected based on comparison with Jupiter. Furthermore, water is a microwave absorber in its gaseous and liquid state, and may be a significant source of opacity. Hydrogen sulfide is included in the thermo-chemical model calculation because of its ability to trap ammonia to form a particulate cloud of NH_4SH.

It is conceivable that some additional minor species, such as PH_3, C_2H_6, and CO, can influence the microwave spectra, especially at millimeter wavelengths. However, little is known about their abundance and distribution. Furthermore, the quality of the millimeter data does not warrant the addition of these minor sources of opacity.

The concentration of each constituent is specified in terms of its mole fraction, X_k. For an ideal gas, $X_k = P_k/P$, where P_k is the partial pressure of the k_{th} gas. This differs somewhat from the usual convention in which a concentration is specified in terms of its mole fraction relative to H_2. The H_2, He, and CH_4 are assumed to be uniformly mixed throughout the atmosphere with mole fractions of 0.963, 0.033, and 0.004 respectively in the upper troposphere (Conrath *et al.*, 1984). The concentrations of the remaining constituents are free parameters in the model, and are expressed in terms of their relative "solar" abundances. In terms of mole fractions, the values of solar abundances from Cameron (1982; as summarized in Atreya, 1986) are: solar $X_{H_2O} = 1.329 \times 10^{-3}$, solar $X_{NH_3} = 1.676 \times 10^{-4}$, and solar $X_{H_2S} = 3.621 \times 10^{-5}$. CH_4 does not condense on Saturn. However, NH_3, H_2O,

and H_2S all undergo phase changes (Weidenschilling and Lewis, 1973; Atreya and Romani), and form clouds in the troposphere.

4.1.4 Clouds and chemistry

The process of cloud formation is important in determining the microwave radiation field because of its ability to control the vertical distribution of the major sources of opacity. Despite the lack of observational constraints, the physics of cloud formation and models of the cloud structure of Saturn have been extensively studied (Weidenschilling and Lewis, 1973; Atreya and Romani, 1985; Carlson *et al.*, 1988). Only recently have models of cloud structure been compared with observations of the deep atmosphere of Saturn (Briggs and Sackett, 1989). We develop here a cloud model sufficient to characterize the vertical distribution of H_2O, NH_3, and H_2S.

The cloud structure for a typical model containing solar abundances of nitrogen, oxygen, and sulfur, and illustrating the full range of possible clouds, is shown in fig. 4.1. NH_3 condenses in the upper troposphere to form an ice cloud with base near 1.3 bar and extending up to several hundred millibar. Condensation occurs whenever the partial pressure exceeds the empirically determined saturated vapor pressure over ice

$$\ln P = \frac{-4122}{T} - 1.81630 \ln(T) + 27.86303, \tag{4.11}$$

where T is in Kelvin and P is in bar (Briggs and Sackett, 1989). This vapor saturation curve is illustrated in fig. 4.2. Rapid convection in the atmosphere suggests that NH_3 is fully saturated in the cloud and this is consistent with Voyager measurements of NH_3 abundance within the cloud (Lindal *et al.*, 1985). Nevertheless, we also examine models in which NH_3 is subsaturated with a relative humidity of less than 100%. The NH_3 abundance is assumed to be constant below the NH_3 cloud to a level where the NH_4SH cloud forms.

The solid NH_4SH cloud forms through the chemical reaction

$$NH_3(g) + H_2S(g) \overset{K}{\rightleftharpoons} NH_4SH(s), \tag{4.12}$$

when the product of the partial pressures of NH_3 and H_2S exceeds the equilibrium constant K for the reaction. The equilibrium constant is given by Lewis (1969) as

$$\ln(K) = \ln(P_{NH_3} P_{H_2S}) = 34.151 - \frac{10834}{T}, \tag{4.13}$$

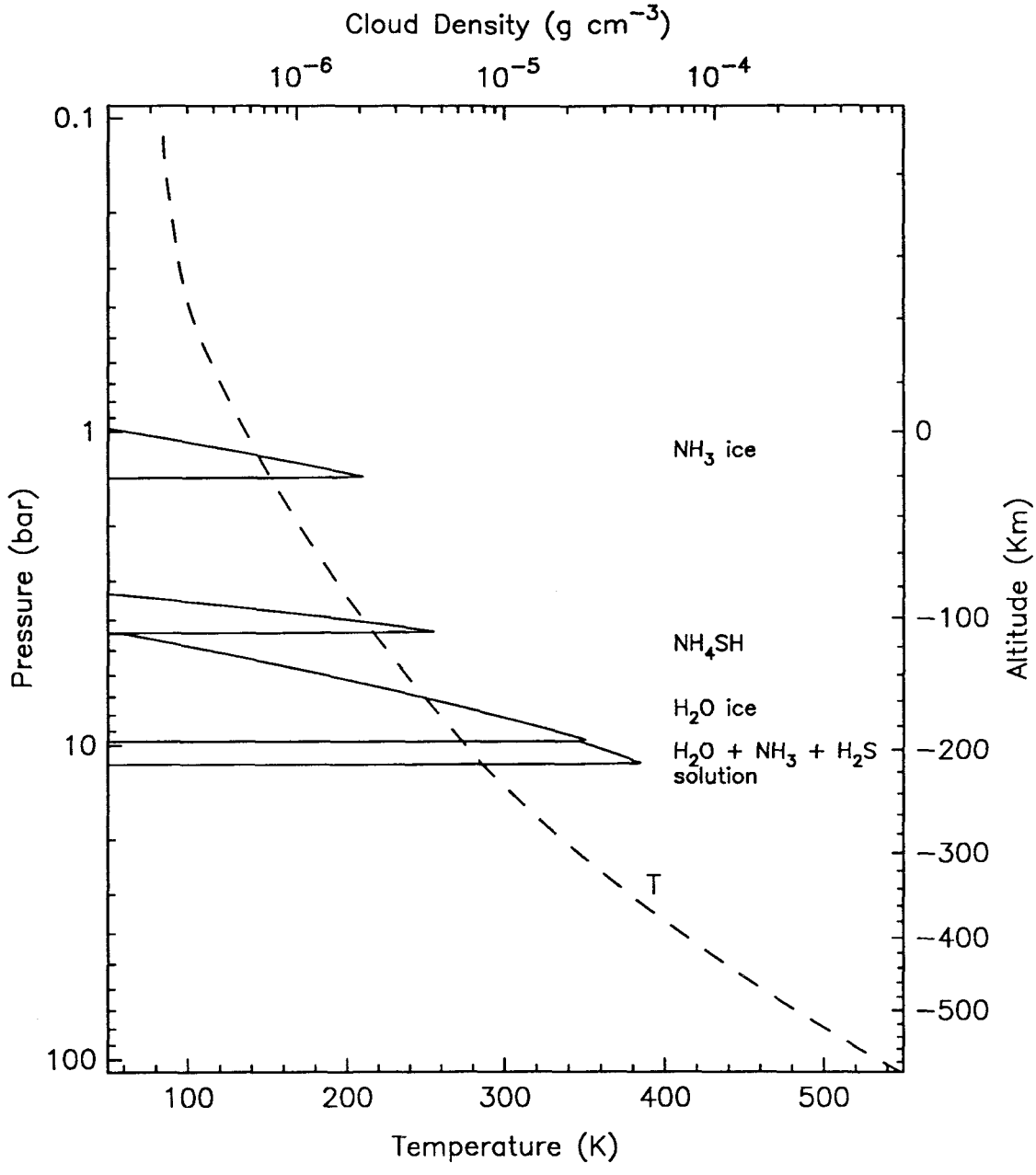

Figure 4.1: The cloud structure of Saturn for a model containing solar abundances of Oxygen in the form of H_2O, Nitrogen in the form of NH_3, and Sulfur in the form of H_2S superimposed on an adiabatic temperature profile (dashed line). An ammonia ice cloud forms below 1 bar, while H_2S and NH_3 react chemically to form a particulate cloud near 4 bar. Deeper still, H_2O condenses to form an ice cloud and a liquid solution in which NH_3 and H_2S readily dissolve.

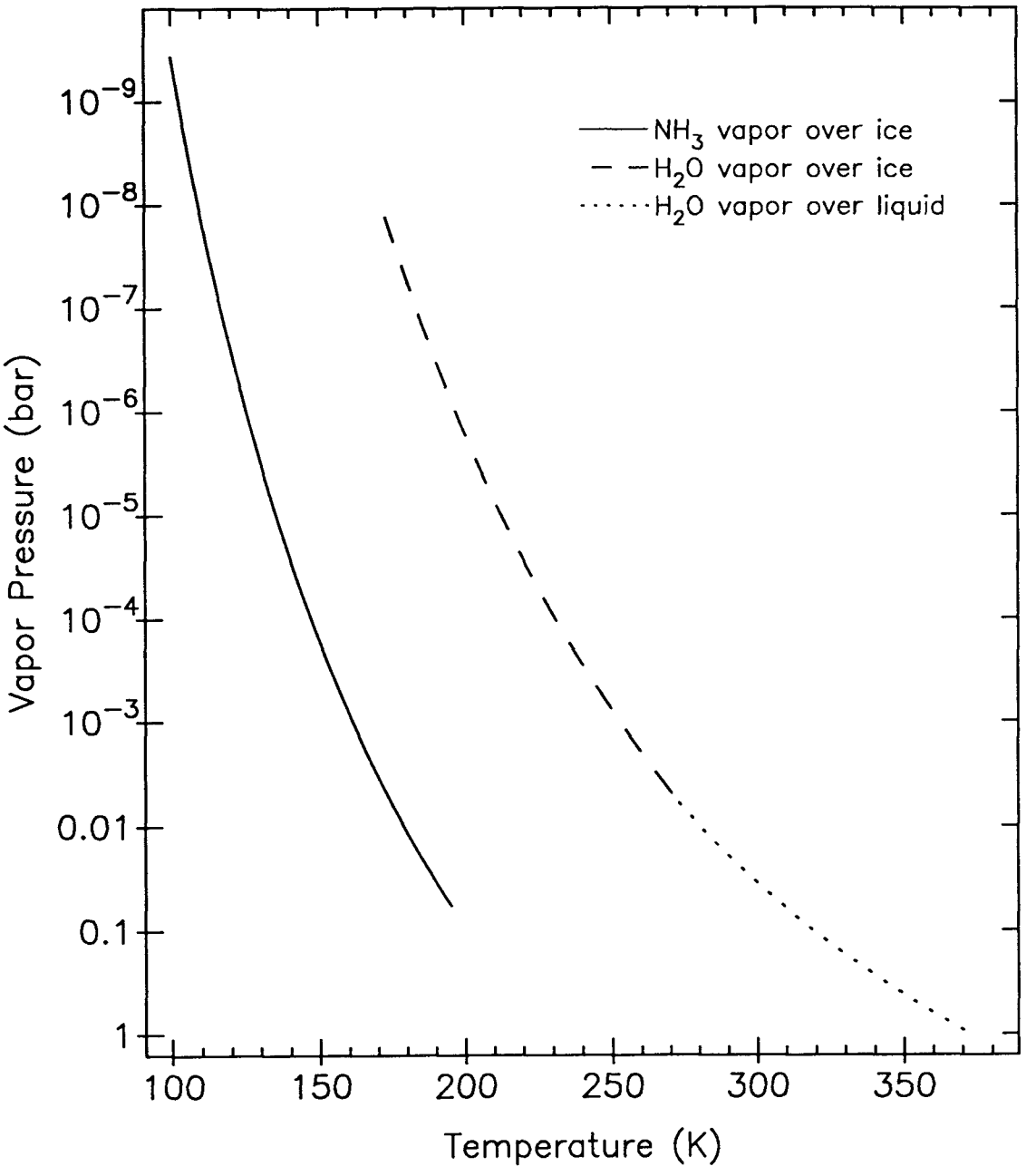

Figure 4.2: Empirical saturated vapor pressures for NH_3 vapor over ice and H_2O vapor over ice and liquid.

where the temperature is in Kelvin and the pressure in bar. The partial pressure of both NH_3 and H_2S in the cloud is calculated by noting that a single molecule of H_2S combines with a single molecule of NH_3. For an ideal gas, $P_k = X_k P$, where P_k is the partial pressure of the $k_{\rm th}$ gas and X_k is the corresponding molar mixing ratio. Thus, the change in partial pressure of the two gases is equal in the cloud. If the partial pressures at the base of the NH_4SH cloud are $P^0{}_{NH_3}$ and $P^0{}_{H_2S}$, then this equality can be written

$$P^0{}_{NH_3} - P_{NH_3} = P^0{}_{H_2S} - P_{H_2S}. \tag{4.14}$$

Substituting Eq. 4.14 into Eq. 4.13, and solving for the partial pressures within the cloud yields

$$P_{NH_3} = \tfrac{1}{2}\left\{P^0{}_{NH_3} - P^0{}_{H_2S} + \sqrt{(P^0{}_{NH_3} - P^0{}_{H_2S})^2 + 4\exp\left(34.151 - \tfrac{10834}{T}\right)}\right\}, \tag{4.15a}$$

$$P_{H_2S} = \tfrac{1}{2}\left\{P^0{}_{H_2S} - P^0{}_{NH_3} + \sqrt{(P^0{}_{NH_3} - P^0{}_{H_2S})^2 + 4\exp\left(34.151 - \tfrac{10834}{T}\right)}\right\}. \tag{4.15b}$$

Below the NH_4SH cloud, H_2O condenses when its partial pressure exceeds its saturated vapor pressure over ice or liquid as given by

$$\ln P = \frac{-5631.1206}{T} + 8.2312\ln(T) - 22.17928 - 0.03861449T + 2.774937\times10^{-5}T^2, \quad (T \le 273\ \text{K}) \tag{4.16a}$$

$$\ln P = \frac{-2313.0338}{T} + 38.053682\ln(T) - 117.848581 - 0.1384434T + 7.4465367\times10^{-5}T^2, \quad (T > 273\ \text{K}), \tag{4.16b}$$

where T is in Kelvin and P in bar (Briggs and Sackett, 1989). Pure liquid water is not found, however, because NH_3 and H_2S will readily dissolve in it to produce an aqueous solution. The molar concentration of dissolved NH_3 and H_2S is small (Briggs and Sackett, 1989), and the net effect on opacity, latent heat, and depression of the freezing point of the solution is correspondingly small. Therefore, we neglect the specific properties of the weak solution and instead use the properties of a pure water liquid cloud.

In each case, the cloud density can be calculated according to the method of Weidenschilling and Lewis (1973). The cloud density between any two layers is simply the difference in weight fraction in the gas phase at the bottom and top of the layer. Specifically, the average cloud density of the $k_{\rm th}$ species between layers z_1 and z_2 is given by

$$D = 100\,\frac{[X_k(z_1) - X_k(z_2)]\,\mu_k \bar{P}^2}{[P(z_1) - P(z_2)]\,\bar{T} R_0}\ \text{g cm}^{-1}, \tag{4.17}$$

where μ_k is the molar weight of the k_{th} species, $\bar{P}$ is the mean pressure of the layer in bar, $\bar{T}$ is the mean temperature of the layer in bar, and R_0 is the universal gas constant.

The condensates in Saturn's atmosphere not only modify the vertical distribution of minor constituents, but they introduce a latent heat that modifies the temperature structure of the atmosphere.

4.1.5 Pressure-Temperature profile

Evaluation of the radiative transfer equation (Eq. 4.3) requires knowledge of the temperature structure of the atmosphere. Furthermore, calculation of the vertical temperature structure, composition, and cloud structure must proceed in parallel, because each depends on the other.

The calculation begins high in the atmosphere, but within the convective region, with the well-known temperature of 107.5 K at 501.19 mbar established by the Voyager radio occultation experiment (Lindal *et al.*, 1985). The temperature at each pressure step is computed from the dry adiabatic lapse rate:

$$\frac{dT}{dP} = \frac{T}{P}\frac{R}{c_p}, \tag{4.18}$$

where c_p is the specific heat per mole of the atmosphere. In the presence of clouds and condensibles, as described in §4.1.4, a wet adiabat must be used.

The wet adiabatic temperature gradient in the presence of condensibles is calculated according to the method of Atreya and Romani (1985), by considering the adiabatic expansion of one mole of gas. In this example the law of conservation of energy requires

$$c_p dT - v dP + L_{\mathrm{NH_3}} dX_{\mathrm{NH_3}} + L_{\mathrm{H_2O}} dX_{\mathrm{H_2O}} + L_R dX_{\mathrm{H_2S}} = 0, \tag{4.19}$$

where c_p is the mean molar heat capacity at constant pressure, dT is the differential change in absolute temperature, v is the molar volume, dP is the differential change in total pressure, L is the molar enthalpy of condensation of the relevant gas, dX is the differential change in the number of moles of the relevant gas, L_R is the molar heat of the reaction (4.12), and $dX_{\mathrm{H_2S}}$ is the differential change in the number of moles of H_2S by the reaction (4.12). We wish to write Eq. 4.19 in terms of dT and dP.

From the equation of state for one mole of an ideal gas, the second term can be

replaced by

$$-vdP = \frac{RT}{P}dP. \tag{4.20}$$

For an ideal gas,

$$X_{NH_3} = \frac{P_{NH_3}}{P}, \tag{4.21}$$

where P_{NH_3} is the partial pressure. Differentiation yields

$$dX_{NH_3} = \frac{1}{P}dP_{NH_3} - \frac{P_{NH_3}}{P^2}dP. \tag{4.22}$$

The dependence on dP_{NH_3} can be eliminated by making use of the Clausius–Clapeyron equation,

$$dP_{NH_3} = \frac{L_{NH_3}P_{NH_3}}{RT^2}dT. \tag{4.23}$$

Thus, the third term in Eq. 4.19 is replaced with

$$L_{NH_3}dX_{NH_3} = \frac{L^2_{NH_3}P_{NH_3}}{PRT^2}dT - \frac{L_{NH_3}P_{NH_3}}{P^2}dP, \tag{4.24}$$

and the fourth term by a similar expression.

The fifth term in Eq. 4.19 is reduced by differentiating Eq. 4.13 to yield

$$L_R dX_{H_2S} = L_R\left[\frac{P_{NH_3}P_{H_2S}}{P(P_{NH_3}+P_{H_2S})}\right]\left[\frac{10834}{T^2}dT - \frac{2}{P}dP\right]. \tag{4.25}$$

Finally, Eq. 4.19 is expressed in terms of dT and dP:

$$\frac{dT}{dP} = \frac{\frac{T}{P} + \frac{L_{NH_3}P_{NH_3}}{P^2R} + \frac{L_{H_2O}P_{H_2O}}{P^2R} + \left(\frac{P_{NH_3}P_{H_2S}}{P_{NH_3}+P_{H_2S}}\right)\frac{2L_R}{P^2R}}{\frac{c_p}{R} + \frac{L^2_{NH_3}P_{NH_3}}{PR^2T^2} + \frac{L^2_{H_2O}P_{H_2O}}{PR^2T^2} + \left(\frac{P_{NH_3}P_{H_2S}}{P_{NH_3}+P_{H_2S}}\right)\frac{10834L_R}{PRT^2}}. \tag{4.26}$$

The latent heats are calculated by applying the Clausius-Clapeyron equation (4.23) to the vapor pressure relations in Eqs. 4.11 and 4.16. The resulting latent heat released per mole is

$$L_{NH_3} = 4122 - 1.81630T \tag{4.27}$$

for NH_3, and

$$\begin{aligned} L_{H_2O} &= 5631.1206 + 8.2312T - 0.03861449T^2 \\ &\quad + 5.549874 \times 10^{-5}T^3, \quad (T \le 273\text{ K}) \end{aligned} \tag{4.28a}$$

$$\begin{aligned} L_{H_2O} &= 2313.0338 + 38.053682T - 0.1384434T^2 \\ &\quad + 1.4893073 \times 10^{-4}T^3, \quad (T > 273\text{ K}) \end{aligned} \tag{4.28b}$$

for H_2O. The latent heat of formation of NH_4SH by the reaction (4.12) is $L_R = 9.0165 \times 10^4$ Joules mole^{-1} (CRC Handbook, 1983).

The lapse rate of the model atmosphere, with or without the presence of condensates, is primarily determined by the specific heat of the atmosphere. The mean specific heat of the atmosphere is obtained from the specific heat of each constituent weighted by its concentration. With the exception of H_2, a constant specific heat was used for each constituent as shown in Table 4.1.

Table 4.1: Specific heats at constant pressure.

Atmospheric Constituent		c_p/R
He	Helium	2.503
CH_4	Methane	4.296
H_2O	Water	4.018
NH_3	Ammonia	4.459
H_2S	Hydrogen Sulfide	4.013

The specific heat of Hydrogen depends exactly on the concentration of *ortho* and *para* Hydrogen. We consider three specific distributions of Hydrogen in the model. If H_2 is cooled down from high temperatures, greater than 300 K, the *ortho–para* ratio will tend to retain its "normal" value of 3:1. However, if conversion from *ortho* to *para* takes place rapidly, then the *ortho–para* ratio at each level is in "equilibrium" with the local temperature. In the third case, commonly referred to as "frozen" equilibrium or "intermediate" (Trafton, 1967; Wallace, 1980), the *ortho–para* ratio is taken at its equilibrium value at each level, but remains unchanged during adiabatic motions. This is equivalent to the assumption that local convective time-scales are shorter that *ortho-para* conversion time-scales.

Voyager observations place some constraints on the *ortho–para* ratio. IRIS spectra indicate that hydrogen is indistinguishable from equilibrium in the range 80–500 mbar (Conrath *et al.*, 1984). In the range 0.7–1.3 bar, however, the observed temperature lapse rate is closer to an intermediate or frozen equilibrium case (Bézard, 1985). We consider all three cases.

The specific heats of Hydrogen are calculated according to Boltzmann statistics as described in Massie and Hunten (1982). The results for *ortho*, *para*, and the three cases described above are shown in fig. 4.3. At low temperatures, the equilibrium value differs greatly from the normal and frozen models. However, at higher temperatures, relevant to

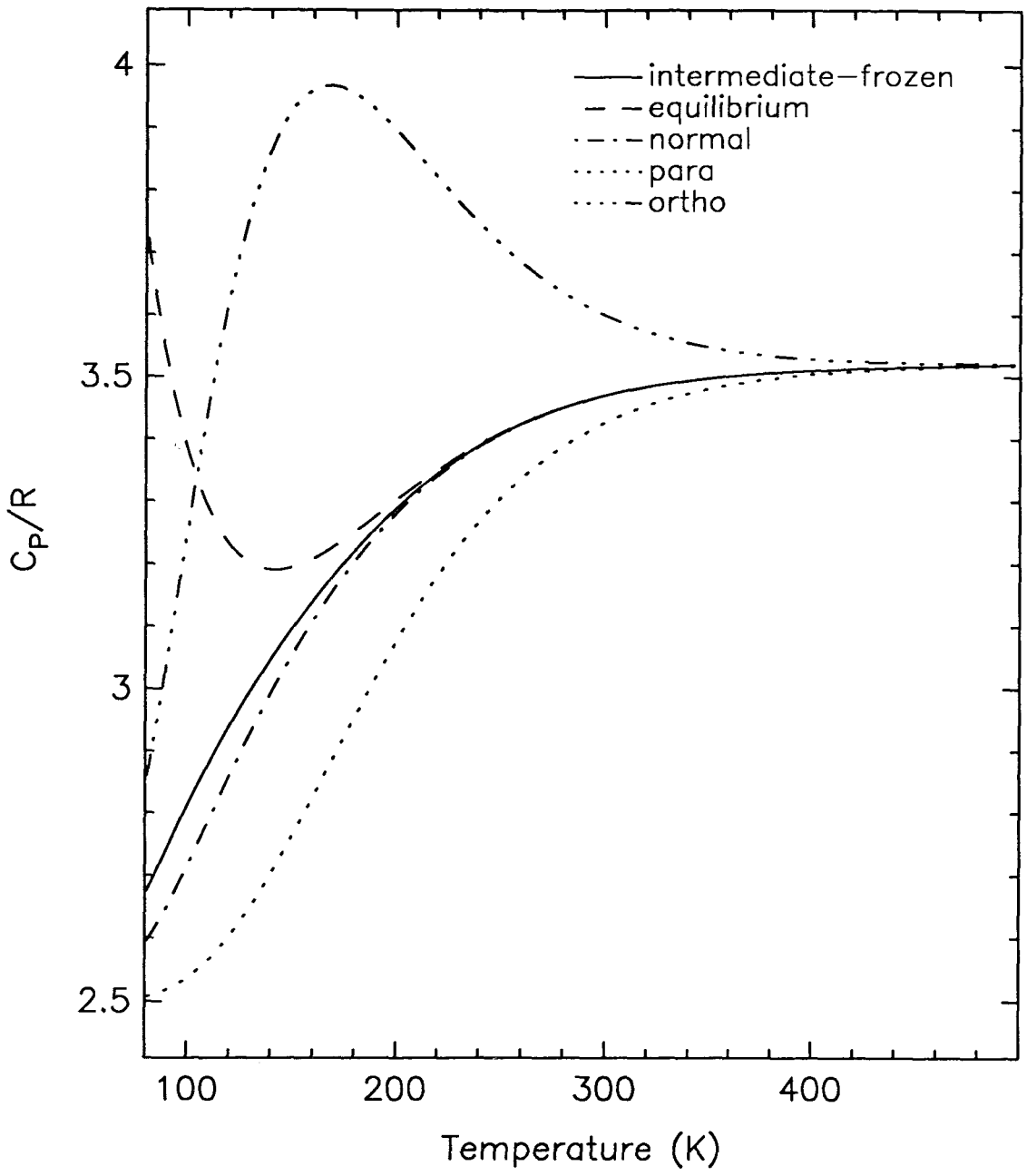

Figure 4.3: Specific heats for *ortho* and *para* hydrogen, and the three cases discussed in the text.

the troposphere of Saturn, all three models converge to a similar specific heat.

The net effect of the *ortho–para* ratio on the temperature profile is shown in fig. 4.4. The resulting temperature profile for the three cases is shown along with a fourth model containing 5 times solar abundance of H_2O. The right panel shows the resulting differences between the models and the most likely intermediate case. The net effect in the region of interest (1–10 bar) is less than 10 K. The change in the temperature profile due to condensation of water is even less significant of an effect above 10 bar.

4.1.6 Opacity

The final step in evaluating the radiative transfer equation (4.3) requires specifying the absorption coefficient $\alpha_\nu(z)$ at each pressure level. The absorption generally depends on the temperature and pressure, as well as on the density of absorber. Thus, the computed atmospheric profile is sufficient to determine $\alpha_\nu(z)$.

In this model we consider absorption due to five distinct interactions:

$$\alpha(\nu) = \alpha_{\mathrm{NH_3\,inv}} + \alpha_{\mathrm{NH_3\,rot}} + \alpha_{\mathrm{H_2}} + \alpha_{\mathrm{H_2O\,vap}} + \alpha_{\mathrm{H_2O\,liq}} \quad \mathrm{cm}^{-1}, \tag{4.29}$$

where the individual terms are the absorption coefficients due to NH_3 inversion bands, NH_3 rotation bands, H_2 collision-induced dipole rotation bands, H_2O vapor rotation bands, and liquid water droplets respectively. Other potential sources of opacity, such as collision-induced dipole CH_4, NH_3 ice clouds, ionosphere, and thermal ionization in the deep atmosphere are negligible and are ignored. Models of microwave opacity are summarized in figs. 4.5–4.7 and discussed in the following sections.

NH_3 opacity

Gaseous ammonia (NH_3) has long been recognized as the primary source of microwave opacity in the giant planets. The microwave opacity is due to the inversion spectrum of ammonia, in which the nitrogen atom moves perpendicular to the plane of the hydrogens. The frequency of the ground state inversion is centered in the microwave band at 1.25 cm. The net microwave opacity due to the NH_3 inversion band is calculated by summing the 119 individual inversion lines as cataloged by Poynter and Kakar (1975).

The exact line shape due to pressure broadening by a hydrogen and helium mixture at temperatures relevant to the Saturn troposphere is not well known. de Pater and Massie

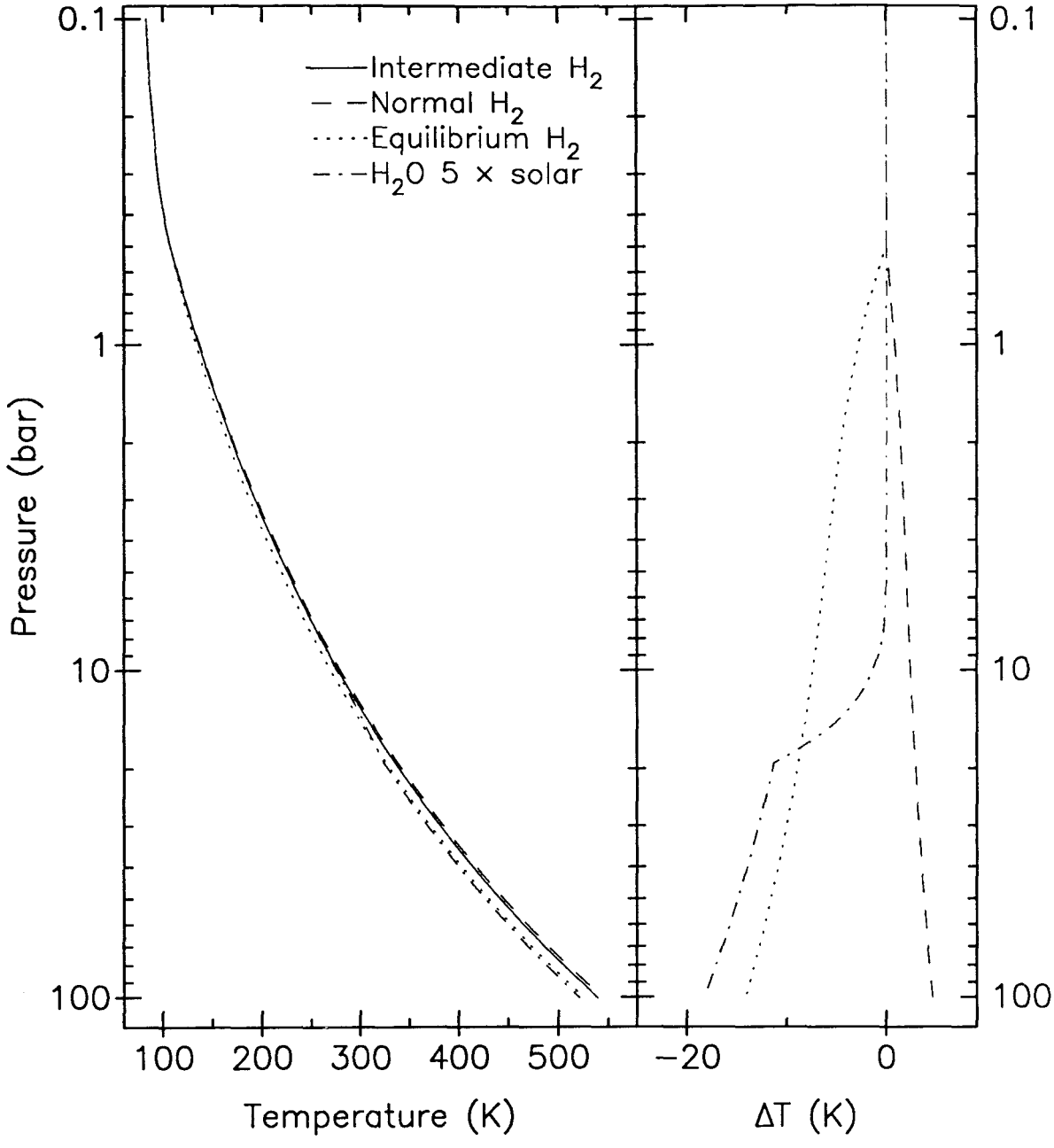

Figure 4.4: Pressure–Temperature profiles for several adiabatic models. The left panel shows the temperature profile for models consisting of solar abundances of NH_3 and three cases of *ortho–para* ratio as discussed in the text. Also shown is a model consisting of intermediate H_2 and 5 times solar abundance of H_2O. The right panel shows the differences between the models and the most likely case of intermediate H_2.

(1985) and Briggs and Sackett (1989) have successfully modeled the centimeter spectrum of Saturn by using the line shape of Ben-Reuven (1966), including a correction factor to fit the high-pressure data of Morris and Parsons (1970; as summarized in Berge and Gulkis, 1976). In addition, Steffes and Jenkins (1987) have measured the opacity of gaseous ammonia in the 1.38–18.5 cm wavelength range under simulated conditions for the Jovian atmosphere. Their measurements, at temperatures from 178 to 300 K and at pressures from 1 to 6 atm in a mixture of 90% hydrogen and 10% helium, indicate that, to within the experimental limits, the modified Ben-Reuven line shape correctly describes the opacity of gaseous ammonia. More recently, Spilker and Eshleman (1988) have measured the opacity of ammonia in the wavelength range 1.7–3.3 cm, and claim that the Ben-Reuven formalism overstates the opacity by 40% at a temperature of 273 K and pressures of 2 atm. At higher pressures, however, the difference is minimal. Furthermore, it is not clear that the discrepancy extends to the lower temperatures $\sim$ 150 K observed at Saturn in the same wavelength range.

Therefore, for wavelengths longer than 1 cm, we use the modified Ben-Reuven line shape as described in Berge and Gulkis (1976). The ammonia absorption coefficient is of the form

$$\alpha_{\mathrm{NH_3\,inv}}(\nu) = C \sum_{J=0}^{\infty} \sum_{K=1}^{J} A(J,K)\, F(J,K,\gamma,\delta,\xi,\nu)\ \mathrm{cm}^{-1}, \tag{4.30}$$

where $\alpha(\nu)$ is the absorption at frequency ν (MHz), and J and K are the rotational quantum numbers specifying the individual absorption lines. In practice the sums are evaluated only for the 119 lines cataloged by Poynter and Kakar (1975). C is the correction factor of Morris and Parsons (1970)

$$C = 1.0075 + 0.0304 \left(\frac{P_{\mathrm{H_2}}}{T}\right) + 0.0537 \left(\frac{P_{\mathrm{H_2}}}{T}\right)^2, \tag{4.31}$$

and A is the line intensity

$$A(J,K) = 1.214\, \frac{(2J+1)K^2}{J(J+1)}\, \frac{\nu_0^2(J,K)}{\gamma}\, S(K) \frac{P_{\mathrm{NH_3}}}{T^{7/2}}\, e^{\frac{4.8}{T}\left[1.09K^2 - 2.98J(J+1)\right]}, \tag{4.32}$$

where $\nu_0(J,K)$ is the frequency of the (J,K) transitions, γ is the pressure broadened line width, and $S(K) = 3$ for K a multiple of 3, and $S(K) = 1.5$ otherwise. The frequency-dependent line shape factor of Ben-Reuven is

$$F(J,K,\gamma,\delta,\xi,\nu) = 2\gamma \left(\frac{\nu}{\nu_0}\right)^2 \frac{(\gamma-\xi)\nu^2 + (\gamma+\xi)\left[(\nu_0+\delta)^2 + \gamma^2 - \xi^2\right]}{\left[\nu^2 - (\nu_0+\delta)^2 - \gamma^2 + \xi^2\right]^2 + 4\nu^2\gamma^2}, \tag{4.33}$$

where γ, ξ, and δ are the pressure-broadened line width, coupling element, and pressure shift term, respectively. They are given by:

$$\gamma = 2288\left(\frac{300}{T}\right)^{\frac{2}{3}} P_{H_2} + 780\left(\frac{300}{T}\right)^{\frac{2}{3}} P_{He} + 740\left(\frac{300}{T}\right)\gamma_0(J,K)P_{NH_3} \text{ MHz}, \quad (4.34a)$$

$$\xi = 1896\left(\frac{300}{T}\right)^{\frac{2}{3}} P_{H_2} + 296\left(\frac{300}{T}\right)^{\frac{2}{3}} P_{He} + 484\left(\frac{300}{T}\right)\gamma_0(J,K)P_{NH_3} \text{ MHz}, \quad (4.34b)$$

$$\delta = -444 P_{NH_3} \text{ MHz}. \quad (4.34c)$$

In these expressions, P_k is the partial pressure of the k_{th} species in bar, T is the temperature in Kelvin, and γ_0 is the self-broadened line width of Poynter and Kakar (1975).

At wavelengths shorter than 1 cm and pressures near 1 bar, the Van Vleck-Weisskopf line shape provides a better fit to the observational data (Berge and Gulkis, 1976; de Pater and Massie, 1985), although no direct laboratory measurements have been made. Therefore at 0.27 cm we use the Van Vleck-Weisskopf line shape as specified by Wrixon and Welch (1971). The expression for the line intensity is the same (Eq. 4.32) and the correction factor reduces to $C = 1.0$; however the frequency-dependent line shape factor becomes

$$F(J,K,\gamma,\delta,\xi,\nu) = 2\gamma\left(\frac{\nu}{\nu_0}\right)^2\left[\frac{\gamma}{(\nu-\nu_0)^2+\gamma^2} + \frac{\gamma}{(\nu+\nu_0)^2+\gamma^2}\right], \quad (4.35)$$

where γ is the pressure-broadened line width as given in Eq. 4.34a.

At millimeter wavelengths, absorption by the rotation lines of NH_3 becomes important. The model includes absorption by the first three rotational lines at frequencies of 572.498, 1168.451, and 1215.245 GHz. The absorption coefficient is functionally similar to that due to inversion,

$$\alpha_{NH_3\,\text{rot}}(\nu) = \sum_{J=0}^{1}\sum_{K=1}^{J} A(J,K)B(J,K)F(J,K,\gamma,\delta,\xi,\nu) \text{ cm}^{-1}, \quad (4.36)$$

(de Pater and Massie, 1985) where F is the Van Vleck-Weisskopf line shape and A and B are the line intensities given by

$$A(J,K) = 1.826\,\frac{\nu_0^2(J,K)}{\gamma}\frac{P_{NH_3}}{T^{7/2}}, \quad (4.37)$$

and

$$B(0,0) = 0.070T(1-e^{-28.6/T}), \quad (4.38a)$$

$$B(1,0) = 0.075T(1-e^{-57.2/T})e^{-28.6/T}, \quad (4.38b)$$

$$B(1,1) = 0.053T(1-e^{-57.2/T})e^{-23.3/T}. \quad (4.38c)$$

H_2 opacity

The collision-induced absorption due to H_2-H_2 and H_2-He collisions has been computed by Goodman for a mixture of hydrogen and helium (1969; as summarized in Berge and Gulkis, 1976). The absorption coefficient at frequency ν (MHz) is given as

$$\alpha_{H_2}(\nu) = 4.329 \times 10^{-20}\,\nu^2 P_{H_2}\left[\left(\frac{273}{T}\right)^{2.8} P_{H_2} + 1.7\left(\frac{273}{T}\right)^{2.61} P_{He}\right] \text{ cm}^{-1}, \quad (4.39)$$

where P_k is the partial pressure of the k_{th} gas (hydrogen or helium) in bar, and T is the temperature in Kelvin.

H_2O opacity

Absorption due to water vapor and liquid water droplets are both included in the model. The water vapor absorption coefficient is due to an electric dipole resonance at 22.235 GHz and a continuum contribution due to transitions in the infrared. The absorption has been calculated by Goodman (1969; as summarized in Berge and Gulkis, 1975) and is of the form

$$\alpha_{H_2O\,vap}(\nu) = \nu^2 P_{H_2O}\left(\frac{273}{T}\right)^{\frac{13}{3}}\left\{4.773\times10^{-18}\gamma + 2.683\times10^{-10}\left[\frac{\gamma}{(\nu-22235)^2+\gamma^2}+\frac{\gamma}{(\nu+22235)^2+\gamma^2}\right]\right\} \text{ cm}^{-1} \quad (4.40)$$

where P_k is the partial pressure of the k_{th} gas in bar, T is the temperature in Kelvin, ν is the frequency in MHz, and γ is the pressure broadened line width given by

$$\gamma = 2.923\times10^3\left(\frac{273}{T}\right)^{\frac{2}{3}}(0.81P_{H_2} + 0.35P_{He}) \text{ MHz}. \quad (4.41)$$

Suspended water droplets are good microwave absorbers. Their estimated size is on the order of 100μm (Carlson *et al.*, 1988), which allows the Rayleigh approximation of Mie scattering theory to be used in calculating the absorption. The appropriate form given by Liebe (1985) is

$$\alpha_{H_2O\,liq}(\nu) = \frac{1.88\times10^{-3}\nu w\,\epsilon''}{(\epsilon'+2)^2+(\epsilon'')^2} \text{ cm}^{-1}, \quad (4.42)$$

where ν is the frequency in MHz, w is the cloud density in grams per cubic centimeter, and ϵ' and ϵ'' are the real and imaginary parts of the dielectric constant of water. The dielectric constants are calculated with the Debye model reported by Chang and Wilheit (1979), which is valid for frequencies $\nu < 300$ GHz:

$$\epsilon' = 4.9 + \frac{185.1 - 0.375T}{1 + \nu^2\tau^2}, \tag{4.43a}$$

$$\epsilon'' = \frac{\nu\tau(185.1 - 0.375T)}{1 + \nu^2\tau^2}, \tag{4.43b}$$

where

$$\tau = 1.99 \times 10^{-6} \frac{e^{2140/T}}{T}. \tag{4.43c}$$

Microwave absorption

The microwave opacity of the model atmosphere is illustrated in figs. 4.5–4.7, where the absorption spectra has been plotted for three levels in Saturn's atmosphere. A solar composition model is used to allow a comparison of absorption by various species and mechanisms.

Figure 4.5 shows the model absorption spectra near the base of the NH_3 cloud at 1.4 bar pressure. The 119 inversion lines of NH_3 are broadened into a single line, which peaks near the ground state energy level of 1.25 cm. Absorption by NH_3 rotation lines and H_2 collision-induced dipole transitions is negligible in comparison with the NH_3 inversion absorption.

Figure 4.6 shows the model absorption spectra near the base of the NH_4SH cloud at 4.0 bar pressure. The ammonia inversion lines are broader than at 1.4 bar, and absorption by water vapor is comparable to that by NH_3 rotation bands, however NH_3 inversion bands are still the dominant absorption mechanism.

Figure 4.7 shows the model absorption spectra near the base of the liquid water cloud at 11.0 bar pressure. Here absorption by water vapor and droplets becomes significant and comparable to NH_3 absorption. Unfortunately, the longest wavelength observation presented here, 20.13 cm, reaches an optical depth $\tau \sim 1$ higher up in the atmosphere under reasonable conditions.

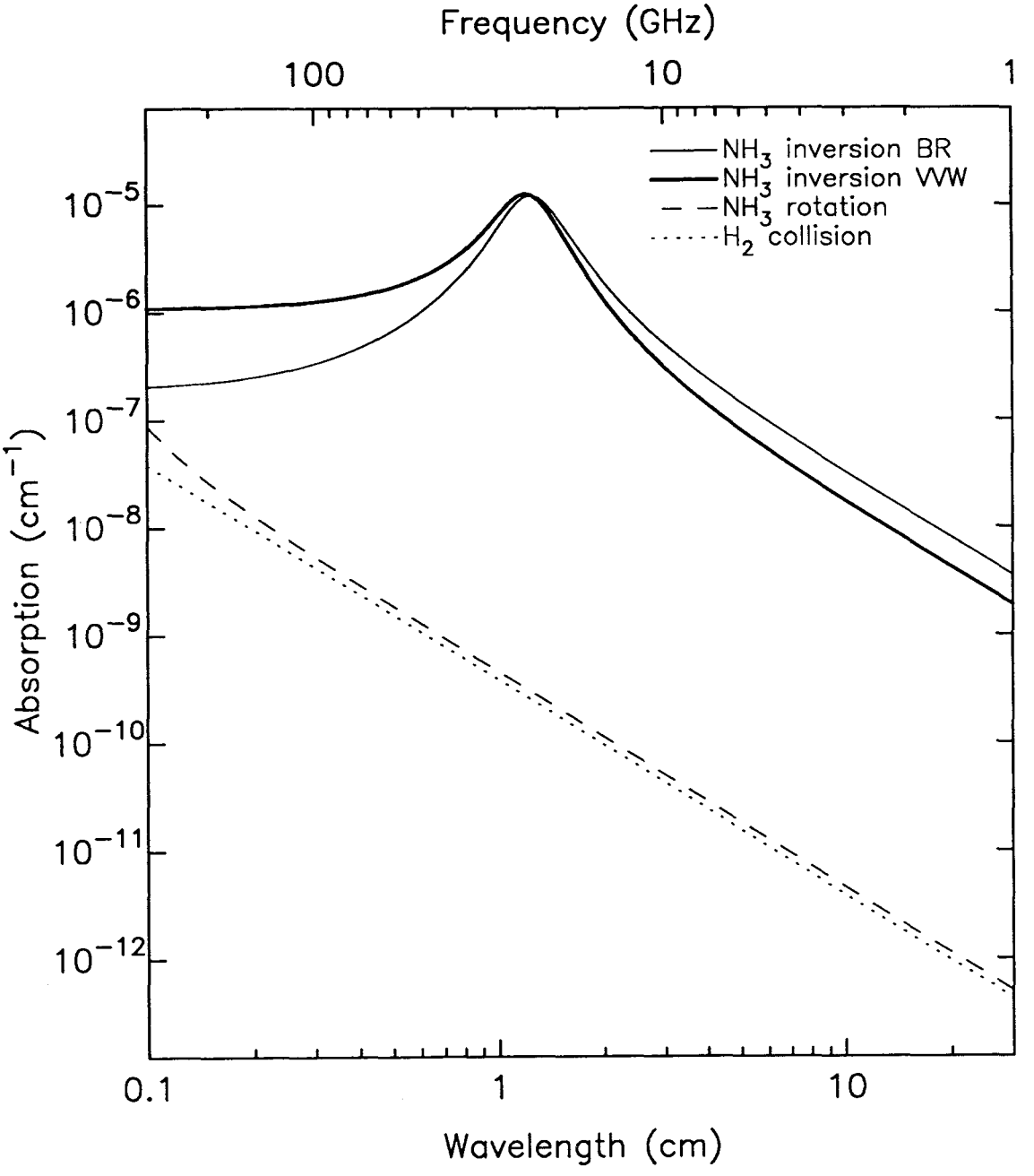

Figure 4.5: Absorption spectra for a solar composition model at 1.4 bar pressure, corresponding to the base of the NH_3 cloud. Primary sources of absorption include NH_3 inversion lines for a Ben-Reuven (BR) and Van Vleck-Weisskopf (VVW) line shape, NH_3 rotation lines, and H_2 collision-induced absorption. The VVW line-shape is used for $\lambda < 1$ cm, otherwise the BR line-shape is used.

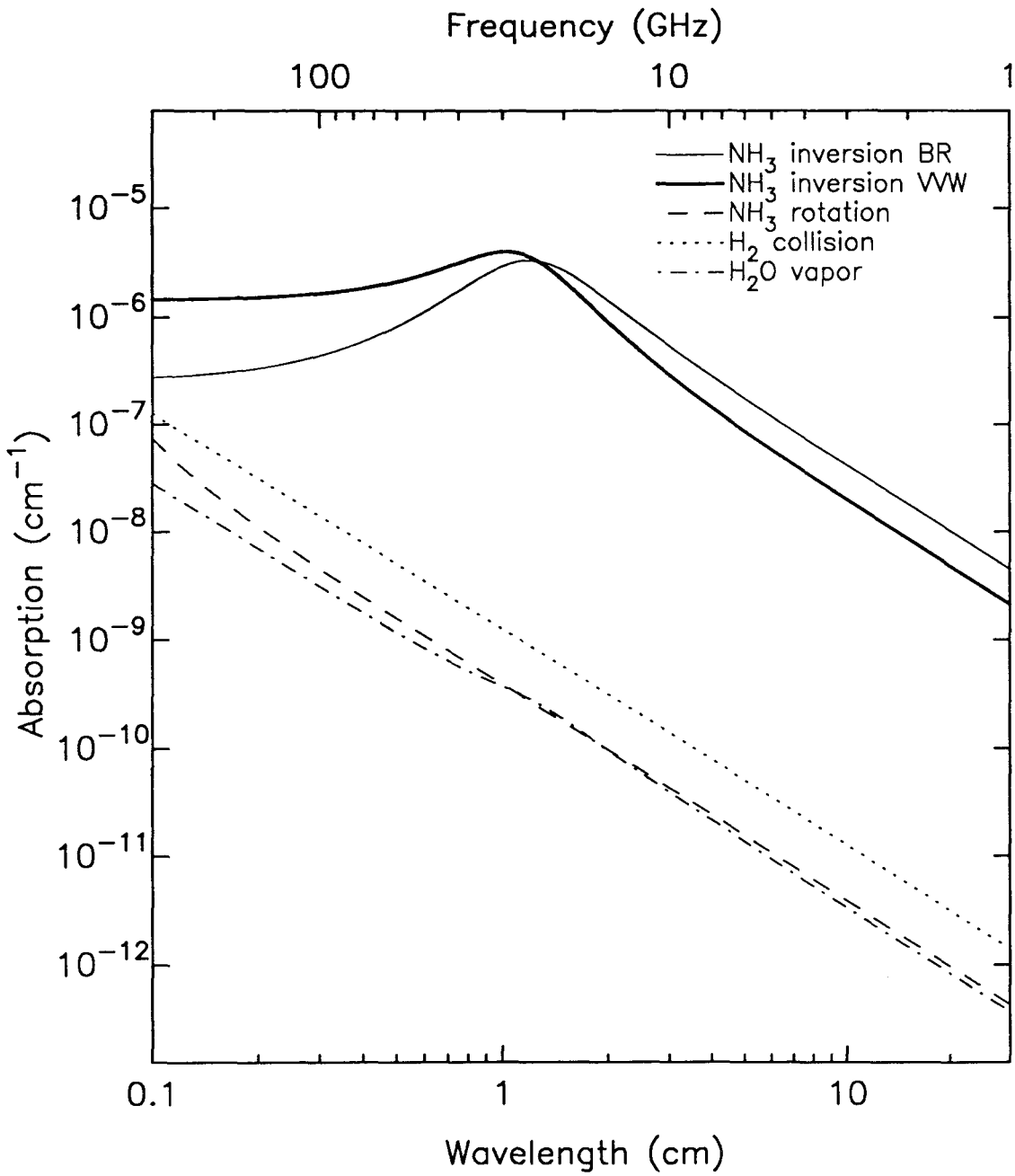

Figure 4.6: Absorption spectra for a solar composition model at 4 bar pressure, corresponding to the base of the putative NH_4SH cloud. Primary sources of absorption include NH_3 inversion lines for a Ben-Reuven (BR) and Van Vleck-Weisskopf (VVW) line shape, NH_3 rotation lines, H_2 collision-induced absorption, and H_2O vapor and liquid droplets.

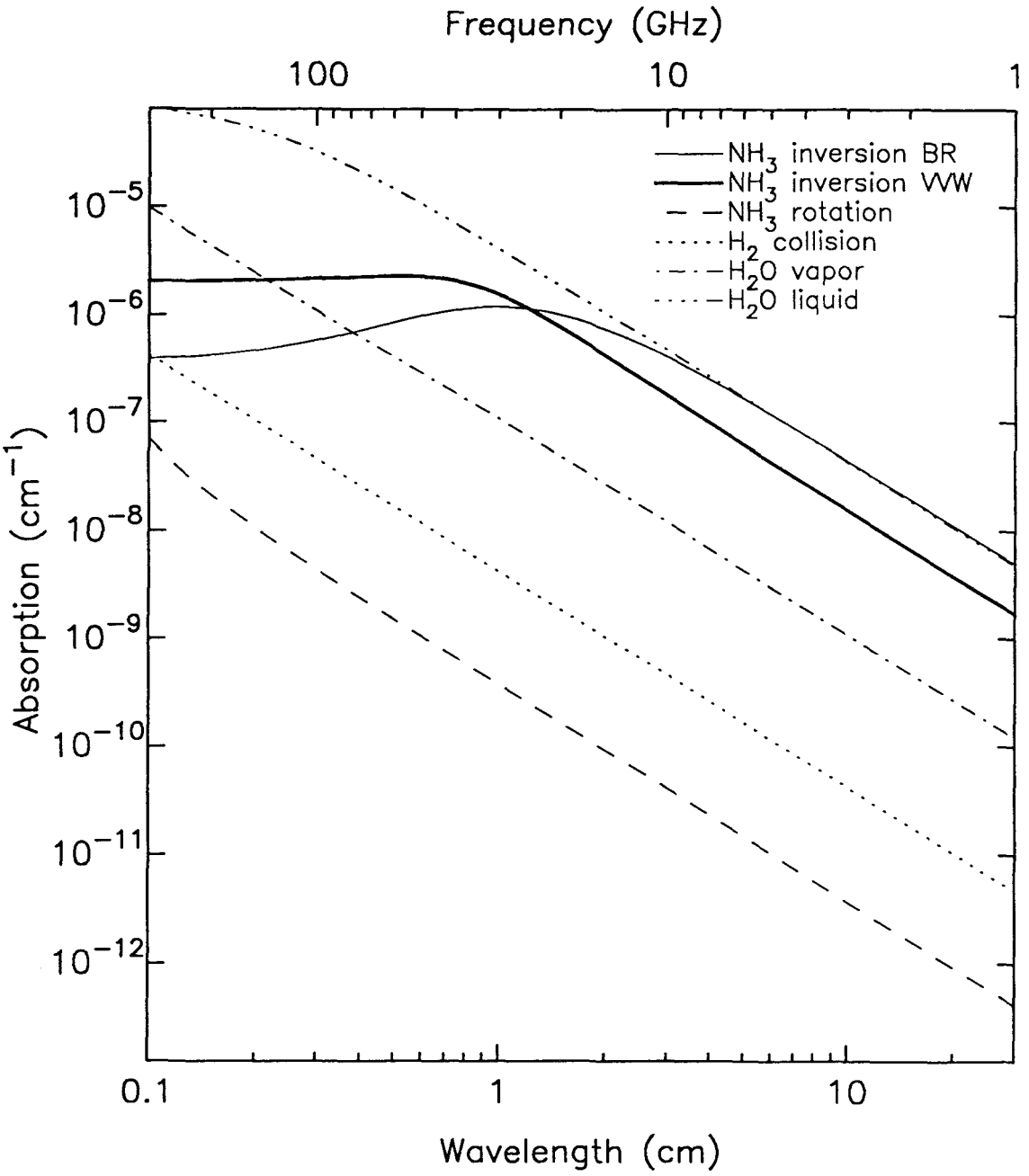

Figure 4.7: Absorption spectra for a solar composition model at 11 bar pressure, corresponding to the base of the putative H_2O liquid cloud. Primary sources of absorption include NH_3 inversion lines for a Ben-Reuven (BR) and Van Vleck-Weisskopf (VVW) line shape, NH_3 rotation lines, H_2 collision-induced absorption, and H_2O vapor and liquid droplets.

4.1.7 Weighting functions

Now that the atmospheric vertical structure has been completely specified, evaluation of the radiative transfer integral (Eq. 4.3) to get brightness is trivial. However, before comparing the observations with the results of the model, it is useful to examine the weighting functions that go into the radiative transfer integral.

The vertical profile and weighting functions for a nominal model atmosphere are shown in fig. 4.8. The model consists of solar abundances of oxygen, nitrogen, and sulfur deep in the atmosphere, and an "intermediate" *ortho-para* ratio as suggested by the Voyager radio occultation temperature profile. The dashed line indicates the wet adiabatic temperature profile while the dotted lines indicate the molar mixing ratios of the condensibles. NH_3 condenses at 1.4 bar; above that point it follows its vapor saturation curve. The open circles are the NH_3 abundances as measured by the Voyager radio occultation experiment, which are consistent with NH_3 being fully saturated in the clouds. Deeper down, NH_3 and H_2S combine to form an NH_4SH particulate cloud with base near 4 bar. One molecule of NH_3 combines with one molecule of H_2S through the reaction 4.12, so that the jump in NH_3 abundance at 4 bar is exactly equal to the H_2S abundance below that point. At 10 bar liquid water condenses to form a cloud with a base near 11 bar.

Figure 4.8 also shows the weighting functions at the five observational wavelengths for nadir viewing at the equator. The weighting functions show that each wavelength is sensitive to different aspects of the vertical structure. The weighting functions for 0.27 and 2.01 cm peak above the NH_3 saturation point, and sample the bulk of the ice cloud, whereas the weighting function at 3.53 cm peaks at the saturation point and evenly samples both above and below the cloud base. In contrast the 6.17 cm weighting function extends deep into the atmosphere to the level of the NH_4SH cloud. The weighting function at 20.13 cm extends to the water ice cloud and has a sharp discontinuity at the top and bottom of the liquid water cloud, indicating a rapid change in absorption.

This simple picture of the microwave weighting functions provides a qualitative indication of the model sensitivity. For example, it is clear from the weighting functions that any change in H_2O abundance would have the most profound effect at 20.13 cm. On the other hand, a decrease in the NH_3 abundance would tend to increase the brightness temperatures, while a decrease in H_2S would have just the opposite effect. In the following section we compare the observations with the model.

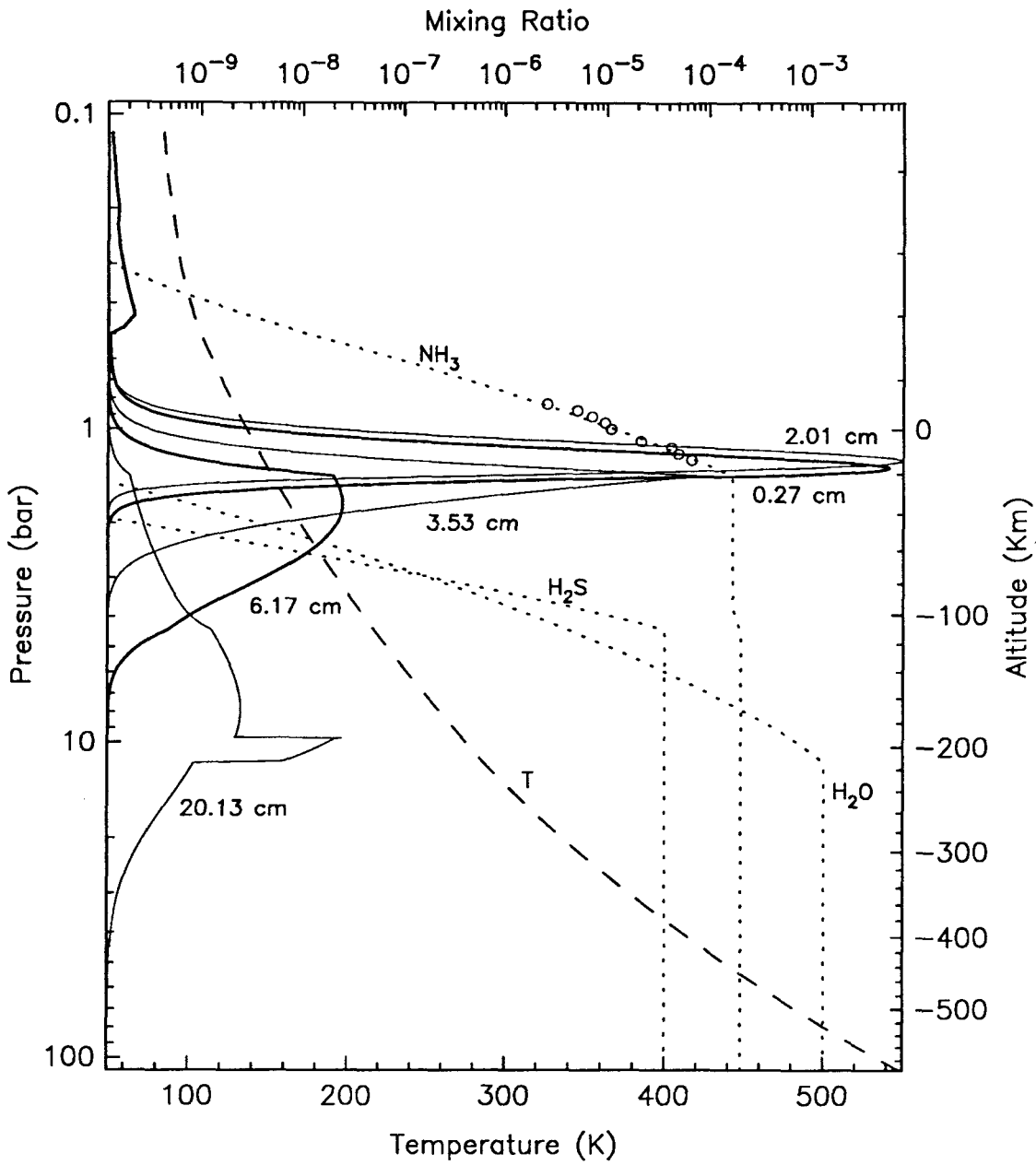

Figure 4.8: The vertical profile of the canonical model atmosphere containing solar abundances. The dashed curve indicates the wet adiabatic temperature profile (T) along the bottom scale, while the dotted curves indicate the molar mixing ratios for H_2O, NH_3, and H_2S along the top scale. Circles show the NH_3 saturation abundance as measured by the Voyager radio occultation experiment. Alternating light and dark curves show the weighting functions for nadir viewing at the five experimental wavelengths.

4.2 Whole-disk Modeling

In this section the results of the atmospheric radiative transfer model are compared with the disk-integrated brightness observations. We begin with a simple model atmosphere containing just H_2, He, CH_4, and NH_3. We then examine more sophisticated models. In each case, the free parameters in the model are adjusted to give the best fit to the data.

4.2.1 Whole-disk integral

The whole-disk brightness (or disk-averaged brightness) is calculated by projecting Saturn onto a two-dimensional grid fixed to the sky plane (see fig. 2.6, page 34). The radiative transfer integral is evaluated at each grid point (x, y), evenly spaced by 1000 km in both directions. The whole-disk brightness is then computed by averaging the brightness at each grid point over the visible hemisphere of Saturn. The disk-averaged brightness is then

$$T_B(\text{whole-disk}) = \frac{\int T_B(x,y)\, dx dx}{\int dx dy}, \tag{4.44}$$

where the integral is over the visible hemisphere of Saturn.

For the current set of observations, the integrated brightness refers primarily to the northern hemisphere, because the southern hemisphere was blocked by the rings. The estimated uncertainty in the whole-disk model brightness due to evaluation on a finite grid is less than 1%.

4.2.2 Model sensitivity to NH_3

Because ammonia is a principle microwave absorber in Saturn's troposphere, the first models considered contain only NH_3 in addition to the principle gases H_2, He, and CH_4. In the first-order model, NH_3 is assumed to have a constant mixing ratio up to the location of the cloud base (i.e., the saturation point) and then to follow the saturation vapor pressure curve. Intermediate H_2 is assumed. Substantial deviations from this uniform model are expected and will be discussed in following sections.

The results of this initial model for three concentrations of NH_3 are summarized in Table 4.2 and fig. 4.9. The figure shows model spectra superimposed on disk-integrated measurements reported here (solid squares) as well as other disk-resolved interferometer

observations (open squares) and single-dish observations (open circles) that have been corrected to remove the effect of Saturn's rings (see §3.2.2 for a summary of the observational data). The lines represent model spectra for NH_3 concentrations of 0.5, 1.0, and 1.5 times solar. The models are computed for the specific viewing geometry of the current observations (see fig. 2.6 for geometry), corresponding to a Saturnocentric latitude of the Earth $B = 25.3°$, and may not be applicable to the full set of observations.

Table 4.2: Disk-integrated brightness temperatures for models containing only NH_3.

	Brightness Temperature T_B at λ_{cm}					χ^2_ν at gain	
	0.27 cm	2.01 cm	3.53 cm	6.17 cm	20.13 cm	1.00	1.02
Observed:	137.3 ±4.5	140.1 ±0.5	161.4 ±3.7	176.4 ±0.6	230.9 ±2.6		
Models:							
0.5 solar NH_3	144.9	142.9	158.0	182.6	287.4	45.9	36.9
1.0 solar NH_3	144.3	142.7	153.6	170.1	245.8	7.6	9.2
1.5 solar NH_3	144.2	142.7	152.4	165.4	227.9	9.9	16.6
$\Delta T_{0.5\ bar} = -5$ K	143.3	142.2	152.2	166.5	235.0	8.4	13.7
$\Delta T_{0.5\ bar} = +5$ K	145.2	143.2	155.3	174.3	257.0	12.3	10.1
0.6 solar NH_3 60% sub-adiabatic	144.6	142.8	156.5	176.5	232.6	1.5	1.8

Table 4.2 allows quantitative comparison between the model results and the disk-integrated observations presented in §3.2.2. In order to estimate the goodness of fit of the models a normalized χ^2 statistic is calculated according to the formula:

$$\chi^2_\nu = \sum_i \frac{(T_{D,i} - T_{M,i})^2}{\sigma^2_{D,i} + \sigma^2_{M,i}}, \tag{4.45}$$

where the sum is taken over all five wavelengths, T_D and T_M are the observational and model disk brightness, and σ_D and σ_M are the data and model errors.

Table 4.2 shows that the model brightness at 2.01 cm is insensitive to the exact concentration of NH_3 below the cloud level. It will soon become clear that the 2.01 cm brightness is insensitive to changes in most model parameters and is confined to the narrow range of 142.2–143.3 K for reasonable models. This can be understood by noticing that the weighting function at 2.01 cm (fig. 4.8) occupies a narrow range of altitudes mostly within

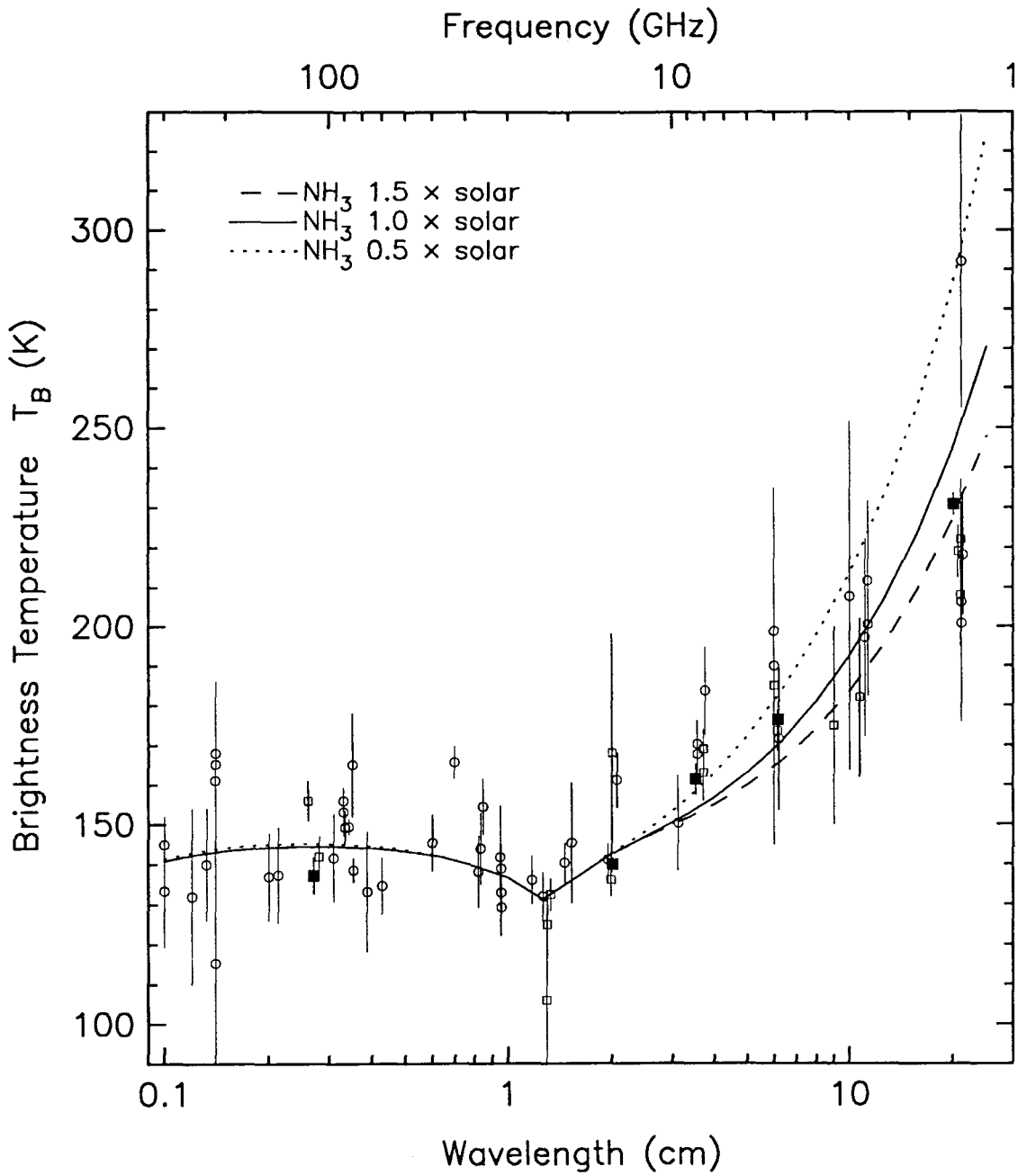

Figure 4.9: Disk-integrated observations and model spectra. The data points are those reported in this work (solid squares), other interferometer data (open squares), and single-dish observations that have been corrected to remove the effect of the rings (open circles). The lines represent three model spectra containing uniform abundances of NH_3 at concentrations of 0.5, 1.0, and 1.5 times solar. Although the model containing 1.0 times solar abundance of NH_3 fits the data best, no model containing a uniform distribution of NH_3 fits the current observations.

the NH_3 cloud. As a result, the 2.01 cm brightness is primarily governed by the physics of NH_3 vapor saturation.

The discrepancy between the data and model brightness at 2.01 cm suggests that there may be a systematic error in the gain of the data or the model. For this reason, a normalized χ^2 statistic is also computed for a gain of 1.02 applied to the data. It is important to keep in mind that this gain is less than the uncertainty in the absolute flux scale of 6% at 0.27 cm and 5% otherwise.

The discrepancy between the data and the model at 0.27 cm is somewhat more puzzling. The 0.27 cm brightness also seems to be somewhat insensitive to changes in the model, but the difference between the data and the models are much larger. Nevertheless, the difference is just less than the 6% error in the absolute flux scale. It is important to keep in mind that 0.27 cm data were calibrated on a different flux scale than the rest of the observations. Thus, the relative error between the mm observations and the cm observations is expected to be higher than the cm data alone.

Furthermore, there may be additional sources of systematic error in the data and models at 0.27 cm than at other wavelengths. The sign of the difference between the model and the data may indicate an extra source of opacity that is significant at 0.27 cm but negligible at longer wavelengths. For example, several of the disequilibrium species that have been observed in the upper troposphere and stratosphere, such as PH_3, C_2H_6, and CO, have absorption features in the millimeter but not at centimeter wavelengths, and thus could account for the low brightness observed at 0.27 cm. However, little is known about the concentration and distribution of these minor species. Another possibility is that the ice particles in the NH_3 cloud present a source of extra opacity. However, this would require a large fraction of them to be comparable in size to the wavelength.

Alternately, the difference may be attributed to systematic errors in the model — primarily in the modeling of the NH_3 absorption spectrum at millimeter wavelengths. The NH_3 inversion line shape has been measured in the laboratory (§4.1.6) at cm wavelengths, but no current laboratory measurements exist to check the validity of using a Van Vleck-Weisskopf line shape at millimeter wavelengths. In the final analysis, though, the formal errors of the 0.27 cm observations cannot distinguish between any of the suggested hypothesis.

From the goodness of fit, it would seem that a model containing 1.0 times solar

abundance of NH_3 best fits the microwave spectrum. But closer examination of the formal errors of the data and fig. 4.9 indicates that no model containing uniform amounts of NH_3 fits the spectrum well. The shorter wavelengths seem to favor a model that contains 0.5 times solar NH_3, but such a model is clearly too hot to fit the long wavelength data, which seem to require either an increased opacity with depth or a decrease in temperature with depth.

We explore several means of satisfying the lower brightness temperature required by the long wavelength observations. First we examine modifications to the temperature-pressure profile of the atmosphere. We also consider two means of increasing opacity with depth: the addition of H_2O as an extra absorber and the modulation of the vertical distribution of NH_3 by the addition of H_2S.

4.2.3 Model sensitivity to temperature-pressure profile

The temperature-pressure profile of the atmospheric model is tied to a temperature of 107.5 K at 501.19 mbar as measured by the Voyager radio occultation experiment for 36°N planetographic latitude (Lindal *et al.*, 1985). This value has a formal uncertainty of $\pm$ 3 K and may differ from the global mean temperature by as much as 5 K. Therefore it is instructive to consider the effect on the microwave spectrum of changing this reference temperature by $\pm$ 5 K. The temperature profile below this level is constrained to follow a wet adiabat as described in §4.1.5.

The disk-integrated brightness for models containing 1.0 times solar abundance of NH_3 and in which the reference temperature is changed by $\pm$ 5 K, is shown in Table 4.2. The corresponding spectrum is plotted in fig. 4.10. Once again the model brightness at 2.01 cm is rather insensitive to changes in the model parameters — in this case, temperature. A 10 K change in physical temperature produces a change in brightness of 1 K. This can be understood by noting that the 2.01 cm brightness reaches an optical depth of unity within the cloud, that is, within the saturation region of NH_3. The location of the cloud is governed by the vapor saturation curve of ammonia and so moves along with changes in temperature. The effect of changing the absolute temperature on brightness is more pronounced at the longer wavelengths. But examination of the χ^2_ν indicates that the preferred model is the original one with no change in reference temperature.

Alternately, the low brightness temperature at long wavelengths could be satisfied

by forcing the atmosphere towards an isothermal profile in the region below the clouds. Such a model would require the lapse rate to be 60% of the adiabatic lapse rate below a pressure level of 3.0 bar for an 0.6 times solar abundance of NH_3. The results of such an "isothermal" model, which are shown in fig. 4.10 and Table 4.2, provide a better fit to the data. Yet the model itself is entirely ad-hoc. There is no physical model that can support a sub-adiabatic lapse rate in the presence of convection. Next we consider a more plausible solution in which the opacity changes with depth in the atmosphere.

4.2.4 Model sensitivity to H_2O

One possible candidate for increasing the opacity with depth is water vapor and liquid water droplets (Klein *et al.*, 1978). Although infrared observations have not detected the presence of water on Saturn, this does not rule out the possibility that water exists deep in the atmosphere. It is expected to condense at a pressure of about 10 bar, and therefore to have little expression in the upper troposphere where infrared observations are sensitive. The microwave absorption properties of liquid and vapor H_2O are discussed in §4.1.6.

The results of fitting models containing only NH_3 and H_2O are presented in Table 4.3 and fig. 4.11. Because water begins to condense at pressures greater than 10 bar, only the longest wavelength of 20.13 cm will feel the cooling effect of the extra opacity. This hypothesis is borne out by examining Table 4.3, which shows the model brightness for H_2O concentrations of 1, 5, and 10 times solar. An improved fit is obtained by adding water and simultaneously decreasing the amount of ammonia. Addition of more than 5 times solar abundance has little effect. The best fitting model contains greater than 5 times solar abundance of H_2O and 0.9 times solar abundance of NH_3. However, these are not firm estimates. The water abundance is merely a lower bound, because increasing water greater than 5 times solar abundance has little effect.

The effect of H_2O is only felt at the longest wavelengths; the shorter wavelengths do not penetrate to the depths of the water cloud and are insensitive to changes in H_2O abundance. Clearly, adding water and decreasing ammonia improves the fit of the model. This alone might argue for the presence of enhanced concentrations of water were it not for an alternate hypothesis involving H_2S.

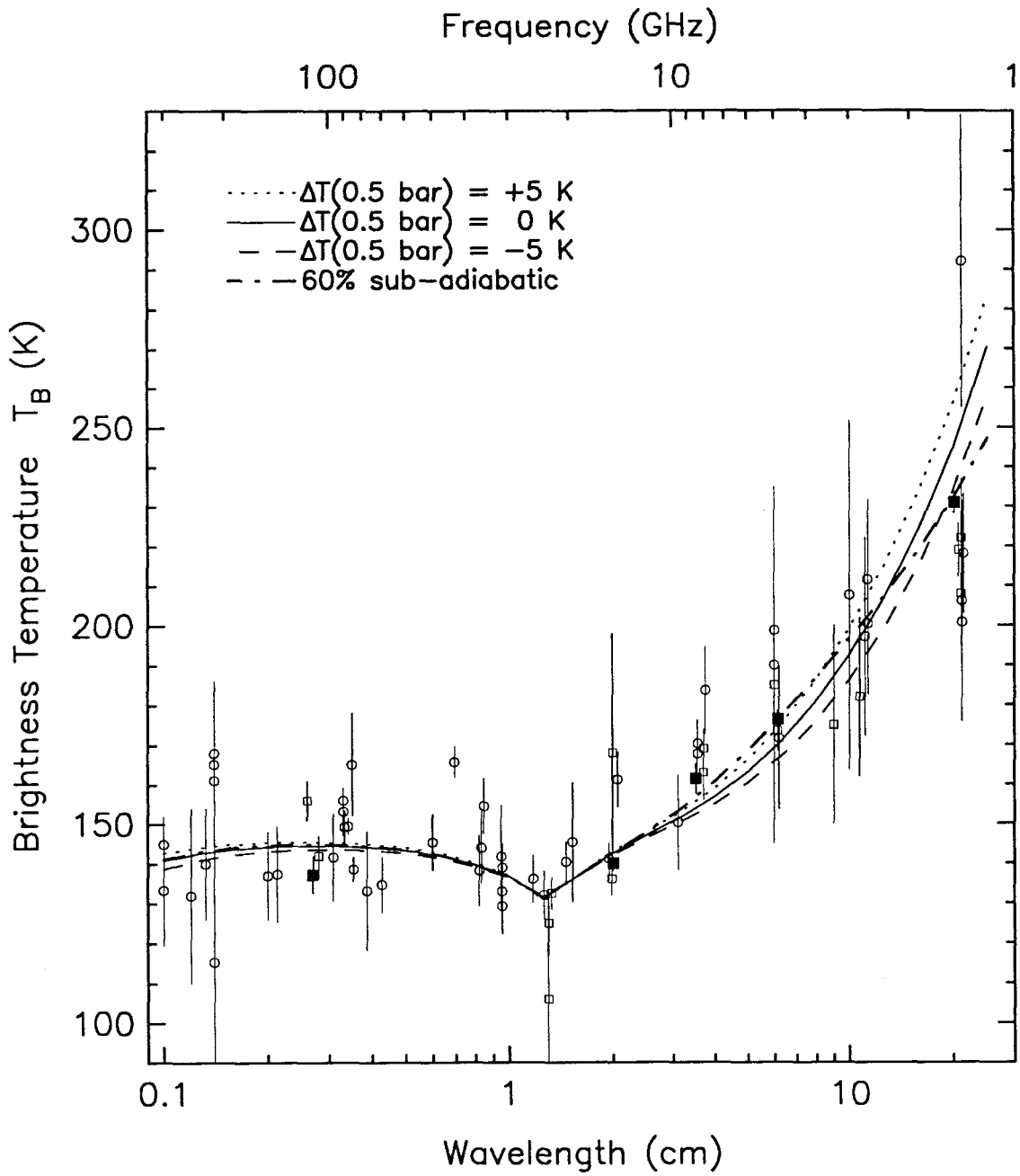

Figure 4.10: Disk-integrated observations and model spectra. The lines represent three model spectra containing a solar abundance of NH_3 for three values of the reference temperature at 0.5 bar. The fourth model contains 0.6 times solar abundance of ammonia and a lapse rate that is 60% of the adiabatic lapse rate.

Table 4.3: Disk-integrated brightness for models containing NH_3, H_2O, and H_2S.

	Brightness Temperature T_B at λ_{cm}					χ^2_ν at gain	
	0.27 cm	2.01 cm	3.53 cm	6.17 cm	20.13 cm	1.00	1.02
Observed:	137.3 ±4.5	140.1 ±0.5	161.4 ±3.7	176.4 ±0.6	230.9 ±2.6		
Models:							
0.9 solar NH_3+							
1 solar H_2O	144.3	142.7	154.0	171.6	246.5	6.9	7.6
5 solar H_2O	144.3	142.7	154.0	171.6	242.2	5.0	6.4
10 solar H_2O	144.3	142.7	154.0	171.6	241.9	5.0	6.3
3.7 solar NH_3	144.6	142.8	156.0	176.6	230.8	1.5	2.1
14 solar H_2S							
2.9 solar NH_3	144.9	142.9	158.0	181.1	235.8	2.9	0.8
11 solar H_2S							
3.7 solar NH_3	144.6	142.8	156.0	176.6	230.4	1.5	2.2
14 solar H_2S							
1 solar H_2O							
2.9 solar NH_3	144.9	142.9	158.0	181.1	235.2	2.9	0.8
11 solar H_2S							
1 solar H_2O							

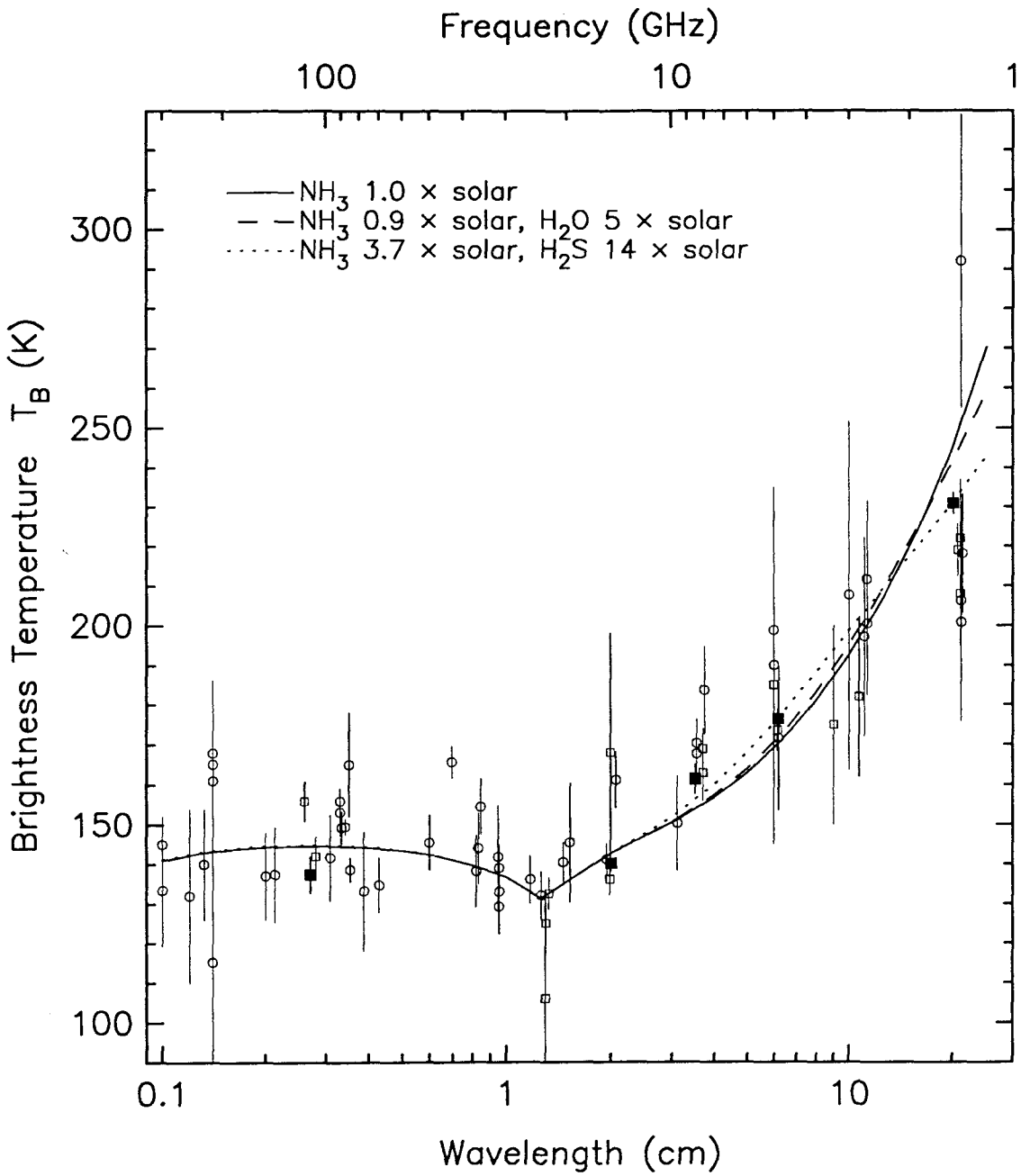

Figure 4.11: Disk-integrated observations and model spectra. The data points are those reported in this work (solid squares), other interferometer data (open squares), and single-dish observations that have been corrected to remove the effect of the rings (open circles). The nominal model consisting of uniformly distributed NH_3 (solid line) fits the data poorly. The addition of H_2O (dashed line) improves the fit slightly. The best fit is provided by a model containing 14 time solar H_2S and 3.7 times solar NH_3.

4.2.5 Model sensitivity to H_2S

In the deep convective atmosphere of Saturn, large-scale mixing and overturning are expected to yield a uniform vertical distribution of NH_3 below the saturation point. Yet, the observed microwave spectrum is not consistent with a model in which NH_3 is uniformly distributed, and instead indicates that the opacity of the atmosphere must increase with depth compared to this model. One mechanism for modulating the vertical distribution of NH_3 in the presence of convection involves the introduction of hydrogen sulfide.

The suggestion that H_2S can remove NH_3 by a particulate-forming reaction (Eq. 4.12) was first advanced to explain the apparent depletion of NH_3 in the Uranian atmosphere (Gulkis *et al.*, 1978). The possibility that such a mechanism can explain the microwave spectrum of Saturn is now considered.

Although H_2S by itself has little opacity in the microwave, it can combine with NH_3 to form a particulate cloud of NH_4SH at a pressure level of 4 bar. The complete thermo-chemical model describing this process is discussed in §4.1.4. Because the reaction involves one molecule each of NH_3 and H_2S, the mixing ratio of NH_3 above the cloud is decreased from that below the cloud (and perhaps the deep atmosphere) by exactly the molar mixing ratio of H_2S. If the amount of H_2S is equal to or greater that NH_3, then the NH_3 is removed completely above the NH_4SH cloud at 4 bar (this may explain the extreme depletion of ammonia on Uranus and Neptune; Gulkis *et al.*, 1978; de Pater and Richmond, 1989). Conversely, if the amount of H_2S is less than NH_3, H_2S is completely removed above the 4 bar level. This may explain, in part, the lack of detection of H_2S on Saturn and Jupiter (Bézard *et al.*, 1983).

The results for models containing H_2S are summarized in Table 4.3 and fig. 4.11. The best fitting model requires an enhancement of H_2S over solar abundances by a factor of 14. NH_3 is also enhanced by 3.7 times solar below the NH_4SH cloud, but is only 0.65 times solar in the region between the NH_4SH cloud and the NH_3 cloud. This model provides a 1.5σ fit to all five data points. The best fit results are summarized in figs. 4.12 and 4.13, which illustrate the vertical profile of an atmosphere containing 14 times solar H_2S, 3.7 times solar NH_3, and 1 times solar H_2O. The inclusion of water in the figures is merely for illustrative purposes, the model results are equivocal about the presence of water.

Adopting a gain factor of 1.02, as suggested by the unyielding 2.01 cm brightness temperature, results in a model that provides an 0.8σ fit to the data. This model contains

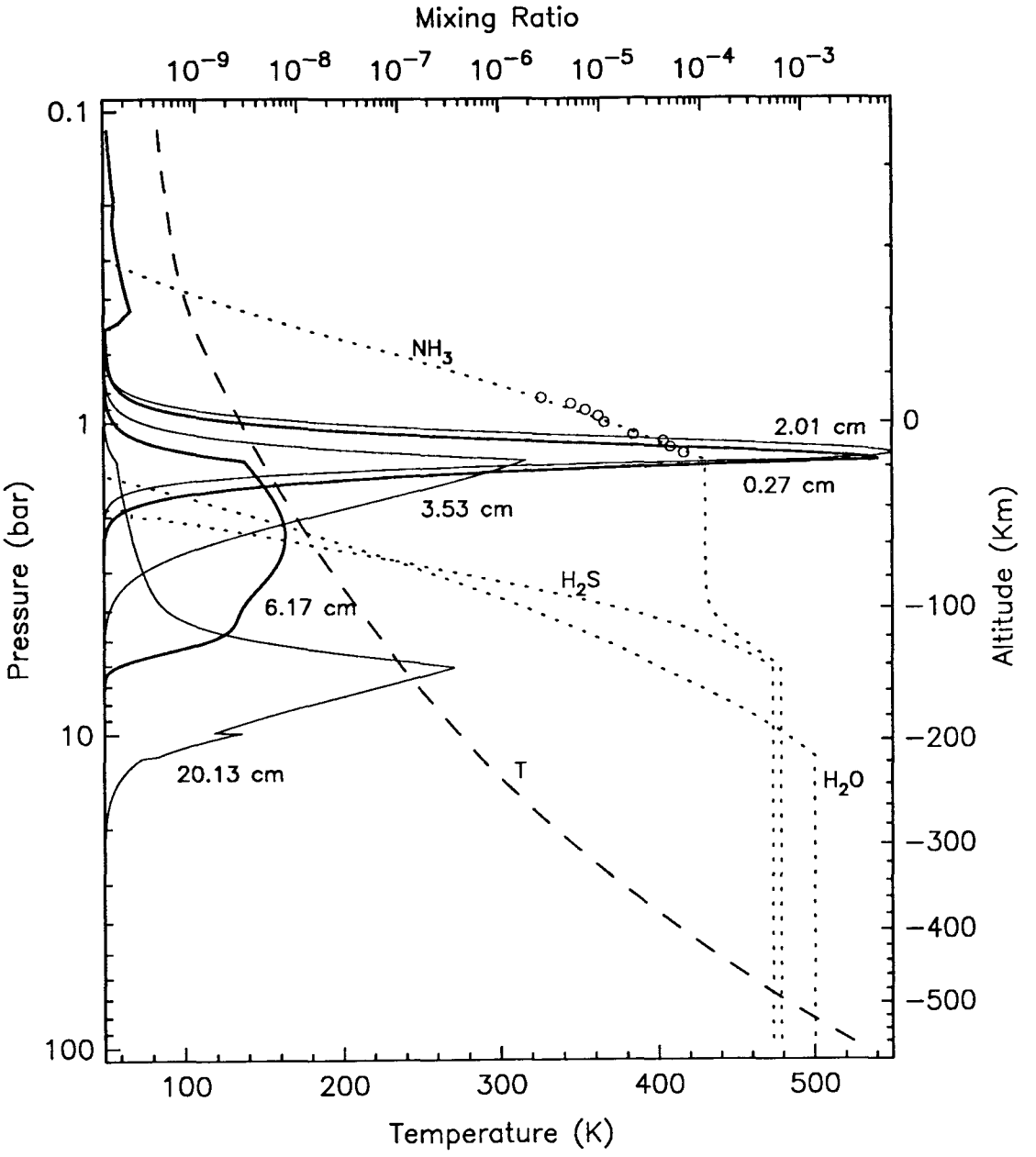

Figure 4.12: The vertical profile of the model atmosphere that best fits the observations. The dashed curve indicates the wet adiabatic temperature profile (T) along the bottom scale, while the dotted curves indicate a concentration of 1 times solar H_2O, 3.7 times solar NH_3, and 14 times solar H_2S along the top scale. Circles show the NH_3 saturation abundance as measured by the Voyager radio occultation experiment. Alternating light and dark curves show the weighting functions for nadir viewing at the five experimental wavelengths.

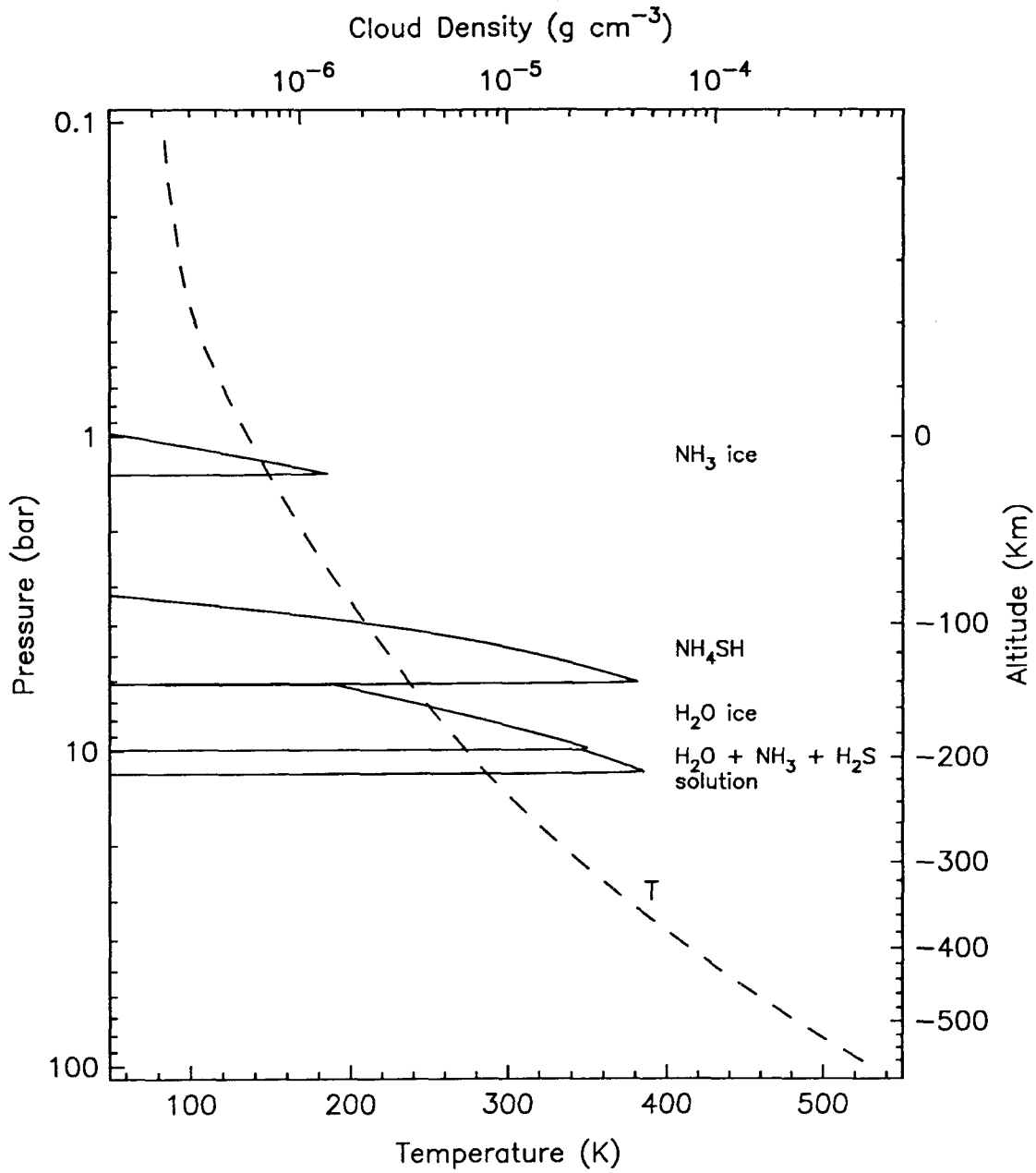

Figure 4.13: The cloud structure of Saturn for the model which best fits the observations. The model contains 1 times solar H_2O, 3.7 times solar NH_3, and 14 times H_2S and assumes an adiabatic temperature profile (dashed line). An ammonia ice cloud forms below 1 bar, while H_2S and NH_3 react chemically to form a particulate cloud near 6 bar. Deeper still, H_2O condenses to form an ice cloud and a liquid solution in which NH_3 and H_2S readily dissolve.

11 solar H_2S and 2.9 solar NH_3 below the NH_4SH cloud and 0.5 solar NH_3 in the region between the NH_4SH cloud and the NH_3 cloud. The exact global value is likely to be between these estimates.

The final two rows of Table 4.3 show the effect of adding water to the existing models. The additional opacity slightly depresses the temperatures at 20.13 cm but the improvement in the fit is indistinguishable from the model without water.

4.2.6 Summary and discussion of whole-disk results

Modeling the whole-disk brightness provides a good overall fit to the data at all wavelengths except 0.27 cm, where the model predicts a greater brightness temperature than observed. This suggests two explanations to account for the discrepancy. One possibility is that the use of the Van Vleck-Weisskopf line shape for gaseous NH_3 absorption at millimeter wavelengths is incorrect. Clearly, additional laboratory measurements of NH_3 absorption are required to address this issue. Alternately, the difference can by attributed to an additional source of opacity at millimeter wavelengths, which is transparent at longer wavelengths. Possible candidates for this extra opacity include the minor species PH_3, C_2H_6, and CO, or the NH_3 ice clouds.

Whole-disk models also show that the brightness temperature near the center of the ammonia inversion band, specifically at a wavelength of 2.01 cm, is restricted to a narrow range of values for a wide variety of model parameters. The brightness temperature at 2.01 cm is tied to the physics of the NH_3 vapor saturation curve, and is not easily perturbed. Therefore, the agreement between the model and the data at 2.01 cm serves as an independent test of the Baars *et al.* (1977) absolute flux scale.

The measurement at 3.53 cm is consistently brighter than any reasonably fit model and is the largest source of error in determining the best model. It is tempting to suggest that this may be evidence for a time variation of NH_3 abundance over a period of two years from 1986, when the 2.01, 6.17, and 20.13 cm data were taken, to 1988, when the 3.53 cm data were taken. The sign of the change is consistent with a global decrease in NH_3 in the sub-cloud region during this period. However, no firm quantitative conclusion can be drawn from the limited data set. It may be more likely that this change is indicative of the difficulty of maintaining an absolute calibration standard. Clearly, additional monitoring of Saturn at cm wavelengths is required to quantify the time variability.

Given the basic assumption of a convective, adiabatic atmosphere, the fundamental result of modeling the whole-disk spectrum of Saturn is inescapable. Namely, that the microwave opacity of the atmosphere increases in the range 1-10 bar. The most likely explanation is that the abundance of NH_3 itself increases from a value near 0.5-0.65 solar below the ice cloud to a maximum of 3-4 times solar at pressures of 4-6 bar. No other microwave absorber exists in sufficient concentration to account for the observations. However, the exact mechanism by which the vertical distribution of NH_3 deviates from a uniform mixing ratio is unclear.

The argument presented in this section, that enrichment of H_2S by a factor of 11-14 times solar is responsible for the vertical distribution of NH_3, is compelling. Such a large enhancement of sulfur, however, is difficult to explain, considering that other elemental abundances, such as carbon, nitrogen, and phosphorus, are only enriched by factors of 2-4 times solar (Lunine, 1989). Furthermore, the lack of detection of any sulfur bearing compounds on the outer planets (Bézard *et al.*, 1983; Larson *et al.*, 1984), argues against an enrichment of sulfur.

The vertical distribution of NH_3 deserves another look. And in the next section we consider methods of retrieving NH_3 abundance independent of H_2S.

4.3 Vertical Profile of NH_3 and Implications

In the previous section, a direct model was developed and compared with observations in an attempt to constrain the physical parameters describing Saturn's atmosphere. In this section, we present a simple approach to the inverse problem. That is, we start with the observed brightness temperatures and try to invert them to yield the physical parameters of interest. The focus is primarily on deriving the vertical abundance of NH_3.

4.3.1 NH_3 retrieval

The retrieval of the vertical distribution of ammonia makes use of the atmospheric model developed in §4.1. In short, an adiabatic atmosphere is assumed, consisting of 96.3% H_2, 3.3% He, and 0.4% CH_4. The *ortho-para* H_2 ratio is modeled as an intermediate or frozen equilibrium distribution. Opacity due to collision-induced H_2, and NH_3 inversion and rotation lines are included.

The method of Newtonian iteration is used to retrieve the ammonia profile. This is simply a matter of linearizing the relationship between brightness temperature and ammonia mixing ratio, and is justified by examining fig. 4.14, which shows the dependence of brightness temperature on the ammonia mixing ratio at the five wavelengths.

The ammonia mixing ratio at the cloud base is held at 8.7×10^{-5} (0.5 times solar) as suggested by the 0.27 and 2.01 cm brightness temperatures. But because the brightness at wavelengths of 0.27 and 2.01 cm is not sensitive to the NH_3 mixing ration at depth, these values are ignored in the iteration scheme. The mixing ratio is adjusted at three deeper levels in the atmosphere at pressures of 1.7, 3.0, and 6.0 bar, corresponding to altitudes sampled by the wavelengths at 3.53, 6.17, and 20.13 cm. Piecewise linear interpolation is used between these levels.

The first step begins with an initial ammonia mixing ratio profile, q_n^i, at each of the three nodal levels i. The model absorption profile and atmosphere is used to evaluate the radiative transfer integral (Eq. 4.3, page 77) and compute the brightness temperature corresponding to each wavelength, T_n^i, and the partial derivatives, $\partial q^i / \partial T^i$. Higher order terms in the series expansion are ignored so that the iterative equation reduces to

$$q_{n+1}^i = q_n^i + \frac{\partial q^i}{\partial T^i}(T_0^i - T_n^i), \tag{4.46}$$

where T_0^i is observed brightness temperature at wavelength i.

The iteration rapidly converges to a solution at the three levels in the atmosphere corresponding to the altitudes sampled by the three wavelengths. These results provide a better than 1σ fit to the data, and are shown in fig. 4.15 along with other direct modeling results.

4.3.2 Vertical distribution of NH_3

The vertical distribution of NH_3 derived from inversion follows the general trend suggested by the direct models, that is, increasing mixing ratio with depth. However, the results of the inversion deviate from the profile of NH_3 modified by H_2S. Specifically, the NH_3 mixing ratio increases more slowly with depth, reaching a maximum value of 2.9 times solar below 6 bar. The discrepancy between the inversion results and the direct model containing 14 times solar H_2S suggests that H_2S alone cannot account for the vertical distribution of NH_3. An additional mechanism may be required to remove NH_3 from below

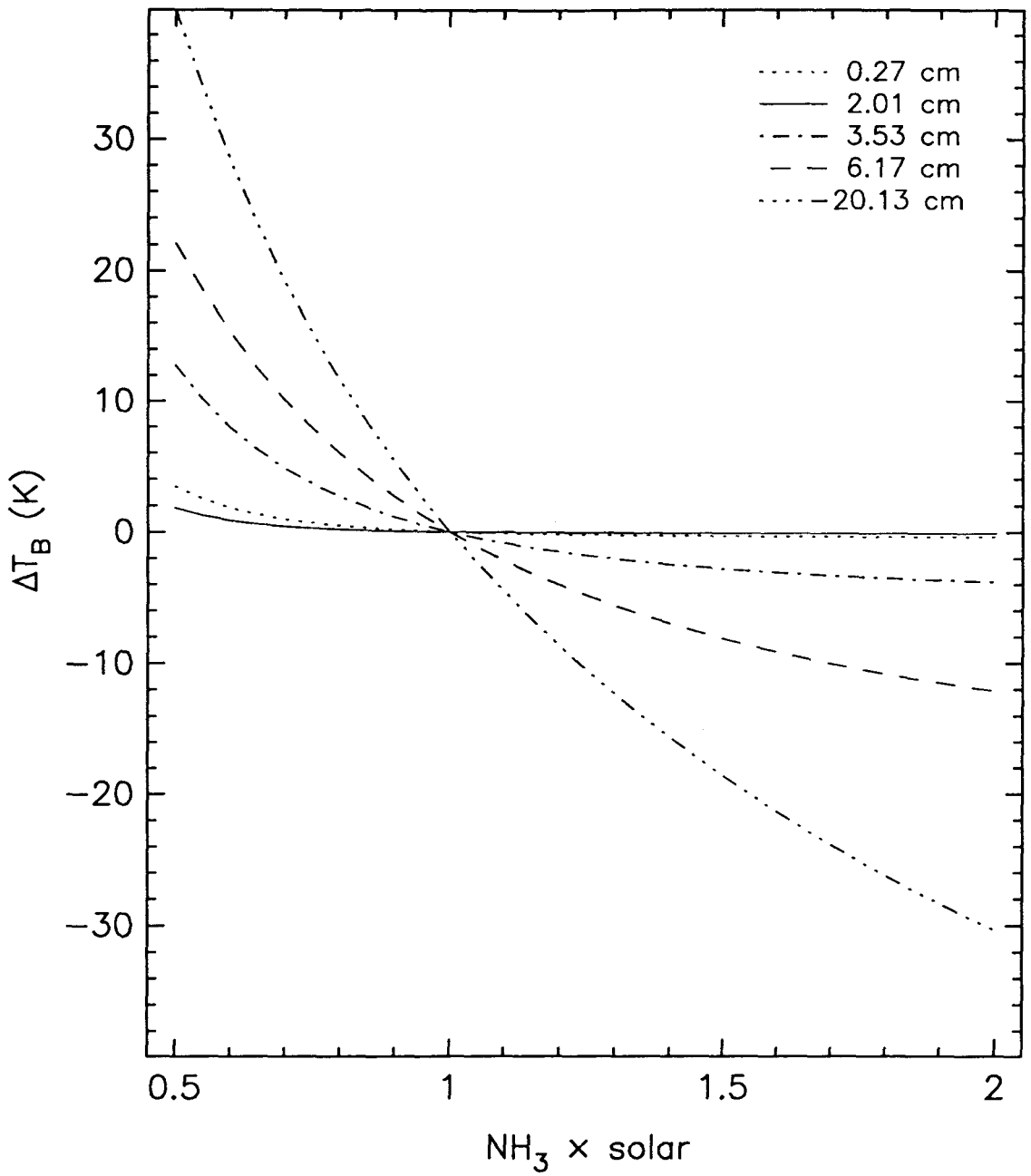

Figure 4.14: Change in brightness temperature at five wavelengths resulting from variations in ammonia mixing ratio normalized to the brightness temperature at 1 times solar NH_3.

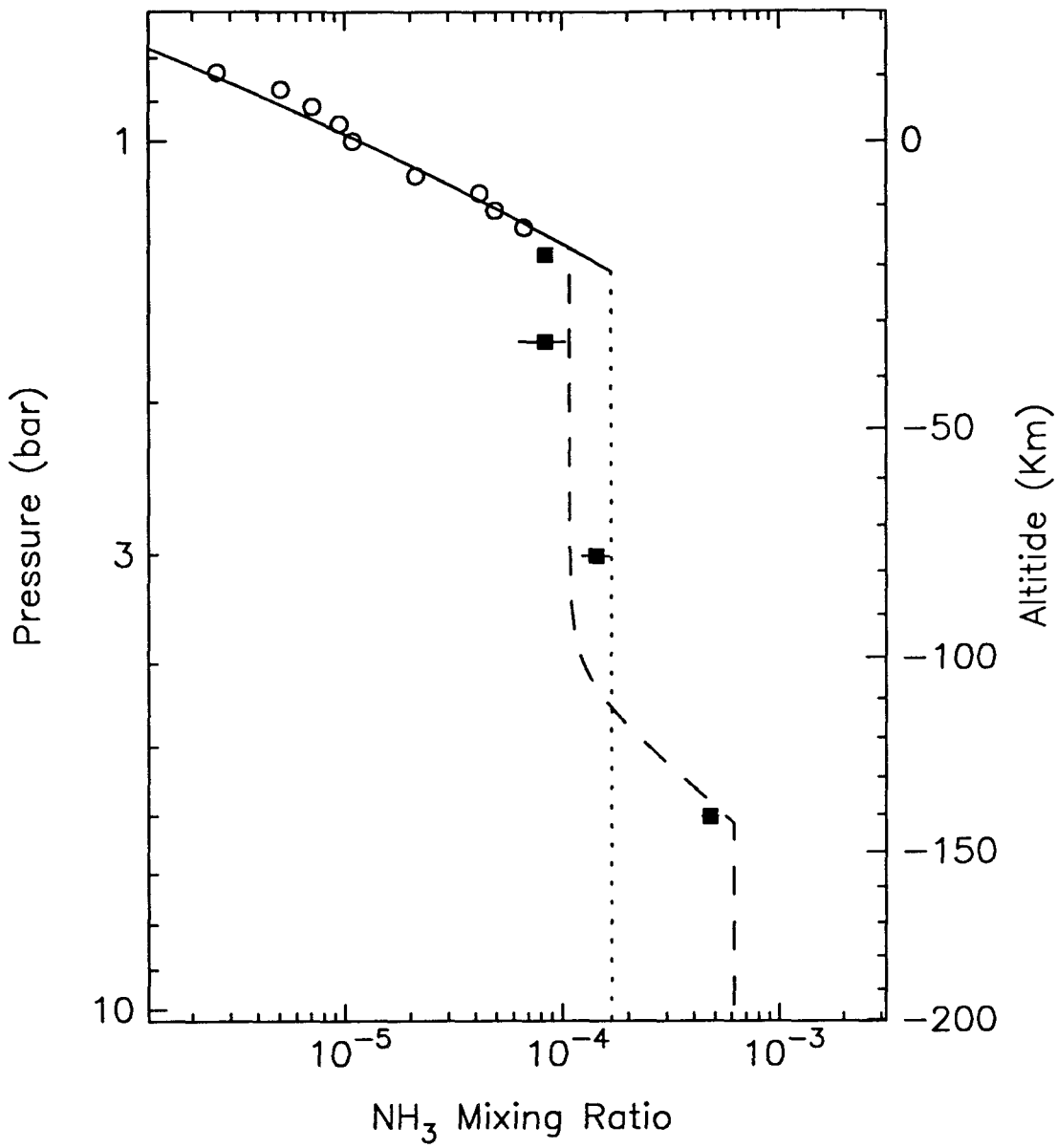

Figure 4.15: Possible vertical profiles of NH_3. In the upper troposphere NH_3 follows the vapor saturation curve (solid line) as measured by the Voyager radio occultation experiment (open circles). Below the saturation point the mixing ratio may follow one of two models: a uniform NH_3 mixing ratio of solar abundance (dotted line), or a NH_3 mixing ratio of 3.7 times solar in the deep atmosphere reduced by 14 times solar abundance of H_2S (dashed line). Iterative inversion of the observations yield a mixing ratio profile indicated by the solid squares.

the sub-cloud region to a level of 6 bar.

Photolysis of NH_3 in the sub-cloud region can be ruled out as a significant mechanism by considering a simplified model. The range of solar UV photons capable of destroying NH_3 through the reaction

$$NH_3 + h\nu \rightarrow NH_2 + H, \tag{4.47}$$

is limited to wavelengths in the range 1600–2350Å by the CH_4 absorption cutoff at the low end and by the vanishing NH_3 cross-section at the high end. In the most conservative case, assuming no opacity above the clouds, the net flux of available solar photons in this range is limited to $< 10^{12}\,cm^{-2}\,sec^{-1}$. If the sub-cloud number density of NH_3 is $\sim 10^{16}\,cm^{-3}$, and assuming that each photon destroys one molecule of NH_3, then the time scale for destroying NH_3 over one scale height ($\sim$ 30 km) is roughly $\sim 3 \times 10^{11}\,sec = 1000$ years. On the other hand, the time scale for transporting NH_3 from deep levels is given by $\sim H^2/K$, where H is the scale height and K is the eddy diffusion coefficient. In the worst case, K could be as low as $10^4\,cm^2\,sec^{-1}$ in the troposphere (Massie and Hunten, 1982). Therefore, the time scale for vertical transport is about 30 years and this vertical mixing dominates over photolysis.

Because ammonia is a major condensate on Saturn, one might expect vertical motions to modify the vertical distribution of NH_3. For example, regions of upwelling bring ammonia-rich parcels of gas from the deep interior. As these parcels rise through the troposphere, ammonia is systematically removed from them, first by dissolving in the putative water cloud at around 10 bar, then by reacting with H_2S to form a particulate NH_4SH cloud at 4-6 bar, and finally by condensing into an ice cloud above 1.4 bar. This ammonia-poor gas is then transported to another latitude where it descends in a region of downwelling. The descending column is depleted in ammonia (relative to the column of rising gas) down to some level where meridional transport and mixing bring the ammonia concentration to its equilibrium value. The globally observed distribution of NH_3 then refers to some mean value between these two extremes.

4.4 Latitudinal Variability of the Atmosphere

In this section, the latitudinal variations in brightness temperature presented in §3.3 are analyzed in the context of the radiative transfer model developed in §4.1. Throughout, longitudinal homogeneity is assumed.

Reference is made to the nominal model, which is simply the model that best fits the global, whole-disk observations. The nominal model, which is fully discussed on section §4.2, contains 0.65 times solar NH_3 below the cloud base at 1.4 bar, increasing to 3.7 times solar NH_3 at 6 bar. The temperature profile follows a pseudo-adiabat governed by an intermediate *ortho-para* H_2 ratio.

4.4.1 Comparison of data and nominal model

Comparison between the images and models is accomplished by evaluating the model brightness on a two-dimensional grid that matches the observing geometry. The model is then averaged in longitude similar to the data (§3.3.1). Figure 4.16 shows the latitudinal brightness variations superimposed on the nominal model brightness. In some cases the absolute level of the model does not match the data, but nevertheless, it has the same relation to the data as the whole-disk results of Table 4.3. For this discussion, the absolute value of the brightness is not important, rather, it is the deviations from a uniform model that are significant.

To correct for geometrical effects, a residual map is created by subtracting the model point-by-point from the data maps. The brightness temperature for nadir-viewing at the equator is then added to the residual map to produce an image free from geometrical effects. The resulting image yields the zonal average brightness temperature for nadir-viewing as shown in fig. 4.17.

The most prominent feature in the latitudinal variability is a brightness peak at 6 and 20 cm at mid-latitudes in the range 25–45°. This is observed in the images (figs. 2.11 and 2.13, pages 39 and 41) as a band of increased brightness. The bright band is clearly above the noise level, and appears to increase in magnitude with increasing depth into the atmosphere. Surprisingly, there is no indication in the 2 cm data of this feature. The sensitivity and resolution of the 0.27 and 3.53 cm data are not sufficient to determine any variability. Therefore, the analysis of latitudinal brightness is limited to the three wavelengths 2.01, 6.17, and 20.13 cm.

In addition to the hot band, there appears to be a gradual increase in brightness from equator-to-pole. This effect is most noticeable at 2 cm, which is free from confusion by the hot band. Here the brightness temperature rises 3.5 K from around 10° to 70°. To first order, many of the variations can be explained in terms of a change in the principle

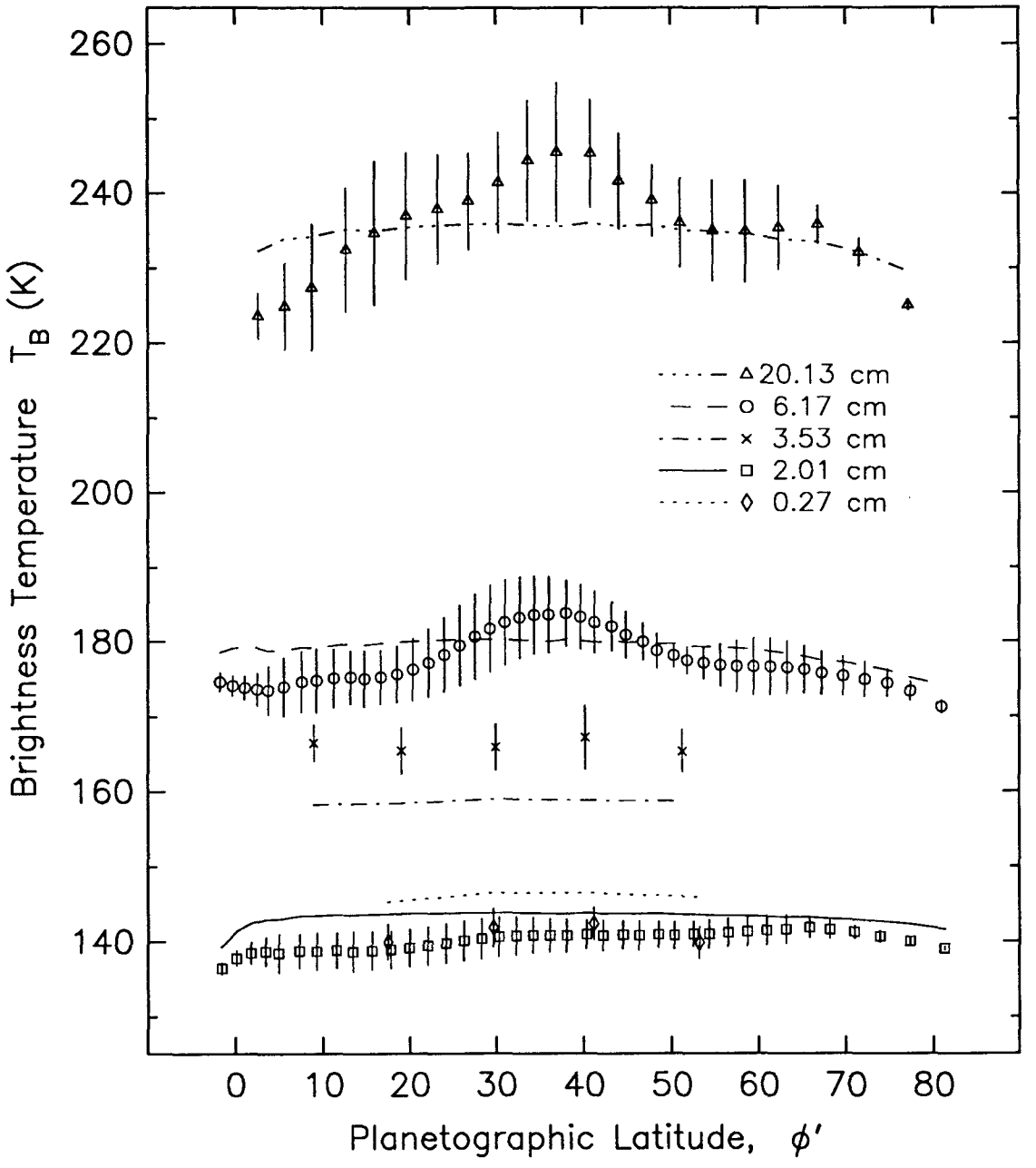

Figure 4.16: Comparison between observed and model latitudinal brightness temperatures. Error bars indicate the standard deviation in each bin. The statistical error of the mean is typically much smaller. Resolution is typically three to four data points in latitude.

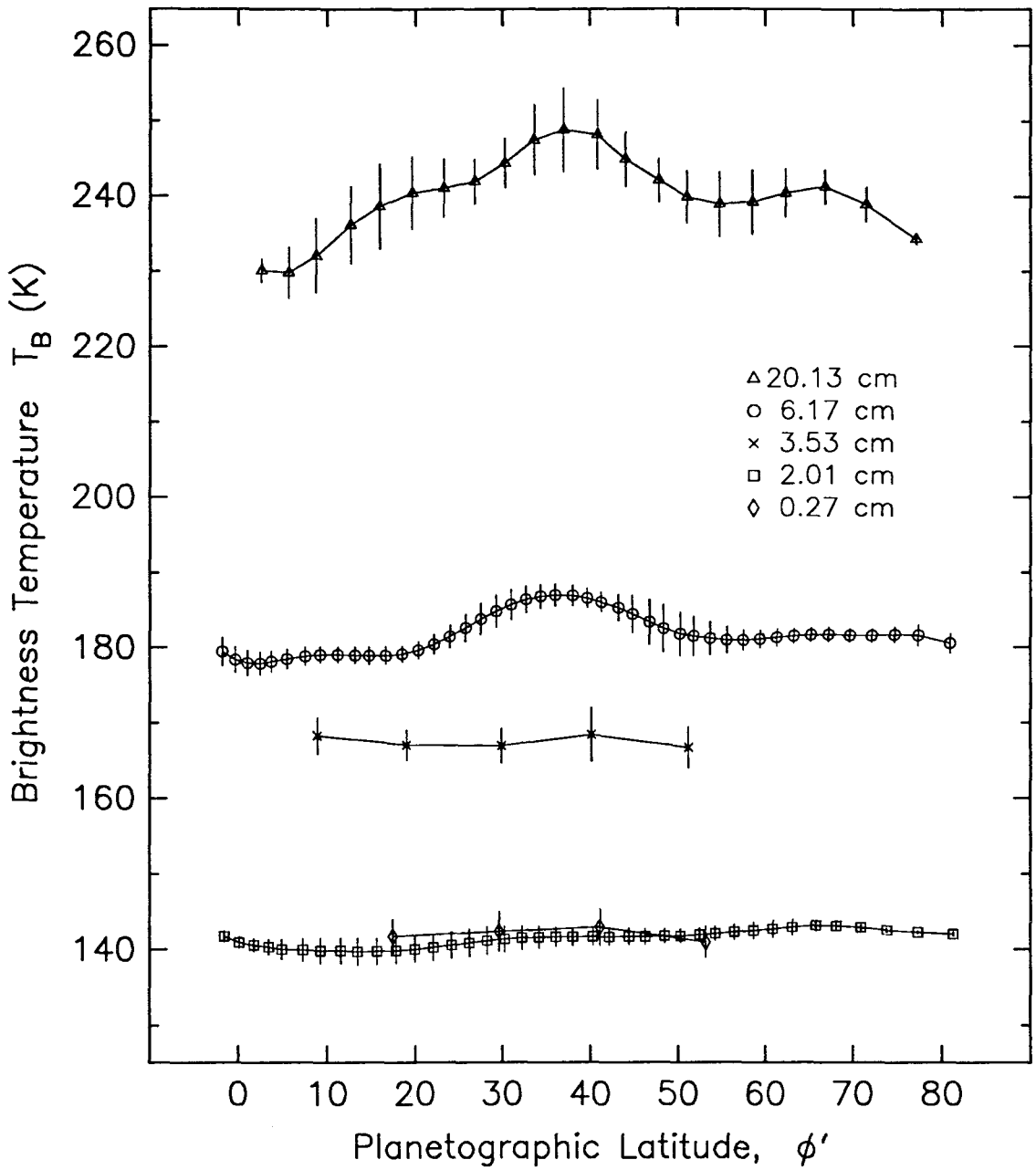

Figure 4.17: Zonal mean brightness temperature for nadir-viewing. Error bars indicate the standard deviation in each bin. The statistical error of the mean is typically much smaller. Resolution is typically three to four data points in latitude.

microwave absorber, NH_3. However, this does not rule out a variation in other parameters such as temperature or lapse-rate as a possible explanation. Clearly, the sensitivity of the brightness temperature to changes in the model parameters must be explored.

4.4.2 Brightness temperature sensitivity

Before attempting to explain the latitudinal variations in microwave brightness, it is helpful to consider the sensitivity of the brightness to changes in model parameters. Accordingly, we consider the variations in brightness of the nominal model due to perturbations in model parameters. In each case, the brightness temperature is calculated for a nadir-viewing geometry. In the following discussion, it is helpful to consider the weighting functions of fig. 4.12 (page 109) associated with the nominal model.

It is natural to expect that changes in the principle absorber, NH_3 would have the largest effect on the outgoing radiation field. Figure 4.18 shows the change in brightness temperature associated with changing the NH_3 mixing ratio below the cloud by $\pm$ 50%. The 6 and 20 cm brightness temperatures, whose weighting functions peak in this region, are the most sensitive to this change. In contrast, the sensitivity at 2 cm is negligible. This is because the 2 cm weighting function peaks in the NH_3 cloud, and does not sense much of the gas below the cloud.

The opposite is true if the NH_3 mixing ratio is changed in the cloud. Figure 4.19 shows the change in brightness temperature achieved by varying the relative humidity in the NH_3 ice cloud. Changing the relative humidity is a convenient way to parameterize changes in the NH_3 vapor within the cloud, and strictly holds only for a condition of vapor pressure equilibrium. Nevertheless, the effect is substantial at 2 cm, and less so at 6 and 20 cm for the simple reason that the 2 cm weighting function is most sensitive to the cloud layer.

As an additional exercise, fig. 4.20 shows the sensitivity to changes in kinetic temperature at a pressure of 1 bar. The brightness at 6 and 20 cm changes almost linearly with kinetic temperature, however the slope is opposite to the ammonia sensitivity. This is generally expected because the radiative transfer integral is linear in temperature. However, the same is not true at 2 cm. Bearing in mind that the 2 cm weighting function peaks in the cloud, and that the cloud forms at the same temperature, it is easy to see that the 2 cm brightness tracks the temperature field and is insensitive to changes in kinetic temperature.

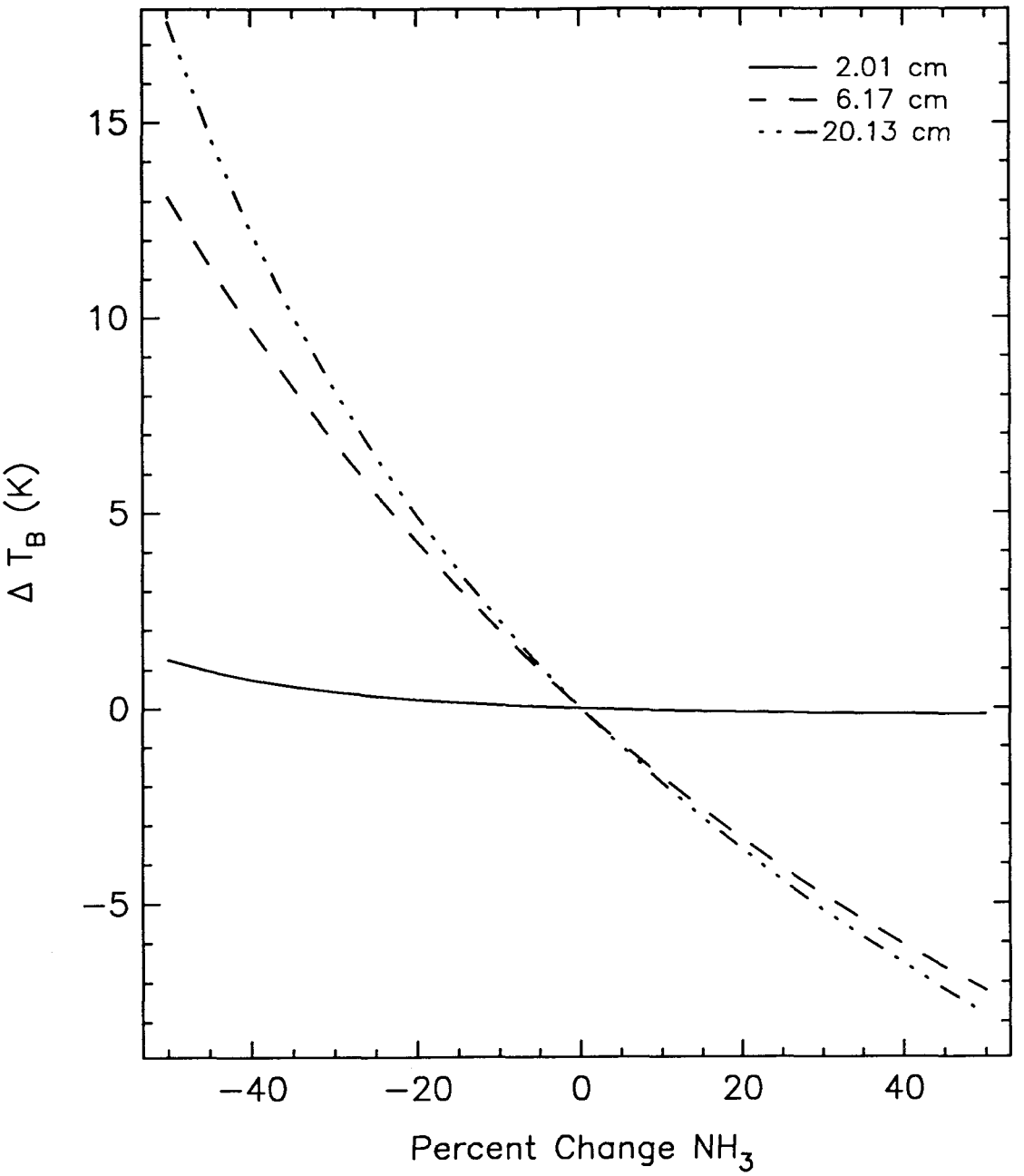

Figure 4.18: Model sensitivity to changes in NH_3 below the cloud.

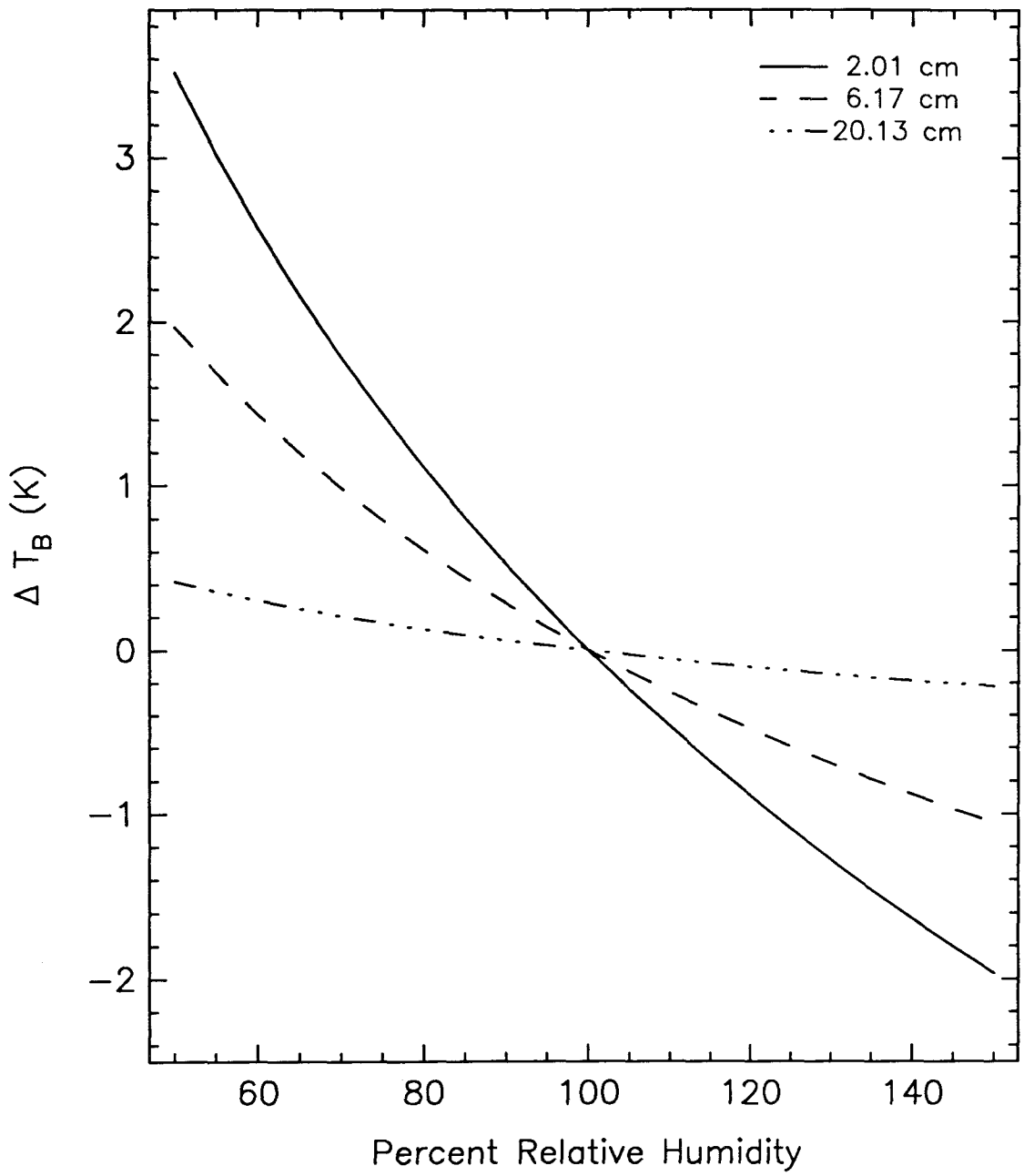

Figure 4.19: Model sensitivity to changes in NH_3 within the cloud. Changes in ammonia vapor abundance within the cloud are parameterized in terms of relative humidity.

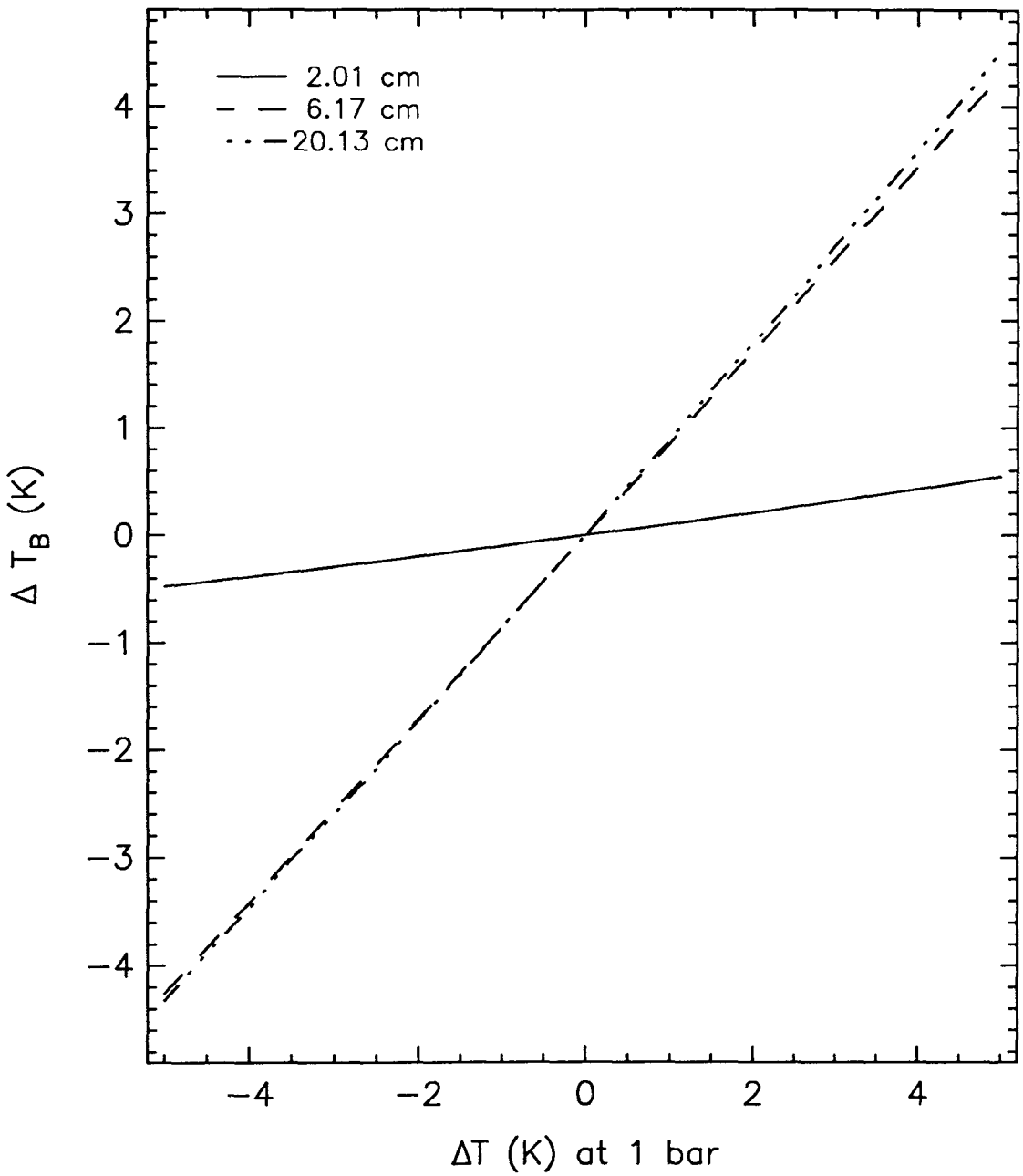

Figure 4.20: Model sensitivity to changes in kinetic temperature at 1 bar.

As a final exercise, we consider the effect of winds on the brightness temperature. The wind speed enters into the radiative transfer equation by changing the effective gravitational potential and thus changing the column abundance of absorber above a specified pressure level. As fig. 4.21 shows, the net effect is much smaller than the observed brightness variability for winds as great as 1000 $\mathrm{m\,sec^{-1}}$.

The results of this sensitivity test show that variations in 2 cm brightness are primarily related to changes in ammonia vapor within the cloud, whereas variations in 6 and 20 cm are related to variations in ammonia abundance below the clouds or changes in kinetic temperature or both. The effect of winds is unimportant at all wavelengths.

4.4.3 Retreived zonal properties

The partial derivatives obtained in the previous section can be used to recover the mean zonal properties of the atmosphere for several simple cases. To first order, it is clear from the sensitivity analysis that the largest variations in brightness (at 6 and 20 cm) are due to variations in ammonia abundance below the clouds or changes in kinetic temperature or both. We examine this case by holding one parameter fixed and allowing the other to vary with latitude.

We solve for the parameter of interest by iterating on the residual brightness temperature. At each step of the iteration, the residual brightness at each latitude bin is used to adjust the parameter by a least-squares fit of a linear model to the three wavelength observations. The results of the fit are shown in fig. 4.22. The latitudinal brightness variations can be fit by either changing ammonia or temperature, or perhaps by changing both. The quality of the data does not favor one solution over another. However, the difficulties of sustaining a large temperature gradient in the presence of convection argues against the model that requires temperature gradients greater than a few Kelvin. Furthermore, large deviations in temperature are contradictory to Voyager IRIS observations of the temperature at 0.73 bar that indicate no substantial gradients due to kinetic temperature (Conrath and Pirraglia, 1983).

Therefore, the large brightness variations observed at 6 and 20 cm are most likely due to latitudinal variations in the abundance of ammonia below the cloud. Such variations have a minimal effect on the 2 cm brightness, and the gradual equator-to-pole increase in 2 cm brightness must be due to changes in ammonia abundance within the cloud. Allowing

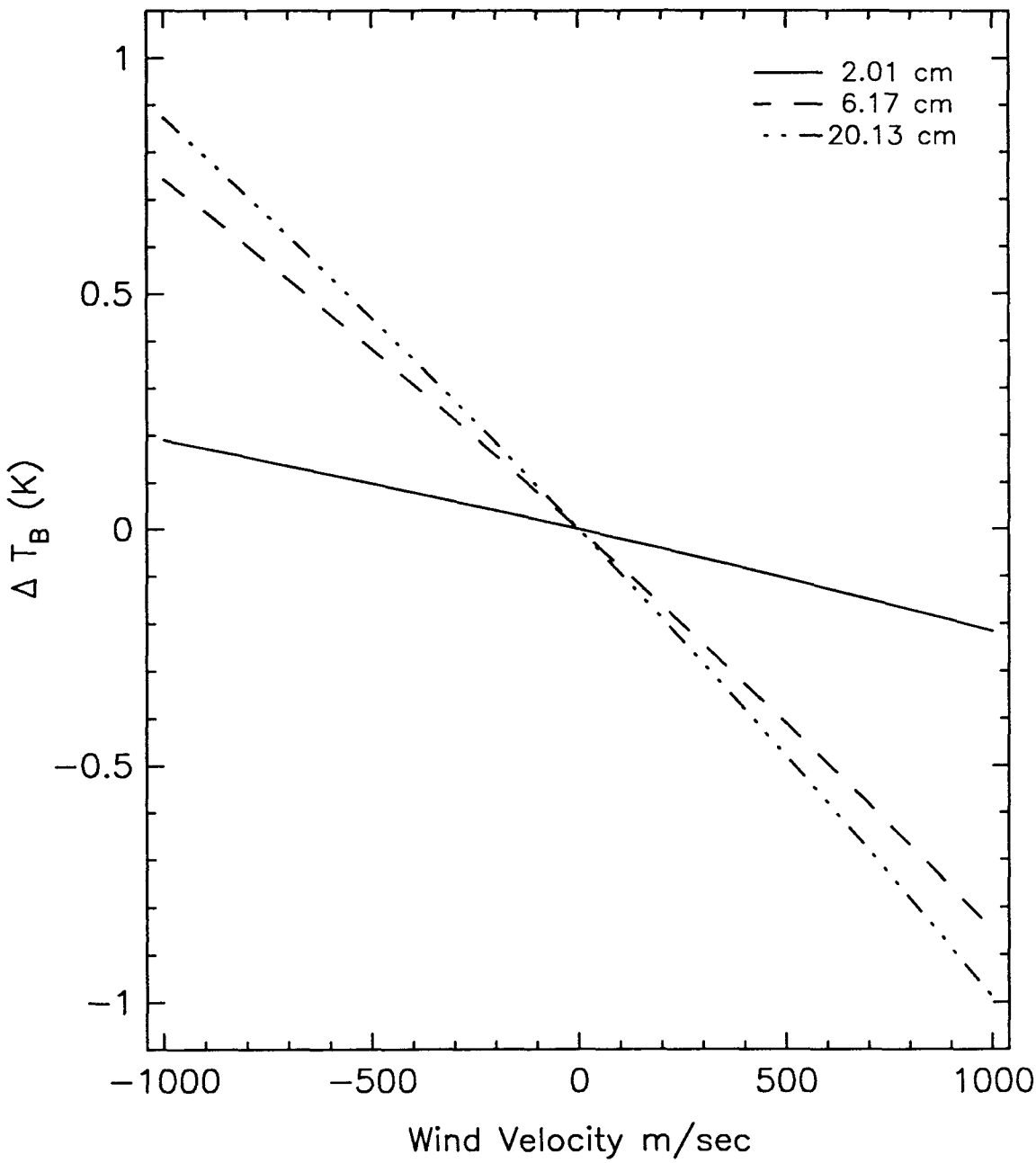

Figure 4.21: Model sensitivity to changes in wind velocity with respect to system III.

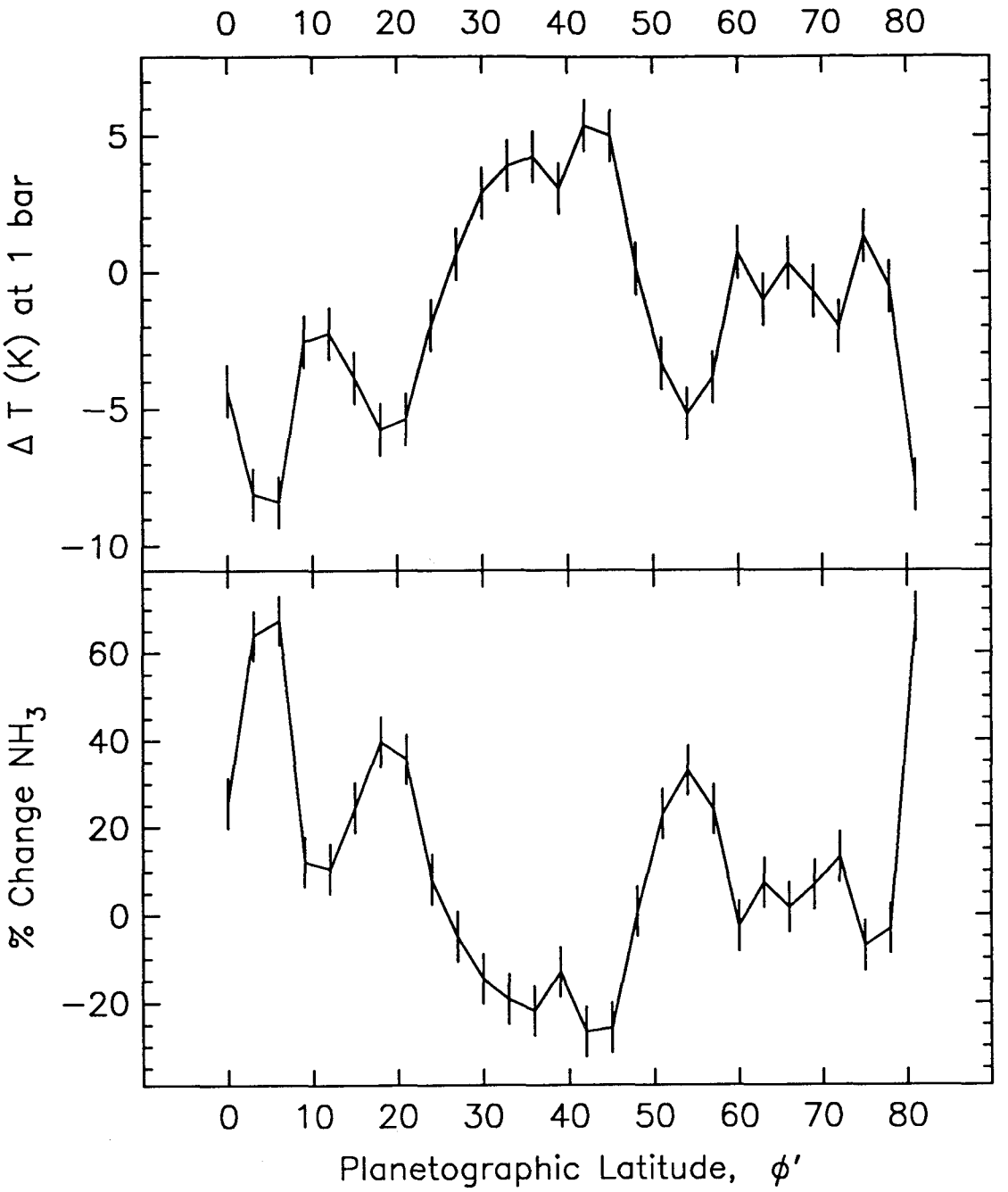

Figure 4.22: Zonal mean ammonia abundance below the cloud base and kinetic temperatures at 1 bar expressed as deviations from the nominal global model. Observed latitudinal variations in brightness fit either curve equally well, and thus cannot distinguish between the competing effects.

the ammonia abundance to vary independently within and below cloud yields the fit shown in fig. 4.23. Here the ammonia concentration within the cloud decreases by a factor of two from equator to pole. The abundance below the cloud appears to alternate between bands of enriched and depleted ammonia, reaching extrema of 0.5 and 1.0 times solar mixing ratio. The observed hot band appears as a region of depletion in northern mid-latitudes.

For purposes of comparison, the best-fit model is shown in fig. 4.24 superimposed on the observed brightness. The model is well matched to the observations, and reproduces the variations in brightness at all three wavelengths.

4.5 Summary and Implications for Atmosphere Dynamics

The model atmospheres presented here are updated versions of long standing thermo-chemical models of the giant planets (Weidenschilling and Lewis, 1973; Atreya, 1986). The general assumptions made about the atmosphere being in hydrostatic equilibrium and thermodynamic equilibrium are plausible. Perhaps the greatest uncertainty in the model lies in evaluating the transfer of microwave radiation. Ammonia vapor is the principle microwave absorber, and the absolute uncertainty in the absorption coefficient may be as large as 30% (Spilker and Eshleman, 1988). This uncertainty has some bearing on the determination of absolute abundances, but the conclusions regarding the variability of ammonia remain firm. The relative errors in measuring ammonia variability are independent of the absolute value.

4.5.1 Whole-disk results

On the basis of comparison between model whole-disk brightnesses and disk-integrated observations, several conclusions can be drawn. The microwave opacity of the atmosphere increases in the range 1-10 bar. The most likely explanation is that the abundance of NH_3 vapor increases from a value of 0.5–0.65 times solar just below the NH_3 ice clouds to a maximum of 3–4 times solar at a pressure of 6 bar. No other microwave absorber exists in sufficient concentration to account for the observations. A similar conclusion was reached by Briggs and Sackett (1989), in their analysis of whole-disk observations.

In a well-mixed atmosphere, NH_3 is expected to be uniformly distributed in altitude. The mechanism by which the vertical distribution of NH_3 deviates from an expected uniform distribution is unclear. A thermo-chemical model can satisfy the observations by

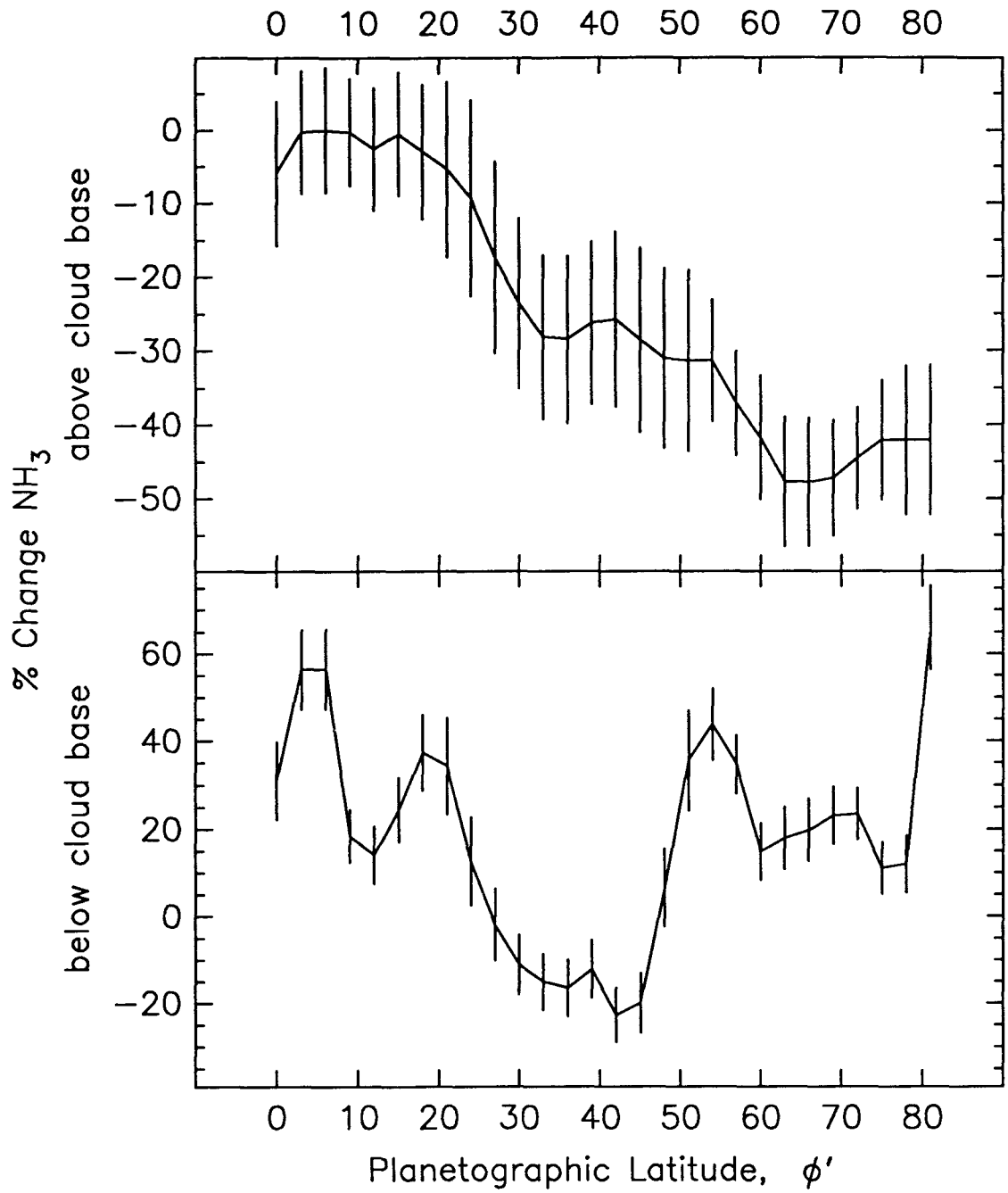

Figure 4.23: Zonal mean ammonia abundance above and below the cloud base expressed as deviations from the nominal global model.

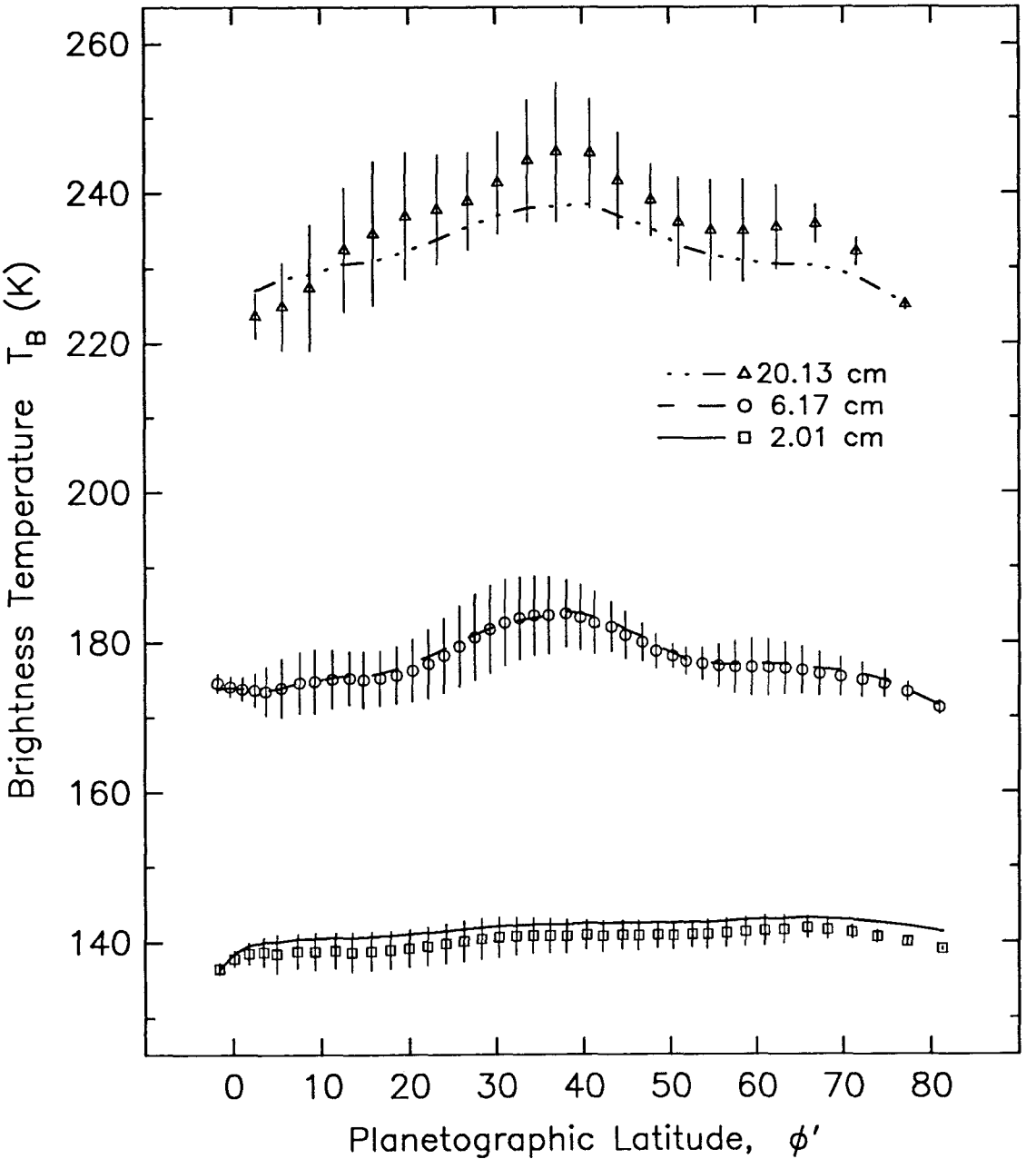

Figure 4.24: Model latitudinal brightness variations compared with observed values. The model includes the best-fit latitudinal variations in NH_3 abundance both below and above the cloud.

postulating an enrichment of H_2S, which acts to remove NH_3 above 3 bar through the formation of a particulate cloud of NH_4SH. However, such a model requires 11-14 times solar abundance of sulfur. Briggs and Sackett (1989) require roughly 11 times solar H_2S to satisfy their observations as well. Although these values may seem high, comparison with the enriched value of N only requires a ratio S/N $\sim$ 3 times solar. Nevertheless, it is clear that if H_2S is the only mechanism that modifies the distribution of NH_3, 11-14 times solar serves as an upper limit to its concentration.

The model has neglected the effects of dynamics and vertical mixing on the vertical distribution of NH_3. Clearly, vertical motions will control the distribution of condensates if mixing is rapid compared to condensation or sublimation time-scales, but this is not likely to be the case. Instead, large-scale circulations, that extend above the ammonia cloud base, are capable of drying parcels of gas and creating regions of downwelling that are relatively depleted in ammonia. Sublimation of entrained ice particles in these downward moving parcels or horizontal mixing could account for the observed increase in ammonia abundance with depth in some of these regions. If vertical motions plays a role in modifying the vertical distribution of NH_3 the constraint on the abundance of H_2S is somewhat relaxed.

The presence of H_2O cannot be confirmed or ruled out on the basis of current observations. Nevertheless, the enrichment of the volatiles CH_4, NH_3, and H_2S in the atmosphere of Saturn must be accounted for by models of formation. The observation that volatiles are enriched seems to favor the core-instability model of formation (Pollack and Bodenheimer, 1989), in which the core formed first and subsequently captured large quantities of gas from the solar nebula. The enrichment of the heavy elements results from their being present in both the sold phase as well as the gas phase. The observed enrichment of S with respect to N may also be a consequence of core-instability scenario because preferentially more S is expected to be present in the solid phase than N.

4.5.2 Latitudinal variability

Although latitudinal variations in the brightness temperature of Saturn were first suggested by the observations of de Pater and Dickel (1982), it is was not until recently that this variation was identified with a hot band in northern mid-latitudes (Grossman *et al.*, 1987; Grossman *et al.*, 1988; Grossman *et al.*, 1989). This observations was partially confirmed by modeling the observations of Briggs and Sackett (1989).

This work presents a detailed analysis and inversion of zonally-averaged brightness temperatures at wavelengths of 2, 6, and 20 cm, which indicate latitudinal variations in ammonia concentrations within the condensate cloud layer as well as below the NH_3 cloud. Ammonia abundance varies by as much as a factor of two in both regions, and extending from the cloud region near 1 bar to levels as deep as 7 bar and possibly deeper. The above conclusion is based on the assumption that horizontal temperature gradients are small. Attributing the brightness variations to changes in kinetic temperature requires temperature differences greater than 15 K along constant pressure surfaces.

Assuming that temperature is uniform on constant pressure surfaces allows determination of the latitudinal ammonia abundance. The ammonia profile below the clouds shows a latitudinal structure of alternating enhancement and depletion reminiscent of the zonal variability observed in the belts and zones of Jupiter (Gierasch *et al.*, 1986). This similarity suggests that vertical motions associated with meridional circulation are responsible for producing the latitudinal variations of ammonia. According to this hypothesis, the regions of high ammonia concentration are due to rising parcels of ammonia-rich gas. The ammonia condenses into a particulate NH_4SH cloud and an ice cloud within the rising column. The parcel, now relatively depleted in ammonia vapor, descends in an adjacent cell, which appears as a region of ammonia depletion.

Latitudinal variations in microwave brightness have also been observed on Jupiter (de Pater, 1986) and Uranus (Hofstadter and Muhleman, 1988). These observations are generally interpreted in terms of variations in ammonia abundance. A strong similarity between the Uranus observations and Voyager infrared measurements suggests that the latitudinal variations are associated with large-scale vertical motions (Hofstadter *et al.*, 1990). Similarly, the latitudinal variations in brightness temperature on Jupiter are well-correlated with ammonia abundances as measured by the Voyager IRIS instrument (Flasar, 1987). Furthermore, the correlation between ammonia and dynamics is well understood in Jupiter. Regions of upwelling have large abundances of ammonia vapor and clouds, while regions of downwelling are relatively depleted in ammonia and clouds (Gierasch *et al.*, 1986). Similar correlations may exist for Saturn.

Voyager IRIS observations of thermal emission in the northern hemisphere of Saturn (Conrath and Pirraglia, 1983) indicate a region of increased brightness similar in shape and position to that observed at 6 and 20 cm. This has been subsequently interpreted as

a decrease in the infrared cloud opacity at northern mid-latitudes (Bézard *et al.*, 1984). In addition, analysis of cloud top heights by Tomasko *et al.* (1984) show maximum cloud heights occurring at high latitudes and near the equator, while northern mid-latitudes show depressed cloud tops. This correlation could be explained if vertical motions contribute to concentrating both ammonia vapor and cloud particles at certain latitudes and depleting both ammonia vapor and cloud particles at other latitudes. If this interpretation is correct, it implies that vertical motions on Saturn are correlated over 4 scale heights and possibly deeper. This may have some consequences for our understanding of the general circulation of Saturn's atmosphere. However, the atmosphere of Saturn is not as well understood as that of Jupiter. While the zonal jets on Jupiter are correlated with vertical motions and ammonia abundances, the retrieved ammonia profile on Saturn is not simply correlated with the structure of the zonal jets.

The lack of large-scale contrasts in troposphere temperature inferred from IRIS observations as well as current microwave observations suggests the existence of an efficient mechanism for meridional heat transport. Ingersoll and Porco (1978) have suggested that the internal heat flux may adjust itself as a function of latitude to compensate for the differential solar heating at Jupiter. At Uranus, the internal heat flux is much less, and meridional heat transport in the atmosphere is more efficient (Friedson and Ingersoll, 1987). At Saturn the meridional transport of heat in the interior would have to compensate for a large variation in solar input due to the large obliquity of Saturn.

The equator-to-pole decrease in ammonia vapor within the cloud is difficult to explain in terms of a simple dynamical model. UV photolytic destruction of NH_3 can occur in some regions above the cloud (Visconti, 1981), but this effect is expected to be opposite to the observed variations. That is, photolysis is expected to preferentially destroy NH_3 at the equator relative to the pole. Because the variability is concentrated within the cloud, the most likely explanation must have to do with the subtle process of cloud formation and condensation.

In the final analysis, a picture of the general circulation of Saturn's troposphere emerges, which consists of alternating latitudes of rising and sinking motion dominated by a region of general downwelling in northern mid-latitudes at 25°–50°. This vertical motion is correlated with depressed cloud tops and appears to persist to at least a level of 7 bar.

Chapter 5

Ring Modeling and Analysis

Although the rings of Saturn have been studied for a long time, there are still many basic questions to be answered regarding the physical nature of the particles that comprise the rings. The size and nature of the ring particles themselves are disputed. The volume density and the vertical structure of the rings are not well determined. It is still not known whether the rings are many-particles thick, as suggested by the classical model of the opposition effect (Lumme *et al.*, 1983) or represented by a monolayer of particles (Froidevaux, 1981; Zebker *et al.*, 1985). To shed some light on many of these questions and related problems, we present an analysis of the high-resolution microwave observations of Saturn's rings reported in Chapter 3.

In contrast to visible or infrared remote sensing, probing the rings with microwaves provides unique information on the physical properties of the individual ring particles. This is because the size of ring particles is comparable to the centimeter wavelengths used in this study. As a result, microwaves penetrate the bulk of the particle rather than just interacting with a thin surface layer. For this reason, our greatest knowledge of the physical properties of Saturn's rings comes from microwave experiments such as the Voyager radio occultation experiment, in which a coherent, monochromatic signal was received on Earth after being occulted by the rings of Saturn (Marouf *et al.*, 1986). The results of that experiment yielded information on the optical depth of the rings and on the size distribution of particles. However, because of signal-to-noise limitations, the measurements were strictly limited to the thinest parts of the classical rings. Here we complement the results of the Voyager radio occultation experiment by providing similar results on all the classical rings, especially the optically thick B ring.

Specifically, we focus here on modeling and understanding measurements of ring brightness and polarization as a function of wavelength, radial distance, and azimuth. Mie scattering calculations are used to model the rings as a power-law size distribution of par-

ticles. Free parameters in the model are the upper and lower limits to the size distribution, the exponent of the power-law, and a parameter F, which characterizes the mass fraction of silicates homogeneously mixed with the ice particles. At each step, the results of the model are compared with the observations. The validity of any model depends on its ability to explain the observations.

Mie calculations yield estimates of angular integral properties such as extinction efficiencies, absorption efficiencies, and single scattering albedos. Strictly speaking, Mie theory is applicable only for spherical particles, however, angular integral properties are similar for spheres and randomly oriented particles (Greenberg *et al.*, 1971; Mugnai and Wiscombe, 1986). The main effect of nonsphericity on scattering behavior is in the angular phase function. Here we must rely in experimental work and empirical phase functions to formulate a working hypothesis.

We begin with a discussion of the interaction of radio waves with hypothetical ring particles. Then the total ring brightness is analyzed as the sum of three independent processes: thermal emission by the rings themselves, diffuse scattering of Saturn's thermal emission by the rings, and extinction of Saturn's emission in the region where the rings cross the disk (the cusp). In the Rayleigh-Jeans limit this can be written in terms of brightness temperatures:

$$T_R = T_E + T_S + T_D e^{-\tau/\sin|B|}, \tag{5.1}$$

where the three terms on the right-hand side are the thermal emission, scattered emission, and extinction of Saturn's disk emission. The last term only applies to the cusp region of the rings.

Two different models are compared with the data: a simple uniformly-bright ring model and a detailed numerical model that predicts ring brightness and optical depth as a function of ring azimuth using radiative transfer calculations. Throughout, the particles are assumed to be widely separated. That is, the particles are assumed to be independent scatterers. Previous attempts to model the radiation field of the rings (Cuzzi and Van Blerkom, 1974; Janssen and Olsen, 1978; Cuzzi *et al.*, 1980; Muhleman and Berge, 1982;) have lacked the observational tests to determine the validity of the models. In light of current observations, these models are inadequate, especially in predicting the azimuthal brightness variations and polarization.

This chapter concludes with a discussion of the limitations of the results, a sum-

mary of newly derived optical depths of the rings, an estimate of the possible range of particle sizes, and inferences regarding the shape of the particles.

5.1 Interaction of Radio Waves with Saturn's Rings

In this section, a brief description of the interaction of electromagnetic radiation with dielectric particles is discussed. This discussion serves as a solid foundation for subsequent modeling of the emission, scattering, and extinction of radiation by Saturn's rings.

We begin by discussing the dielectric properties of a single particle, and then extend the theory to an ensemble of particles. Throughout, it is assumed that the particles act independently; that there is no coherent scattering. This is equivalent to assuming the mean spacing between particles is greater than a few particle radii. Volume density implied by the opposition effect indicates that this condition is satisfied at Saturn (Kawata and Irvine, 1974), but may not hold for the rings of Uranus (Gresh, 1990).

5.1.1 Dielectric properties of ice-rock mixtures

The interaction of electromagnetic radiation with the ring particles depends most strongly on the dielectric properties of the particles. Direct observations of water-ice spectral features (Kuiper *et al.*, 1970; Pilcher *et al.*, 1970) and the high particle albedo suggest that particles are composed primarily of water ice. The particles also may contain a small fraction of dark, silicate material as suggested by the low visible albedo in the C ring and Cassini division. Therefore we consider several models of particles composed of ice-rock mixtures.

The absorption coefficient of ice at microwave wavelengths is caused by difference bands from translational lattice vibrations. The absorption spectrum in the range 8–25 cm^{-1} has been measured at temperatures of 80, 100, 150, and 202 K in the laboratory by Mishima *et al.* (1983) and is described by the equation

$$\alpha_{\mathrm{H_2O\,ice}} = \frac{A_0}{T} \frac{e^{hc\nu_0/kT}}{(e^{hc\nu_0/kT}-1)^2} \frac{1}{\nu_0^2} \nu^2 + B\nu^4, \tag{5.2}$$

where T is the temperature in Kelvin and ν is the wavenumber in cm^{-1}. The constants were obtained by fitting Eq. 5.2 to a number of measurements. The best-fit was obtained for $\nu_0 = 233\,\mathrm{cm}^{-1}$, $A_0 = 1.188 \pm 0.01 \times 10^5\,\mathrm{cm}^{-1}$ K, and $B = 1.11 \pm 0.03 \times 10^{-6}\,\mathrm{cm}^{-4}$.

The resulting curve extrapolated to microwave frequencies is shown in figure 5.1, where the dominant $1/\lambda^2$ dependence is evident.

The corresponding absorption lengths in cold water ice for the frequencies relevant to the current observations varies from about 10^2–10^6 cm. This, in part, helps explain the observed low brightness temperature of Saturn's rings. It is clear from fig. 5.1 that homogeneous ice is very transparent at low frequencies. However, to characterize the full range of possible particle compositions, the effect of silicate or rock impurities should be considered.

The refractive index of water ice can be written in terms of the absorption coefficient as

$$m = m_r - im_i = 1.78 - i\frac{\alpha\lambda}{4\pi}. \tag{5.3}$$

This can be related to the complex dielectric constant ϵ through the equation $n^2 = \epsilon = \epsilon' + i\epsilon''$, which leads to the relation

$$\epsilon' = m_r^2 - m_i^2 = 3.17 - \left(\frac{\alpha\lambda}{4\pi}\right)^2 \tag{5.4a}$$

$$\epsilon'' = 2m_r m_i = 3.56\frac{\alpha\lambda}{4\pi}. \tag{5.4b}$$

The index of refraction can also be written in terms of the dielectric constant as

$$m_r^2 = \frac{1}{2}\left\{\sqrt{\epsilon'^2 + \epsilon''^2} + \epsilon'\right\} \tag{5.5a}$$

$$m_i^2 = \frac{1}{2}\left\{\sqrt{\epsilon'^2 + \epsilon''^2} - \epsilon'\right\}. \tag{5.5b}$$

The complex dielectric constant of a powder silicate soil of density $\sim 1\,\mathrm{gm\,cm^{-3}}$ has been determined to be

$$\epsilon_{\mathrm{soil}} = 3.0 - i0.03, \tag{5.6}$$

for a wide variety of rocks (Campbell and Ulrichs, 1969). A mixture of rock and ice can be parameterized by a value F, which is the mass fraction of soil mixed with ice. In this case a reasonable scaling law for the dielectric properties of the uniform mixture is

$$\epsilon_{\mathrm{mix}} = (1 - F)\epsilon_{\mathrm{ice}} + F\epsilon_{\mathrm{soil}}. \tag{5.7}$$

The dielectric constant of the mix is then

$$\epsilon'_{\mathrm{mix}} = \left\{3.17 - \left(\frac{\alpha\lambda}{4\pi}\right)^2\right\}(1 - F) + 3.0F \tag{5.8a}$$

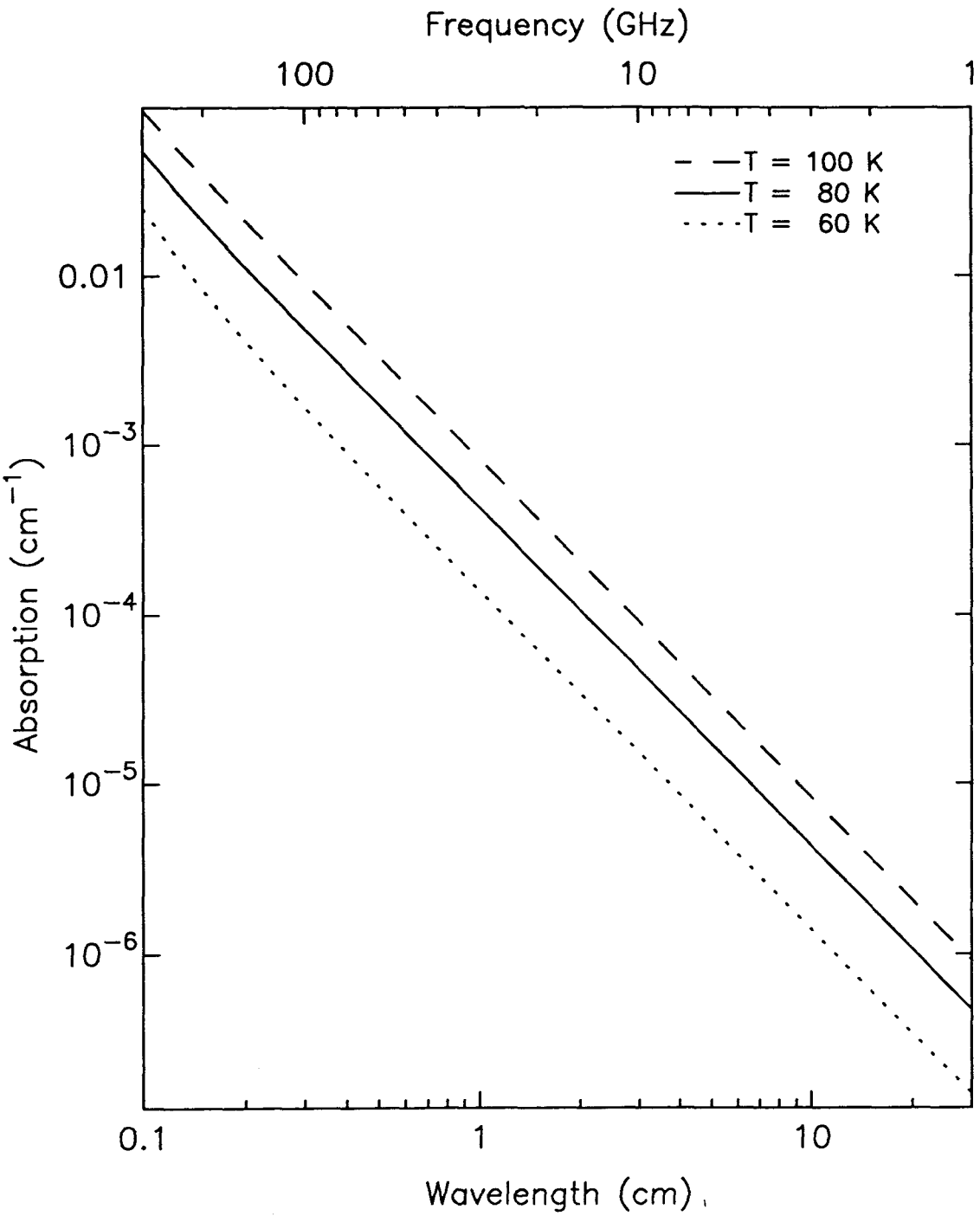

Figure 5.1: Absorption spectra of water ice in the range $\lambda = 0.1$–30 cm. The lines are theoretical curves fit to empirical observations described by Eq. 5.2.

$$\epsilon''_{\rm mix} = 3.56\left(\frac{\alpha\lambda}{4\pi}\right)(1-F)+0.03F, \tag{5.8b}$$

and the refractive index is given by eq. 5.5. The refractive indexes for four model particles containing 0%, 2%, 5%, and 10% mass fraction silicates are summarized in table 5.1.

Table 5.1: Model particle refractive indexes: $m = m_r - im_i$ for rock-ice spheres at 85 K.

F^1	m_r	m_i at $\lambda_{\rm cm}$				
		0.27 cm	2.01 cm	3.53 cm	6.17 cm	20.13 cm
0.00	1.78	0.000129	0.000017	0.000010	0.000006	0.000002
0.02	1.78	0.000295	0.000185	0.000178	0.000174	0.000170
0.05	1.78	0.000545	0.000438	0.000431	0.000427	0.000423
0.10	1.78	0.000961	0.000860	0.000853	0.000850	0.000846

[1]Mass fraction silicates.

5.1.2 Scattering by a single particle

Consider a plane wave of wavelength λ and wavenumber $k = 2\pi/\lambda$ described by the Stokes vector $\mathbf{I_0} = \{I_0, Q_0, U_0, V_0\}$ incident on an arbitrary particle. The scattered wave in the far field is a spherical wave and can be described by an angle θ, which it makes with the direction of propagation of the incident light and an azimuth angle ϕ. The intensity of the scattered light at a distance r can be written in terms of the Stokes parameters as

$$\mathbf{I} = \frac{\mathbf{F}}{k^2r^2}\mathbf{I_0}, \tag{5.9}$$

where $\mathbf{F}$ is a four-by-four transformation matrix of dimensionless functions that depend on direction (θ, ϕ) but not on distance r (van de Hulst, 1957).

Let the total energy scattered in all directions be equal to the energy of the incident wave falling on the area σ_s. This defines the scattering cross-section

$$\sigma_s = \frac{1}{k^2}\int F(\theta,\phi)\sin\theta d\theta d\phi, \tag{5.10}$$

which has units of area. Similarly the energy absorbed inside the particle can be set equal to the energy incident on the area σ_a, the cross-section for absorption. The extinction cross-section is then the sum

$$\sigma_e = \sigma_s + \sigma_a. \tag{5.11}$$

It is convenient to introduce the efficiency factor for scattering, absorption, and extinction, which is the dimensionless ratio of the respective cross-section to the geometrical cross-section:

$$Q_s = \sigma_s/G \tag{5.12a}$$

$$Q_a = \sigma_a/G \tag{5.12b}$$

$$Q_e = \sigma_e/G. \tag{5.12c}$$

For problems involving multiple scattering, is is useful to know the single scattering albedo, ϖ, which is the ratio of scattered energy to the total energy removed from the beam:

$$\varpi = \frac{Q_s}{Q_e}. \tag{5.13}$$

In conjunction with the transformation matrix it is useful to define a parameter called a phase matrix

$$\mathbf{P} = \frac{4\pi}{k^2\sigma_s}\mathbf{F}, \tag{5.14}$$

where the constant of proportionality follows from the normalization condition

$$\int_0^{2\pi}\int_0^{\pi} P^{11}(\theta,\phi)\sin\theta d\theta d\phi = 4\pi. \tag{5.15}$$

The element of the first row and first column, P^{11}, represents the probability for scattering of unpolarized incident light in a given direction (θ,ϕ). The shape of the phase function can be characterized by a single number,

$$g = \frac{1}{4\pi}\int_0^{2\pi}\int_0^{\pi}\cos(\theta)P^{11}(\theta,\phi)\sin\theta d\theta d\phi, \tag{5.16}$$

which is called the anisotropy parameter or asymmetry factor. The parameter g varies between -1 and 1, and is strictly 0 for isotropic scattering.

These quantities generally depend on the orientation of the incident field with respect to the particle, however, in many practical applications the efficiency factors, single scattering albedo, and anisotropy parameter can be taken as constants and P as a function only of scattering angle with at most six independent parameters. Additional simplifications can be made for the case of scattering from spheres or ensembles of randomly oriented particles.

5.1.3 Scattering by a sphere

The scattering matrix of a homogeneous dielectric sphere of radius a has been exactly solved by Mie, and is commonly referred to as Mie theory (van de Hulst, 1957). It is most useful when the size of the particle is comparable to the wavelength ($a \sim \lambda$), which is the case for the current experiment.

Mie theory provides the solution in the form of two infinite series:

$$S_1 = \sum_{n=1}^{\infty} \frac{2n+1}{n(n+1)} [a_n \pi_n + b_n \tau_n], \tag{5.17a}$$

$$S_2 = \sum_{n=1}^{\infty} \frac{2n+1}{n(n+1)} [b_n \pi_n + a_n \tau_n], \tag{5.17b}$$

which are the complex scattering amplitudes for two orthogonal directions of incident polarization. The scattering and extinction efficiency and asymmetry can also be written in the form of infinite series:

$$Q_s = \frac{2}{x^2} \sum_{n=1}^{\infty} (2n+1)(a_n a_n^* + b_n b_n^*), \tag{5.18a}$$

$$Q_e = \frac{2}{x^2} \sum_{n=1}^{\infty} (2n+1) \Re(a_n + b_n), \tag{5.18b}$$

$$g = \frac{4}{x^2 Q_s} \sum_{n=1}^{\infty} \left[\frac{n(n+2)}{n+1} \Re(a_n a_{n+1}^* + b_n b_{n+1}^*) + \frac{2n+1}{n(n+1)} \Re(a_n b_n^*) \right]. \tag{5.18c}$$

The equations scale with the size parameter, $x = 2\pi a/\lambda$, which is just the particle circumference divided by the wavelength. The complex-valued Mie coefficients a_n and b_n depend on x and on the complex refractive index $m = m_r - im_i$. They are expressed in terms of spherical Bessel functions.

In practice the number of terms that must be evaluated in this series is slightly larger than the size parameter, x, since the Mie coefficients rapidly approach zero as n becomes larger than x. Computational evaluation of the infinite series is accomplished using the improved algorithms of Wiscombe (1980), which provide greater speed and efficiency with little loss of accuracy over previous computational methods.

The results for a single sphere can be considered by examining the extinction efficiency for a range of size parameters. Figure 5.2 shows the extinction of a single sphere as a function of size parameter. The curve is characterized by a series of large ripples of wavelength $\sim$ 10 and a series of superimposed ripples of shorter wavelength. The major

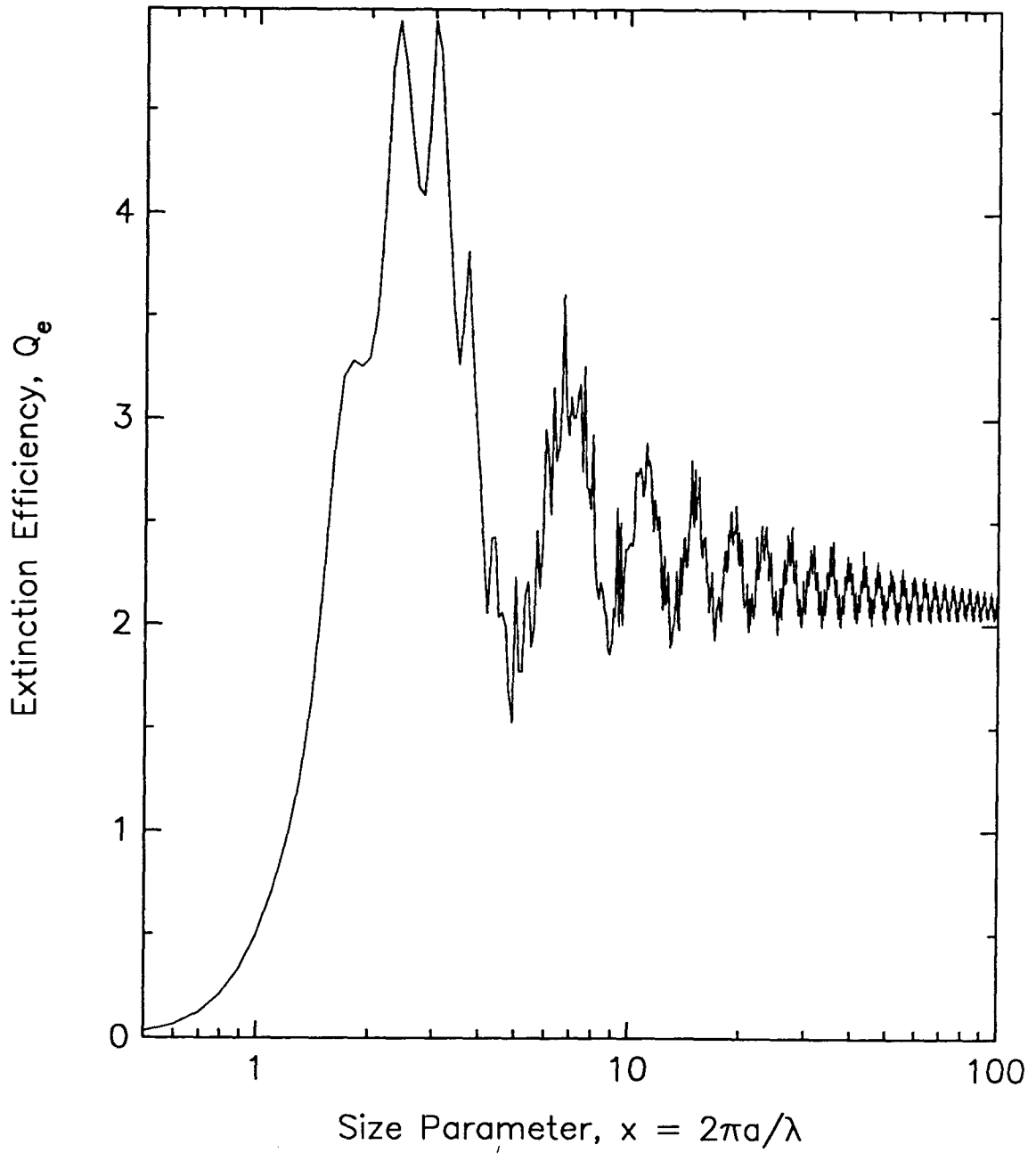

Figure 5.2: Extinction efficiency, Q_e, for a single water ice sphere as a function of the size parameter, x. The refractive index is $m = 1.78 - i0.00001$.

maxima and minima are due to interference by the light diffracted and transmitted by the particle. The slight ripple is due to edge rays grazing the sphere. However, a slight absorption in the particle, or a dispersion in particle sizes, tends to wash out the ripples in the extinction curve. For large x, Q_e asymptotically approaches 2. This is a consequence of Babinet's principle, which states that in the geometrical optics limit, a particle intercepts an amount of energy equal to its geometrical cross-section, while also diffracting an equal amount of the incident energy (van de Hulst, 1957). As a result, the total amount of energy removed from the incident field is exactly *twice* the particle cross-section.

We are primarily interested in the ring particle scattering of unpolarized thermal emission by Saturn. In this case, the Stokes vector of unpolarized light scattered by spheres or an ensemble of randomly oriented particles contains just the first two terms, $\mathbf{I} = \{I, Q, 0, 0\}$. These two terms can be described by just two elements of the phase matrix, P^{11} and P^{21}. These are the phase function for unpolarized light and linearly polarized light, and correspond to the I and Q Stokes parameters. These two components can be written in terms of the amplitude functions:

$$P^{11} = \frac{2\pi}{k^2\sigma_s}(S_1 S_1^* + S_2 S_2^*), \tag{5.19a}$$

$$P^{21} = \frac{2\pi}{k^2\sigma_s}(S_1 S_1^* - S_2 S_2^*). \tag{5.19b}$$

The sign of P^{21} differs from the conventional definition but is consistent with the convention used here that the Q Stokes polarization is positive for linear polarization perpendicular to the scattering plane.

The angular distribution of the amplitude of the scattered polarized and unpolarized light is then described entirely by the phase functions. Figure 5.3 shows the angular functions for an ice sphere of size parameter $x = 1$. The unpolarized component shows a distinct forward lobe, due to the diffracted component and typical of scattering from large particles, as well as a slight backscatter peak. The polarization is a maximum at intermediate angles, which is almost entirely due to the first scattering event from the exterior of the particle. Figure 5.4 shows the angular scattering functions for a larger sphere of size parameter $x = 10$. The unpolarized light shows several peaks and resonances due to "rainbows" and glories. The polarization is oscillatory, with both positive and negative peaks.

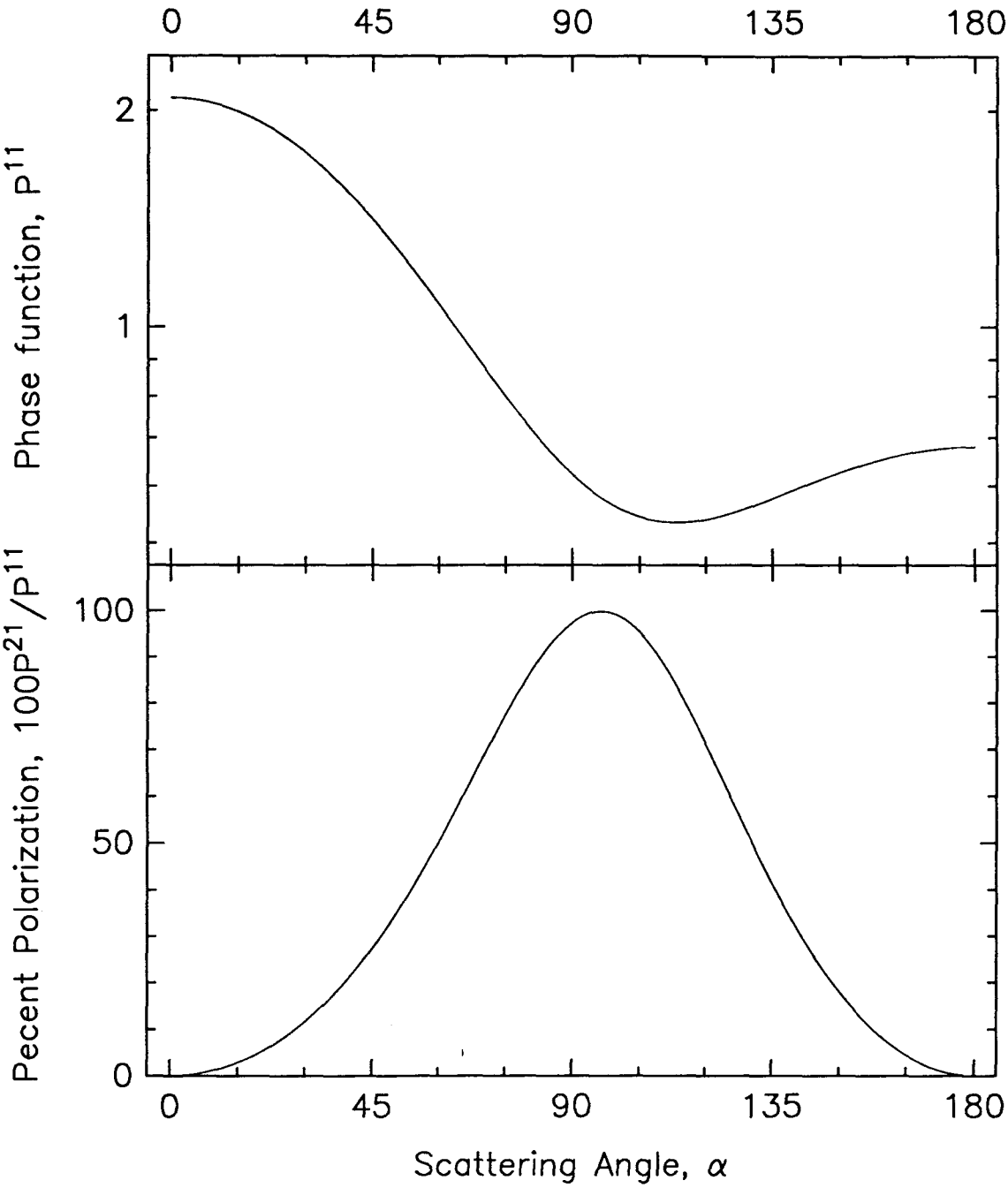

Figure 5.3: Phase functions and percent polarization for single scattering of unpolarized light. The size parameter is $x = 1$ and the refractive index is that of an ice sphere, $m = 1.78 - i0.0001$.

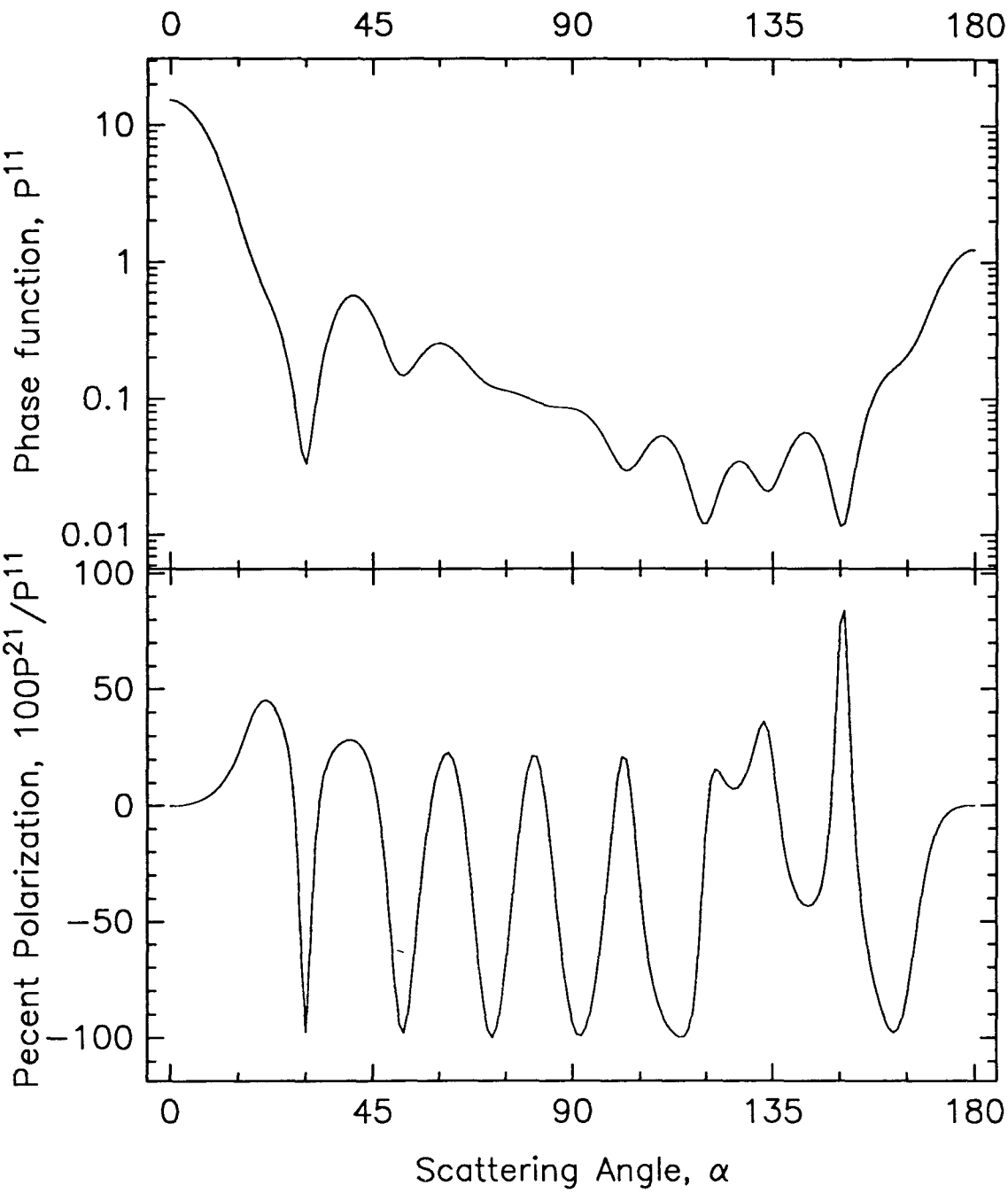

Figure 5.4: Phase functions and percent polarization for single scattering of unpolarized light. The size parameter is $x = 10$ and the refractive index is that of an ice sphere, $m = 1.78 - i0.0001$.

5.1.4 Scattering by an ensemble of particles

The particles in Saturn's rings most naturally follow a power-law size distribution (Marouf *et al.*, 1983). Therefore we consider particle size distributions of the form

$$n(a) = n(a_0)\left(\frac{a}{a_0}\right)^{-q}, \quad a_{\min} \leq a \leq a_{\max}, \tag{5.20}$$

otherwise $n(a) = 0$, where q is the power-law index and $a_{\min}$ and $a_{\max}$ are the lower and upper size cutoffs. By this definition, $n(a)da$ is the number of particles per unit column with radius between a and $a + da$.

Under the assumption of independent scattering, the elements of the scattering phase matrix are given by integrating the amplitude functions over the size distribution. For example,

$$P^{11} = \frac{2\pi}{k^2\sigma_s}\int_{a_{\min}}^{a_{\max}}(S_1S_1^* + S_2S_2^*)n(a)da, \tag{5.21}$$

where the functions S_1 and S_2 depend on a through the size parameter, x. The primary effect of the integration over sizes is to average out the oscillations in the phase functions (Liou and Hansen, 1971).

Figure 5.5 shows the scattering phase functions for scattering from a distribution of ice spheres with size $1 \leq x \leq 100$ and power-law index $q = 3$. The unpolarized intensity is sharply peaked in the forward direction but continues to show the backscatter peak as well. However, all indications of resonance phenomena, such as rainbows have disappeared. The percent linear polarization is mostly negative, however, the polarization should be studied along with the gain. For example, the positive polarization at small scattering angles does not appear prominent, but it can be very important because of the large energy in that component. In general, the polarization is very sensitive to the size distribution because the different oscillating components associated with different size particles can overlap to cause unusual polarizations.

5.2 Thermal Emission

The thermal emission from Saturn's rings at radio wavelengths is governed by several factors: the physical temperature of the ring, the absorption coefficient of the ring material, and the total path length for emission. These values are in turn related to the composition of the ring particles and to the relevant length scale on the order of the ring

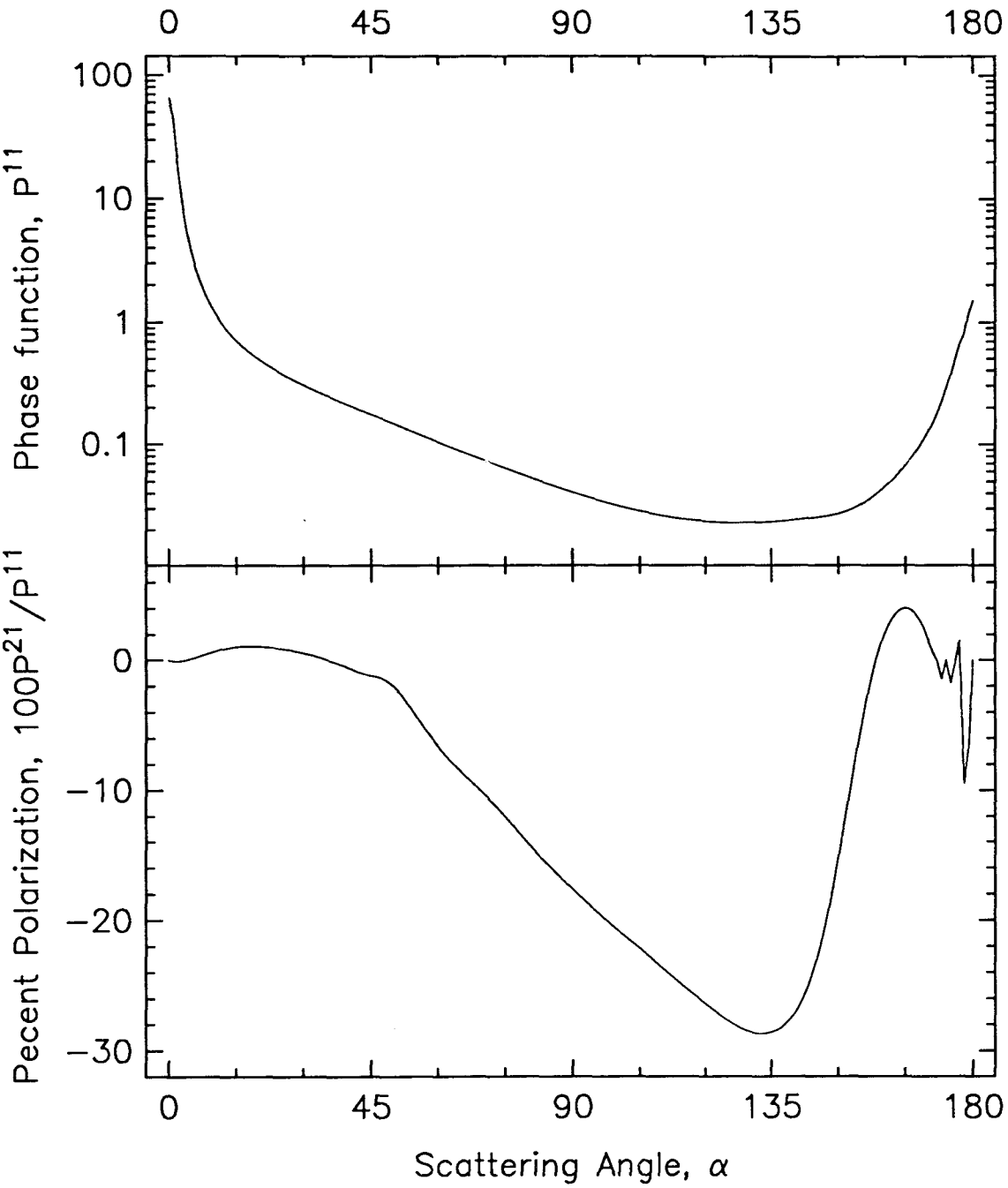

Figure 5.5: Phase function and percent polarization for single scattering from a power-law size distribution of the form $n(x) \propto x^{-3}$ for $1 < x < 100$. The size parameter is $x = 2\pi a/\lambda$ and the refractive index is that of an ice sphere, $m = 1.78 - i0.0001$.

thickness or the size of the largest particles in the rings. On a longer time-scale, the thermal emission may also change due to variations in the physical temperature of the ring particles brought about by changes in insolation (Kawata, 1983; Froidevaux, 1981).

5.2.1 Slab model of thermal emission

The simplest model for thermal emission from the rings consists of the uniform slab model (Briggs, 1974; Janssen and Olsen, 1978; Epstein *et al.*, 1980; Muhleman and Berge, 1982). The ring is replaced by a uniform, rough layer of thickness z, optical depth τ, and physical temperature T_0. The thermal emission from such a layer, in terms of the brightness temperature, is given by

$$T_B = T_0 \alpha z (1 - e^{-\tau/\sin|B|}), \tag{5.22}$$

where α is the absorption coefficient of ice from Eq. 5.2. We can then place an upper limit on the average "thickness" of the slab by assuming that the observed brightness at 0.27 cm is entirely due to thermal emission. We take $T_0 = 85$ K, $T_B = 16.7$ K, $\tau/\sin|B| = .72$, and $\alpha = 6 \times 10^{-3}$ cm^{-1}. This yields an estimated upper limit to the mean particle size of

$$z \leq 64 \pm 14 \text{ cm}. \tag{5.23}$$

This estimate is consistent with current knowledge of particle sizes in Saturn's rings and previous determinations by similar methods (Janssen and Olsen, 1978; Schloerb *et al.*, 1979a), but is at best a crude approximation. Next we consider a more detailed model of emission by a size distribution of particles.

5.2.2 Thermal emission by a distribution of particles

The thermal emission by an isothermal layer of ring particles can be derived by first considering the absorption of a photon incident on a layer of particles of optical depth τ at an angle B. The probability for traveling through the layer, a distance of $\tau/\sin|B|$, and not being absorbed or scattered is $e^{-\tau/\sin|B|}$, while the probability for interacting with the particles, by either being absorbed or scattered, is $(1 - e^{-\tau/\sin|B|})$. Of the fraction of photons that interact with a particle, the single scattering albedo, ϖ, indicates the probability for scattering. Thus, the quantity $(1 - \varpi)$ is the probability for absorption. The

joint probability for absorption is then the product $(1-\varpi)(1-e^{-\tau/\sin|B|})$, which is equal to the probability for emission by Kirchhoff's theorem. Thus, the net emission from a thin layer of ring particles, including scattering, is given by:

$$T_E = T_0(1-\varpi)(1-e^{-\tau/\sin|B|}), \tag{5.24}$$

where T_0 is the physical temperature of the rings.

The behavior of the model described by Eq. 5.24 is investigated by calculating the efficiencies for scattering and extinction of a power-law size distribution of varying mixtures of ice and rock spheres. The Mie scattering calculations for an ensemble of particles are used (§5.1.4). The size distribution follows the form of Eq. 5.20 and the dielectric properties are described in table 5.1.

We first model the thermal emission from the combined A and B ring using an optical depth of $\tau = 0.8$. Figure 5.6 shows the observed brightness temperature of the combined ring from this work and others (see §3.2.3) and the thermal emission spectrum for four power-law size distributions of dirt-ice spheres of radius $a < 100$ cm, as suggested by Cuzzi *et al.*(1980). The results of the models are summarized in table 5.2. At this point it is not possible to discriminate between the models, because the scattered component of the radiations has not been included in the models. Therefore, detailed comparison between the model results and the observations is postponed until the following section. Nevertheless, some qualitative comparisons can be made.

The first curve shows the model result for a pure ice distribution of particles with a $q = 2.6$ power-law exponent. Clearly, the brightness predicted by this model is too low to match the observation. The remaining curves illustrate attempts to increase the brightness of the model, while still maintaining a maximum particle size of 100 cm. The second curve, for a lower particle size limit of 10 cm, shows a slight increase in brightness. However, as examined in section 5.4, the optical depths observed at the cusp suggest a low particle limit in the neighborhood $\sim$ 1 cm. The third curve shows the effect of adding 2% mass fraction silicates to the ice particles. The result is a dramatic increase in brightness at all wavelengths. Our observations at 2.01 cm are especially sensitive to this change. The fourth and final model shows the effect of increasing the silicate mass fraction to 5% accompanied with a change in the power-law. Clearly the upper particle size limit must be increased beyond 100 cm to match the observations.

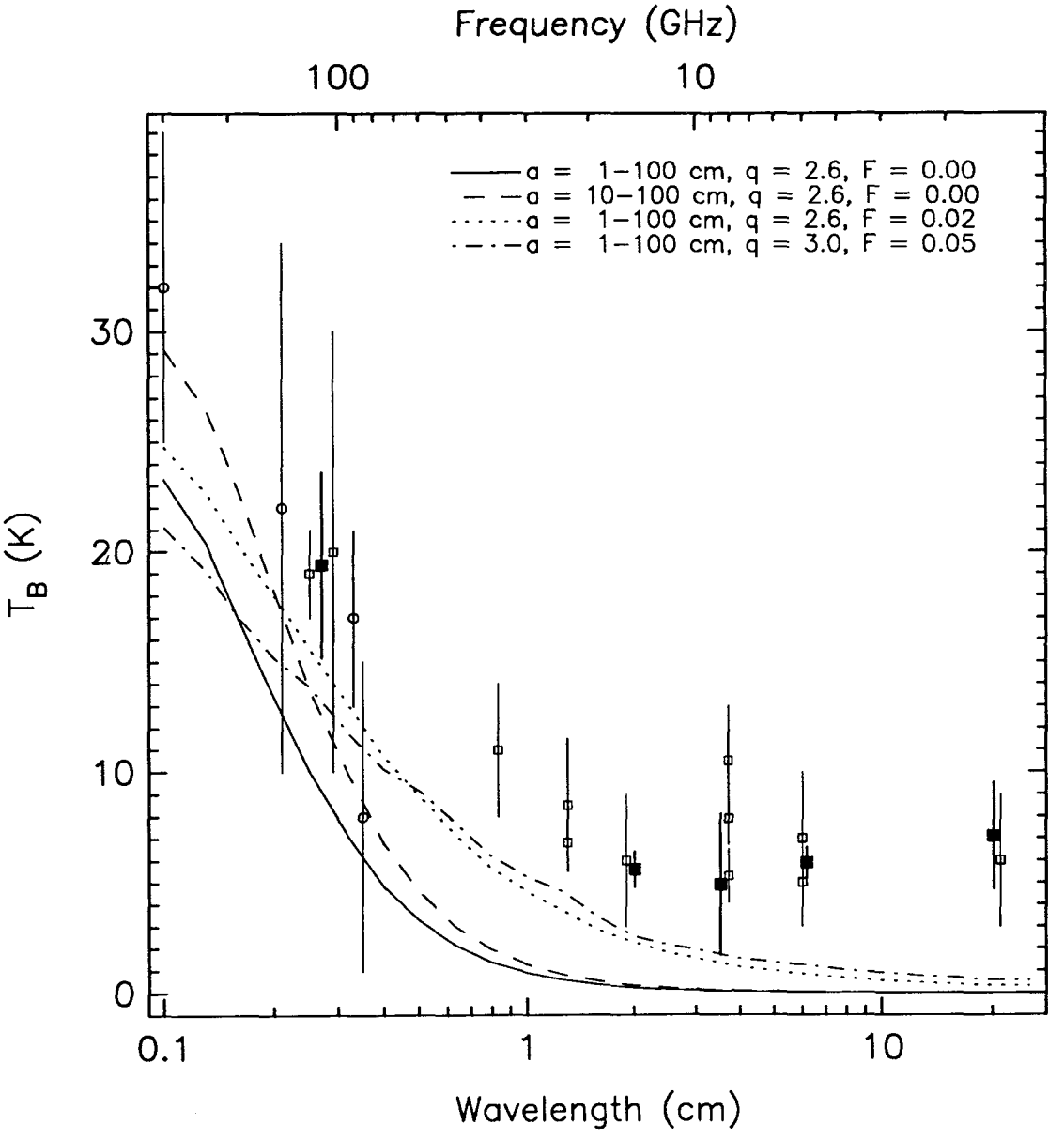

Figure 5.6: Thermal emission spectra of rock-ice spheres with radius a, described by a power-law size distributions of the form $n(a) \propto a^{-q}, where a < 100$ cm. F indicates the fractional mass of uniformly mixed silicates. Squares represent disk-resolved interferometer observations of the combined A+B ring brightness while circles represent single-dish observations that have been corrected to remove the influence of the rings. Solid squares are the new data of this work.

Table 5.2: Thermal emission models for the combined A+B ring.

Model	a_{min}–a_{max}[1] (cm)	q	F[2]	Brightness Temperature T_B at λ_{cm} 0.27 cm	2.01 cm	3.53 cm	6.17 cm	20.13 cm
Observed:				19.4 ± 4.2	5.6 ± 0.8	4.9 ± 3.2	5.9 ± 0.7	7.1 ± 2.4
Models:								
A	1–100	2.6	0.00	9.0	0.2	0.1	0.0	0.0
B	10–100	2.6	0.00	12.4	0.3	0.1	0.0	0.0
C	1–100	2.6	0.02	14.8	2.3	1.3	0.8	0.2
D	1–100	3.0	0.05	13.3	2.5	1.7	1.2	0.6
E	1–500	2.6	0.00	18.9	1.0	0.3	0.1	0.0
F	1–500	3.0	0.00	10.9	0.4	0.2	0.1	0.0
G	1–500	3.0	0.01	13.1	2.2	1.3	0.9	0.4
H	1–500	3.0	0.02	14.6	3.6	2.3	1.6	0.7

[1]Lower and upper size cutoff
[2]Mass fraction silicates

The Voyager radio occultation experiment has obtained size distributions with particles in the range 0.01 – 15 meters for several specific regions in the A and C rings. We next consider particles up to 500 cm in size. Figure 5.7 shows model results for four size distributions of dirt-ice spheres with $a < 500$ cm, as summarized in table 5.2. Brightness temperatures are increased with respect to the previous set of models. We return to these models after considering the scattered radiation from the rings.

5.3 Scattered Radiation

The microwave radiation emitted by Saturn and scattered by the rings contributes greatly to their brightness. In this section we construct a model of the ring brightness due to diffuse scattering of planetary emission. The scattering is treated according to the Mie theory and applied to a power-law size distribution of particles.

The computation is complicated by the geometry of the incident and scattered radiation, and the uncertainty in the scattering phase function applicable to the ring particles. Therefore, two different models are developed to compare with the data. First, we introduce a simplified model consisting of isotropic scatterers, and use the results as an estimate of the mean diffuse brightness of the rings. We also develop an empirical scattering model, including polarization, which matches the azimuthal brightness of the rings. Both models are used to analyze and interpret the data presented in chapter 3.

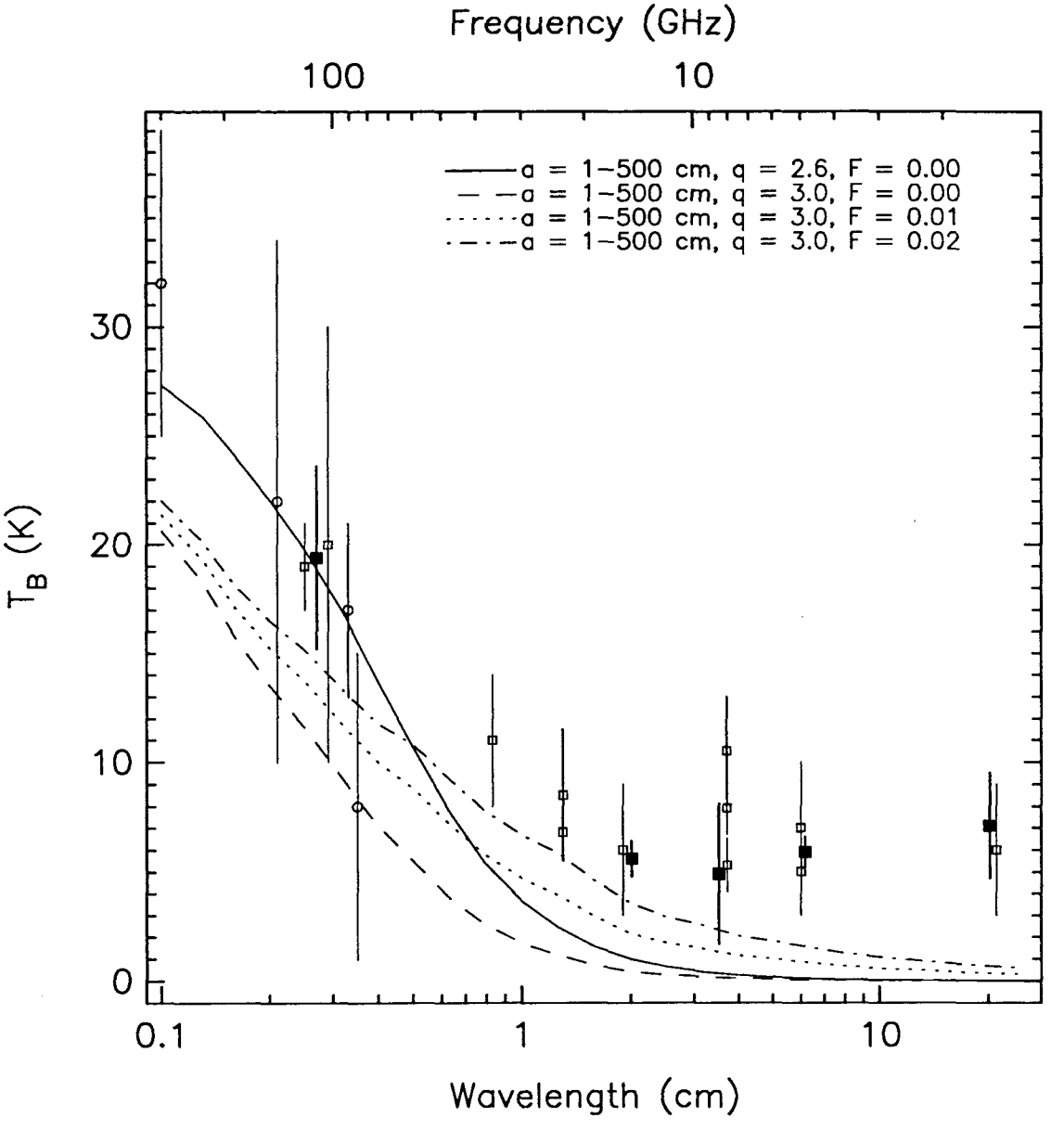

Figure 5.7: Thermal emission spectra of rock-ice spheres with radius a, described by a power-law size distributions of the form $n(a) \propto a^{-q}, where a < 500$ cm. F indicates the fractional mass of uniformly mixed silicates. Squares represent disk-resolved interferometer observations of the combined A+B ring brightness while circles represent single-dish observations that have been corrected to remove the influence of the rings. Solid squares are the new data of this work.

In the following calculations, multiple scattering has been neglected. The importance of multiple scattering in Saturn's rings depends on the optical depth of the ring and on the scattering phase function. For small optical depths and near-isotropic phase functions, multiple scattering can be neglected (Cuzzi *et al.*, 1984). Furthermore, the observation of polarized radiation provides direct evidence of significant single scattering rather than multiple scattering. Hansen (1971) has shown that the primary effect of multiple scattering is to reduce the magnitude of polarization; the zero points of polarization remain fixed (Hansen, 1971). Nevertheless, comparison is made with the multiple scattering results of Cuzzi *et al.* (1980) applied to Saturn's rings. In addition, the minor effect of multiple scattering on the results derived from single scattering is easily estimated. The primary effect of multiple scattering on the unpolarized intensity is to reduce secondary resonance effects such as rainbows and halos. However, this is already occurring, because integration over a size distribution and over the extended source function of Saturn has a similar effect. The relevant point for this discussion is that the angular distribution remains the same, neglecting multiple scattering.

5.3.1 Scattering formulation

In order to simplify the radiative transfer calculation, the ring is approximated by a plane-parallel layer of optical thickness τ. Consider an arbitrary point P on the surface of the ring at a radial distance ρ from the center of the planet. In the Rayleigh-Jeans limit, we can write the illumination this point receives from a small patch on the surface of Saturn in terms of the brightness temperature T_P:

$$T_P = \frac{T_D \cos\gamma}{d^2}, \tag{5.25}$$

where T_D is the disk brightness of Saturn, γ is the emission angle at Saturn measured with respect to the outward normal, and d is the linear distance between the selected point on the planet and P. Let the angle measured at the center of Saturn between these two points be denoted δ. Then, using planar trigonometry, we have

$$d = (\rho^2 + R^2 - 2\rho R\cos\delta)^{\frac{1}{2}}, \tag{5.26}$$

and

$$\gamma = \arcsin\left[\rho\sin(\delta/d)\right]. \tag{5.27}$$

The incident radiation arriving at point P is partially reflected and transmitted and the observed brightness temperature is given by

$$T_R = \frac{T_D \varpi \cos\gamma}{4d^2} S(\mu_0, \mu, \alpha), \quad \mu_0 > 0, \tag{5.28a}$$

$$T_R = \frac{T_D \varpi \cos\gamma}{4d^2} T(\mu_0, \mu, \alpha), \quad \mu_0 < 0, \tag{5.28b}$$

where S and T are the diffuse reflectivity and transmissivity functions characterizing the medium (Cuzzi *et al.*, 1984). In addition, μ_0 is the cosine of the angle of incidence at P with respect to the outward normal to the ring plane, μ is is the cosine of the angle of reflection with respect to the outward normal, and α is the scattering angle. Because our vantage point is on the Earth, the parameter μ is taken equal to B, the saturnocentric latitude of the Earth.

For an optically thin ring, or for low-albedo particles, or for grazing illumination, multiple scattering can be neglected. The reflectivity and transmissivity then take the simple form:

$$S = \left(\frac{\mu_0 + \mu}{\mu_0 \mu}\right)\left(1 - e^{-\tau/\mu_0 - \tau/\mu}\right) P(\alpha), \tag{5.29a}$$

$$T = \left(\frac{\mu_0 + \mu}{\mu_0 \mu}\right)\left(e^{-\tau/\mu_0} - e^{-\tau/\mu}\right) P(\alpha), \tag{5.29b}$$

where $P(\alpha)$ is the scattering phase function (Chandrasekhar, 1960). $P(\alpha)$ must satisfy Eqs. 5.14 and 5.15.

The total brightness of the scattering radiation from any point on the ring surface may then be obtained by integrating the relevant source function over the disk of Saturn.

To formulate the integral, each point on the surface of the disk is specified in a spherical polar coordinate system. The origin is at the center of Saturn, and the rotation axis is the line joining the center of the planet to the ring point. The angular distance of a point on the surface of Saturn is measured by the angle δ. Values for δ cover the range

$$0 \leq \delta \leq \arcsin(\frac{\rho}{R}). \tag{5.30}$$

The angular rotation of a point about the rotation axis is specified by angle λ. Values for λ lie in the range

$$0 \leq \lambda \leq \pi \quad \text{in the northern hemisphere,} \tag{5.31a}$$

$$\pi \leq \lambda \leq 2\pi \quad \text{in the southern hemisphere.} \tag{5.31b}$$

The cosine of the incidence angle at point P from a point on the disk at (δ, λ) is given by:

$$\mu_0 = \sin(\gamma - \delta) \sin \lambda. \tag{5.32}$$

The integral describing the total brightness of the ring point is

$$T_B = \int_0^{2\pi} \int_0^{\arcsin(\rho/R)} T_R R \sin \delta d\delta d\lambda. \tag{5.33}$$

The integral is evaluated numerically in a 100×60 grid.

5.3.2 Isotropic scattering

The integrated brightness of the rings is modeled in this section by an isotropic scattering phase function. This approximation seems justified when modeling the integrated brightness averaged over all angles. Furthermore, the azimuthal variations in ring brightness shown in figure 5.11 suggest that this approximation is valid for at least the A and B rings. Ultimately the validity of the model depends on how well it can explain the data.

As in the model for the thermal emission, we consider the combined A and B rings, and use an optical depth of 0.8. The scattered emission is shown in fig. 5.8 for four models. The general shape of the scattered component of the ring radiation follows the shape of Saturn's own thermal emission spectrum, and reproduces the local minimum near 1.25 cm. All four models show a similar spectrum for a different range of particle sizes and power laws. This is not unusual, because the scattering efficiency depends primarily on the cross section, which asymptotically approaches a value of 2 for large, non-absorbing particles. One can only discriminate between the models at the shortest wavelength, where the particles become slightly lossy.

5.3.3 Combined thermal emission and isotropic scattering

In this section, the results of modeling the thermal emission of Saturn's rings and the isotropically reflected diffuse radiation are combined. The results are used to constrain the particle properties. The models are summarized in table 5.3. Figure 5.9 shows the results for models with particle radii smaller than 100 cm. The model that best fits the data has a lower particle size limit of 10 cm. However, this result can be ruled out on the basis of the optical depths discussed in §5.4, and the results of the Voyager radio occultation

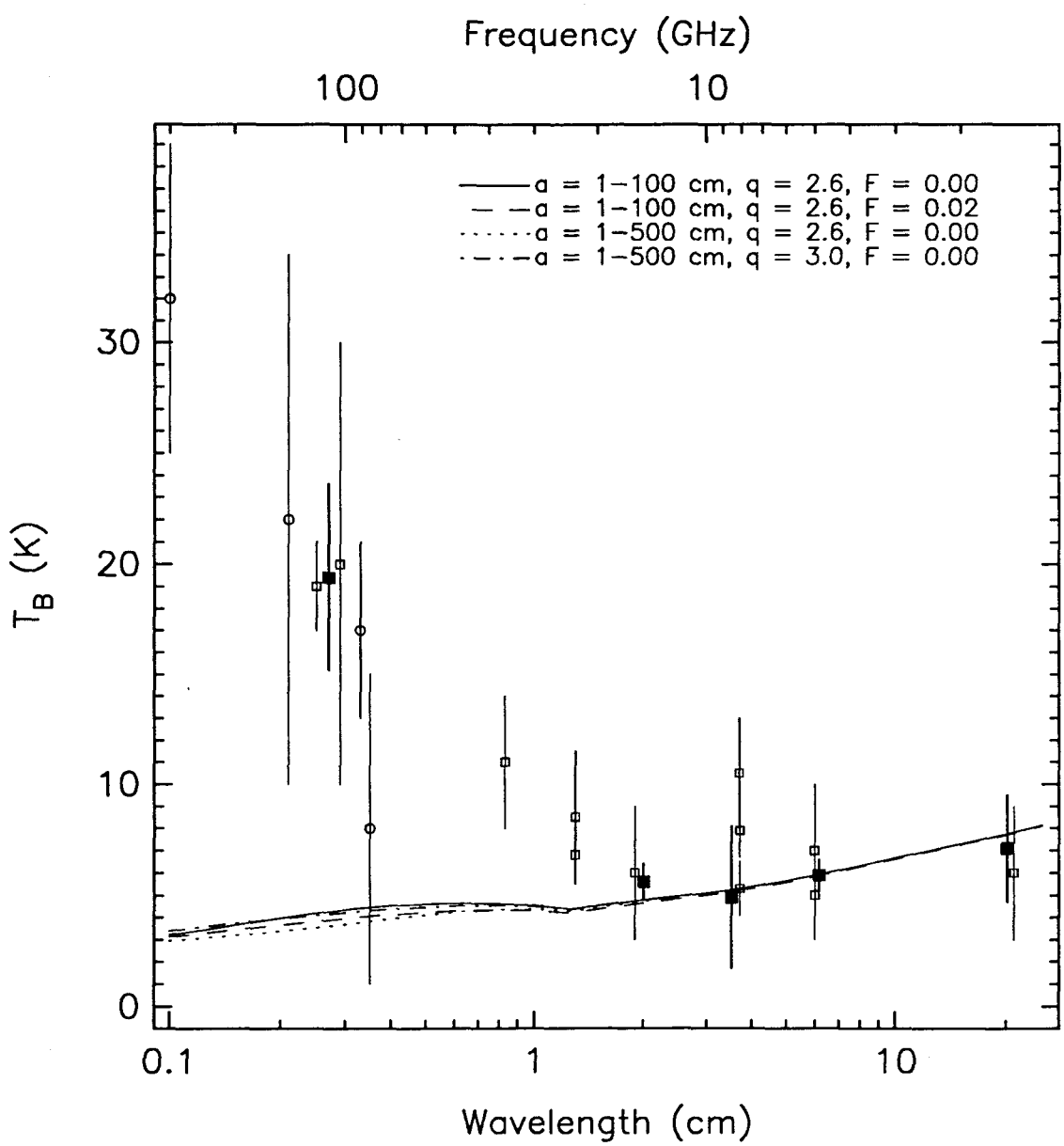

Figure 5.8: Diffusely scattered radiation models for Saturn's combined A+B rings. The models are from Mie calculations of isotropic scattering from rock-ice spheres of radius a, described by a power-law size distribution of the form $n(a) \propto a^{-q}$. The source function is the thermal spectrum of Saturn. F indicates the fractional mass of uniformly mixed silicates. Squares represent disk-resolved interferometer observations of the combined A+B ring brightness while circles represent single-dish observations that have been corrected to remove the influence of the rings. Solid squares are the new data of this work.

(Tyler *et al.*, 1983), which showed a significant number of centimeter size particles in the A ring.

Table 5.3: Model ring brightness calculations due to intrinsic thermal emission and isotropic scattering from a power-law size distribution of rock-ice spheres for the combined A+B ring.

Model	a_{min}–a_{max}[1] (cm)	q	F[2]	Brightness Temperature T_B at λ_{cm} 0.27 cm	2.01 cm	3.53 cm	6.17 cm	20.13 cm
Observed:				19.4 ± 4.2	5.6 ± 0.8	4.9 ± 3.2	5.9 ± 0.7	7.1 ± 2.4
Models:								
A	1–100	2.6	0.00	13.3	5.0	5.3	5.9	7.8
B	10–100	2.6	0.00	16.4	5.1	5.3	5.9	7.8
C	1–100	2.6	0.02	18.7	7.0	6.5	6.7	7.9
D	1–100	3.0	0.05	17.3	7.1	6.8	7.0	8.3
E	1–500	2.6	0.00	22.5	5.7	5.5	6.0	7.8
F	1–500	3.0	0.00	15.0	5.2	5.4	6.0	7.8
G	1–500	3.0	0.01	17.1	6.9	6.4	6.8	8.1
H	1–500	3.0	0.02	18.5	8.1	7.4	7.4	8.4

[1]Lower and upper size cutoff
[2]Mass fraction silicates

Next we consider the results for models consisting of larger particles. Figure 5.10 shows the model results for size distributions with particles as large as 5 meters. The data point at 0.27 mm seems to be the most discriminating with regard to the power-law for the size distribution, and favors an exponent in the range $2.6 < q < 3.0$. The centimeter wavelength data points are relatively insensitive to this parameter. On the other hand, the centimeter points, especially at 2.01 cm, are sensitive to the addition of silicates to model particles. There is clearly a tradeoff between the power-law exponent and the mass fraction of silicates, F. However, even values of F as low as 1% are ruled out by the observations at 2.01 cm. It is interesting to note that the net brightness due to thermal emission and diffusely scattered radiation exhibits a minimum in the range 2-4 cm.

5.3.4 Side scatter

We now turn to the puzzling subject of the azimuthal variations in Saturn's rings initially presented in section 3.4.2. Although the variations in ring brightness have been predicted for some time (Cuzzi and van Blerkom, 1974; Muhleman and Berge, 1982), this work presents the first direct evidence for the variation of both ring brightness and polarization

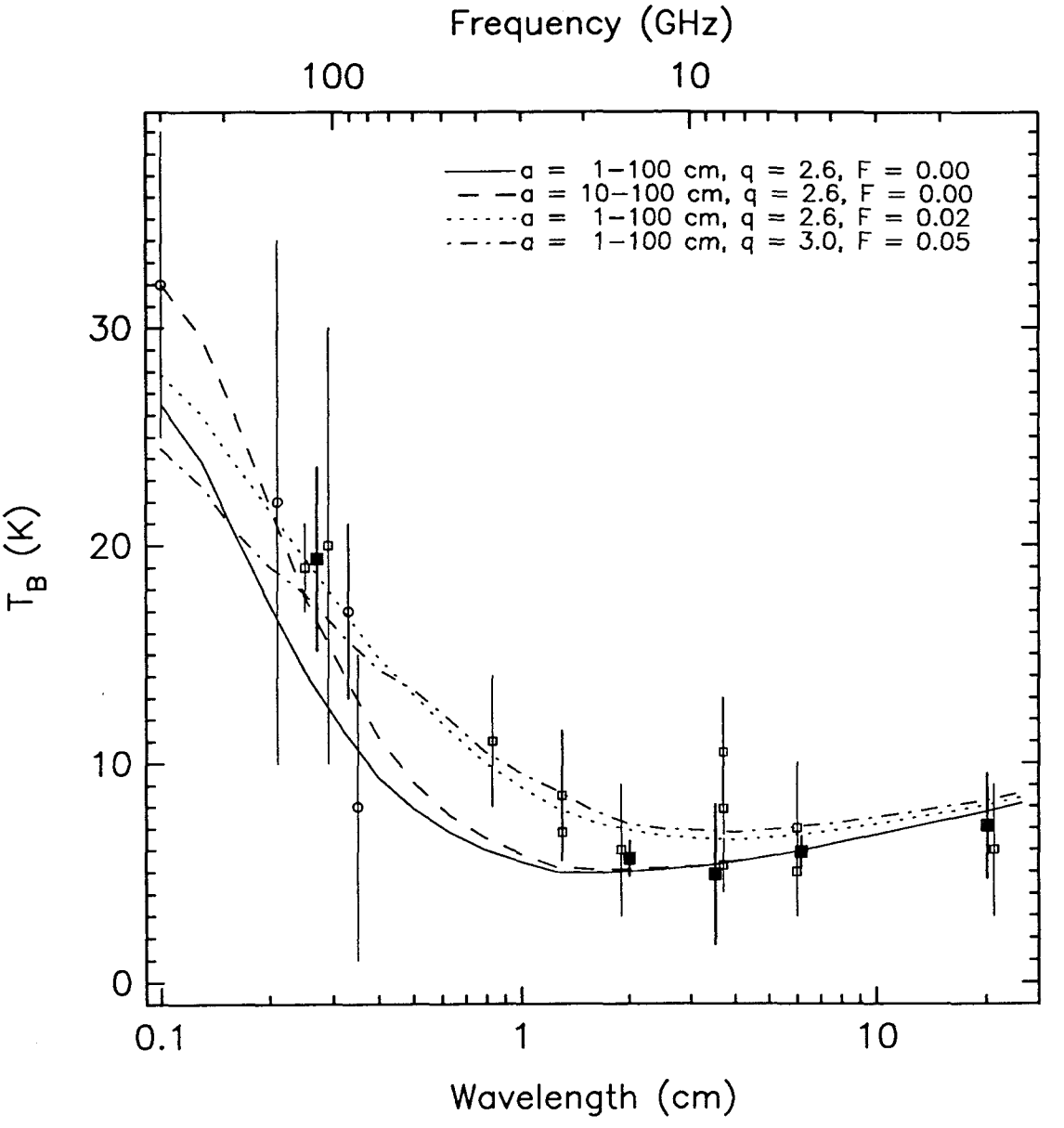

Figure 5.9: Thermal emission and diffusely scattered radiation models for Saturn's combined A+B rings. The models are from Mie calculations of isotropic scattering from rock-ice spheres of radius a, described by a power-law size distribution of the form $n(a) \propto a^{-q}$. The source function is the thermal spectrum of Saturn. F indicates the fractional mass of uniformly mixed silicates. Squares represent disk-resolved interferometer observations of the combined A+B ring brightness while circles represent single-dish observations that have been corrected to remove the influence of the rings. Solid squares are the new data of this work.

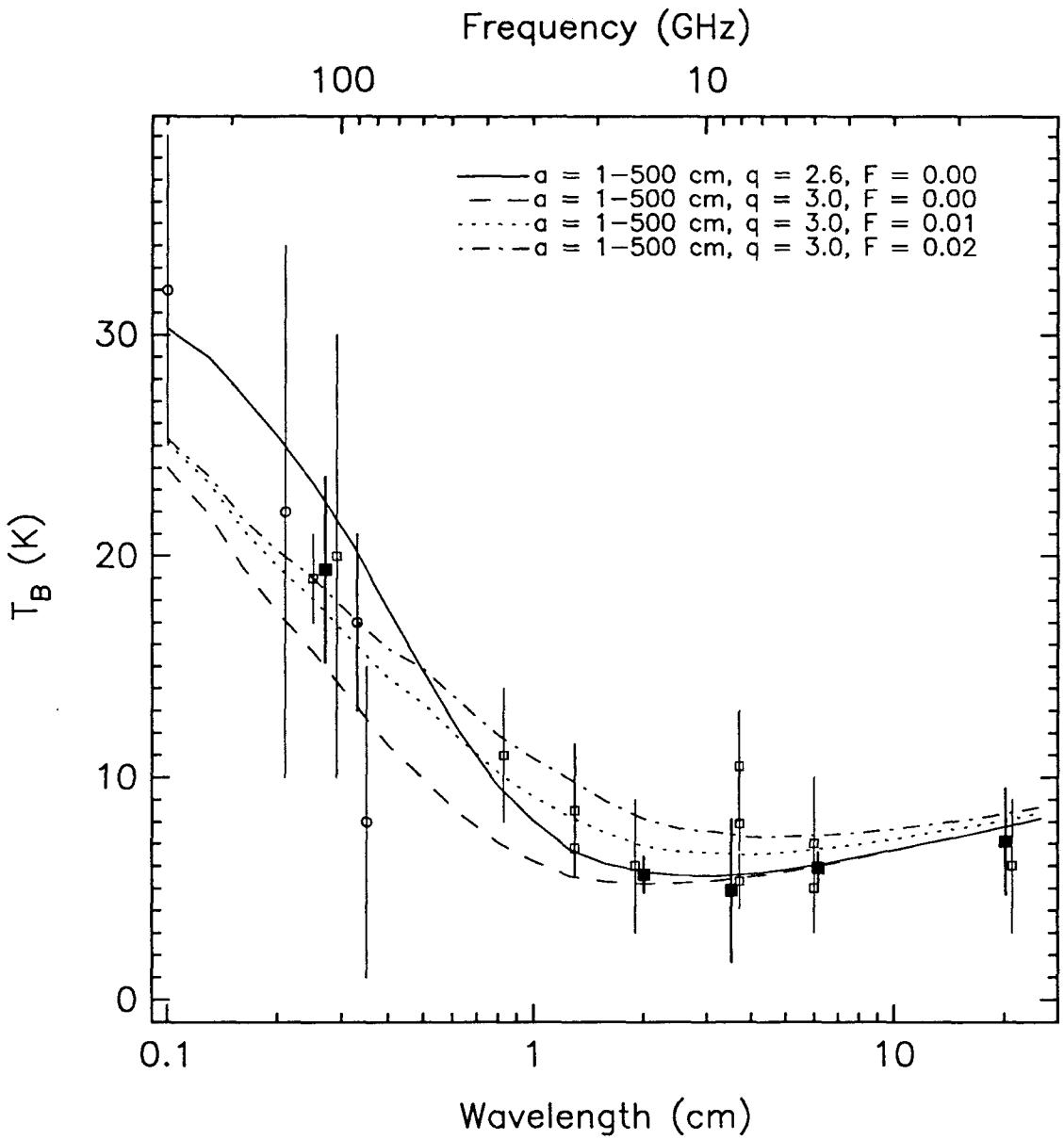

Figure 5.10: Thermal emission and diffusely scattered radiation models for Saturn's combined A+B rings. The models are from Mie calculations of isotropic scattering from rock-ice spheres of radius a, described by a power-law size distribution of the form $n(a) \propto a^{-q}$. The source function is the thermal spectrum of Saturn. Squares represent disk-resolved interferometer observations of the combined A+B ring brightness while circles represent single-dish observations that have been corrected to remove the influence of the rings. Solid squares are the new data of this work. The observations favor a model containing a power-law size distribution of nearly pure ice spheres with radii $1 < a < 500$ cm and power-law index $q = 2.6$–3.0.

with azimuth.

The results of the previous section show quite clearly that the thermal emission from the rings rapidly diminishes for wavelengths greater than a few centimeters. On the other hand, the diffusely scattered component of brightness increases with wavelength; the crossover point being at slightly less than 1 cm. It is therefore expected that at centimeter wavelengths, the angular variations in ring brightness bear some relation to the scattering phase function of the individual particles at intermediate scattering angles. Because the geometry of scattering from a particle at the ring ansea requires integrating the source function over a large range of angles, specific angular features of the phase function are expected to be washed out.

In this context, observations of the centimeter brightness variations of Saturn's rings present a natural scattering experiment. However, this is by no means the first such scattering experiment on Saturn's rings. The Voyager radio occultation observed the forward diffraction lobe of radiation scattered from the rings (Zebker *et al.*, 1983). Similarly, radar observations of Saturn's rings have obtained information on the cross-section for backscatter (Goldstein and Morris, 1973; Ostro *et al.*, 1982). Passive microwave observations complement these two methods by sampling the scattering phase function at intermediate angles; a method referred to as "side scatter."

The radiation scattered at intermediate angles contains distinct and unique information about the particles. Whereas the forward diffraction peak and the radar backscatter are sensitive to particle sizes and cross-sections, the radiation scattered at intermediate angles contains information about the particle *shape*. It is no surprise then that the assumptions of Mie calculations regarding spherical shape, which are useful for modeling the radio occultation and radar backscatter, may break down when used to model phenomena of side scatter. The significance of shape is clearly dependant on wavelength. Deviations from sphericity are negligible for particles smaller than a wavelength and can be adequately described entirely by Rayleigh scattering, regardless of shape. For large particles, the shape as well as the surface roughness is important. Since Mie theory cannot adequately describe the angular scattering from nonspherical particles, we consider an empirical approach.

5.3.5 Empirical scattering functions

In this section, the radiative transfer model developed in §5.3.1 is used to find a relationship between the observed azimuthal brightness variation and empirical angular scattering functions. The phase matrix elements P^{11} and P^{21} specify the angular scattering pattern for unpolarized and polarized radiation. The observations are compared with the empirical model by examining plots of unpolarized and polarized brightness as a function of mean scattering angle. The mean scattering angle is the supplement of the phase angle, which is the angle between Saturn, the ring particle, and the Earth. Comparison with the data is limited to the classical A, B, and C rings at wavelengths of 2.01, 6.17, and 20.13 cm by the intrinsic resolution in the images.

In studying the angular variations in ring brightness and polarization it is expected that some signature of the phase matrix of the individual particles remains after integration over the angles characterized by the source function of Saturn. This principle will serve as a reference to modeling the angular variations. In particular, the models should reproduce the general angular behavior of the observations, which are shown in figure 5.11 for reference. With the exception of the I Stokes parameter for the C ring, the angular brightness variations show remarkable symmetry about $\alpha = 90°$ for both unpolarized and linearly polarized brightness. Therefore, it is expected that the angular phase functions, P^{11} and P^{21}, reflect this symmetry. The unpolarized brightness (I Stokes) reaches a minimum at intermediate angles and peaks at small and large angles. In contrast, the linearly polarized component (Q Stokes) is a maximum at medium angles and approaches zero at small and large angles. The phase functions should exhibit similar characteristics.

The properties of the angular variations in ring brightness and polarization suggest that a phase function similar to the Rayleigh phase function for scattering from a single small particle may suffice. Figure 5.12 shows an empirical phase function derived from the Rayleigh phase function for a small particle. The intensity peaks in the forward and backward directions and reaches a minimum at 90°. The polarization has been decreased to a maximum of 25% at intermediate angles in order to match the observations. This phase function is applied to the radiative transfer model of Saturn's rings using nominal optical depths of 0.6, 1.0, and 0.1 for the A, B, and C rings. The results are plotted as lines on fig. 5.11 for comparison with the observations. A uniform brightness of 1.0, 0.1, and 0.0 K has been added at 2, 6, and 20 cm to account for the thermal emission component.

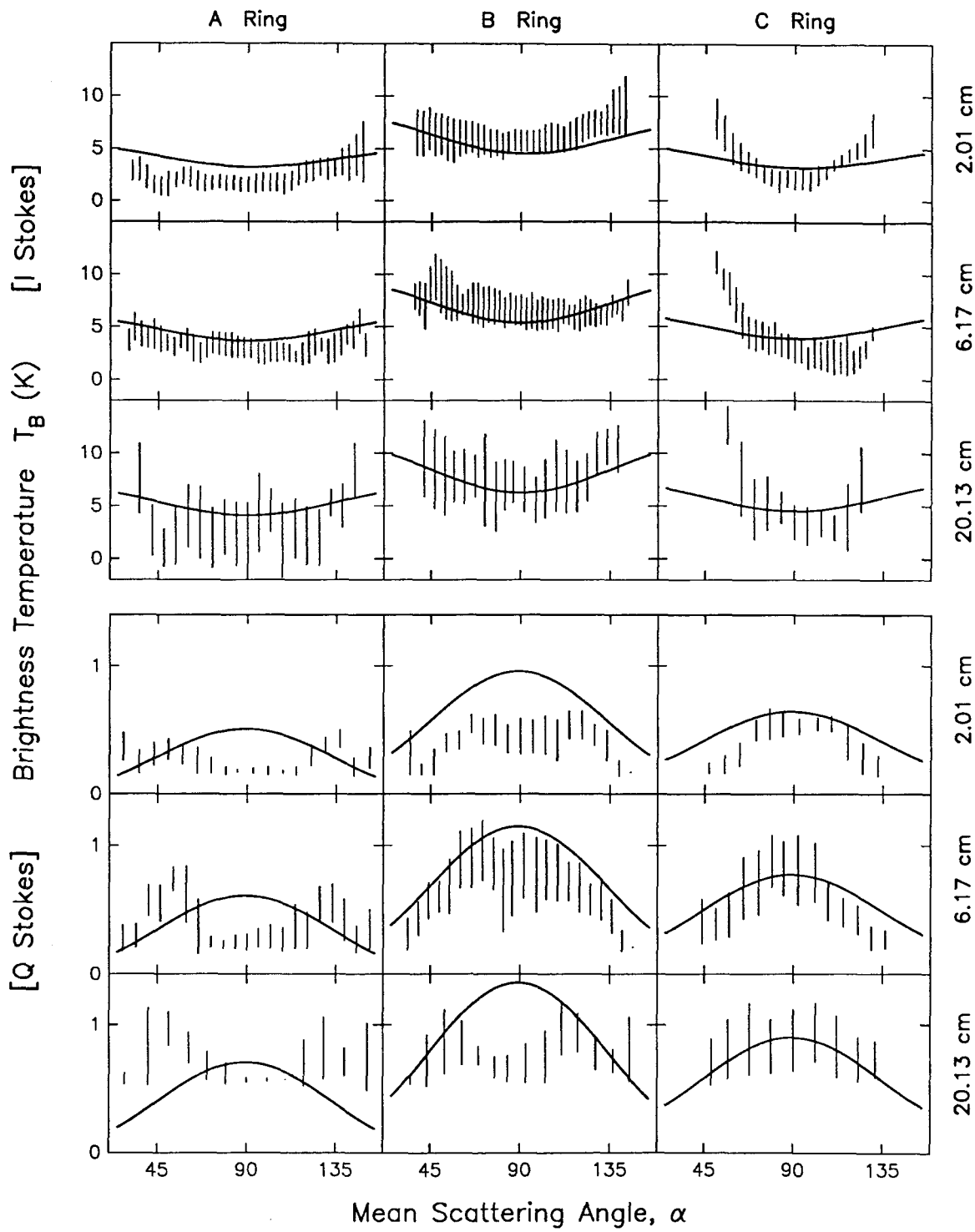

Figure 5.11: Ring brightness as a function of scattering angle for both I and Q stokes parameters. Error bars indicate the standard error based on scatter of the data. Solid lines are model results based on the phase function shown in fig. 5.12.

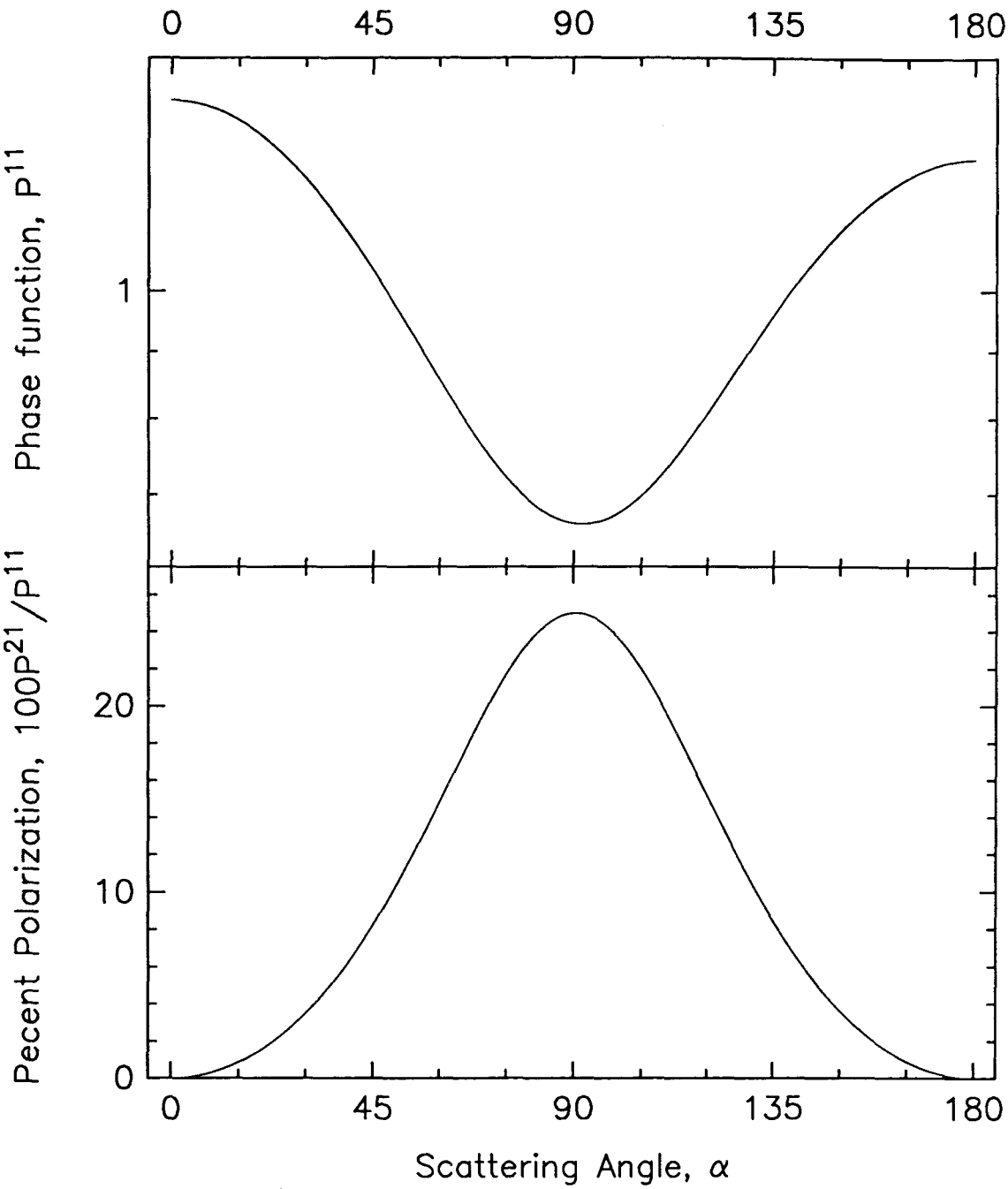

Figure 5.12: Phase function and percent polarization model that provides a reasonable fit to the observations.

Comparison of the empirical model results with the observations yields a reasonably good fit. The model phase function reproduces many of the properties of the observed brightness variations. However, the similarity between the model phase function and the Rayleigh phase functions does not necessarily mean that the scattering process is the result of scattering by small particles in the Rayleigh limit. Such a model requires that the particles be much smaller than the wavelength, $a << \lambda$. However, the Voyager radio occultation experiments and the radar observations of the rings rule out the existence of much mass contained in particles smaller than a centimeter. Furthermore, the current observations are inconsistent with the wavelength dependence of Rayleigh scattering which predicts that the intensity be proportional to $\sim 1/\lambda^4$. Although the phase function resembles the Rayleigh phase function, the scattered radiation from Saturn's rings is clearly not Rayleigh scattering from individual small particles.

The empirically-derived scattering function shown in fig. 5.12 invites some comparison with well-known and studied phase functions. Large spherical particles, especially size distributions of spherical particles, are not consistent with the empirical scattering function. The scattering phase function for an ensemble for a power-law size distribution of particles is illustrated in fig. 5.5. The phase function for unpolarized light, P^{11}, is characterized by a large forward peak, which contains much of the scattered energy in the form of a diffracted wave. A peak also occurs in the backscatter direction. Little energy is scattered at intermediate angles. The phase function for linear polarization, P^{21}, generally shows a negative polarization at intermediate angles, however there is little energy in this component. Such a phase function is clearly inconsistent with the observed angular variations of brightness in both Stokes parameters and the empirically derived scattering function.

Pollack and Cuzzi have developed a semi-empirical approach to characterize the scattering phase function of nonspherical particles (1980), and have subsequently applied their results to modeling the brightness of Saturn's rings (Cuzzi *et al.*, 1980). In this approximation the authors try to modify the Mie theory in definite size regions to account for the differences in scattering properties of spherical and nonspherical particles. Their results apply only to the unpolarized component, and indicate a sharp peak in brightness at forward azimuths and a minimum at azimuths $> 120°$. However, at the time of its development, this model lacked any observational constraints, and provides poor agreement with current observations. However, scattering from nonspherical particles invites further

investigation.

5.3.6 Scattering from nonspherical particles

In recent years it has become apparent that Mie theory cannot adequately describe the angular scattering behavior of nonspherical particles (Hodkinson, 1963; Zerull and Giese, 1974). The scattering phase function for irregular particles differs from that for spherical particles, especially at large scattering angles (Chýleck, 1976; Zerull *et al.*, 1977). Accurate numerical results for the scattering from nonspherical particles have been obtained for a limited number of specific cases. However, laboratory measurements of scattering from irregular particles are available and provide a basis from which some generalizations can be drawn (Schuerman, 1979).

The results of experimental measurements can be easily summarized as follows. The scattering behavior of spherical and irregular particles is similar at small angles, because this region is dominated by diffraction. As the size of the particle increases, the differences between spherical and non-spherical particles increase, especially at large angles. Depending on the size of the particles, nonspherical intensities can dramatically exceed spherical intensities in the side scatter region (Wiscombe and Mugnai, 1988). Most experimental studies find that the side scattering is not only larger, but flat, compared to spheres. The distinction is even more important for polarization.

Scattering is well known as the cause of polarization in many objects (Angel, 1974). In particular, polarization of sunlight scattered from Saturn's rings has been observed extensively (Dollfus, 1979a), and the depolarization of radar signals from the rings is also observed (Cuzzi and Pollack, 1978). However, these effects bear little relation to the observed linear polarization of scattered unpolarized light. The light scattered from an ensemble of large spheres is generally negatively polarized, as calculated by Mie theory. In contrast, unpolarized light scattered from rough or irregular particles shows either neutral polarization or, in some cases, positive linear polarization at large angles (Zerull *et al.*, 1977; Coffeen and Hansen, 1974) due to Fresnel reflection at the surface of properly oriented facets.

The empirical phase function shares some of the characteristics of rough, irregular particles. As is found for irregular particles, the forward peak is diminished and much energy is scattered at intermediate angles. Similarly, the polarization exhibits a broad

positive peak similar to scattering from irregular "fluffy" particles, which are aggregates of small particles (Zerull *et al.*, 1979). Although not really acting as individuals, the smaller constituents of the conglomerates preserve some of their individual features. The scattering from conglomerates can be understood by a simple theoretical approach.

The scattering from a randomly oriented conglomerate of particle can be crudely modeled by considering just three terms (Giese *et al.*, 1978). The first term takes into account diffraction by the whole particle. The second term considers just the external Fresnel reflection by appropriately oriented surface elements. The third term represents the combined effects of multiple reflection, refraction and internal scattering. For large particles, the diffraction term is restricted to small angles. The single Fresnel reflection is positively polarized and strong, compared to the refracted wave, for an absorbing particle. For a weakly absorbing particle, the radiation which enters the particle will contribute to the unpolarized component. This enhances the scattered intensity and lowers the polarization. Shadowing effects also need to be considered. The net effect of shadowing is to reduce the influence of the Fresnel reflection component.

Giese *et al.* (1978) have conducted microwave analog measurements on rough and irregular particles of both dense and fluffy configurations in an attempt to model the scattering behavior of interplanetary dust. Dense particles show a slightly enhanced backscatter compared to Mie calculations for spheres of equal volume. Furthermore, they show a positive polarization similar to that expected from Fresnel reflection. For weakly absorbing particles in a loose arrangement, the positive polarization is decreased in magnitude and the maximum is shifted towards $\alpha = 90°$, i.e., closer to the empirically derived scattering function for Saturn's rings. This suggests, by analogy, that the ring particles are loose conglomerates of particles rather than compact, convex bodies.

This observation lends support to the theory that describes the ring particles as dynamical ephemeral bodies (DEB) (Weidenschilling *et al.*, 1984). According to the authors, small particles in the rings tend to gather together, forming large bodies. However, the large bodies are only temporary agglomerations. Such a large body exhibits a cross-section similar to that for an equivalent large sphere, however, the angular function at intermediate angles may preserve some of the features of the individual constituent particles. Furthermore, the DEB match the concept of conglomerate, loose particles that yield phase functions similar to those observed. Clearly the scattering properties of dynamically ephemeral bodies warrant

additional modeling beyond the scope of this work.

5.4 Extinction

In this section the Mie scattering calculations for power-law distributions are applied to simple scaling laws for extinction. Results are compared to the optical depths derived for the combined A and B ring in §3.2.4. Although the Mie scattering formulation is not applicable to describe the angular variations in brightness, the extinction by irregular particles preserves the shape of the extinction curve (Wang, 1979). However, the oscillation of the extinction curve vanishes for irregular particles and the absolute magnitude of the extinction is slightly greater (see fig. 5.2, page 141). It is understood that the oscillation is a result of interference specific to the geometry of a sphere, and hence vanishes for irregular particles. The increase in magnitude is not well understood, but has some relation to the fact that an irregular particle of the same volume as a sphere has a larger surface area. Nevertheless, we focus here on a qualitative comparison of the extinction properties of power-law distributions.

Cuzzi *et al.* (1980), have shown that the optical depth of the rings at radio wavelengths, $\tau(\lambda)$, can be scaled to the optical depth at visible wavelengths, $\tau(\text{vis})$. That is,

$$\tau(\lambda) = \frac{Q_e(\lambda)}{Q_e(\text{vis})}\tau(\text{vis}). \tag{5.34}$$

We take $Q_e(\text{vis}) = 2.0$, the geometrical optics limit, and $\tau(\text{vis}) = 0.8$, as before. $Q_e(\lambda)$ is calculated for power-law size distributions of ice spheres according to Mie theory. The results for several models are shown in fig. 5.13 along with the observed optical depths presented in Table 3.4 (page 59).

The data point at 3.53 cm was obtained under circumstances of poor resolution, and most likely includes some influence from the C ring optical depth. Thus, it is an underestimate of true optical depth at that wavelength, but is included for completeness. The remaining values are more reliable. They seem to show a peak in optical depth followed by a rapid decrease in optical depth with increasing wavelength. The peak is similar to the peak in the extinction curve (fig. 5.2, page 141). The decrease in optical depths at large wavelengths occurs because of the decreasing opacity of the smaller particles. Clearly the most diagnostic feature of the extinction curves is the position of the peak, which appears to be reproduced in the data at a wavelength of 2.01 cm. The location of this peak seems

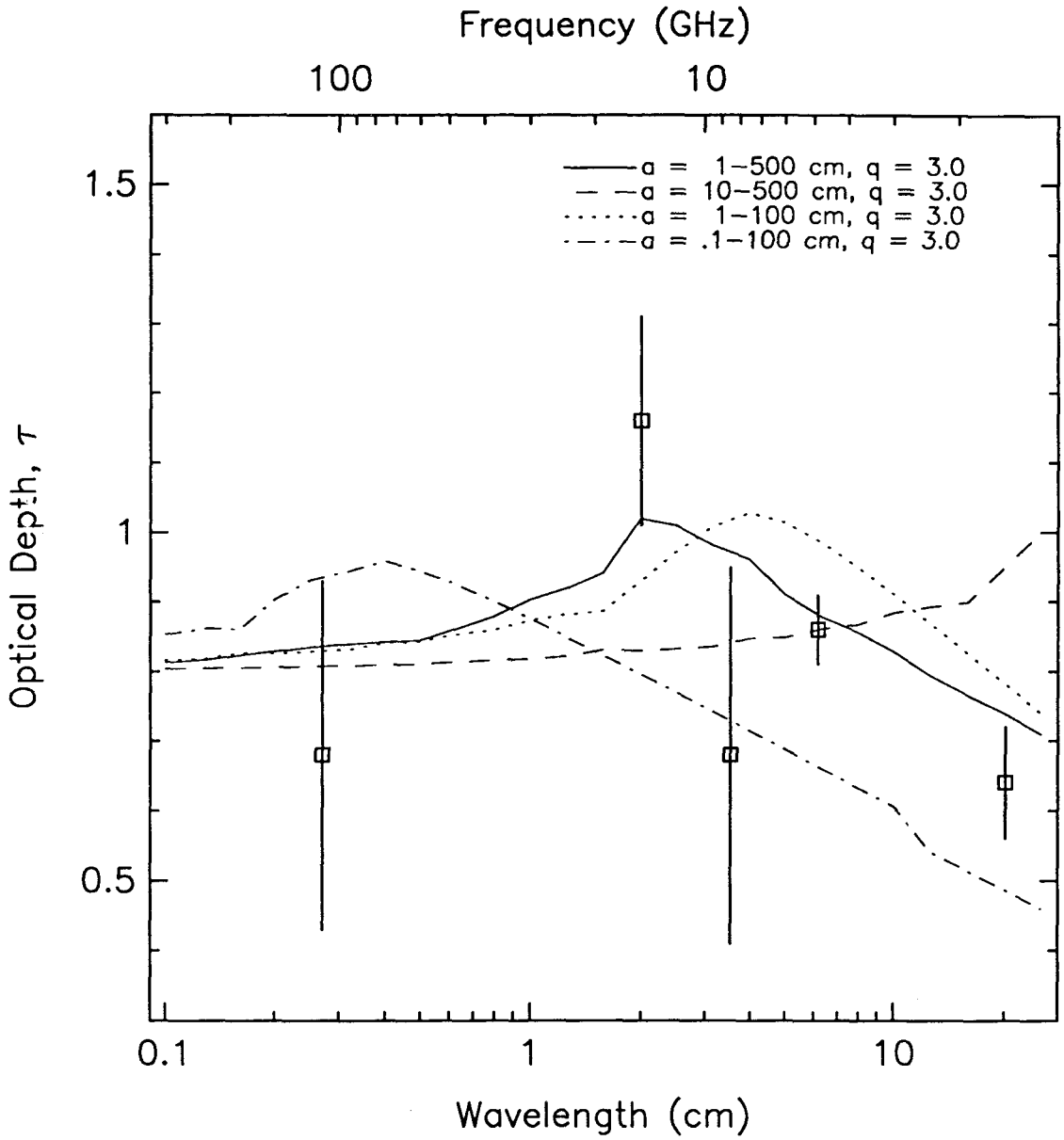

Figure 5.13: Model optical depths of pure water ice spheres with power-law size distributions of the form $n(a) \propto a^{-q}$, calculated from Mie theory and a scaling described in the text. The data points are derived from observations of extinction of emission from Saturn by the rings. The wavelength of the peak optical depth is most diagnostic, and favors a model of particles in the range 1-500 cm described by a power-law index of $q \approx 3$.

to be most sensitive to the lower cutoff of the particle size distribution. Of all the models presented, only the first model (solid line), consisting of particles with radii $1 < a < 500$ cm, exhibits the peak at 2.01 cm followed by a rapid decrease in opacity. The size distribution with a lower limit of $a = 10$ cm presents a constant optical depth out to $\lambda < 10$ cm, and then begins to rise, while the size distribution with a lower limit of $a = 0.1$ cm shows a peak at $\lambda = 0.2$ cm. Clearly these models are ruled out by the observations.

5.5 Summary and Discussion

Observations of emission, scattering, and extinction of radiation by the rings of Saturn can be generally described by Mie scattering theory applied to a power-law size distribution of particles. Although Mie theory only holds for spherical particles, it can approximate the angular integral quantities of single scattering albedo and extinction efficiencies. The specific angular scattering functions, however, are described by an empirical phase function, where the Mie theory does not apply. In addition, it is assumed that the individual particles scatter incoherently. This requires the particles to be separated by more a few radii.

Models of ring thermal emission and isotropic scattering combined with observations at short wavelengths of 0.27 and 2.01 cm place constraints on the size of the largest particles in the ring, the exponent of the power-law, and the mass fraction of uniformly mixed silicates. Although there is a tradeoff between the size of the largest particle in the ring and the exponent of the power-law, the observations favor a size distribution with particles as large as 500 cm described by an exponent in the range $2.6 < q < 3.0$ for the combined A and B rings. This agrees with interpretations of radar observations of Saturn's rings, which yielded an exponent of 3.0 (Cuzzi and Pollack, 1978). Similarly, Voyager radio occultation observations of the A ring determined a value in the range $2.70 < q < 3.03$ (Zebker *et al.*, 1985). The upper limit is not a firm one, but it is also consistent with Voyager radio occultation model for the A ring. It could increase if the particles are porous or if amorphous ice is present.

This size distribution is not consistent with a model of ring evolution that is dominated by fragmentation processes (Greenberg *et al.*, 1977). Such a model predicts a power-law exponent of 3.3. However, an analytic theory to determining the particle size distribution using the so-called "dynamical ephemeral bodies" model yields compatible

results (Longaretti, 1989). This theory predicts an upper size cutoff of $\sim$ 500 cm, and a power-law exponent consistent with that determined from the Voyager radio occultation experiment.

The transparency of ice to microwaves allows impurities to be visible. Thus, models of thermal emission severely restrict the mass fraction of uniformly mixed silicate impurities to less than 1%. This is a stronger constraint than the 10% limit suggested by previous microwave observations (Epstein *et al.*, 1984), but similar to the results of near-infrared observations (Clark and Lucey, 1984), which imply greater than 98% water ice. This result does not rule out scenarios in which the rocky material is not uniformly distributed or segregated from the icy material.

The spectrum of optical depths constrains the lower size limit of the power-law distribution to be $\sim$ 1 cm for the combined A and B ring. Although there is some trade off between the lower limit and the upper limit power-law exponent, lower limits of 10 cm and 0.1 cm are ruled out for upper limits of 500 cm and power-law indexes of $q \sim 3.0$.

The phase function of the particles in Saturn's rings are specific to shape rather than size or composition. Empirically determined scattering phase functions of the ring particles cannot be explained by spherical particles or existing semi-empirical theories for large rough particles (Pollack and Cuzzi, 1980). However, a similarity exists between the empirical phase functions and experimentally determined phase functions for weakly absorbing, irregular particles, and conglomerates of smaller particles. Such a model is also consistent with current theories that describe the ring particles as dynamical ephemeral bodies (Weidenschilling *et al.*, 1984).

The observational constraints on particle composition, size, and shape must be satisfactorily explained by a theory of formation and evolution of Saturn's rings. The low silicate content of the ring material favors a model in which the rings are formed in place, close to the end of the condensation period (Pollack *et al.*, 1976). However, such a conclusion requires the rings to be as old as the solar system, and is in contradiction with estimates of ring age due to collisional dissipation of energy and erosion by micrometeorite bombardment (Northrop and Connerney, 1987). Alternately, the rings may have formed by tidal disruption or collision of satellites or captured bodes. In this case, a consistent theory would also have to explain the apparent segregation of rock and ice in the rings.

Chapter 6

Summary and Conclusions

In this work, the observational methods of radio interferometry and the techniques of synthesis imaging have been successfully applied to imaging the Saturn system. Maps of radio intensity at five wavelengths and polarization at three wavelengths have revealed new features in the atmosphere and rings. This work extends our current knowledge of the atmosphere to deeper levels and presents the first analysis of latitudinal variations with depth. Observations of the rings extend the Voyager result regarding particle size to the thick B ring. The main conclusions are summarized independently for the atmosphere and the rings.

6.1 Conclusions Regarding the Atmosphere

On the basis of comparison between model whole-disk brightnesses and disk-integrated observations, several conclusions can be drawn. The main conclusion of the whole-disk modeling is inescapable, namely that the microwave opacity of the atmosphere increases in the range 1-10 bar. The most likely explanation is that the abundance of NH_3 vapor increases from a value of 0.5–0.65 times solar just below the NH_3 ice clouds to a maximum of 3–4 times solar at a pressure of 6 bar. No other microwave absorber exists in sufficient concentration to account for this observation. A similar conclusion was reached by Briggs and Sackett (1989), in their analysis of whole-disk observations.

The mechanism by which the vertical distribution of NH_3 deviates from an expected uniform distribution is unclear. However, a thermo-chemical model can satisfy the observations by postulating an enrichment of H_2S, by a factor of 11 to 14 times solar. This requirement can be relaxed if another mechanism can act to control the vertical distribution of NH_3. The presence of H_2O cannot be confirmed or ruled out on the basis of current observations. Nevertheless, the enrichment of the volatiles CH_4, NH_3, and H_2S in the atmo-

sphere of Saturn can be accounted for by the core-instability model of formation (Pollack and Bodenheimer, 1989).

This work presents a detailed analysis and inversion of zonally-averaged brightness temperatures at wavelengths of 2, 6, and 20 cm which indicate latitudinal variations in ammonia concentrations within the condensate cloud layer as well as below the NH_3 cloud. The ammonia profile below the cloud shows a latitudinal structure of alternating enhancement and depletion similar to the zonal variability observed in the belts and zones of Jupiter (Gierasch *et al.*, 1986). This similarity suggests that vertical motions associated with meridional circulation are responsible for producing the latitudinal variations of ammonia. According to this hypothesis, the regions of high ammonia concentration are due to rising parcels of ammonia-rich gas. The ammonia condenses into a particulate NH_4SH cloud and an ice cloud within the rising column. The parcel, now relatively depleted in ammonia vapor, descends in an adjacent cell, which appears as a region of ammonia depletion.

A hot band observed at northern mid-latitudes at 25–50°appears as a region of ammonia depletion. This latitude is correlated with a decreased infrared opacity and depressed cloud top levels and suggests the presence of large-scale downwelling existing over 4 scale heights. However, there is no apparent correlation with the zonal wind field.

Finally, the ammonia vapor abundance within the cloud decreases by 50% from equator to pole. This variation cannot be accounted for by current models and requires further analysis.

6.2 Conclusions Regarding the Rings

Models of ring thermal emission and isotropic scattering, combined with observations at short wavelengths of 0.27 and 2.01 cm, place constraints on the size of the largest particles in the ring, the exponent of the power law, and the mass fraction of uniformly mixed silicates. Although there is a tradeoff between the size of the largest particle in the ring and the exponent of the power law, the observations favor a size distribution with particles as large as 500 cm described by an exponent in the range $2.6 < q < 3.0$ for the combined A and B rings. This agrees with interpretations of radar observations of Saturn's rings which yielded an exponent of 3.0 (Cuzzi and Pollack, 1978). Similarly, Voyager radio occultation observations of the A ring determined a value in the range $2.70 < q < 3.03$ (Zebker *et al.*, 1985). The upper limit is not a firm one, but it is consistent with Voyager

radio occultation models for the A ring. It could increase if the particles are porous or if amorphous ice is present.

The transparency of ice to microwaves allows impurities to be visible. Thus, models of thermal emission severely restrict the mass fraction of uniformly mixed silicate impurities to less than 1%. This is a stronger constraint than the 10% limit suggested by previous microwave observations (Epstein *et al.*, 1984), but similar to the results of near-infrared observations (Clark and Lucey, 1984), which imply greater than 98% water ice. This result does not rule out scenarios in which the rocky material is not uniformly distributed or segregated from the icy material.

The spectra of optical depths constrain the lower size limit of the power law distribution to be $\sim$ 1 cm for the combined A and B ring. Although there is some tradeoff between the lower limit, the upper limit, and the power law exponent, lower limits of 10 cm and 0.1 cm are ruled out for upper limits of 500 cm and power law indexes of $q \sim 3.0$.

The scattering phase function of the particles in Saturn's rings is specific to shape rather than size or composition. An empirically determined scattering phase function of the ring particles cannot be explained by spherical particles or existing semi-empirical theories for large rough particles (Pollack and Cuzzi, 1980). However, a similarity exists between the empirical phase function and experimentally determined phase functions for a weakly absorbing, conglomerate of loose particles. Such a model is also consistent with current theories that describe the ring particles as dynamical ephemeral bodies (Weidenschilling *et al.*, 1984).

6.3 Directions for Future Studies

The results of this investigation of microwave emission from Saturn's atmosphere and rings raise more questions than answers. The following is a brief summary of additional research topics that might prove fruitful for future investigation.

The conclusions of this work would naturally benefit from additional microwave observations of Saturn. For example, this work has not addressed any issues regarding the time-variability of the Saturn system. Much could be learned from consistent and uniform monitoring of the planet and rings. Any information about the seasonal variability of the atmospheric composition, temperature, and dynamics would greatly improve our understanding of the physical processes active in the atmosphere. Observations of the rings

at different ring inclinations may constrain models of the vertical distribution of the ring particles.

Observations at new wavelengths would also improve current models. Good observations at wavelengths longer than 20 cm would probe deeper levels of the atmosphere and may provide the first unambiguous detection of water in the atmosphere. Additional observations at shorter wavelengths can constrain the composition of the rings.

All these observations would of course benefit from improved models and laboratory measurements. Two crucial measurements in this area are determining the appropriate line-shape for foreign gas broadening of the ammonia inversion lines at millimeter wavelengths, and measurements of the scattering phase function of candidate ring particles.

Our next leap of knowledge about the Saturn system must wait until the year 2002, when the Cassini spacecraft is scheduled to be inserted into a highly elliptical orbit about the planet. This mission may realize the true potential of microwave remote sensing. The strawman payload calls for the implementation of two microwave sensing experiments in addition to the radio science subsystem. These two instruments are a long-wavelength radiometer, called the Saturn atmosphere mapper (SAM), and a microwave spectrometer and radiometer (MSAR).

These instruments have the combined capability to carry out the types of studies presented in this thesis with improved accuracy and resolution. The SAM instrument has the potential to probe the deep atmosphere of Saturn at wavelengths of 2, 3.5, and 13 cm, and will return full three-dimensional data maps of temperature and composition in a matter of hours. The MSAR instrument can accurately map the brightness of the rings at 0.13, 0.17, and 1.2 cm, and determine the ring particle composition. It is hoped that this study has shown the enormous potential of microwave remote sensing of the planets.

Bibliography

Angel, J. R. P. (1974) Mechanisms that produce linear and circular polarization. In *Planets, Stars and Nebulae Studies with Photopolarimetry* (T. Gehrels, Ed.), pp. 54–63. University of Arizona Press, Tucson.

Atreya, S. K. (1986). *Atmospheres and Ionospheres of the Outer Planets and Their Satellites.* Springer-Verlag, Berlin.

Atreya, S. K. and P. N. Romani (1985). Photochemistry and clouds of Jupiter, Saturn and Uranus. In *Recent Advances in Planetary Meteorology* (G. E. Hunt, Ed.), pp. 17–68. Cambridge University Press, Cambridge.

Baars, J. W. M., R. Genzel, I. I. Pauliny-Toth, and A. Witzel (1977). The absolute spectrum of Cas A: an accurate flux density scale and a set of secondary calibrators. *Astron. Astrophys.* **61**, 99–106.

Ben-Reuven, A. (1966). Impact broadening of microwave spectra. *Phys. Rev.* **145**, 7–22.

Berge, G. L. and S. Gulkis (1976). Earth-based observations of Jupiter, millimeter to meter wavelengths. In *Jupiter* (T. Gehrels, Ed.), pp. 621–692. University of Arizona Press, Tucson.

Berge, G. L. and D. O. Muhleman (1973). High-angular-resolution observations of Saturn at 21.1-centimeter wavelength. *Astrophys. J.* **185**, 373–381.

Berge, G. L. and R. B. Read (1968). The microwave emission of Saturn. *Astrophys. J.* **152**, 755–764.

Bézard, B. (1985). Thermal structure of Saturn's atmosphere. In *The Atmospheres of Saturn and Titan*, ESA SP-241, (E. Rolfe and B Battrick, Eds.), pp. 21–31. European Space Agency, Paris.

Bézard, B., D. Gautier, and B. Conrath (1984). A seasonal model of the Saturnian upper troposphere: Comparison with Voyager infrared measurements. *Icarus* **60**, 274–288.

Bézard, B., A. Marten, J. P. Baluteau, D. Gautier, J. Flaud, and C. Camy-Peyret (1983). On the detectability of H_2S in Jupiter. *Icarus* **55**, 259-271.

Bohlander, R. A., R. W. McMillan, and J. J. Gallagher (1985). Atmospheric effects on near-millimeter-wave propagation. *Proc. IEEE* **73**, 49–60.

Born, M. and E. Wolf (1980). *Principles of Optics,* sixth edition. Pergamon Press, Oxford.

Briggs, F. H. (1974). The microwave properties of Saturn's rings. *Astrophys. J.* **189**, 367–377.

Briggs, F. H. (1973). Observations of Uranus and Saturn by a new method of radio interferometry of faint moving sources. *Astrophys. J.* **182**, 999–1011.

Briggs, F. H. and P. D. Sackett (1989). Radio observations of Saturn as a probe of its atmosphere and cloud structure. *Icarus* **80**, 77–103.

Cameron, A. G. W. (1982). Elementary and nuclidic abundances in the solar system. In *Essays in Nuclear Astrophysics* (C. A. Barnes, D. D. Clayton, and D. N. Schramon, Eds.), pp. 23–43. Cambridge University Press, Cambridge.

Campbell, M. J. and J. Ulrichs (1969). Electrical properties of rocks and their significance for Lunar radar observations. *J. Geophys. Res.* **74**, 5867–5881.

Carlson, B. E., W. B. Rossow, and G. S. Orton (1988). Cloud microphysics of the giant planets. *J. Atmos. Sci.* **45**, 2066–2081.

Chandrasekhar, S. (1960). *Radiative Transfer.* Dover, New York.

Chang, A. T. C. and T. T. Wilheit (1979). Remote sensing of atmospheric water vapor, liquid water, and wind speed at the ocean surface by passive microwave techniques from the Nimbus 5 satellite. *Radio Science* 14(5), 793-802.

Chýlek P., G. W. Grams, and R. G. Pinnick (1976). Light scattering by irregular randomly oriented particles. *Science* **193**, 480–482.

Clark, B. G. (1980). An efficient implementation of the algorithm CLEAN. *Astron. Astrophys.* **79**, 377–378.

Clark, B. G. and A. D. Kuz'min (1965). The measurement of the polarization and brightness distribution of Venus at 10.6 cm wavelength. *Astrophys. J.* **142**, 23–44.

Clark, R. N. and P. G. Lucey (1984). Spectral properties of ice-particulate mixtures and implications for remote sensing. 1. Intimate mixtures. *J. Geophys. Res.* **89**, 6341–6348.

Coffeen, D. L. and J. E. Hansen (1974). Polarization studies of planetary atmospheres. In *Planets, Stars, and Nebulae Studied with Photopolarimetry* (T. Gehrels, Ed.), pp. 518–581. University of Arizona Press, Tucson.

Conrath, B. J., D. Gautier, R. A. Hanel, and J.S. Hornstein (1984). The helium abundance of Saturn from Voyager measurements. *Astrophys. J.* **282**, 807–815.

Conrath, B. J. and J. A. Pirraglia (1983). Thermal structure of Saturn from Voyager infrared measurements: Implications for atmosphere dynamics. *Icarus* **53**, 286–292.

Cornwell, T. J (1989). The applications of closure phase to astronomical imaging. *Science* **245**, 263–269.

Courtin, R., N. Coron, T. Encrenaz, R. Gispert, P. Bruston, G. Leblanc, G. Dambier, and A. Vidal-Madjar (1977). Observations of the giant planets and 1.4 mm and consequences on the effective temperatures. *Astron. Astrophys.* **60**, 115–123.

CRC Press (1983). *CRC Handbook of Chemistry and Physics* (R. C. Weast, Ed.). CRC Press, Boca Raton, Florida.

Cuzzi, J. N (1985). Rings of Uranus: not so thick, not so black. *Icarus* **63**, 312–316.

Cuzzi, J. N. and W. A. Dent (1975). Saturn's rings: the determination of their brightness temperature and opacity at centimeter wavelengths. *Astrophys. J.* **198**, 223–227.

Cuzzi, J. N., J. J. Lissauer, L. W. Esposito, J. B. Holberg, E. A. Marouf, G. L. Tyler, and A. Boischot (1984). Saturn's rings: particles and processes. In *Planetary Rings* (R. Greenberg and A. Brahic, Eds.), pp. 73-199. University of Arizona Press, Tucson.

Cuzzi, J. N., J. B. Pollack, and A. L. Summers (1980). Saturn's rings: particle composition and size distribution as constrained by microwave observations. II. Radio interferometric observations. *Icarus* **44**, 683–705.

Cuzzi, J. N. and J. B. Pollack (1978). Saturn's rings: particle composition and size distribution as constrained by microwave observations I. Radar observations. *Icarus* **33**, 233–262.

Cuzzi, J. N. and D. van Blerkom (1974). Microwave brightness of Saturn's rings. *Icarus* **22**, 149–158.

Dollfus, A. (1979a). Optical reflectance polarimetry of Saturn's globe and rings I. *Icarus* **37**, 404–419.

Dollfus, A. (1979b). Optical reflectance polarimetry of Saturn's globe and rings II. *Icarus* **40**, 171–179.

Dollfus, A. (1961). Polarization studies of the planets. In *Planets and Satellites* (G. P. Kuiper Ed.), pp. 343–399. University of Chicago Press, Chicago.

Dowling, T. E., D. O. Muhleman, and G. L. Berge (1987). Aperture synthesis observations of Saturn and its rings at 2.7-mm wavelength. *Icarus 70,* 506–516.

Epstein, E. E., M. A. Janssen, and J. N. Cuzzi (1984). Saturn's rings: 3-mm low-inclination observations and derived properties. *Icarus* **58**, 403–411.

Epstein, E. E., M. A. Janssen, J. N. Cuzzi, W. G. Fogarty, and J. Mottman (1980). Saturn's rings: 3-mm observations and derived properties. *Icarus* **41**, 103–118.

Esposito, L. W., J. N. Cuzzi, J. B. Holberg, E. A. Marouf, G. L. Tyler, and C. C. Porco (1984). Saturn's rings: structures, dynamics, and particle properties. In *Saturn* (T. Gehrels, Ed.), pp. 463–545. University of Arizona Press, Tucson.

Esposito, L. W., M. O'Callaghan, K. E. Simmons, C. W. Hord, and R. A. West (1983). Voyager photopolarimeter stellar occultations of Saturn's rings. *J. Geophys. Res.* **88**, 8643–8649.

Flasar, F. M. (1987). Temporal behavior of Jupiter's meteorology. In *Time-Variable Phenomena in the Jovian System*, NASA SP–492, (M. J. S. Belton, R. A. West, and J. Rahe, Eds.), pp. 324-343. NASA, Washington, DC.

Fomalont, E. B. and M. C. H. Wright (1974). Interferometry and aperture synthesis. In *Galactic and Extra-Galactic Radio Astronomy* (G. L. Vershur and K. I. Kellerman, Eds.), chapter 10, pp. 256–290. Springer–Verlag, New York.

Franklin, F. A., A. F. Cook II, R. T. F. Barney, C. A. Roff, G. E. Hunt, and H. B. Rueda (1987). Voyager observations of the azimuthal brightness variations in Saturn's rings. *Icarus* **69**, 280–296.

Friedson, J. and A. P. Ingersoll (1987). Seasonal meridional energy balance the thermal structure of the atmosphere of Uranus: a radiative-convective-dynamical model. *Icarus* **69**, 135-156.

Froidevaux, L. (1981). Saturn's rings: infrared brightness variations with solar elevation. *Icarus* **46**, 4–17.

Gierasch, P. J., B. J. Conrath, and J. A. Magalhães (1986). Zonal mean properties of Jupiter's upper troposphere from Voyager infrared observations. *Icarus* **67**, 456–483.

Giese, R. H., K. Weiss, R. H. Zerull, and T. Ono (1978). Large fluffy particles: A possible explanation of the optical properties of interplanetary dust. *Astron. Astrophys.* **65**, 265–272.

Goldstein, R. M. and G. A. Morris (1973). Radar observations of the rings of Saturn. *Icarus* **20**, 260–262.

Goodman, G. C. (1969). *Models of Jupiter's Atmosphere.* Ph.D. thesis, University of Illinois, Urbana.

Greenberg, J. M., R. T. Wang, and L. Bangs (1971). Extinction by rough particles and the use of Mie theory. *Nature Phys. Sci.* **230**, 110.

Gresh, D. L. (1990). *Voyager Radio Occultation by the Uranian Rings: Structure, Dynamics, and Particle Sizes.* Ph.D. thesis, Stanford University.

Grossman, A. W., D. O. Muhleman, and G. L. Berge (1989). High-resolution microwave images of Saturn. *Science* **245**, 1211–1215.

Grossman, A. W., D. O. Muhleman, and G. L. Berge (1988). Ammonia and temperature variations in Saturn's deep atmosphere. *Bull. Amer. Astron. Soc.* **20**, 880.

Grossman, A. W., D. O. Muhleman, and G. L. Berge (1987). High resolution observations of Saturn at 6 cm. *Bull. Amer. Astron. Soc.* **19**, 848.

Gulkis, S., M. A. Janssen, and E. T. Olsen (1978). Evidence for the depletion of ammonia in the Uranus atmosphere. *Icarus* **34**, 10–19.

Gulkis, S., T. R. McDonough, and H. Craft (1969). The microwave spectrum of Saturn. *Icarus* **10**, 421–427.

Hanel, R., B. Conrath, F. M. Flasar, V. Kunde, W. Maguire, J. Pearl, J. Pirraglia, R. Samuelson, D. Cruikshank, D. Gautier, P. Gierasch, L. Horn, and C. Ponnamperuma (1982). Infrared observations of the Saturnian system from Voyager 2. *Science* **215**, 544–548.

Hansen, J. E. (1971). Multiple scattering of polarized light in planetary atmospheres. Part III. Sunlight reflected by terrestrial water clouds. *J. Atmos. Sci.* **28**, 1400–1426.

Hansen, J. E. and L. D. Travis (1974). Light scattering in planetary atmospheres. *Space Sci. Rev* **16**, 527–610.

Hodkinson, J. R. (1963). Light scattering and extinction by irregular particles larger than the wavelength. In *Electromagnetic Scattering* (M. Kerker, Ed.) pp. 87–100. Pergamon Press, New York.

Hofstadter, M. D., G. L. Berge, and D. O. Muhleman (1990). Vertical motions in the Uranian atmosphere: an analysis of radio observations. *Icarus* **84**, 261–267.

Hofstadter, M. D., and D. O. Muhleman (1988). Latitudinal variations of ammonia in the atmosphere of Uranus: an analysis of microwave observations. *Icarus* **81**, 396–412.

Hogbom, J. (1974). Aperture synthesis with non-regular distribution of interferometer baselines. *Astrophys. J. Supp. Ser.* **15**, 417–426.

Houghton, J. T., F. W. Taylor, and C. D. Rogers (1984). *Remote Sounding of Atmospheres.* Cambridge University Press, Cambridge.

Hubbard, W. B. and M. S. Marley (1989). Optimized Jupiter, Saturn, and Uranus interior models. *Icarus* **78**, 102–118.

van de Hulst, H. C. (1957). *Light Scattering by Small Particles.* Dover Publications Inc., New York.

Ingersoll, A. P. and C. C. Porco (1978). Solar heating and internal heat flow on Jupiter. *Icarus* **35**, 27-43.

Janssen, M. A. and E. T. Olsen (1978). A measurement of the brightness temperature of Saturn's rings at 8-mm wavelength. *Icarus* **33**, 263–278.

Jennison, R. C. (1958). A phase sensitive interferometer technique for the measurement of the Fourier transforms of spatial brightness distributions of small angular extent. *Mon. Not. Roy. Astron. Soc.* **118**, 276–284.

Kaiser, M. L., M. D. Desch, W. S. Kurth, A. Lecacheux, F. Genova, B. M. Pedersen, and D. R. Evans (1984). Saturn as a radio source. In *Saturn* (T. Gehrels, Ed.), pp. 378-415. University of Arizona Press, Tucson.

Kawata, Y. (1983). Infrared brightness temperatures of Saturn's rings based in the inhomogeneous multilayer assumption. *Icarus* **56**, 453–464.

Klein, M. J., M. A. Janssen, S. Gulkis, and E. T. Olsen (1978). Saturn's microwave spectrum: implications for the atmosphere and the rings. In *The Saturn System*, NASA CF–2068, (D. M. Hunten and D. Morrison, Eds.), pp. 195–216. NASA, Washington, DC.

Krotikov, V. D. and S. A. Pelyushenko (1987). On using the moon as a source with a standard intensity in the 0.1-30 cm wavelength range. *Sov. Astron.* **31**, 216–219.

Kuiper, G. P., D. P. Cruikshank, and U. Fink (1970). The composition of Saturn's rings. *Sky and Telescope* **39**, 14.

Larson, H. P., D. S. Davis, R. Hofmann, and G. L. Bjoraker (1984). The Jovian atmospheric window at 2.7 μm: A search for H_2S. *Icarus* **60**, 621–639.

Lewis, J. S. (1969). The clouds of Jupiter and the NH_3–H_2O and NH_3–H_2S systems. *Icarus* **10**, 365–378.

Liebe, H. J. (1985). An updated model for millimeter wave propagation in moist air. *Radio Science* 20(5), 1069–1089.

Lindal, G. F., D. N. Sweetnam, and V. R. Eshleman (1985). The atmosphere of Saturn: an analysis of the Voyager radio occultation measurements. *Astrophys. J.* **90**, 1136–1146.

Liou, K. N., and J. E. Hansen (1971). Intensity and polarization for single scatting by polydisperse spheres: a comparison of ray optics and Mie theory. *J. Atmos. Sci.* **28**, 995–1004.

Longaretti, P. Y. (1990). Saturn's main ring particle size distribution: An analytic approach. *Icarus* **80**, 51-73.

Luthey, J. L (1973). Possibility of Saturnian synchrotron radiation. *Icarus* **20**, 125–135.

Lumme, K. A., W. M. Irvine, and L. W. Esposito (1983). Theoretical interpretations of the ground-based photometry of Saturn's B ring. *Icarus* **53**, 174–184.

Lunine, J. I. (1989). Origin and evolution of outer solar system atmospheres. *Science* **245**, 141-147.

Lyot, B. (1929). Recherches sur la polarisation de la lumière de planètes et de quelques substances terrestres. *Ann. Obs. Meudon VIII,* In English: NASA TTF-187.

Marouf, E. A., G. L. Tyler, and P. A. Rosen (1986). Profiling Saturn's rings by radio occultation. *Icarus* **68**, 120–166.

Marouf, E. A., G. L. Tyler, H.A. Zebker, R. A. Simpson, and V. R. Eshleman (1983). Particle size distributions in Saturn's rings from Voyager 1 radio occultation. *Icarus* **54**, 189–211.

Massie, S. T. and D. M. Hunten (1982). Conversion of *para* and *ortho* hydrogen in the Jovian planets. *Icarus* **49**, 213–226.

Masson, C. R., G. L. Berge, M. J. Claussen, G. M. Heiligman, R. B. Leighton, K. Y. Lo, A. T. Moffet, T. G. Phillips, A. I. Sargent, S. L. Scott, D. P. Woody, and A. Young

(1985). The Caltech millimeter wave interferometer. In *International Symposium on Millimeter and Submillimeter Wave Astronomy,* pp. 65–74. U.R.S.I., Granada, Spain.

Mishima, O., D. D. Klug, and E. Whalley (1983). The far-infrared spectrum of ice Ih in the range 8-25 cm^{-1}. Sound waves and difference bands, with application to Saturn's rings. *J. Chem. Phys.* **78,** 6399–6404.

Morris, E. C. and R. W. Parsons (1970). Microwave absorption by gas mixtures at pressures up to several hundred bars. *Austr. J. Phys.* **23,** 335–349.

Mugnai, A. and W. J. Wiscombe (1986). Scattering from nonspherical Chebyshev particles. 1: Cross sections, single scattering albedo, asymmetry factor, and backscattered fraction. *Appl. Opt.* **25,** 1235.

Muhleman, D. O. and G. L. Berge (1990). Observations of Mars, Uranus, Neptune, Io, Europa, Ganymede and Callisto at a wavelength of 2.66 millimeters. *Icarus*, submitted.

Muhleman, D. O. and G. L. Berge (1982). Microwave emission from Saturn's rings. In *Planetary Rings* (A. Brahic, Ed.), pp. 57–70. I.A.U., Cepadues-Editions. Toulouse, France.

Napier, P. J., A. R. Thompson, and R. D. Ekers (1983). The Very Large Array: design and performance of a modern synthesis radio telescope. *Proc. IEEE* **71,** 1295–1322.

National Radio Astronomy Observatory (1986). *Aips Cookbook.* NRAO, Charlottesville, VA.

Newhall, X. X., R. A. Preston, and P. B. Esposito (1984). Relating the JPL VLBI reference frame and the planetary ephemerides. In IAU Symposia No. 109: *Astrometric Techniques.* Gainseville, Florida.

Northrop, T. G. and J. E. P. Connerney (1987). A micrometeorite erosion model and the age of Saturn's rings. *Icarus* **70,** 124-137.

Ostro, S. J., G. H. Pettengill, D. B. Campbell, and R. M. Goldstein (1982). Delay-doppler radar observations of Saturn's rings. *Icarus* **49,** 367–381.

de Pater, I. (1986). Jupiter's zone-belt structure at radio wavelengths. *Icarus* **68,** 344-365.

de Pater, I. and J. R. Dickel (1982). VLA observations of Saturn at 1.3, 2 and 6 cm. *Icarus* **50,** 88–102.

de Pater, I. and S. T. Massie (1985). Models of the millimeter–centimeter spectra of the giant planets. *Icarus* **62**, 143–171.

de Pater, I. and M. Richmond (1989). Neptune's microwave spectrum from 1 mm to 20 cm. *Icarus* **80**, 1-13.

Pearson, T. J. and A. C. S. Readhead (1984). Image formations by self-calibration in radio astronomy. *Ann. Rev. Astron. and Astrophys. 22,* 97–130.

Perley, R. A., F. R. Schwab, and A. H. Bridle, Eds. (1979). *Synthesis Imaging in Radio Astronomy,* Astronomical society of the Pacific conference series, volume 6. San Francisco.

Pilcher, C. B., C. R. Chapman, L. A. Lebofsky, and H. H. Kieffer (1970) Saturn's rings: Identification of water frost. *Science* **178**, 1087–1089.

Pollack, J. B. and P.Bodenheimer (1989). Theories of the origin and evolution of the giant planets. In *Origin and Evolution of Planetary and Satellite Atmospheres* (S. K. Atreya, J. B. Pollack, and M.S. Mathews, Eds.), pp. 564–602. University of Arizona Press, Tucson.

Pollack, J. B. and J. N. Cuzzi (1980). Scattering by nonspherical particles of size comparable to the wavelength: a new semi-empirical theory and its application to tropospheric aerosols. *J. Atmos. Sci.* **37**, 868–881.

Pollack, J. B., A. S. Grossman, R. Moore, and H. C. Graboske, Jr. (1976). The formation of Saturn's satellites and rings, as influenced by Saturn's contraction history. *Icarus* **29**, 35-48.

Pollack, J. B., A. Summers, and B. Baldwin (1973). Estimates of the size of the particles in the rings of Saturn and their cosmogonic implications. *Icarus* **20**, 263–278.

Poynter, R. L. and R. K. Kakar (1975). The microwave frequencies, line parameters, and spectral constants for $^{14}NH_3$. *Astrophys. J. Supp. Ser.* **29**, 87–96.

Rudy, D. J. (1987). *Mars: High Resolution VLA Observations at Wavelengths of 2 and 6 cm and Derived Properties.* Ph.D. thesis, California Institute of Technology.

Schloerb, F. P., D. O. Muhleman, and G. L. Berge (1980). Interferometry of Saturn and its rings at 1.30-cm wavelength. *Icarus* **42**, 125–135.

Schloerb, F. P., D. O. Muhleman, and G. L. Berge (1979b). Interferometric observations of Saturn and its rings at a wavelength of 3.71 cm. *Icarus* **39**, 214–231.

Schloerb, F. P., D. O. Muhleman, and G. L. Berge (1979a). An aperture synthesis study of Saturn and its rings at 3.71-cm wavelength. *Icarus* **39**, 232–250.

Schloerb, F. P., D. O. Muhleman, and G. L. Berge (1976). Lunar heat flow and regolith structure inferred from interferometric observations at a wavelength of 49.3 cm. *Icarus* **29**, 329–341.

Schuerman, D. W. (1979). *Light Scattering by Irregularly Shaped Particles.* Plenum, New York.

Schwab, F. R. (1984). Relaxing the isoplanatism assumption in self-calibration; applications to low-frequency radio interferometry. *Astrophys. J.* **89**, 1076–1081.

Schwartz, U. J. (1978). Mathematical-statistical description of the iterative beam removing technique (method CLEAN). *Astron. Astrophys.*, **65**, 345–356.

Smith, B. A., L. Soderblom, R. F. Beebe, J. M. Boyce, G. Briggs, A. Bunker, S. A. Collins, C. Hansen, T. V. Johnson, J. L. Mitchell, R. J. Terrile, M. H. Carr, A. F. Cook, J. N. Cuzzi, J. B. Pollack, G. E. Danielson, A. P. Ingersoll, M. E. Davies, G. E. Hunt, H. Masursky, E. M. Shoemaker, D. Morrison, T. Owen, C. Sagan, J. Veverka, R. Strom, and V. E. Suomi (1981). Encounter with Saturn: Voyager 1 imaging science results. *Science* **212**, 163–191.

Spilker, T. R. and V. R. Eshleman (1988). A new formalism for predicting microwave absorption by ammonia based on laboratory measurements under varying conditions. *Bull. Amer. Astron. Soc.* **20**, 867.

Standish, M. E. (1982). Orientation of the JPL ephemerides, DE200/JE200, to the dynamical equinox of J2000. *Astron. Astrophys.* **114**, 297.

Steffes, P. G. and J. M. Jenkins (1987). Laboratory measurements of the microwave opacity of gaseous ammonia (NH_3) under simulated conditions for the Jovian atmosphere. *Icarus* **72**, 35-47.

Thompson, A. R., J. M. Moran, and G. W. Swenson Jr. (1986). *Interferometry and Synthesis in Radio Astronomy.* John Wiley & Sons, New York.

Tomasko, M. G., R. A. West, G. S. Orton, and V. G. Tejfel (1984). Clouds and aerosols in Saturn's atmosphere. In *Saturn* (T. Gehrels, Ed.), pp. 150–194. University of Arizona Press, Tucson.

Trafton, L. M., (1967). Model atmospheres of the major planets. *Astrophys. J.* **147,** 765-781.

Tyler, G. L., V. R. Eshleman, J. D. Anderson, G. S. Levy, G. F. Lindal, G. E. Wood, and T. A. Croft (1981). Radio science investigations of the Saturn system with Voyager 1: preliminary results. *Science* **212,** 201–206.

Tyler, G. L., E. A. Marouf, R. A. Simpson, H. A. Zebker, and V. R. Wshleman (1983). The microwave opacity of Saturn's rings at wavelengths of 3.6 and 13 cm from Voyager 1 radio occultation. *Icarus* **54,** 160–188.

Ulich, B. L. (1981). Millimeter-wavelength continuum calibration sources. *Astron. J.* **86,** 1619–1626.

Ulich, B. L., J. R. Dickel, and I. de Pater (1984). Planetary observations at a wavelength of 1.32 mm. *Icarus* **60,** 590–598.

Valdes, F., W. J. Welch, and D. Haber (1982). The Jovian ammonia abundance from interferometric observations of limb darkening at 3.4 mm. *Icarus* **49,** 17–26.

Visconti, G. (1981). Penetration of solar UV radiation and photodissociation in the Jovian Atmosphere. *Icarus* **45,** 638–652.

Wallace, L. (1980). The structure of the Uranus atmosphere. *Icarus* **43,** 231–259.

Wardle, J. F. C. and P. P. Kronberg (1974). The linear polarization of quasi-stellar radio sources at 3.71 and 11.1 centimeters. *Astrophys. J.* **194,** 249–255.

Weidenschilling, S. J., C. R. Chapman, D. R. Davis, and R. Greenberg (1984). Ring particles: Collisional interaction and physical nature. In *Planetary Rings* (R. Greenberg and A. Brahic, Eds.), pp. 367–415. University of Arizona Press, Tucson.

Weidenscilling, S. J., and J. S. Lewis (1973). Atmospheric and cloud structure of the Jovian planets. *Icarus* **20,** 465–476.

Werner, M. W., G. Neugebauer, J. R. Houck, and M. G. Hauser (1978). One-millimeter brightness temperatures of the planets. *Icarus* **35**, 289–296.

Wang, R. T. (1979). Extinction signatures of non-spherical/non-isotropic particles. In *Light Scattering by Irregularly Shaped Particles* (D. W. Schuerman, Ed.,) pp. 255–272. Plenum, New York.

Whalley, E. and H. J. Labbé, (1969). Optical spectra of orientationally disordered crystals III. Infrared spectra of the sound waves. *J. Chem. Phys.* **51**, 3120–3127.

Wiscombe, W. J. (1980). Improved Mie scattering algorithms. *Appl. Opt.* **19**, 1505–1509.

Wiscombe, W. J., and A. Mugnai (1988). Scattering from nonspherical Chebyshev particles. 2: Means of angular scattering patterns. *Appl. Opt.* **27**, 2405–2412.

Woody, D. P., R. E. Millera, and M. J. Wengler (1895). 85-115–GHz receivers for radio astronomy. *IEEE Trans. Microwave Theory and Techniques* **MTT-33**, 90–95.

Wrixon, G. T. and W. J. Welch (1970). The millimeter wave spectrum of Saturn. *Icarus* **13**, 163–172.

Wrixon, G. T., W. J. Welch, and D. D. Thornton (1971). The spectrum of Jupiter at millimeter wavelengths. *Astrophys. J.* **169**, 171–183.

Zebker, H. A., E. A. Marouf, and G. L. Tyler (1985). Saturn's rings: particle size distributions for thin layer models. *Icarus* **64**, 531–548.

Zerull, R. and R. H. Giese (1974). Microwave analogue studies. In *Planets, Stars, and Nebulae Studies with Photopolarimetry* (T. Gehrels, Ed.), pp. 518–581. University of Arizona Press, Tucson.

Zerull, R. H., R. H. Giese, S. Schwill, and K. Weiss (1979). Scattering by particles of nonspherical shape. In *Light Scattering by Irregularly Shaped Particles* (D. W. Schuerman, Ed.,) pp. 273–282. Plenum, New York.

Zerull, R. H., R. H. Giese, and K. Weiss (1977). Scatting functions of nonspherical dielectric and absorbing particles vs Mie theory. *Appl. Opt.* **16**, 777–778.

Zharkov, V. N. and V. P. Trubitsyn (1978). *Physics of Planetary Interiors* (W.B. Hubbard, Ed.), vol. 6 of *Astronomy and Astrophysics Series*. Pachart Publishing House, Tucson.